Impact of Porosity on the Charge Transport in Mesoporous Oxides and Composite Materials

Einfluss der Porosität auf den Ladungstransport in mesoporösen Oxiden und Kompositmaterialien

Dissertation

zur Erlangung des Grades

Doktor der Naturwissenschaften

− Dr. rer. nat. −

vorgelegt dem

Fachbereich Mathematik und Informatik, Physik, Geographie

der Justus-Liebig-Universität Gießen

von

Erdogan Celik

Laubach, Juni 2022

Dekan / dean	Prof. Dr. Stefan B. Hennemann
1. Gutachter / 1st reviewer	Dr. Matthias T. Elm
2. Gutachter / 2nd reviewer	Prof. Dr. Peter J. Klar
Eingereicht / submitted	Juni / June 2022

Danksagung

Zu aller erst möchte ich Dr. Matthias T. Elm für die Aufnahme in die Arbeitsgruppe, die allzeitige Unterstützung und das entgegengebrachte Vertrauen danken. Seine hervorragende persönliche Betreuung und fachliche Unterstützung haben maßgeblich zum Erfolg meiner wissenschaftlichen Arbeit beigetragen.

Des Weiteren gilt mein Dank Prof. Dr. Peter J. Klar für die Übernahme des Zweitgutachtens.

Außerdem möchte ich mich bei Prof. Dr. Jürgen Janek für das angenehme Arbeitsumfeld am Physikalisch-Chemischen Institut bedanken.

Insbesondere gilt mein Dank Dr. Torsten Brezesinski für die enge fachliche Zusammenarbeit, die hilfreichen Diskussionen sowie die gemeinsame Bearbeitung des DFG-Projekts. Hier möchte ich mich auch bei Dr. Yanjiao Ma, Dr. Andrey Mazilkin und Dominic Boll bedanken.

Für die großartige Hilfe bei technischen Problemen im Labor möchte ich Dr. Boris Mogwitz danken.

Ich danke allen Kollegen und Mitarbeitern am Zentrum für Materialforschung, die mich auf vielfältige Art und Weise unterstützten sowie für eine allzeit freundschaftliche Arbeitsatmosphäre sorgten. Ausdrücklich danke ich an dieser Stelle Rajendra Singh Negi, Michele Bastianello und Hendrik Hemmelmann für den Austausch von Fachwissen, ihre Hilfsbereitschaft und vor allem die angenehme sowie lustige Atmosphäre im Büro. Auch möchte ich mich bei Dr. Pascal Cop für die wissenschaftliche Kooperation bedanken. Ebenso danke ich Dr. Ralph Henning für das Korrekturlesen dieser Doktorarbeit.

Zuletzt gilt mein Dank allerdings meinen Eltern, meinem Bruder und meiner Freundin für die stete Unterstützung.

Die vorliegende Arbeit wurde im Zeitraum vom 01.01.2018 bis 30.09.2021 am Zentrum für Materialforschung der Justus-Liebig-Universität Gießen unter Betreuung von Dr. Matthias T. Elm angefertigt.

Hiermit erkläre ich: Ich habe die vorgelegte Dissertation selbstständig und ohne unerlaubte fremde Hilfe und nur mit den Hilfen angefertigt, die ich in der Dissertation angegeben habe. Alle Textstellen, die wörtlich oder sinngemäß aus veröffentlichten Schriften entnommen sind, und alle Angaben, die auf mündlichen Auskünften beruhen, sind als solche kenntlich gemacht. Ich stimme einer eventuellen Überprüfung meiner Dissertation durch eine Antiplagiat-Software zu. Bei den von mir durchgeführten und in der Dissertation erwähnten Untersuchungen habe ich die Grundsätze guter wissenschaftlicher Praxis, wie sie in der „Satzung der Justus-Liebig-Universität Gießen zur Sicherung guter wissenschaftlicher Praxis“ niedergelegt sind, eingehalten.

Laubach, 01.06.2022

Erdogan Celik

Zusammenfassung

Poröse Materialien sind aufgrund ihres großen Oberflächen-Volumen-Verhältnisses und ihrer Korngrößen im Nanometerbereich ein ideales Modellsystem, um den Einfluss von Oberflächen- und Grenzflächeneffekten auf die elektrischen und protonischen Transporteigenschaften zu untersuchen. Die Defektchemie nanostrukturierter Oxidkeramiken mit einer hohen Grenzflächendichte ist nicht mit der entsprechender Volumenmaterialien vergleichbar, da die Bildung einer Raumladungszone (Space charge layers - SCLs) an den Grenzflächen zu Änderungen der lokalen Defektchemie führt und somit die elektrischen Transporteigenschaften beeinflusst. Ziel dieser Dissertation ist es, ein besseres Verständnis des Einflusses der (Oberflächen-) Defektchemie von (meso-)porösen Oxiden auf die elektrischen und protonischen Transporteigenschaften zu erlangen. Als Modellsysteme wurden Yttriumoxid-stabilisiertes Zirconiumdioxid (YSZ) sowie CeO_2- und TiO_2-beschichtetes YSZ verwendet.

Die poröse YSZ-Dünnschichten mit einer hohen spezifischen Oberfläche wurden auf zwei unterschiedlichen Wegen hergestellt. Mit Hilfe gepulster Laserdeposition wurden poröse Oxid-Dünnschichten mit einer unregelmäßigen Porenstruktur abgeschieden, während mit Hilfe des EISA-Verfahrens (EISA: evaporation-induced self-assembly, deutsch: evaporationsinduzierte Selbstorganisation) mesoporöse Oxide mit einer regelmäßigen Porenstruktur präpariert wurden. Zur Herstellung der beschichteten Systeme wurde die Oberfläche mittels Atomlagenabscheidung gleichmäßig mit unterschiedlich dicken CeO_2 oder TiO_2-Beschichtungen unterschiedlicher Dicken Oxidmaterialien modifiziert, um Kompositmaterialien mit definierten strukturellen und elektrischen Eigenschaften herzustellen. Die Dünnschichten wurden mittels verschiedener analytischer Verfahren strukturell charakterisiert. Die elektrochemische Charakterisierung erfolgte bei unterschiedlichen Temperaturen, Sauerstoffpartialdrücken und relativer Luftfeuchtigkeit mittels elektrochemischer Impedanzspektroskopie.

Die Doktorarbeit ist in drei Teile gegliedert. In Kapitel 1 wurden die Transportmechanismen der Ladungsträger in Metalloxiden detailliert beschrieben. Darüber hinaus gibt dieses Kapitel einen Überblick über die Defektchemie der in dieser Arbeit untersuchten Metalloxide sowie die Beschreibung von Raumladungsschichten an Grenzflächen. Das zweite Kapitel fasst die wissenschaftlichen Ergebnisse dieser Dissertation zusammen, die in drei Forschungsartikeln veröffentlicht wurden. Hierzu wurden die Transporteigenschaften poröser YSZ-Dünnschichten untersucht, welche mittels PLD hergestellt wurden. Die Schichten zeigen in trockener Atmosphäre eine

konstante Sauerstoffionen-Leitfähigkeit. In steigender Luftfeuchtigkeit tritt ebenfalls eine protonische Leitfähigkeit auf, da Wassermoleküle an der Oberfläche adsorbieren. Durch eine dünne Beschichtung mit amorphem TiO_2 wird die Adsorption der Wassermoleküle erschwert, wodurch die protonische Leitfähigkeit unterdrückt wird. Eine Erhöhung der Schichtdicke führt zu einer Kristallisation der TiO_2-Beschichtung, was die Adsorption der Wassermoleküle erleichtert und somit wieder zu einer Erhöhung der protonischen Oberflächenleitfähigkeit führt. Impedanzmessungen der elektrischen Eigenschaften mesoporöser YSZ-Dünnschichten zeigen, dass eine Variation der Porengröße nahezu keinerlei Einfluss auf die ionische Leitfähigkeit der Dünnfilme hat. Eine Beschichtung mit einer dünnen CeO_2-Schicht ermöglicht es, gemischtleitende Kompositmaterialien herzustellen, wobei die CeO_2-Beschichtung insbesondere bei tieferen Temperaturen eine dominante elektronische Leitfähigkeit zeigt. Zusätzlich zeigen die Untersuchungen, dass die elektronische Teilleitfähigkeit mit zunehmender CeO_2-Schichtdicke abnimmt. Insgesamt zeigen die gewonnenen Ergebnisse den großen Einfluss einer Oberflächenbeschichtung auf die Transporteigenschaften der untersuchten Kompositmaterialien und weisen Möglichkeiten auf, die elektrochemischen Eigenschaften der Komposite für elektrochemische Anwendungen durch eine Optimierung der Beschichtung anzupassen. Eine Zusammenfassung der Ergebnisse, abschließende Bemerkungen zu den zukünftigen wissenschaftlichen Herausforderungen und Vorschläge für weitere Arbeiten schließen die Dissertation ab.

Abstract

Porous materials are an ideal model system to study the influence of the surface on the electrical and protonic transport properties due to their large surface-to-volume ratio and their grains in the nanometer size range. The defect chemistry of nanostructured oxide ceramics with a high density of interfaces, such as grain boundaries and free surfaces, is not comparable with that of the respective bulk materials. This is due to space charge layers (SCLs) at the interfaces, which cause changes to the local defect chemistry, and thus affect the electrical transport properties. The objective of this dissertation was to get a better understanding of the impact of the (surface) defect chemistry on the electrical and protonic transport properties of (meso-)porous zirconia-based oxide materials, in particular of yttria-stabilized zirconia (YSZ) and CeO_2- and TiO_2-coated YSZ.

Accordingly, porous thin films of YSZ with a high surface area were prepared using two different routes. Pulsed laser deposition (PLD) has been used to produce porous oxide thin films with a random pore structure, while an evaporation-induced self-assembly (EISA) process has been used to deposit mesoporous oxides with a regular pore arrangement. The pores were uniformly coated by means of atomic layer deposition (ALD) with varying thicknesses of oxide materials, such as CeO_2 and TiO_2, to prepare composite materials with tailored structural and electrical properties. The thin films were structurally characterized by several analytical techniques, and electrochemical characterization was done by electrochemical impedance spectroscopy (EIS) measurements varying temperature, oxygen partial pressure or relative humidity.

The thesis is divided into three parts. In chapter 1, a detailed description of the transport mechanisms of the charge carriers in metal oxides is presented. In addition, this chapter gives an overview about the defect chemistry of the metal oxides investigated in this work as well as the description of space charge layers at interfaces. The second chapter summarizes the scientific results of this doctoral thesis, which have been published in three research articles.

The transport properties of porous PLD-derived YSZ thin films were investigated using EIS. Under dry conditions, the pristine YSZ thin film exhibits only dominant oxygen ion conductivity. However, a significant increase in total conductivity with increasing relative humidity is observed. Here, the additional protonic contribution arises from the adsorption of water molecules at the material surface. While an amorphous titania coating layer results in a decrease of the protonic conductivity compared to pristine YSZ, the crystalline TiO_2 layer increases the protonic conductivity contribution again. The crystallinity of the titania layer can be adjusted by varying the thickness, which

significantly influences the transport properties of the composites. EIS measurements of mesoporous sol–gel-derived YSZ thin films reveal no effect of pore size on the total electrical conductivity. The composites with thin ceria coatings exhibit mixed ionic/electronic conductivity, but a dominant electronic contribution at low temperatures. In addition, investigations show that the electronic contribution significantly decreases with increasing CeO_2 layer thickness. Surface engineering enables to modify certain structural and electrochemical properties by active oxide layer coating, which tailors the transport mechanisms (electronic, ionic and protonic conductivity) in the nanostructured composites. A short summary of the results, final comments on the prospective scientific challenges, and suggestions for further work conclude the thesis.

Table of contents

1. Introduction

Solid-state ion conductors play an important role in electrochemical devices in the field of modern energy technology, particularly for catalysis and energy storage and conversion.[1–4] For example, yttria-stabilized zirconia (YSZ) is a very important component for solid oxide fuel cells (SOFCs), as it combines a high oxygen ion conductivity at elevated temperatures with excellent chemical and mechanical stability.[5–10] Using cubic YSZ as electrolyte material, SOFCs operate at high temperatures around 650 °C to 1000 °C,[11] which involves some disadvantages, including high costs, faster loss of overall performance and degradation of the system. In particular, the high operation temperature leads to structural changes (cubic to tetragonal phase), which are accompanied by a reduction of the ionic conductivity.[10] Consequently, it is desirable to reduce the operation temperatures for SOFC applications. Therefore, it is necessary to develop electrolyte materials that possess enhanced oxygen ion conductivity at low temperatures. One major aspect is that the ionic conductivitiy of YSZ can be altered by tailoring the dopant concentration, which in turn affects the concentration and mobility of the mobile oxygen vacancies. The maximum conductivity value has been obtained between 8 and 9 mol % Y_2O_3.

Besides the composition control, nanostructuring is a promising approach to alter the defect chemistry of oxide materials. Thus, nanostructured materials open fresh perspectives and research areas on fuel cell technology, providing a promising strategy to overcome the above mentioned disadvantages of SOFCs associated with the reduced operation temperatures. Nanostructuring primarily increases the density of interfaces and the specific surface area, which simultaneously affects the structural and physico-chemical properties of ionic and mixed-conducting materials. Related studies have shown a great potential of ionic conductors based on nanocrystalline structures.[12–14] In several scientific works, an enhancement of the ionic conductivity by several orders of magnitude has been demonstrated for YSZ thin films, achieved either by nanostructuring or by decreasing the film thickness.[15–22] On the other hand, there are also reports of the contrary observations, where the ionic conductivity of nanostructured thin films decreases.[23,24] The variation of the conductivity is attributed to space charge effects in the vicinity of the grain boundaries, misfit dislocations and/or strain effects at the interface between thin film and substrate.[25,26] In addition, there are reports that nanostructured materials can exhibit a visible change in the conduction mechanism with decreasing grain size, i.e., from ionic to mixed ionic-electronic conduction.[27,28] However, the advantages of nanocrystalline YSZ is still controversially discussed in the literature.

Electrochemical properties of oxide ceramics can be tailored by developing a porous structure, thus a high surface-to-volume ratio. One of the most characteristic features of porous materials is the high accessibility of their internal pore structure to the surrounding atmosphere. Previous studies using porous materials have indicated an excellent electrochemical performance and functionality, attributed to the higher density of electrochemically active surface sites compared to their bulk counterparts.[29–33] The surface area exhibits a different defect chemistry than the bulk due to several effects, including the presence of a space charge layer, surface reconstruction and charges.[34–37] For instance, oxygen kinetics are determined by the surface chemistry. Literature results indicate enhanced oxygen exchange kinetics in ceria- and zirconia-based oxides for SOFC applications by different surface modification strategies, e.g., the deposition of thin coatings and incorporation of aliovalent impurities.[36,38–44]

Since the last decade, atomic layer deposition (ALD) plays a fundamental role in the improvement of SOFC properties.[45–50] ALD can be used to deposit conformal and uniform coatings on complex structures, like mesoporous thin films. Different materials, such as TiO_2, CeO_2 and Al_2O_3, can be deposited with a precise control of the layer thickness. During the process, the substrate is exposed to chemical precursors. A coating can alter and modify the ionic/electronic conductivity as well as the surface oxygen exchange kinetics, having a great influence on the transport mechanisms and charge transfer reactions in SOFCs, as summarized by Shin *et al.*[46] In addition, the interfacial electrode-electrolyte reactions can be tailored by layers with defined composition and thickness. Another important application of the ALD process is the deposition of protective films to improve the chemical and mechanical stability of the device. As reported for example by Dubraja *et al.*, Al_2O_3-ALD improved the thermal stability of mesoporous Rh_2O_3 thin films significantly.[51] Several thin film composites, such as CeO_2/ZrO_2,[52] have been investigated and analyzed, but further research is still required in this field to continue the development of novel two-phase nanocomposites with promising properties for electrochemical applications. Therefore, detailed studies of the structural and physicochemical properties of these films are required to gain a deeper insight into the nanoionics and surface effects.

In this thesis, the impact of the surface area and of surface modifications by ALD on the electrical and protonic transport properties as well as the defect chemistry of (meso-)porous oxide nanomaterials have been investigated. Studies on the defect chemistry were performed as a function of temperature (25 to 700 °C), oxygen partial pressure (10^{-5} to $10^{-0.6}$ bar) or relative humidity using electrochemical impedance spectroscopy (EIS). To realize desired oxygen partial pressure values, gas mixtures of Ar/O_2 were used.

Thin films of non-ordered porous 9.5 mol% YSZ with grains in the range of 15 – 20 nm were deposited via pulsed laser deposition (PLD) on (0001)-oriented single-crystalline sapphire substrates. The pore surface of the YSZ films was uniformly coated by ALD with a titania layer of either 6 or 18 nm thickness. The thickness of the coating affects the crystallinity. While the thinner titania layer was amorphous, the thicker layer showed the anatase phase. The total conductivity of these thin films was investigated under dry and ambient atmosphere, revealing significant differences between pristine and TiO_2-coated YSZ. The non-coated YSZ showed an increase in conductivity with increasing humidity. While the protonic contribution was significantly suppressed in YSZ coated by a TiO_2 layer of 6 nm thickness, the protonic conductivity increased again in 18 nm thin titania-coated YSZ. This was attributed to filling of reduced-size pores with water. Overall, these results indicated that proton transport largely depends on the surface properties and the pore structure.

Secondly, highly ordered mesoporous 8 mol% YSZ thin films with different pore sizes (15 – 40 nm) were produced by solution-phase coassembly of salt precursors with different polymer structure-directing agents using an evaporation-induced self-assembly (EISA) process. The pore walls of the thin films were uniformly coated via ALD with varying thicknesses (3 and 7 nm) of ceria to functionalize the material surface. In this way, the pore size was adjusted in a controlled way. Similar to the TiO_2 coating, the thickness of the ceria coating affects the crystallinity and composition of the material. Only the thickness of the ceria surface layer affected the electrical transport properties, whereas the porosity showed no effect at all. ALD-derived two-phase nanocomposites with a 3 nm coating exhibited mixed ionic/electronic conductivity, those with a 7 nm coating only showed ionic conductivity. Accordingly, the electrical transport properties of these material systems can be tailored by varying the coating thickness.

Furthermore, in the invited perspective article, the state-of-the-art in the synthesis of mesoporous metal oxides, their structural and physicochemical properties, and their potential as electrode materials for electrochemical applications were addressed. Here, the advantages and disadvantages of the structural properties regarding the electrochemical device performance are discussed in detail.

2. Theoretical Background

In this chapter, the fundamental and relevant concepts for the interpretation of the results obtained in this doctoral thesis are introduced. This includes a brief theoretical introduction of the transport properties and the defect chemistry of solid oxides.

2.1. Electrical Transport in Solids

The total electrical conductivity σ_{total} of a material is defined as the sum of the partial conductivities of charged carriers of type i, such as electrons and ions:[53]

$$\sigma_{\text{total}} = \sum \sigma_i \ . \tag{1.1}$$

The partial conductivity σ_i depends on the concentration per unit volume c_i, the charge q_i and mobility μ_i of the moving carriers:

$$\sigma_i = c_i q_i \mu_i \ . \tag{1.2}$$

2.1.1. Ionic Conductivity

A fundamental requirement for the oxygen ion conductivity is the presence of defects in the crystal lattice of the oxide material. In an ionic crystal lattice mainly three types of defects can be formed, intrinsic Frenkel and Schottky defects, and extrinsic defects, as described in chapter (2.3.). Depending on the crystal structure, oxygen vacancies or interstitials are considered to be the most common point-defects. Generally, in fluorite-type oxides, the migration of oxygen vacancies gives rise to the ionic conductivity.

By applying an external electric field E_υ, the transport of oxygen ions occurs by hopping via available oxygen vacancy sites, i.e., oxygen ions move from one oxygen vacancy to another. During the jump to adjacent lattice sites, a defined energy barrier must be surmounted (Fig. 1). This energy barrier is the Gibbs free energy of migration ΔG_{m}. The net velocity υ of ion migration is given by:

$$\upsilon = \frac{\nu \gamma Z e a^2 E_\upsilon}{k_{\text{B}} T} \exp\left(-\frac{\Delta G_m}{k_B T}\right) \ . \tag{1.3}$$

with the Boltzmann constant k_{B}, the temperature T, the attempt frequency ν for a jump, the geometrical factor γ depending on the crystal structure, the distance between the

adjacent lattice sites a and the nominal charge on the ions Ze. Furthermore, the mobility μ_{i} is defined as being the ratio of velocity and electric field strength:

$$\mu_{\mathrm{i}} = \frac{v\gamma Zea^2}{k_{\mathrm{B}}T}\exp\left(-\frac{\Delta G_m}{k_B T}\right). \tag{1.4}$$

By combining equations (1.2) and (1.4), the temperature dependence of σ_i is given by:

$$\sigma_i = \frac{\gamma cvZe^2a^2}{k_{\mathrm{B}}T}\exp\left(-\frac{\Delta G_{\mathrm{m}}}{k_{\mathrm{B}}T}\right). \tag{1.5}$$

The Gibbs free energy of migration can be separated into the enthalpy ΔH_{m} and the entropy ΔS_{m} of migration:

$$\Delta G_{\mathrm{m}} = \Delta H_{\mathrm{m}} - T\Delta S_{\mathrm{m}}, \tag{1.6}$$

leading to the following equation for the conductivity:

$$\sigma_i = \frac{\gamma cvZe^2a^2}{k_{\mathrm{B}}T}\exp\left(-\frac{\Delta H_{\mathrm{m}}}{k_{\mathrm{B}}T}\right)\exp\left(\frac{\Delta S_{\mathrm{m}}}{k_{\mathrm{B}}}\right) = \frac{\sigma_0}{T}\exp\left(-\frac{\Delta H_{\mathrm{m}}}{k_{\mathrm{B}}T}\right). \tag{1.7}$$

Here, the pre-exponential factor includes the entropy term of migration, the lattice constant and the attempt frequency.

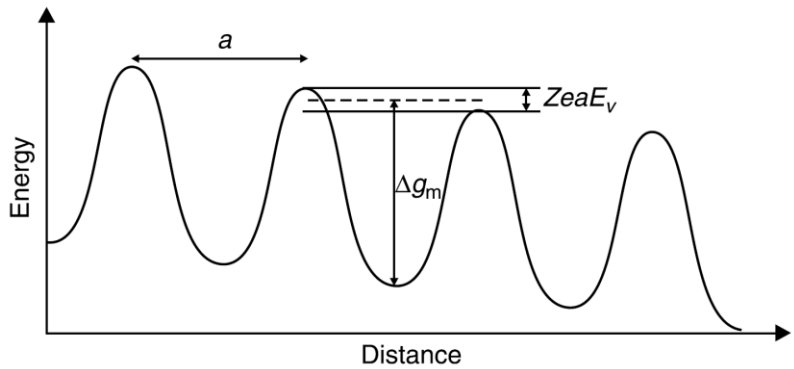

Fig. 1: Schematic representation of the potential barrier for the migration of an ionic charge carrier in the presence of an applied electric field. Reproduced from Tilley et al. with permission.[53]

The conductivity of a pure oxygen ion conductor ($\sigma_{\mathrm{total}} = \sigma_{\mathrm{ionic}}$), such as YSZ, depends strongly on temperature. The ionic conductivity increases with increasing temperature due to the thermally activated mobility of the free charge carriers for a fixed charge carrier

concentration. For example, bulk YSZ is consistently reported to have a conductivity of around 1 S/cm at 800 °C.[54]

2.1.2. Electronic Conductivity

Most metal oxide materials, such as CeO_2 and TiO_2, are mixed conductors, whereas only few are classified as pure ionic conductors. Electrons, electron holes, anions and cations can serve as charge carriers in mixed conductors. Thus, the contribution of electronic and ionic components to the total conductivity is given by:

$$\sigma_{\text{total}} = \sigma_{\text{ionic}} + \sigma_{\text{electronic}} \,. \tag{2.1}$$

The ionic transport process is described in the previous section (2.1.1.). In several metal oxides, e.g., transition metal oxides, the electronic transport occurs by a hopping mechanism instead of a band conduction mechanism.[55–58] The presence of crystallographic defects in the material breaks the regular periodicity of the electronic charge density. This structural disorder leads to the formation of localized electronic states in the band gap, close to the band edges.[59,60] This results in a smearing out of the band gap. However, localized electronic states can also be formed in highly crystalline oxide materials. This phenomenon is described as a modification of the band structure induced by polaron (quasiparticle) formation. A polaron is formed by the Coulomb interaction between charge carriers (i.e., electrons or holes) and phonons. When ions are attracted (repelled) to charge carriers with an opposite (same) electric charge, a polarization (distortion) of the structure is generated, following the charge carrier when it moves through the crystal lattice. Furthermore, polarons are classified as large or small depending on the size and strength of the phonon cloud. Whereas small polarons are governed by short-range electron-phonon interactions, large polarons are formed by long-range interactions. In metal oxides, the electronic conductivity σ_e can be described by a charge carrier jumping through the material between the localized states. In order to move, the charge charrier has to overcome the energy barrier during the hopping between two adjacent sites. This electrical transport mechanism is thermally activated. In such materials, the mobility of the charge carriers μ increases with increasing temperature, in contrast to the classical band theory:[53]

$$\mu \propto \frac{1}{T} \exp\left(-\frac{\Delta H_{\text{m,elec}}}{k_{\text{B}} T}\right). \tag{2.2}$$

Here, $\Delta H_{\mathrm{m,elec}}$ is the migration enthalpy of the electronic defects. The transport mechanism of polaron hopping is similar to that of the ionic conductivity:[53]

$$\sigma_e = (1-\varphi)\left(\frac{cve^2a^2}{k_\mathrm{B}T}\right)\exp\left(-\frac{\Delta H_{\mathrm{m,elec}}}{k_\mathrm{B}T}\right)\exp\left(\frac{\Delta S_{\mathrm{m,elec}}}{k_\mathrm{B}}\right). \tag{2.3}$$

The geometrical factor in equation (1.5) is replaced by the term $(1-\varphi)$. The parameter φ represents the fraction of total sites that mobile charges occupy, which varies with the degree of nonstoichiometry. A high degree of nonstoichiometry leads to an increase in the mobile charge carrier concentration c. ΔS_m denotes the migration entropy of the electronic defects. The electronic conductivity is exponentially correlated with the temperature.[61]

The formation of small polarons has been already observed in several metal oxides, like ceria and titania, which both exhibit a large band gap with an energy higher than 3 eV.[62] Polarons originate from intrinsic defects, such as oxygen vacancies or metal interstitials. The polaron formation is attributed to a change of the transition metal oxidation state, for example, in ceria from Ce^{4+} to Ce^{3+}. Particularly in oxide materials, the charge transfer and the electron-phonon coupling occur more easily in the vicinity of the surface than in the bulk due to the different defect chemistry and structure.

2.1.3. Protonic Conductivity

In the last years, nanostructured oxides gained much attention as proton conducting materials in several electrochemical devices, such as humidity sensors[63–65] and proton exchange membranes,[66–68] at ambient conditions, where protons were found to be the dominant charge carriers. Nanostructured oxides, such as YSZ,[69–73] CeO_2[74–76] and TiO_2[72,77–79], can exhibit notably high protonic conduction at temperatures below 150 °C, as demonstrated in several studies.

The protonic conductivity arises from the adsorption of water molecules at the material surface and/or its grain boundaries. However, the type, concentration and migration mechanism of protonic charge carriers, as well as the process of the adsorption of different water layers on the surface, are determined by the physicochemical properties of the material's surface. Depending on temperature and relative humidity, chemisorbed and/or physisorbed water layers are formed, as schematically shown in Fig. 2.[80,81] Generally at high temperatures ($T > 450$ °C)[82] and/or low relative humidity, chemisorbed layers are present, which are mostly forming covalent bonds to the substrate material in

the form of hydroxyl groups. Typical values of the adsorption enthalpy range between 1 and 2 eV.[83,84] In addition to the dissociative adsorption, water molecules can molecularly adsorb onto the surface. Common adsorption sites are metal ions and surface defects. For instance, when a metal oxide material with surface defects, such as oxygen vacancies $V_O^{\cdot\cdot}$, is exposed to a humid atmosphere, the water molecule $H_2O_{(g)}$ fills the vacancy according to the defect reaction shown in the Kroeger–Vink notation:[85,86]

$$H_2O_{(g)} + V_O^{\cdot\cdot} + O_O^x \leftrightarrow 2(OH_O^{\cdot}), \tag{3.1}$$

where hydroxide ions are formed. At lower temperatures, additional physisorbed water layers are formed, whose number increases with increasing relative humidity. Compared to chemisorbed water molecules, physisorbed molecules exhibit a lower adsorption enthalpy on the order of 0.2 eV to 1 eV.[83,84]

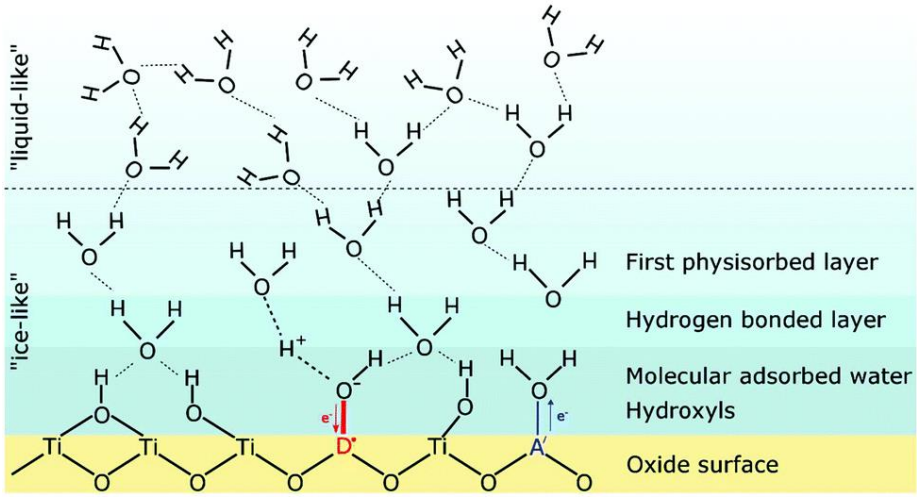

Fig. 2: Schematic illustration of the structure of adsorbed water layers on a titania surface. The influence of a surface acceptor A and a donor D on the water dissociation is shown. Reproduced from Stub et al. with permission.[81]

The transport of protons occurs in two different ways, either by Grotthuss or vehicle mechanisms, depending on the structure of the adsorbed water layers.[73,87,88] In the chemisorbed water layers, the protons typically propagate by a hopping mechanism (Grotthuss mechanism) between the different oxygen atoms of the adsorbed water molecules, where the activation energy varies between 0.1 and 0.4 eV. In physisorbed water layers, the transport of hydroxide ions (vehicle mechanism) is preferred, which has a higher activation energy typically in the range between 0.4 and 1 eV.[83,88,89]

2.2. Defect Chemistry at Interfaces (Space Charge Region)

The presence of a high density of interfaces, such as grain boundaries or free surfaces, can significantly affect the electrochemical transport properties in metal oxides. At interfaces, the concentration and mobility of the charge carriers are changed due to the formation of a space charge region. Thus, the defect chemistry at interfaces differs significantly from that of the bulk material. The first description of space charge regions of ionic solids was discussed by Kliewer and extended to metal oxides by Maier.[90–92]

Generally, the concentration of each defect i is related to its electrochemical potential $\tilde{\mu}_i$, which comprises the chemical potential μ_i^0 and the electrical potential $\Phi(x)$:

$$\tilde{\mu}_i = \mu_i^0 + Z_i F \Phi(x), \tag{4.1}$$

with Z_i being the effective charge of the defect i and F the Faraday constant. At an interface, the local symmetry of the crystal structure is distorted, i.e., the chemical potential of the interface ($x = 0$) deviates from that of the bulk ($x = \infty$). In order to maintain electroneutrality, i.e., a constant electrochemical potential, charged mobile species in the vicinity of the interface redistribute and vary their local concentration, resulting in the formation of a space charge layer. The concentration profile $c_i(x)$ for each mobile defect at the distance x from the interface is given by:

$$c_i(x) = c_{i,\infty} \exp\left(-\frac{Z_i e \cdot \Delta\Phi(x)}{kT}\right), \tag{4.2}$$

where $c_{i,\infty}$ refers to the defect concentration of i in the bulk. $\Delta\Phi(x) = \Phi(x) - \Phi_\infty$ is the electrostatic potential at the distance x from the interface relative to the bulk potential Φ_∞. The potential profile can be determined by solving the Poisson-Boltzmann differential equation (one-dimensional form):

$$\frac{\partial^2 \Phi}{\partial x^2} = -\frac{e}{\varepsilon_0 \varepsilon_r} \sum_i Z_i c_{i,\infty} \exp\left(-\frac{Z_i e \cdot \Delta\Phi(x)}{kT}\right). \tag{4.3}$$

Equation (4.3) and, thus the description of the charge carrier spatial distribution at the interface can be solved for two prominent cases, the Gouy-Chapman case and the Mott-Schottky case. In the Gouy-Chapman case, two defects of opposite sign are assumed to be mobile, while in the other case one of the defects is immobile. The two different situations are described in more detail in the first publication of this thesis.

Numerous studies have investigated the properties of the space charge layer of ionic and mixed ionic-electronic conductors.[93–100] By decreasing the grain size to the nanometer level, the concentration of oxygen ions in ceria- and zirconia-based oxides is reduced and those of the electrons increases in the space charge region. The reason is that in fluorite-based materials, the grain boundaries typically exhibit a positively charged core. The change in carrier concentration in the vicinity of the interface affects the local defect chemistry and thus the corresponding electrical conductivity. The transport properties in polycrystalline ceria- and zirconia-based materials can be obviously controlled by micro- and nanostructuring. An overview of the correlation between grain boundary, grain size and space charge region in metal oxides can also be found in the first publication of this thesis.

2.3. Defect Chemistry of Solid Metal Oxides

2.3.1. Defect Chemistry of Yttria-stabilized Zirconia (YSZ)

Cubic yttria-stabilized zirconia is one of the most common ceramic materials, as it is well suited as solid-state electrolyte for SOFCs due to its comparably high ionic conductivity and chemical stability over wide temperature and oxygen partial pressure ranges.[1,101,102] The incorporation of yttria (Y_2O_3) in pure zirconia (ZrO_2) generates double positively charged oxygen vacancies $\mathrm{V_O^{\cdot\cdot}}$. Here, yttrium ions ($Y^{3+}$) replace the zirconium sites $\mathrm{Y'_{Zr}}$ with a relative charge of -1 and oxygen vacancies are formed to maintain charge neutrality. This can be described in Kroeger-Vink notation by the defect reaction:[103,104]

$$\mathrm{Y_2O_3 \rightarrow 2Y'_{Zr} + V_O^{\cdot\cdot} + 3O_O^x}. \tag{5.1}$$

$\mathrm{O_O^x}$ indicates the lattice oxygen ions on regular oxygen sites with a neutral charge. Yttria does not only provide oxygen vacancies, which increase the ionic conductivity. It also stabilizes the cubic phase of zirconia, which is thermodynamically stable only at high temperatures. The cubic fluorite-type YSZ exhibits the highest ionic conductivity. Generally, zirconia as a polymorphic material exists in three different phases: cubic, tetragonal and monoclinic.[105] However, the ion conductivity depends on the oxygen vacancy concentration $[\mathrm{V_O^{\cdot\cdot}}]$ on the anionic sublattice, which is determined by the yttrium ion concentration $[\mathrm{Y'_{Zr}}]$:

$$[\mathrm{V_O^{\cdot\cdot}}] = 0.5[\mathrm{Y'_{Zr}}]. \tag{5.2}$$

Several studies found an optimal doping concentration of Y_2O_3 to obtain the highest oxygen ion conductivity of about 8 and 9 mol % Y_2O_3.[106–110] A higher doping concentration leads to a drastic reduction of the ionic conductivity due to the decrease in mobility. At low temperatures or high doping concentration, the formation of two different defect clusters are involved.[111–113] Oxygen vacancies and yttria form a complex with a positive effective charge:

$$\mathrm{Y'_{Zr}} + \mathrm{V_O^{\cdot\cdot}} \leftrightarrow (\mathrm{Y'_{Zr}V_O^{\cdot\cdot}})^{\cdot}. \tag{5.3}$$

An even higher doping concentration results in the formation of clusters, which are electrostatically neutral. These defects can be described as:

$$2\mathrm{Y'_{Zr}} + \mathrm{V_O^{\cdot\cdot}} \leftrightarrow (\mathrm{Y'_{Zr}V_O^{\cdot\cdot}Y'_{Zr}})^{\mathrm{x}}. \tag{5.4}$$

Furthermore, oxygen ions move from a regular oxygen lattice site $\mathrm{O_O^x}$ to an interstitial position $\mathrm{O_i''}$ in the lattice, creating simultaneously oxygen vacancies (Frenkel-type anion disorder):

$$\mathrm{O_O^x} + \mathrm{V_i^x} \leftrightarrow \mathrm{V_O^{\cdot\cdot}} + \mathrm{O_i''}, \tag{5.5}$$

with the corresponding equilibrium constant of the mass action law:

$$K_\mathrm{F} = [\mathrm{V_O^{\cdot\cdot}}][\mathrm{O_i''}]. \tag{5.6}$$

The oxygen interstitial $\mathrm{O_i''}$ has a double negative charge relative to the lattice. Depending on the oxygen partial pressure $p_{\mathrm{O_2}}$, YSZ can exhibit a dominant ionic, electronic or mixed conduction. The correlation between different charge carrier concentrations and the $p_{\mathrm{O_2}}$ is represented in so-called Brouwer diagrams, where the logarithm of the defect concentration log[def] is plotted versus the logarithmic value of the oxygen partial pressure. As seen in Fig. 3, several defect regimes for YSZ can be constructed, illustrating the case of the stoichiometric region (intrinsic ionic conduction), along with an oxygen excess (p-type) and oxygen deficient (n-type) region by a variation of $p_{\mathrm{O_2}}$. However, YSZ offers a dominant ionic conductivity over a wide range of oxygen partial pressures and temperatures due to the doping with Y_2O_3, whereas dominant p-type or n-type conduction is not observed under real (experimental) conditions.

Using the Kroeger-Vink notation, the defect reaction of oxygen release under reducing atmosphere is given by:

$$\mathrm{O_O^x} \leftrightarrow \mathrm{V_O^{\cdot\cdot}} + 2\mathrm{e'} + 0.5\ \mathrm{O_{2(g)}},$$

(5.7)

which forms oxygen vacancies in the lattice and excess electrons $\mathrm{e'}$ in the conduction band. The respective mass action law K_{Red} for reaction (5.7) is given by:

$$K_{\mathrm{Red}} = [\mathrm{V_O^{\cdot\cdot}}][\mathrm{e'}]^2 {p_{\mathrm{O_2}}}^{1/2}.$$

(5.8)

Similarly, the incorporation of oxygen under oxidizing atmosphere can be described by the following reaction and equilibrium constant K_{Ox}:

$$0.5\ \mathrm{O_{2(g)}} + \mathrm{V_O^{\cdot\cdot}} \leftrightarrow \mathrm{O_O^x} + 2\mathrm{h^{\cdot}},$$

(5.9)

$$K_{\mathrm{Ox}} = [\mathrm{V_O^{\cdot\cdot}}]^{-1}[\mathrm{h^{\cdot}}]^2 {p_{\mathrm{O_2}}}^{-1/2}.$$

(5.10)

Here, $\mathrm{h_{VB}^{\cdot}}$ denotes a defect electron in the valence band. The dopant concentration $[\mathrm{Y'_{Zr}}]$ is constant for the whole $p_{\mathrm{O_2}}$ range.

(Near-)stoichiometric region:

In the vicinity of the stoichiometric point, the concentration of oxygen vacancies is intrinsically large due to doping and remains constant over a broad range of oxygen partial pressures ($[\mathrm{V_O^{\cdot\cdot}}] \approx$ const.). Here, the total conductivity is equal to the oxygen ion conductivity (i.e. $\sigma_{\mathrm{total}} \approx \sigma_{\mathrm{ion}}$). Cation diffusion of $\mathrm{Y'_{Zr}}$ can be neglected, and the influence of electrons $\mathrm{e'}$ and holes $\mathrm{h_{VB}^{\cdot}}$ on the total conductivity is negligible due to the large band gap, leading to a low electron concentration, i.e. $[\mathrm{e'}] \ll [\mathrm{V_O^{\cdot\cdot}}]$. Here, the electron-hole disorder can be written as:

$$\mathrm{nill} \leftrightarrow \mathrm{e'} + \mathrm{h^{\cdot}}.$$

(5.11)

According to equation (5.11), the equilibrium constant K_e is given by:

$$K_e = [\mathrm{e'}][\mathrm{h^{\cdot}}],$$

(5.12)

where $[\mathrm{e'}]$ and $[\mathrm{h^{\cdot}}]$ are the concentration of electrons and holes in the conduction and valence band, respectively. The charge neutrality condition can be described by:

$$\mathrm{Y'_{Zr}} + 2\mathrm{O''_i} + \mathrm{e'} \leftrightarrow 2\mathrm{V_O^{\cdot\cdot}} + \mathrm{h^{\cdot}}.$$

(5.13)

Combining the law of mass action in equation (5.9) with the assumption $[\mathrm{V_O^{\cdot\cdot}}] \approx$ const. results in the $p_{\mathrm{O_2}}$-dependence of the electron concentration in YSZ:

$$[\mathrm{e'}] \propto {p_{\mathrm{O_2}}}^{-1/4}.$$

(5.14)

Similarly, the dependence of the hole concentration on the oxygen partial pressure can be described as:

$$[\mathrm{h^{\cdot}}] \propto {p_{\mathrm{O_2}}}^{+1/4}.$$

(5.15)

Reducing conditions:

By decreasing the oxygen partial pressure, the oxygen vacancy concentration increases in YSZ due to the release of oxygen. Here, the double positive charge of an oxygen vacancy is compensated by two additional electrons. If the concentration of electrons reaches the oxygen vacancy concentration, the Brouwer approximation for the n-type region holds:

$$2[\mathrm{V_O^{\cdot\cdot}}] = [\mathrm{e'}].$$

(5.16)

The dependence of certain defect species on the oxygen partial pressure can be determined on the basis of equations (5.7), (5.8), (5.11), (5.12) and (5.16):

$$[\mathrm{V_O^{\cdot\cdot}}] \propto {p_{\mathrm{O_2}}}^{-1/6}, [\mathrm{O_i''}] \propto {p_{\mathrm{O_2}}}^{+1/6}$$

(5.17)

and

$$[\mathrm{e'}] \propto {p_{\mathrm{O_2}}}^{-1/6}, [\mathrm{h^{\cdot}}] \propto {p_{\mathrm{O_2}}}^{+1/6}.$$

(5.18)

Under reducing conditions, the defect concentration changes with a characteristic slope of ± 1/6 in the Brouwer diagram.

Oxidizing conditions:

With a reasonably high partial pressure of oxygen, the hole concentration approaches the dopant concentration:

$$[\mathrm{Y}'_{\mathrm{Zr}}] = [\mathrm{h}^{\cdot}]. \tag{5.19}$$

In this region, the number of electrons and holes can be assumed to be constant (Brouwer approximation). The dependence of the oxygen vacancy and interstitial concentration on the oxygen partial pressure is calculated using equations (5.9), (5.10) and (5.19), respectively:

$$[\mathrm{V}_{\mathrm{O}}^{\cdot\cdot}] \propto {p_{\mathrm{O}_2}}^{-1/2}, [\mathrm{O}_{\mathrm{i}}''] \propto {p_{\mathrm{O}_2}}^{+1/2}. \tag{5.20}$$

Thus, the logarithmus of the oxygen vacancy concentration decreases with a slope of -1/2 with increasing $\log(p_{\mathrm{O}_2})$, while those of interstitials increases with a characteristic slope of +1/2.

Strongly oxidizing conditions:

At an even higher oxygen partial pressure, the incorporation of oxygen increases the concentration of oxygen interstitials and holes. In this regime, the double negative charge of an oxygen interstitial is compensated by two additional holes. The corresponding Brouwer approximation is formulated as:

$$2[\mathrm{O}_{\mathrm{i}}''] = [\mathrm{h}^{\cdot}]. \tag{5.21}$$

The dependence of certain defect species on the oxygen partial pressure can be calculated on the basis of equations (5.9), (5.10), (5.11), (5.12) and (5.21):

$$[\mathrm{V}_{\mathrm{O}}^{\cdot\cdot}] \propto {p_{\mathrm{O}_2}}^{-1/6}, [\mathrm{O}_{\mathrm{i}}''] \propto {p_{\mathrm{O}_2}}^{+1/6} \tag{5.22}$$

and

$$[\mathrm{e}'] \propto {p_{\mathrm{O}_2}}^{-1/6}, [\mathrm{h}^{\cdot}] \propto {p_{\mathrm{O}_2}}^{+1/6}. \tag{5.23}$$

In this region, the number of oxygen interstitials exceeds those of yttria. The corresponding Brouwer diagram is shown in Fig. 3.

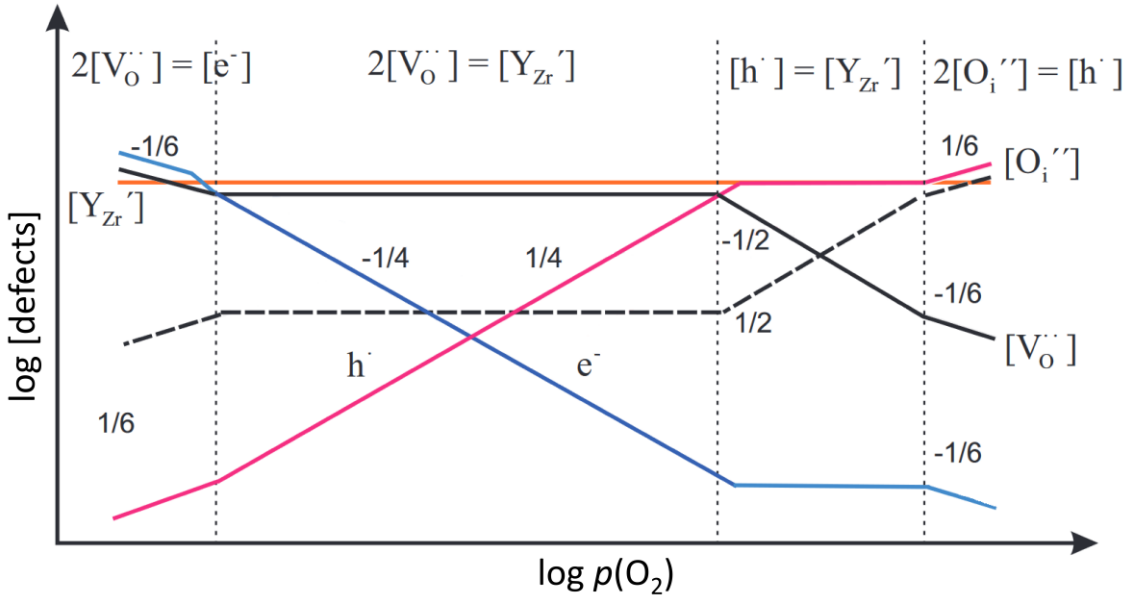

Fig. 3: Brouwer diagram for yttria-stabilized zirconia (YSZ). Reproduced from ref. 114.

2.3.2. Defect Chemistry of Cerium (IV) oxide (CeO_2)

In fluorite-type oxides, such as ceria (CeO_2), Schottky disorder is energetically unfavorable. The intrinsic defect formation in stoichiometric ceria is based on the formation of oxygen vacancies $V_O^{\cdot\cdot}$ and oxygen interstitials O_i'', which is represented by means of Kroeger-Vink notation (here: Frenkel-type anion disorder):

$$O_O^x + V_i^x \leftrightarrow V_O^{\cdot\cdot} + O_i'', \tag{6.1}$$

with the respective law of mass action:

$$K_F = [V_O^{\cdot\cdot}][O_i''] \,. \tag{6.2}$$

Intrinsic defects are mainly formed due to the increase in entropy at elevated temperatures.[115] Electron-hole disorder is intrinsically low because of the large band gap between the O-2p and Ce-5d orbital states ($E_{gap} = 4 - 6$ eV).[116–118] In addition, the redox activity is a well-known characteristic of the cubic fluorite-type ceria, as cerium easily changes the oxidation state between Ce^{3+} ($4f^1$ orbital) and Ce^{4+} ($4f^0$ orbital). The defect equilibria Ce^{3+}/Ce^{4+} can be adjusted by varying the temperature and oxygen partial pressure. During the reduction of ceria, oxygen can be easily removed from the crystal lattice. Thus, oxygen vacancies $V_O^{\cdot\cdot}$ and excess electrons e' are formed under reducing conditions:

$$\mathrm{O_O^x} \leftrightarrow \mathrm{V_O^{\cdot\cdot}} + 2\mathrm{e}' + 0.5\ \mathrm{O_{2(g)}}. \tag{6.3}$$

Note that non-stoichiometric ceria ($CeO_{2-\delta}$) is a typical mixed ionic and electronic conductor (MIEC), where oxygen vacancies are responsible for the ionic conductivity, while electrons propagate through the lattice by small polaron hopping between Ce^{3+} and Ce^{4+}:[53,56]

$$2\mathrm{Ce_{Ce}^x} + 2\mathrm{e}' \leftrightarrow 2\mathrm{Ce_{Ce}'}, \tag{6.4}$$

where Ce^{3+} and Ce^{4+} are denoted as $\mathrm{Ce_{Ce}'}$ and $\mathrm{Ce_{Ce}^x}$, respectively. Combining equations (6.3) and (6.4), the reduction reaction can be written as:

$$2\mathrm{Ce_{Ce}^x} + \mathrm{O_O^x} \leftrightarrow 2\mathrm{Ce_{Ce}'} + \mathrm{V_O^{\cdot\cdot}} + 0.5\ \mathrm{O_{2(g)}}, \tag{6.5}$$

with the respective equilibrium constant:

$$K_{\mathrm{Red}} = [\mathrm{Ce_{Ce}'}]^2[\mathrm{V_O^{\cdot\cdot}}]\ {p_{\mathrm{O_2}}}^{1/2}. \tag{6.6}$$

Under oxidizing conditions, the oxygen incorporation into the material generates oxygen interstitials and holes:

$$0.5\ \mathrm{O_{2(g)}} + \mathrm{V_O^{\cdot\cdot}} \leftrightarrow\ \mathrm{O_i''} + 2\mathrm{h_{VB}^{\cdot}}\ , \tag{6.7}$$

$$K_{\mathrm{Ox}} = [\ \mathrm{O_i''}][\mathrm{h}^{\cdot}]^2 {p_{\mathrm{O_2}}}^{-1/2}. \tag{6.8}$$

Combining the reaction of the extrinsic defect formation of ceria (6.5) with the intrinsic defect formation reactions, the Brouwer diagram of ceria can be constructed when maintaining charge neutrality conditions. The Brouwer diagram with the corresponding approximations depending on the oxygen partial pressure range is shown in Fig. 4.

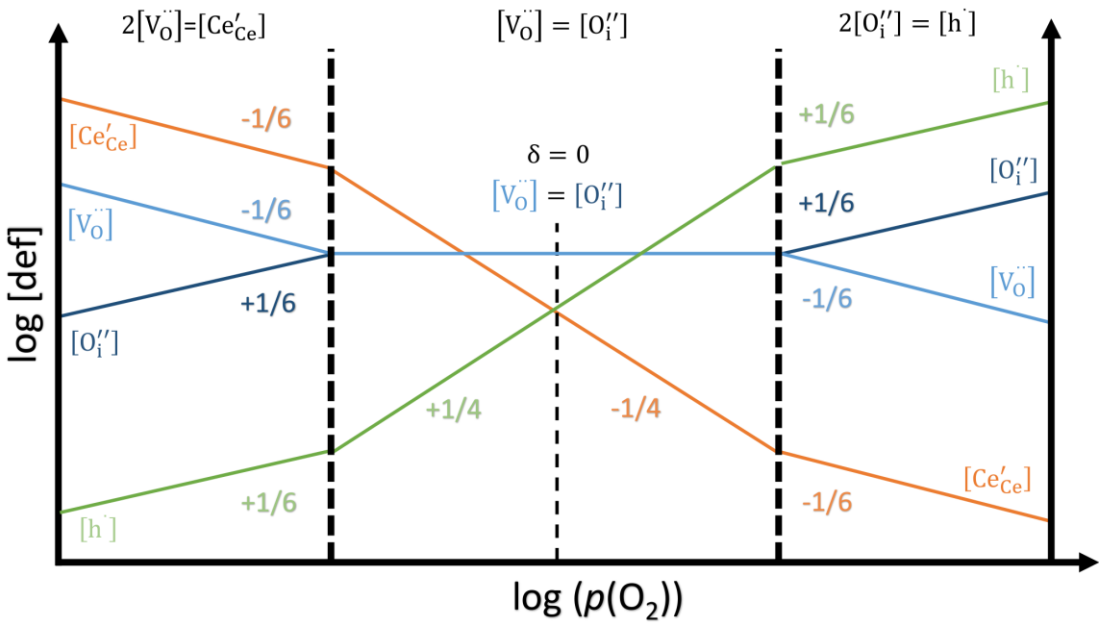

Fig. 4: Brouwer diagram for ceria (CeO_2).

2.3.3. Defect Chemistry of Titanium (IV) oxide (TiO_2)

Anatase titania (TiO_2) is a wide-bandgap semiconductor with an energy of around 3.2 eV.[119,120] TiO_2 tends to be an intrinsic n-type material at elevated temperatures, as generated oxygen vacancies are compensated by electrons. Electrons exhibit a considerably high mobility in the conduction band, while localized holes show an extremely low mobility, due to the strong electronegativity of the O-2p orbitals. The defect equations for the redox reaction and formation of an electron-hole pair are:

$$\mathrm{O_O^x} \leftrightarrow \mathrm{V_O^{\cdot\cdot}} + 2\mathrm{e}' + 0.5\ \mathrm{O_{2(g)}}\ , \tag{7.1}$$

$$\mathrm{nill} \leftrightarrow \mathrm{e}' + \mathrm{h}^{\cdot}, \tag{7.2}$$

with the equilibrium constants:

$$K_{\mathrm{V_O^{\cdot\cdot}}} = [\mathrm{V_O^{\cdot\cdot}}][\mathrm{e}']^2 {p_{\mathrm{O_2}}}^{1/2}, \tag{7.3}$$

$$K_e = [\mathrm{e}'][\mathrm{h}^{\cdot}]. \tag{7.4}$$

For anatase, it is still under debate whether Schottky or cation Frenkel disorder is energetically favored.[121–128] In case of Schottky disorder, doubly ionized oxygen

vacancies $V_O^{\cdot\cdot}$ and titanium vacancies V_{Ti}'''' with a charge of -4 relative to the lattice are present. Meanwhile, electrically neutral TiO_2 molecules leave the lattice sites and are placed at the surface of the material:

$$Ti_{Ti}^{x} + 2O_O^{x} \leftrightarrow V_{Ti}'''' + 2V_O^{\cdot\cdot} + TiO_{2\,(surf)}\,. \tag{7.5}$$

In this case, the equilibrium constant K_S is:

$$K_S = [\,V_{Ti}''''][V_O^{\cdot\cdot}]^2. \tag{7.6}$$

Assuming that Frenkel disorder is dominant, a Ti^{4+} ion changes its position from an occupied lattice site Ti_{Ti}^{x} to a vacant interstitial site V_i^{x} according to:

$$Ti_{Ti}^{x} + V_i^{x} \leftrightarrow Ti_i^{\cdot\cdot\cdot\cdot} + V_{Ti}''''. \tag{7.7}$$

$Ti_i^{\cdot\cdot\cdot\cdot}$ denotes Ti^{4+} on an interstitial site with a relative charge of +4. The corresponding mass action law is given by:

$$K_F = [V_{Ti}^{\cdot\cdot\cdot\cdot}][\,V_{Ti}'''']. \tag{7.8}$$

As for YSZ and CeO_2, the defect concentration of titania is associated with its nonstoichiometry. Changing the oxygen partial pressure of the surrounding atmosphere, the defect concentration can be tailored. Nowotny *et al*. illustrated the concentration of specific defects as a function of the oxygen partial pressure.[125,128–130] In addition to the above mentioned defect formations, the following defect equilibria need to be considered for titania:

$$Ti_{Ti}^{x} + 2O_O^{x} \leftrightarrow Ti_i^{\cdot\cdot\cdot} + 3e' + O_{2(g)}, \tag{7.9}$$

$$Ti_{Ti}^{x} + 2O_O^{x} \leftrightarrow Ti_i^{\cdot\cdot\cdot\cdot} + 4e' + O_{2(g)}, \tag{7.10}$$

$$O_{2(g)} \leftrightarrow V_{Ti}'''' + O_O^{x} + 4h^{\cdot}. \tag{7.11}$$

Under extremely reducing conditions, trivalent titanium interstitials $Ti_i^{\cdot\cdot\cdot}$ become the most dominant defects. The formation of $Ti_i^{\cdot\cdot\cdot}$ is described in equation (7.9) and its equilibrium constant is expressed as follows:

$$K_{\mathrm{Ti_i^{\cdot\cdot\cdot\cdot}}} = [\,\mathrm{Ti_i^{\cdot\cdot\cdot\cdot}}][\mathrm{e'}]^3 p_{\mathrm{O_2}}.$$

(7.12)

Here, titanium interstitials are compensated by electrons:

$$3[\,\mathrm{Ti_i^{\cdot\cdot\cdot\cdot}}] = [\mathrm{e'}].$$

(7.13)

In the strongly reduced regime, the predominant defects are oxygen vacancies $\mathrm{V_O^{\cdot\cdot}}$, which are compensated by electrons. The formation of oxygen vacancies is described by equation (7.1) with the equilibrium constant (7.3). Thus, the corresponding Brouwer approximation for this regime is:

$$[\mathrm{e'}] = 2[\mathrm{V_O^{\cdot\cdot}}].$$

(7.14)

At slightly higher oxygen partial pressure (reducing conditions), oxygen vacancies and titanium vacancies are the predominant defect species. The defect disorder (7.5) in this regime is governed by the charge compensation:

$$2[\,\mathrm{V_{Ti}''''}] = [\mathrm{V_O^{\cdot\cdot}}].$$

(7.15)

With further increase of the $p_{\mathrm{O_2}}$, oxidation leads to the formation of p-type titania (oxidizing conditions). During the oxidation, titanium vacancies are formed. The reaction is described by the equilibrium (7.11) with the corresponding equilibrium constant $K_{\mathrm{V_{Ti}''''}}$:

$$K_{\mathrm{V_{Ti}''''}} = [\,\mathrm{V_{Ti}''''}][\mathrm{h^{\cdot}}]^4 p_{\mathrm{O_2}}{}^{-1}.$$

(7.16)

Only holes predominate as the majority charge carrier and compensate the titanium vacancies:

$$4[\,\mathrm{V_{Ti}''''}] = [\mathrm{h^{\cdot}}].$$

(7.17)

Assuming the defect reaction of each oxygen partial pressure regime and the corresponding Brouwer approximation for the electroneutrality condition, a schematic representation of the ionic and electronic charge carriers in the above regimes is shown in Fig. 5.

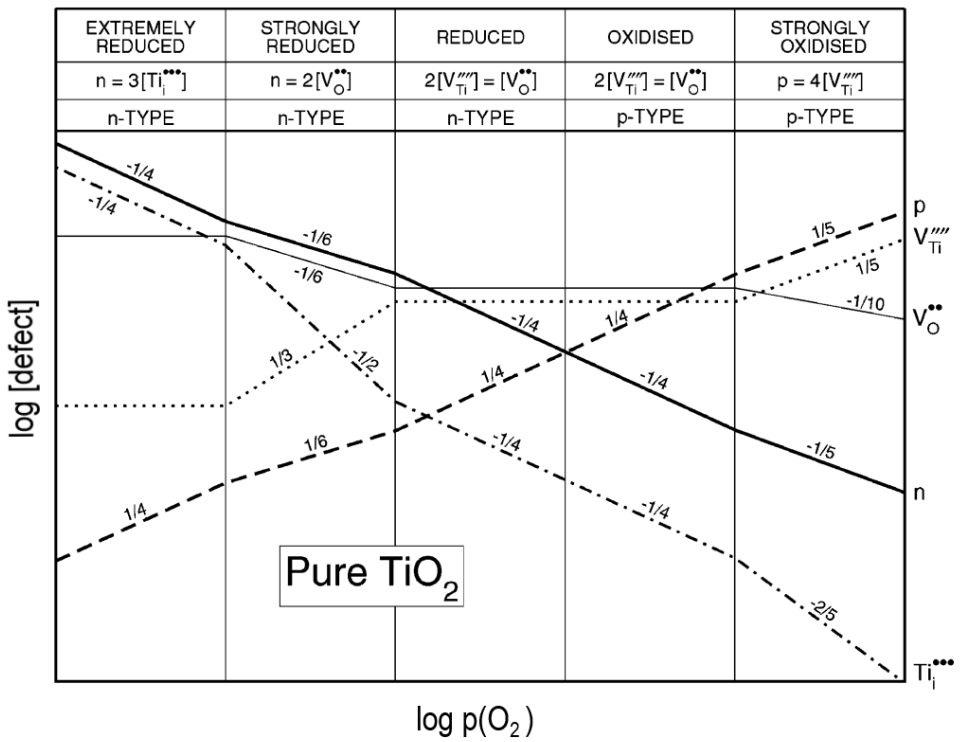

Fig. 5: Brouwer diagram for titania (TiO_2), according to the Schottky disorder. Variation of the concentration of each defect as a function of the oxygen partial pressure. Reproduced from Nowotny et al. with permission.[128]

2.4. Sample Preparation

2.4.1. Pulsed Laser Deposition (PLD)

Pulsed laser deposition (PLD), a physical vapor deposition (PVD) technique introduced by Smith and Turner in 1965,[131] is a versatile method for the deposition of thin films of a wide spectrum of materials.[132–136] In a typical PLD process, a pulsed laser beam is focused by a set of optical components onto the surface of a solid target to be deposited, leading to ablation and evaporation of the material inside the deposition chamber. The evaporated target material expands in a plasma plume consisting of target species, such as atoms, electrons and ions. After that, the vapor condenses on the substrate, which is mounted opposite to the target. During the deposition process, the substrate can be heated to a certain temperature. The process can be carried out in a ultra-high vacuum (UHV) or in the atmosphere of different background gasses, for example, oxygen, nitrogen or argon. In addition, several experimental parameters (laser energy, pulse duration, substrate temperature, substrate-target distance, background gas pressure and type) affect the expansion dynamics of the plasma and thus have direct influences on the thin film growth and its properties. The possibility to adjust these parameters

allows to influence the crystallinity, morphology, thickness and stoichiometry of the deposited thin film. Fig. 6 shows a schematic diagram of a typical PLD system.

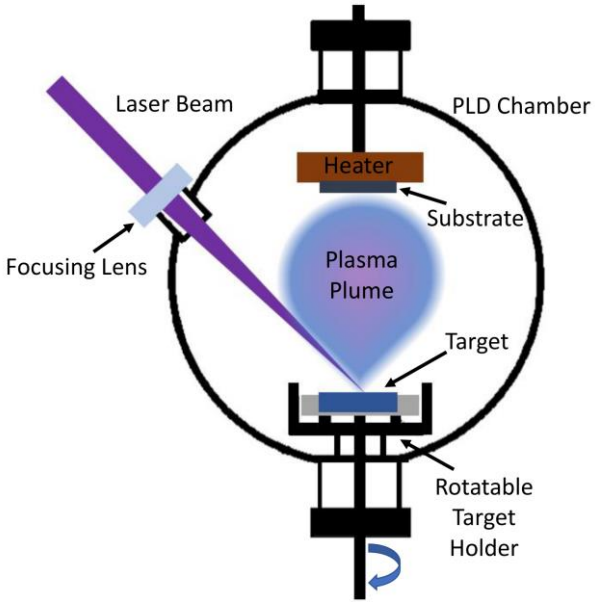

Fig. 6: Scheme of the PLD chamber equipped with a laser, a rotatable target holder stage, a substrate heater and various pressure gauges. An excimer laser, such as krypton fluoride or argon fluoride, is the most commonly used energy source in PLD systems.

PLD is a well-known technique also for the deposition of metal oxides. In 1969, the first growth of oxide films, $BaTiO_3$ and $SrTiO_3$, was achieved by PLD.[137] In the course of time, this technique has been used extensively in the preparation of numerous complex oxides.[138] An important aspect is that structural properties of metal oxides, such as composition and morphology, can be controlled by tailoring the oxygen background pressure and the substrate temperature during deposition.[138] In this context, an oxygen background is commonly needed to implement stoichiometric transfer of the desired material from the target to the substrate. Secondly, it is possible to prepare thin film structures ranging from dense to highly porous ones by variation of the oxygen pressure. At low oxygen pressures, thin films with compact and dense morphologies are typically deposited. For example, the preparation of dense PLD-prepared YSZ thin films is attained at low oxygen pressures during the deposition, whereas the formation of porous YSZ with a high specific surface area is facilitated at high pressures, as reported in several studies.[82,138–141] The substrate temperature is mainly responsible for the nucleation density of the film.[139,142,143] High temperatures enhance the nucleation, thereby improving the crystallization and producing strongly ordered and larger grains.

Moreover, PLD-deposited thin films usually require post-annealing treatments to obtain high-quality films.

2.4.2. Evaporation-induced Self-assembly (EISA)

The EISA process is well-suited to synthesize ordered mesoporous thin films with a high specific surface area and nanoscale features.[30,144–149] This process has been developed by Ogawa and Brinker for the preparation of mesostructured silica thin films.[150,151] In recent years, various mesostructured materials have been prepared by combining sol-gel chemistry with surfactants and/or polymer structure-directing agents. The EISA process is illustrated in Fig. 7. In general, it is based on the combination of sol-gel chemistry and self-assembly of amphiphilic molecules. The approach combines the advantages of both soft- and hard-templating chemistries. Typically, a planar substrate is sprayed, dip-coated or spin-coated with a solution of a structure-directing agent (e.g., block copolymer), inorganic precursor(s), and an organic solvent (e.g., alcohol). During the evaporation of the solvent, the self-assembly drives the generation of supramolecular micelles and leads to the formation of a hybrid mesophase with short- or long-range periodicity. This step is followed by a heating process to remove the polymer template and to enable crystallization of the pore wall structure and control of grain size, leading to the formation of ordered mesoporous materials with nanocrystalline walls. The final mesostructure of the thin film can be carefully controlled by several intrinsic and extrinsic processing parameters. The EISA process is a simple, efficient, and rapid method for the preparation of uniform and robust thin films. Due to the high variability of EISA parameters compared to other sol-gel approaches, this process has been routinely used to produce a large number of mesoporous films in recent years. Particularly, metal oxide thin films, such as Fe_2O_3, TiO_2 and WO_3, with an ordered pore network of 10 to 20 nm pores and crystalline walls have been synthesized.[152–157] These thin films are used in diverse applications, such as optics, catalysis, separation, photovoltaics, low dielectric layers and sensors, to name a few.

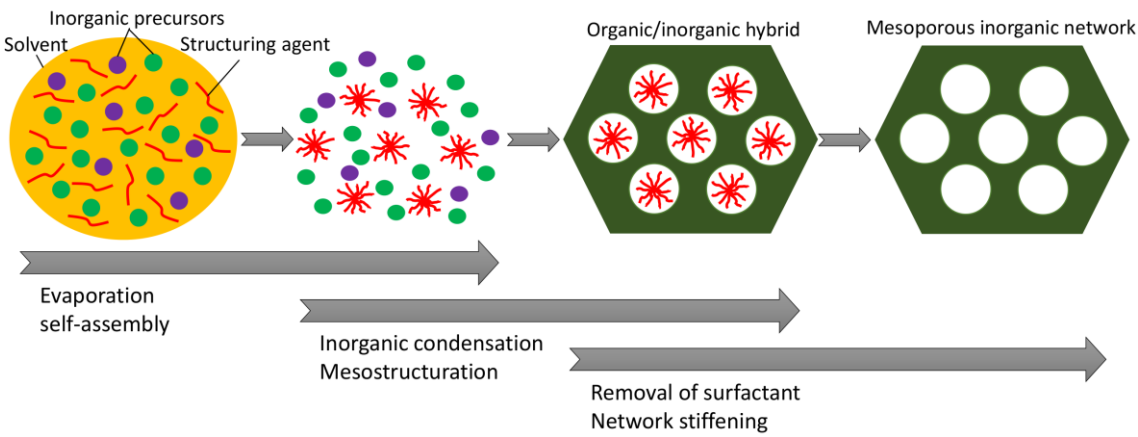

Fig. 7: Schematic illustration of different steps involved in the evaporation-induced self-assembly (EISA) process.

2.4.3. Atomic Layer Deposition (ALD)

ALD is a thin film deposition method, which provides conformal and uniform coatings on complex surfaces. ALD is a special type of chemical vapor deposition (CVD) introduced by Suntola and Antson in 1977.[158–161] Over the past decades, surface modification via ALD has gained attention as a promising route to improve structural and electrical properties of dense and porous materials. For instance, coatings lead to functionalization and protection of surfaces. This technique is based on sequential, self-limiting gas-solid surface reactions, leading to controlled layer-by-layer growth down to the atomic level of the desired material (Frank-Van der Merwe growth). ALD is a cycle process, consisting of sequential pulsing of at least two reactive precursor gases that chemisorb on the whole substrate surface. This step is followed by intermediate purging or evacuation steps in order to remove unreacted gaseous precursor and thus to avoid gas phase reactions. As shown in Fig. 8, the precursors are pulsed alternately and separated by purge periods. In this way, it is possible to deposit a variety of materials, such as oxides, nitrides, sulfides and pure elements.

Ideally, a monolayer of the respective material is formed during each ALD cycle. However, in practice, the layer growth per cycle is significantly influenced by the steric hindrance of the gaseous precursor molecules as well as the interaction between precursor and substrate surface. The desired coating thickness can be achieved by repeating the process sequence including all reaction and purging steps, i.e., by the number of ALD cycles. An illustration of the process is provided in Fig. 8. Here, the growth rate is mainly influenced by three parameters, the substrate temperature, the

vapor pressure of precursor(s), and the purge/pulse duration. Depending on the material, the ALD process occurs at temperatures between room temperature and ~500 °C.

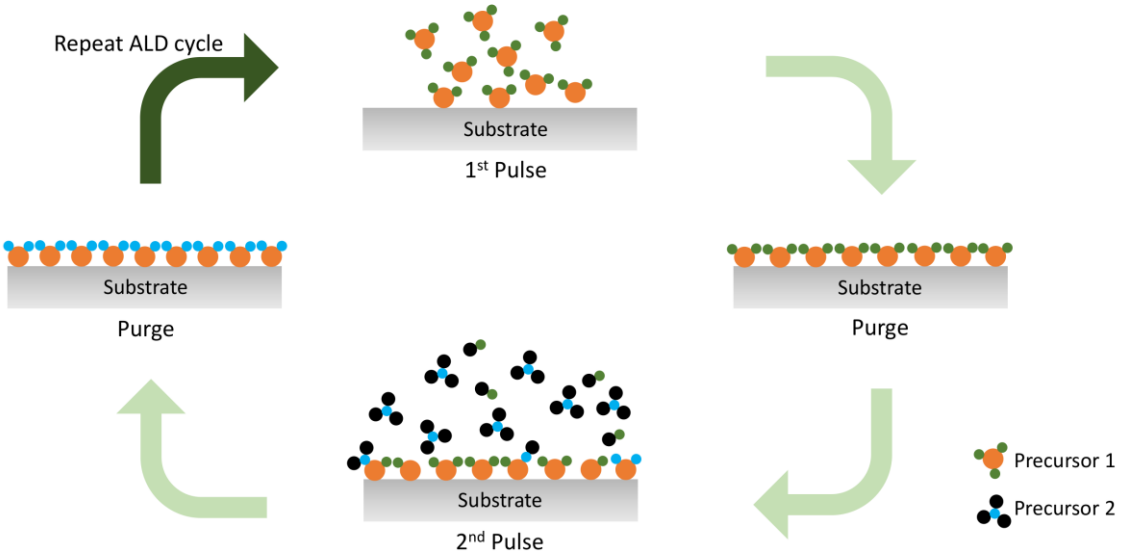

Fig. 8: Schematic representation of a typical ALD cycle. Typically, the duration of one cycle is between one and several seconds.

3. Results and Discussion

3.1. Publication I: Ordered Mesoporous Metal Oxides for Electrochemical Applications: Correlation between Structure, Electrical Properties and Device Performance

The first publication of this doctoral thesis addresses the state-of-the-art in the synthesis of mesoporous metal oxides, their structural and physicochemical properties and their potential for electrochemical applications in batteries, for (photo-) electrocatalysis or as gas sensor. In this invited Perspective article, we discuss the advantages and disadvantages of the unique structural properties of ordered mesoporous oxides, such as the regular pore structure and the resulting high surface area, regarding their performance for different electrochemical device applications.

To gain a fundamental understanding of the physicochemical properties of mesoporous metal oxides, the defect chemistry at interfaces and the impact of the resulting space charge region on the partial electronic and ionic conductivity are discussed. Here, Gouy-Chapman and Mott-Schottky models are introduced as the most promising cases for the description of the charge carrier distribution at the interface. In addition, the publication discusses the role of humidity on the protonic surface conductivity. In particular, the general aspects of the protonic transport mechanisms are discussed. Finally, we highlight the benefits of surface modification via ALD, which tailors the functionality of mesoporous materials and provides new design principles for the development of high performance devices in the field of modern energy technology.

The perspective article was written by me and edited by all co-authors. Reprinted with permission from *Physical Chemistry Chemical Physics*. Copyright (2021) Royal Society of Chemistry. This article is part of the *PCCP* Perspectives and 2021 *PCCP HOT* Articles.

Erdogan Celik, Yanjiao Ma, Torsten Brezesinski and Matthias T. Elm, Ordered Mesoporous Metal Oxides for Electrochemical Applications: Correlation between Structure, Electrical Properties and Device Performance, *Phys. Chem. Chem. Phys*., **2021**, 23, 10706-10735.

Volume 23
Number 18
14 May 2021
Pages 10693–11106

PCCP

Physical Chemistry Chemical Physics

rsc.li/pccp

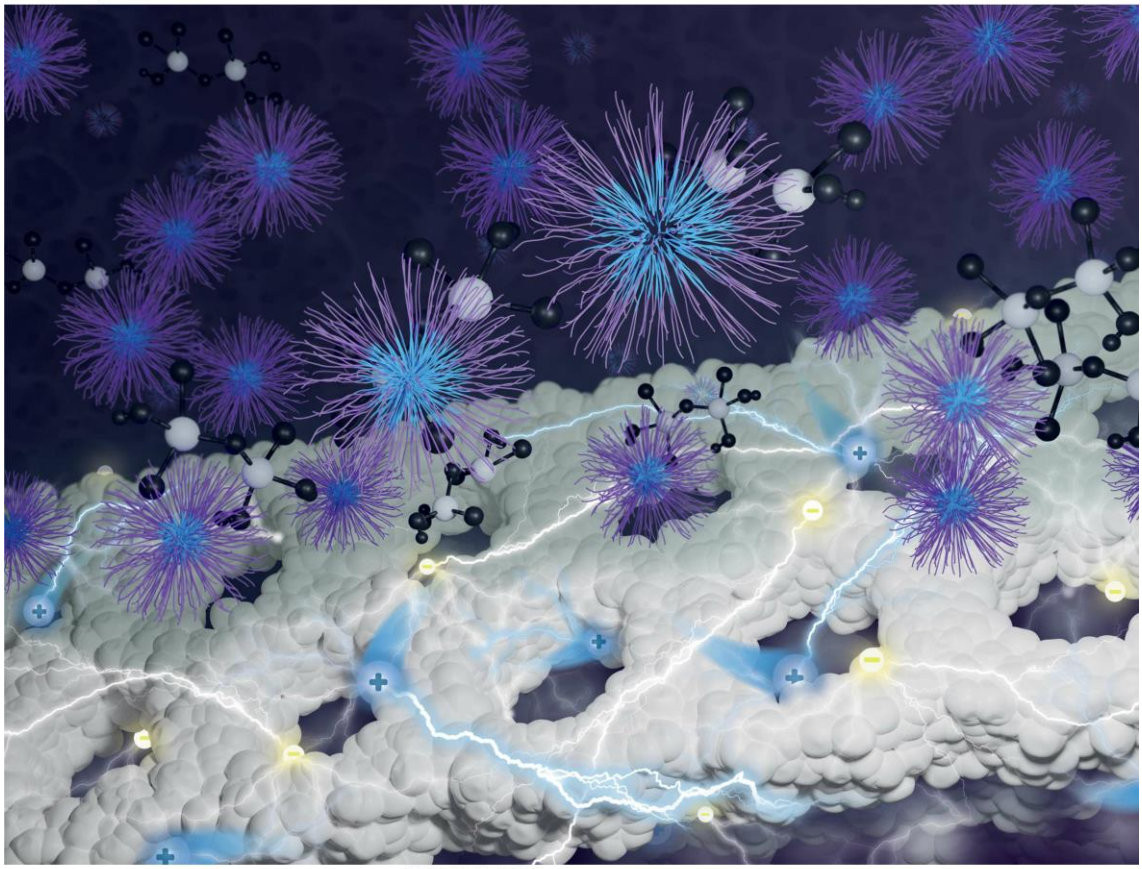

ISSN 1463-9076

ROYAL SOCIETY OF CHEMISTRY

PERSPECTIVE
Torsten Brezesinski, Matthias T. Elm *et al.*
Ordered mesoporous metal oxides for electrochemical applications: correlation between structure, electrical properties and device performance

PCCP

ROYAL SOCIETY OF CHEMISTRY

PERSPECTIVE

View Article Online
View Journal | View Issue

Check for updates

Cite this: *Phys. Chem. Chem. Phys.*, 2021, **23**, 10706

Ordered mesoporous metal oxides for electrochemical applications: correlation between structure, electrical properties and device performance

Erdogan Celik,[a] Yanjiao Ma,[b] Torsten Brezesinski *[b] and Matthias T. Elm *[acd]

Received 23rd February 2021,
Accepted 30th March 2021

DOI: 10.1039/d1cp00834j

rsc.li/pccp

Ordered mesoporous metal oxides with a high specific surface area, tailored porosity and engineered interfaces are promising materials for electrochemical applications. In particular, the method of evaporation-induced self-assembly allows the formation of nanocrystalline films of controlled thickness on polar substrates. In general, mesoporous materials have the advantage of benefiting from a unique combination of structural, chemical and physical properties. This Perspective article addresses the structural characteristics and the electrical (charge-transport) properties of mesoporous metal oxides and how these affect their application in energy storage, catalysis and gas sensing.

1. Introduction

With the introduction of surfactant-templating methods and the evaporation-induced self-assembly (EISA) process in the 1990s, interest in the preparation of ordered mesoporous materials in powder and thin film form has become widespread.[1–6] While initial efforts focused on siliceous materials, soft-templating methods, in general, lend themselves to the formation of mesostructured metal oxides with nanocrystalline walls.[7–16] The preparation usually relies on the solution-phase co-assembly of either sol–gel precursors or preformed (nanocrystal) building blocks with a surfactant or an amphiphilic polymer structure-directing agent to achieve different pore symmetries, followed by some post-treatment.[13–22] Because of their unique structural and compositional diversity, mesoporous materials are currently drawing increasing attention for energy applications (batteries, catalysis, gas storage and sensing, *etc.*).[23–27] In principle, an open pore–solid architecture provides good accessibility of the material and its internal structure to the surrounding medium (note that gasses or liquids can readily penetrate into the porosity), thereby offering a large number of active surface sites. In addition, it enables effective transport of charge carriers due to short diffusion pathways, among others, and endows the material with mechanical flexibility. Most importantly, because of the small dimensions of the crystallites in the pore walls and the high interface density, defect chemistry and surface space-charge effects strongly affect the device performance and provide the unique possibility of tailoring the materials properties. In this Perspective, we review and describe the interplay between structure and electrical transport properties of mesoporous metal oxides (mainly as thin films), with a particular focus on applications in electrochemical energy storage, catalysis and gas sensing. Challenges and future prospects are also discussed.

[a] *Center for Materials Research, Justus Liebig University Giessen, 35392 Giessen, Germany. E-mail: matthias.elm@phys.Chemie.uni-giessen.de*
[b] *Institute of Nanotechnology, Karlsruhe Institute of Technology (KIT), Hermann-von-Helmholtz Platz 1, 76344 Eggenstein-Leopoldshafen, Germany. E-mail: torsten.brezesinski@kit.edu*
[c] *Institute of Experimental Physics I, Justus Liebig University Giessen, 35392 Giessen, Germany*
[d] *Institute of Physical Chemistry, Justus Liebig University Giessen, 35392 Giessen, Germany*

2. Mesoporous metal oxide thin films

2.1. Evaporation-induced self-assembly

The principles of self-assembly for sol–gel-derived mesoporous materials have been described in considerable detail elsewhere and will not be further discussed here.[13–17,28–32] However, in the following, we briefly describe the EISA-based preparation of mesostructured thin films, which affords a high degree of control over the intrinsic (chemistry) and extrinsic (environment) processing parameters. In the past two decades, many important metal oxides, primarily with pores in the size range between 5 and 30 nm, and with different crystalline phases have been produced by EISA and related methods. However, crystallization of the wall structure with retention of the porosity is challenging. This is due, in part, to the lack of broad availability of suitable structure-directing agents.

In general, the processing scheme shown in Fig. 1 can be described as follows: a solution containing the structure-directing

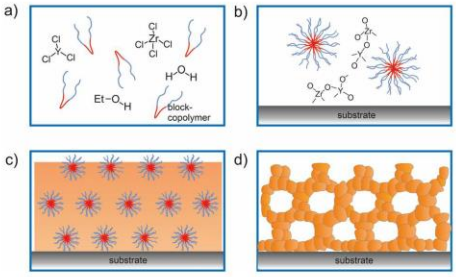

Fig. 1 Schematic illustration of the fabrication steps for ordered mesoporous thin films using an EISA process. (a) Solution consisting of structure-directing agent and inorganic precursors (shown for $ZrCl_4$ and YCl_3; chemical reactions with the solvent are omitted for clarity), (b) micelle formation, coassembly and condensation of the inorganic reagents, (c) inorganic–organic hybrid thin film formation upon solvent evaporation and (d) thermally-induced crystallization of the inorganic wall structure and combustion of the organic structure-directing agent.

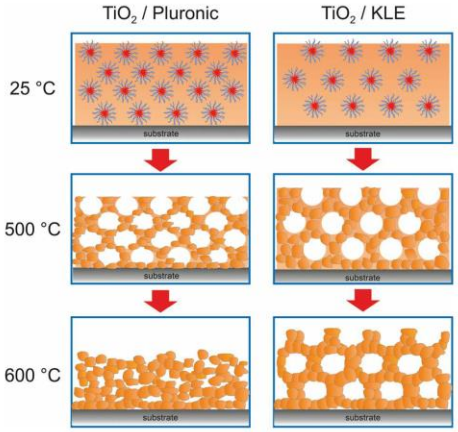

Fig. 2 The effect of annealing temperature on the pore structure of Pluronic- and KLE-templated TiO_2 thin films. Adapted from ref. 54 with permission.

agent and the precursor(s), and possibly an organic additive (*e.g.*, swelling or stabilizing agent), is sprayed, spin- or dip-coated onto a planar substrate. Upon solvent evaporation, a mesostructured inorganic–organic hybrid thin film with short- or long-range periodicity is formed. Finally, the material is made porous by removing the structure-directing agent *via* extraction or combustion. Note that heating at elevated temperatures is typically used to drive condensation of the inorganic framework, crystallize the pore walls and tailor the grain size.

In general, mesoporous materials have the advantage of benefiting from a unique combination of structural, chemical and physical properties, making them interesting for a variety of applications. Especially amphiphilic polymers as structure-directing agents have been shown well suited for the preparation of crystalline metal oxide thin films with cubic or hexagonal pore structures. In this regard, KLE diblock copolymers [KRATON LIQUID-*block*-poly(ethylene oxide) or poly(ethylene-*co*-butylene)-*block*-poly(ethylene oxide)] seem to somewhat stand out due to their favorable templating properties.[11,12,19,33] However, other di- and triblock copolymers, such as poly(ethylene oxide)-*block*-poly(propylene oxide)-*block*-poly(ethylene oxide) (referred to as Pluronic), polyisobutylene-*block*-poly(ethylene oxide), poly(ethylene oxide)-*block*-polybutadiene-*block*-poly(ethylene oxide) or poly-(ethylene oxide)-*block*-polystyrene, have also proven to be robust structure-directing agents.[7,8,13,16,20,34–37]

A variety of binary and multinary metal oxide thin films with cubic mesoporous morphologies have been synthesized from KLE and alkoxide or salt precursors, including TiO_2, Al_2O_3, CeO_2, HfO_2, MoO_3, SnO_2, $SrTiO_3$, $Li_4Ti_5O_{12}$, $REVO_4$, $BiFeO_3$ and PZT, to name a few.[11,12,19,38–49] In the following, we use TiO_2, which is often considered as a prototype material for applications in photocatalysis, solar cells or batteries, as an example.[50–53] Smarsly *et al.* reported on the preparation of cubic mesoporous TiO_2 thin films from EtOH:THF solution containing $TiCl_4$ and KLE by the dip-coating method. Crystallization into the anatase phase was found to begin at 450 °C and the nanoscale porosity was retained up to about 700 °C.[11] In a related study, Fattakhova-Rohlfing *et al.* examined the Li-storage properties of KLE- and Pluronic P123-templated mesostructured TiO_2 thin films, which allowed quantifying the fraction of crystalline and amorphous phases in the samples.[54] They showed that the Pluronic P123-derived films display a strong tendency for anatase formation already well below 450 °C (approx. 50% crystallinity at 400 °C) and that full crystallization at temperatures ≥600 °C is accompanied by collapse of the pore network. This behavior is in stark contrast to that of the KLE-templated material, as schematically shown in Fig. 2. Brezesinski *et al.* also synthesized cubic mesoporous TiO_2 thin films by a conventional sol–gel route using KLE and $TiCl_4$ as polymer structure-directing agent and precursor, respectively, and by a particle-based route, with anatase nanocrystals serving as preformed building blocks.[19] The authors demonstrated that the nanocrystal films can withstand much higher temperatures (up to 900 °C) before losing nanoscale order. In addition, they showed much improved Li-storage properties, especially greater power density due to high levels of pseudocapacitive charge storage.

Hartmann *et al.* compared the photoelectrochemical water splitting properties of cubic mesoporous TiO_2 thin films produced using the same synthetic routes described by Brezesinski and coworkers.[20] Both materials differed significantly in the pore walls thickness, see scanning electron microscopy (SEM) images in Fig. 3, despite using the same polymer structure-directing agent in the preparation process. Interestingly, the sol–gel material showed a significantly higher efficiency, which the authors explained by insufficient electronic connectivity of the nanocrystal films. Overall, these results indicate that not only the pore accessibility and specific surface area but also the transport properties have a profound effect on the device performance.

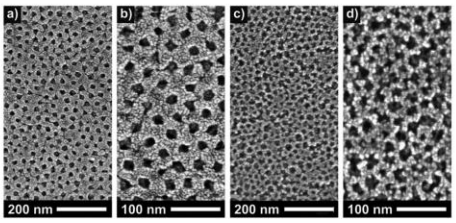

Fig. 3 Top-view SEM images of sol–gel-derived (a and b) and preformed nanoparticle-based (c and d) mesoporous TiO_2 thin films. Reproduced from ref. 20 with permission.

3. Transport properties

As briefly discussed in the previous sections, mesoporous oxides are of interest for a broad range of electrochemical applications. For the functionality of such devices, efficient transport of electrical charge carriers (mobile defects of the ideal crystal structure) is required. As mesoporous materials are typically polycrystalline and made from individual crystallites connected in a 3-dimensional framework, as schematically shown in Fig. 4, they contain a high density of interfaces. Solid/solid (grain boundaries), solid/liquid and solid/gas interfaces may significantly alter the mobility of electronic and ionic charge carriers due to the formation of a space-charge region. In general, the electrical conductivity of a charge carrier is given by:

$$\sigma = Ze\mu n, \tag{1}$$

where Z is the valence, e is the elementary charge, μ is the mobility and n represents the charge-carrier density contributing to the transport. In the presence of an interface, both the charge-carrier density and mobility may differ from the respective bulk values, making detailed understanding of the effect of interfaces on the electrical transport properties indispensable. Apart from elemental doping, optimization of the electronic properties of mesoporous materials, and therefore of the electrochemical device performance, is feasible by tailoring the interface density, for example, by controlling the pore size, the wall thickness or the size of the crystallites (grains) in the wall structure.

In the following, we will give a short description of both the formation of a space-charge layer at interfaces and the characterization of electronic and ionic conductivity using electrochemical impedance spectroscopy (EIS). The influence of a space-charge layer on the electronic and ionic transport properties has been reported in detail for CeO_2- and ZrO_2-based ceramics when the crystallite size becomes comparable to its extension. The findings for these systems will be briefly summarized, followed by reports on the investigation of transport properties in mesoporous materials. Finally, we also discuss the protonic conductivity in nanoscale oxides.

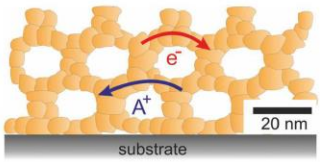

Fig. 4 Schematic illustration of the 3-dimensional architecture of mesoporous oxide thin films with efficient transport pathways for electrons and ions and a vast number of interfaces.

3.1. Defect chemistry at interfaces

As indicated by eqn (1), the electrical conductivity of a material depends on the concentration and mobility of charge carriers. While the mobility is determined by the electronic and ionic structure of the crystal, the carrier concentration is related to the electrochemical potential of the corresponding defect A, which is given by the sum of the chemical potential and the electrical potential:[55]

$$\tilde{\mu}_A = \mu_A^0 + Z_A F\phi(x). \tag{2}$$

In the absence of an electrical field, the electrochemical potential is constant throughout the bulk. However, at an interface, the local symmetry is broken. This means the chemical potential ($x = 0$) differs from that in the bulk ($x = \infty$):

$$\mu_A(x = 0) \neq \mu_A(x = \infty). \tag{3}$$

To ensure constant electrochemical potential, the mobile charge carriers redistribute, resulting in charging of the interface and local variation of the electrical potential $\phi(x)$, the so-called space-charge region, which compensates for the difference in chemical potential. The redistribution of charge carriers affects the carrier concentration at the interface, and therefore the corresponding electrical conductivity.

For an ideal interface, the change in charge-carrier concentration relative to the bulk concentration c_∞ is given by (1-dimensional case):[56–58]

$$\zeta(x) = \frac{c(x)}{c_\infty} = \exp\left(-\frac{Ze\Delta\phi(x)}{k_B T}\right), \tag{4}$$

where $\Delta\phi(x) = \phi(x) - \phi_\infty$ is the potential relative to the bulk potential ϕ_∞. The distribution of charge carriers can then be calculated by solving the Poisson–Boltzmann equation.[56]

Depending on the mobile charge carriers present in the system, different profiles of the resulting charge-carrier distribution are obtained. The two most prominent cases are Gouy–Chapman and Mott–Schottky,[59] both of which are schematically shown in Fig. 5.

In the Gouy–Chapman case, two charge carriers of opposite sign are mobile and contribute to the surface charging. In the space-charge region, the carrier with the opposite sign to the surface charge accumulates at the interface, while the other is depleted. The width of the space-charge region is then given by the Debye length:[59]

$$\lambda_D = \sqrt{\frac{\varepsilon_0 \varepsilon_r k_B T}{2Z^2 e^2 n_\infty}}, \tag{5}$$

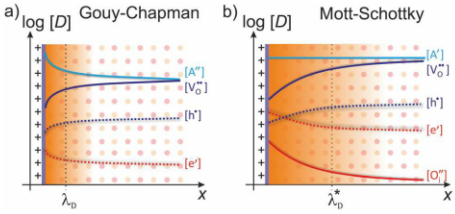

Fig. 5 Schematic illustration of the space-charge region for (a) Gouy–Chapman and (b) Mott–Schottky case. Adapted from ref. 60 with permission.

with ε_0 and ε_∞ being the vacuum permittivity and permittivity of the material, respectively.

If one of the charge carriers is immobile, that is, its concentration profile is independent of the distance to the boundary, redistribution of mobile charge carriers follows a Mott–Schottky profile. Compared with the Gouy–Chapman case, redistribution results in an extended space-charge region of effective width:[59]

$$\lambda^* = \sqrt{\frac{2\varepsilon_0\varepsilon_r\Delta\phi(0)}{Zen_\infty}} = \lambda_D\sqrt{\frac{4Ze}{\varepsilon_0\varepsilon_r k_B T}\Delta\phi(0)}. \quad (6)$$

As the space-charge profile can only be calculated analytically for two charge carriers of opposite sign, for mixed cases or for low space-charge potentials, approximations are needed. Göbel *et al.* presented a numerical approach to calculate the concentration profile for these cases, allowing to obtain more precise analytical solutions of the Poisson–Boltzmann equation.[61,62] However, determination of the space-charge profile by solving the Poisson–Boltzmann equation does not account for interactions between the charge carriers, which can become important for high defect concentrations. In 2015, Mebane and De Souza presented a generalized space-charge model (Poisson–Cahn theory) to account for defect–defect interactions at high defect concentrations.[63,64] While in the dilute case, the results of the analytic model described above are well reproduced, the profile of the space charge is modified for higher defect concentration. At the positively charged interface, the oxygen-vacancy concentration increases significantly (segregation of oxygen vacancies at the interface). Interestingly, depletion of oxygen vacancies in the adjacent space-charge region is accompanied by an enrichment of carriers before the bulk value is reached.

3.2. Electronic and ionic conductivity

The effect of a space-charge layer on the electronic and ionic transport is reasonably well understood for polycrystalline CeO_2- and ZrO_2-based ceramics. In both material systems, grain boundaries exhibit a positively charged core, resulting in depletion of oxygen vacancies in the space-charge region, and therefore in a highly resistive grain boundary. The latter hinders the transport of oxygen ions. To investigate the influence of the internal interfaces on the total resistivity, EIS is the most prominent and commonly used tool,[65–70] as this method allows distinguishing to some extent between contributions of the grain and the grain boundary due to differences in the corresponding dielectric relaxation times.[66,68,71]

In microcrystalline oxides, the total impedance is typically described using the brick-layer model (BLM),[71–73] where a transport path through the bulk, across and along the grain boundaries is considered. In oxides with highly resistive grain boundaries, such as yttria-stabilized zirconia (YSZ), the transport path parallel to the grain boundary can be neglected.[67,74]

The resulting impedance spectra exhibit two semicircles, as shown in Fig. 6, and can be described with an equivalent circuit consisting of two resistance–capacitance elements connected in series, representing the transport along the grain and across the grain boundary. Analysis then allows determining the grain boundary thickness δ_{gb}:[75,76]

$$\delta_{gb} = \frac{\varepsilon_{gb}}{\varepsilon_{bulk}}\frac{C_{gb}}{C_{bulk}}\delta_g, \quad (7)$$

where δ_g denotes the grain size and C_{gb} and C_{bulk} are the capacitance values from EIS for the grain boundary and bulk, respectively. Furthermore, the space-charge potential at the interface can be calculated according to:[74]

$$\rho_{gb} = \rho_{bulk}\frac{\exp(Ze\Delta\phi(0)/k_B T)}{Ze\Delta\phi(0)/k_B T}. \quad (8)$$

A detailed analysis of the impedance of microcrystalline ZrO_2 (Mott–Schottky case) using the BLM confirms that the blocking behavior of grain boundaries is caused by the formation of a

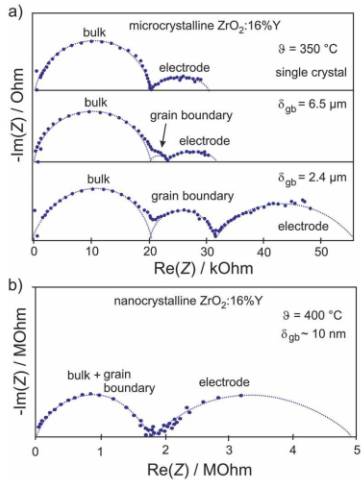

Fig. 6 (a) Impedance spectra for single-crystal and microcrystalline YSZ. The grain boundaries of the microcrystalline sample lead to the appearance of an additional semicircle. (b) Reducing the grain size to the nanometer level results in merging of semicircles representing the bulk and grain boundary transport processes. Adapted from ref. 77 with permission.

space-charge region[74,79,80] and not solely by segregation effects, as previously assumed.[67,81,82] The influence of the space-charge region on the overall impedance becomes even more important when the grain size is comparable to the width of the space-charge region,[83,84] which is typically a few nanometers for oxide ceramics. Then, interface effects are more pronounced and may even dominate the impedance.[57,72] As shown in Fig. 6, the decrease in grain size results in merging of the semicircles representing the bulk and grain boundary transport processes,[56,77,85] making their separation difficult. Furthermore, the accumulated charge carriers may also contribute to the transport through the sample. This is typically observed for the Gouy–Chapman case,[59] but can also occur for the Mott–Schottky case at low doping concentration.[86] For large effects, the electrons result in an additional contribution to the conductivity along the grain boundaries:[26,59]

$$\sigma_{\mathrm{eff}}^{\parallel} = 2\lambda_{\mathrm{D}}\sigma_{\mathrm{bulk}}\sqrt{\frac{n_0}{n_\infty}} = 2\lambda_{\mathrm{D}}\sigma_{\mathrm{bulk}}\exp\left(\frac{Ze\Delta\phi(0)}{k_{\mathrm{B}}T}\right), \qquad (9)$$

where n_0 and n_∞ denote the electron concentration at the interface and in the bulk, respectively. An overview of the conductivity/resistivity contributions for different space-charge situations due to accumulation/depletion of charge carriers at the interface is given in ref. 59 and 61.

A prominent example, where transport along the grain boundary becomes important, is nanostructured CeO_2.[59,85,87] Here, the space-charge region results in accumulation of electrons at the grain boundary (Fig. 7). While in microcrystalline samples the transport is mainly determined by oxygen ions, nanostructured CeO_2 reveals a dominant electronic conductivity.[59] As shown in Fig. 8, Tschöpe *et al.* were capable of describing the change from ionic to electronic transport with decreasing grain size using the space-charge model.[88,89] Furthermore, their numerical calculations revealed that, due to the space-charge layer and segregation effects at the interface, not only the apparent activation energy of the transport process depends on the grain size (Fig. 8) but also the characteristic exponent of the $p(O_2)$-dependence of conductivity.[88–90] A decrease of the bulk ionic conductivity with decreasing grain size is found for nanocrystalline YSZ due to depletion of oxygen vacancies in the grain, caused by the increasing impact of the space-charge layer.[79]

However, the analytical description of transport properties using the space-charge model is only valid as long as the grain size is four times larger than the Debye length, $\delta_g > 4\lambda_D$.[55,75,90]

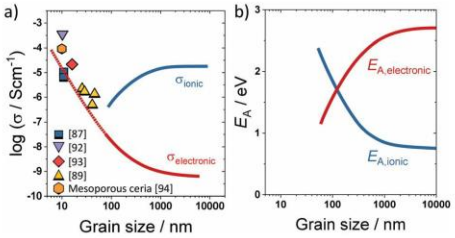

Fig. 8 (a) Change in electronic/ionic partial conductivity with the grain size; experimental data taken from ref. 87, 89 and 92–94. (b) Change in apparent activation energy of ionic/electronic transport with the grain size. Adapted from ref. 90 with permission.

If the grain size is further reduced, the space-charge regions of opposite grain boundaries start to overlap (Fig. 7) and the concentration profiles according to eqn (4) are not valid anymore. In CeO_2 and ZrO_2, this condition is typically fulfilled for grain sizes below approx. 20 nm. If the grain size is further reduced to $\delta_g \ll 4\lambda_D$, the space charges completely extend throughout the grain, resulting in an almost constant carrier concentration.[91]

For small space-charge potential, Maier derived a so-called nano-factor g to describe the resulting enhancement of conductivity:[55]

$$g = \frac{4\lambda_{\mathrm{D}}}{\delta_{\mathrm{g}}}\sqrt{\frac{c_0 - c^*(\delta_{\mathrm{g}})}{c_0}}. \qquad (10)$$

Here, $c^*(\delta_g)$ is the concentration of accumulated charge carriers in the center of the grain, which is given by elliptical integrals depending on the grain size δ_g, the bulk concentration c_{bulk} and the concentration at the interface c_0.

The influence of the space-charge region on the electrical properties is well reported for nanocrystalline oxides with a high grain-boundary density. In case of mesoporous oxides, not only the grain boundaries act as an interface but also the free surface. Although the same description holds as for grain boundaries,[55] the surface potential, and therefore the extension of the space-charge layer in the crystallites, is more sensitive to variations in the surrounding atmosphere (gas or liquid penetrating into the pores), thereby allowing to tailor the

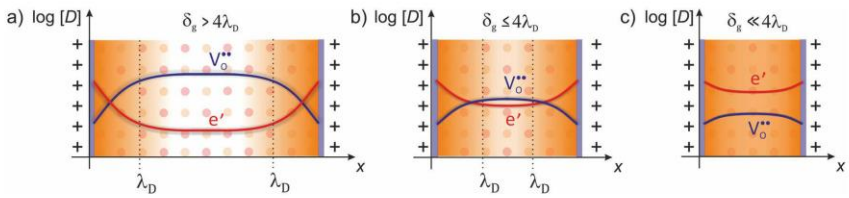

Fig. 7 Defect concentration for different grain sizes (schematically shown for CeO_2). (a) The space-charge region affects the defect concentration near the interface in microcrystalline material. (b) For grain sizes smaller than four times the Debye length, the space-charge region starts to overlap and (c) finally completely dominates the defect concentration of the whole grain. Adapted from ref. 78 with permission.

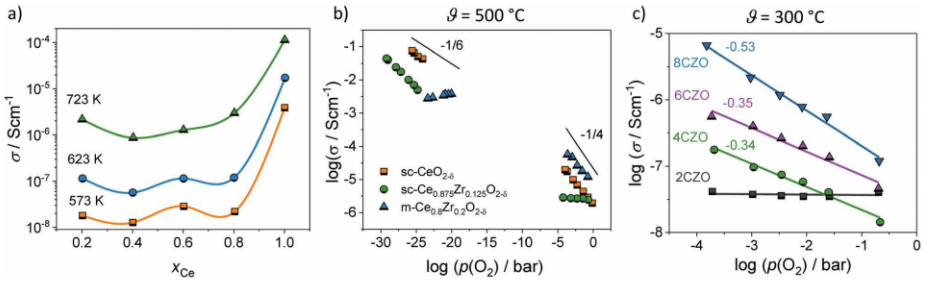

Fig. 9 (a) Total conductivity of mesoporous $Ce_xZr_{1-x}O_{2-\delta}$ solid solutions. Adapted from ref. 94 with permission. (b) Comparison of the oxygen-partial-pressure-dependence of conductivity for mesoporous $Ce_{0.8}Zr_{0.2}O_{2-\delta}$ thin films and for CeO_2 and $Ce_{0.875}Zr_{0.15}O_{2-\delta}$ single crystals at 500 °C. (c) Oxygen-partial-pressure-dependence of conductivity for mesoporous $Ce_xZr_{1-x}O_{2-\delta}$ solid solution thin films at 300 °C. Adapted from ref. 94 with permission.

electrical properties. However, because of their unique architecture, mesoporous thin films may show significant differences compared to nanocrystalline materials.

Hartmann *et al.* studied the electrical conductivity of mesoporous ceria–zirconia ($Ce_xZr_{1-x}O_{2-\delta}$) solid solutions of different composition under varying oxygen partial pressure by means of EIS.[94] Because of the small crystallite size in the range between 4 and 12 nm, only one semicircle was observed experimentally, as discussed above. Consequently, only the total impedance could be determined. Fig. 9 shows the calculated conductivity values for the different materials. Especially for the pure CeO_2 sample, high conductivity was found. This result can be attributed to the electronic conductivity in the space-charge layer both at the surface and at the grain boundaries, as the obtained value is in good agreement with that expected from the model of Tschöpe *et al.* (Fig. 8). However, it is worth mentioning that the conductivity was calculated assuming dense films. This means the actual conductivity in the pore walls is expected to be even higher.

Fig. 9 also shows a comparison of the $p(O_2)$-dependence of electrical conductivity at 500 °C for mesoporous $Ce_{0.8}Zr_{0.2}O_2$ thin film and single crystals of comparable composition. The latter serve as a kind of reference without the influence of interfaces. Similar to the pure CeO_2, mesoporous $Ce_{0.8}Zr_{0.2}O_2$ showed a significant increase in total conductivity (increased electronic conductivity). The $p(O_2)$-dependence of conductivity further supports the assumption of dominant electronic transport, as the slope of −1/4 at high oxygen partial pressure is characteristic of electronic transport according to the standard defect chemical description (if the oxygen vacancy concentration can be assumed constant [extrinsic regime]).[85,95,96] For low oxygen partial pressure, standard defect chemistry predicts a −1/6-dependence (intrinsic regime) when the concentration of electrons becomes comparable to the oxygen-vacancy concentration.[85,95–97] The mesoporous thin film showed a maximum in conductivity and a decrease with further decreasing oxygen partial pressure, which can be attributed to a hopping maximum of the electronic transport in the Ce^{3+} sublattice. Because the electronic conductivity in CeO_2 is determined by electron hopping from Ce^{3+} to Ce^{4+} sites, the hopping probability depends on the fraction of Ce^{3+} and Ce^{4+} ions in the lattice according to:[98,99]

$$\sigma_e = \frac{n_{Ce} x_{Ce^{3+}} (1 - x_{Ce^{3+}}) e^2 a^2 \nu_0}{k_B T} \exp\left(-\frac{\Delta H_m}{k_B T}\right), \qquad (11)$$

with a being the distance between the hopping sites, ν_0 the attempt frequency, n_{Ce} the number of cerium lattice sites and ΔH_m the migration enthalpy of the hopping process. The product $x_{Ce^{3+}}(1 - x_{Ce^{3+}})$ takes into account that hopping can only occur from Ce^{3+} to Ce^{4+}. Hence, at high electron concentration, $x_{Ce^{3+}} \gtrsim 0.5$, the hopping probability decreases again due to the reduced number of available Ce^{4+} species, leading to a decrease in electronic conductivity, as recently reported for Pr-doped CeO_2 single crystals, where the electrons hop in the Pr-sublattice.[99] The increase in electronic conductivity and the occurrence of a hopping maximum suggest high electron concentration, and therefore significantly higher reducibility of the mesoporous material compared to nanocrystalline (dense) material (due to the higher specific surface area).

However, more interesting is the $p(O_2)$-dependence of conductivity at lower temperatures. As shown in Fig. 9, the mesoporous $Ce_{0.8}Zr_{0.2}O_2$ thin film revealed a much stronger $p(O_2)$-dependence, with a characteristic slope of −1/2 at 300 °C, while for both mesoporous $Ce_{0.6}Zr_{0.4}O_2$ and $Ce_{0.4}Zr_{0.6}O_2$ thin films, a $p(O_2)$-dependence with an exponent of approx. −1/3 was observed. The unusual $p(O_2)$-dependence cannot be explained using the standard defect chemical model. Hartmann *et al.* proposed that oxygen vacancies with a relative charge lower than +2 are responsible for the behavior. Specifically, two scenarios have been discussed. First, formation of defect associates (due to high electron concentration) may either result in not completely ionized vacancies, $(V_O^{\bullet\bullet} + xe') \rightleftharpoons V_O^{(2-x)\bullet}$, or defect associates formed by vacancies and Ce^{3+} ions.[101,102] Second, O^- instead of O^{2-} ions were suggested to exist at the surface to compensate the Ce^{3+} ions. While the origin of the unusual $p(O_2)$-dependence still remains largely unclear, the results show that the high surface area of mesoporous materials can significantly alter their electrical properties.

3.3. Protonic conductivity

In recent years, especially nanostructured materials are receiving much attention, as significant protonic conductivity may be observed under wet atmospheric conditions for oxides, such as YSZ,[103–106] doped CeO_2,[107–110] Al_2O_3,[111] SiO_2[112] or TiO_2.[113–115] Note that their dense counterparts show no signs of protonic conductivity. The increase in conductivity under wet atmospheric conditions is shown in Fig. 10 for various materials. In contrast to high-temperature proton conductors with a perovskite structure,[116,117] like Y-doped $BaZrO_3$, where the protons are incorporated into the bulk of the material, the protonic conductivity in nanostructured oxide ceramics at low temperatures relies on the adsorption of water molecules at the surface and grain boundaries (interfaces). Because it is directly related to the nanostructure, this offers an additional degree of freedom to tailor the protonic conductivity of mesoporous oxides, rendering them interesting as water sensors,[118–121] as proton exchange membranes[122–124] or for applications in energy storage and conversion.[106,125]

Although the high interface density is responsible for the increased protonic conductivity, at first glance, it is not obvious if the transport of protons occurs along grain boundaries or the (inner) surface. First studies on nanocrystalline YSZ revealed an increase in protonic conductivity with decreasing grain size,[105,114] suggesting that the transport does occur along the grain boundaries[126] (or at least is related to the grain-boundary density). However, it is now widely accepted that the increased conductivity arises from protons moving in chemisorbed and physisorbed water layers along the pores and surface of nanostructured oxides.[100,104,127–130] The strong dependence of the protonic conductivity on relative humidity and temperature is related to the structure of the adsorbed water molecules, as summarized by Stub *et al.*[131] The structure of the water layer on TiO_2 is schematically shown in Fig. 11.

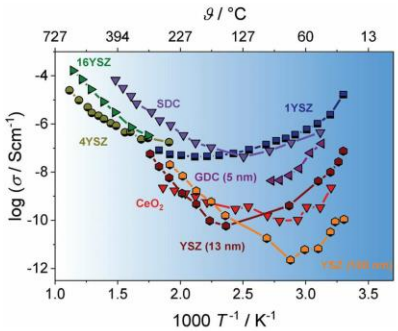

Fig. 10 Arrhenius plot of the temperature-dependent conductivity for different nanostructured oxides. Under wet atmospheric conditions, the adsorption of water molecules at the interfaces leads to significant increases due to surface protonic conductivity. Adapted from ref. 100 with permission.

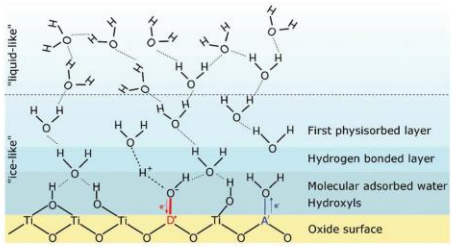

Fig. 11 Schematic illustration of the structure of adsorbed water molecules on an oxide (TiO_2) surface. The influence of an acceptor A′ or a donor D• on the water dissociation is also indicated. Reprinted from ref. 132 with permission.

At high temperature and/or low relative humidity, an "ice-like" layer is formed on the surface, consisting of chemisorbed and physisorbed molecules. In the former case, the oxide surface chemistry determines the amount of adsorbed water molecules and the type of protonic charge carriers. For instance, for an ideal ZrO_2 surface, hydroxyl groups are formed in the chemisorbed layer, which apparently are stable up to 600 °C.[100,131,133,134] Hydroxyl groups can also be formed due to the presence of surface defects, such as oxygen vacancies, where the water molecule fills the vacancy according to (Kröger–Vink notation):[110,117,135]

$$H_2O_{(g)} + V_O^{\bullet\bullet} + O_O^{\times} \leftrightarrow 2(OH)_O^{\bullet}. \qquad (12)$$

At higher relative humidity, the number of physisorbed layers increases, resulting in transition from "ice-like" to "liquid-like" water layer on the surface. The increase in water layer thickness is also accompanied by a change in transport mechanism. While in the "ice-like" layer, the protonic charge carriers move *via* Grotthuss hopping,[131] vehicle-type transport of hydronium ions is found in the physisorbed layers due to the weaker bonding between the water molecules.[100,131,133]

Stub *et al.* probed the protonic conductivity in porous TiO_2 with varying doping levels.[132] High-valent dopants, which are more acidic, are likely to attract electrons, thereby increasing the dissociation of water. This in turn increases the protonic charge-carrier concentration, and consequently also their mobility. Overall, donor-dopants improve the protonic conductivity, while the opposite effect is expected for acceptor-doped oxides. Hence, higher surface acidity results in increased protonic conductivity, as also reported for Cl-doped, mesoporous Al_2O_3, for example.[111] The profound effect of pore wall chemistry on the protonic conductivity has also been observed by Vichi *et al.*, who investigated the protonic conductivity of mesoporous TiO_2 pretreated in solutions of different pH and by modifying the surface with phosphate anions.[137] Similar results have been reported by Marschall *et al.*, who studied the influence of sulfonic acid functionalization on the protonic conductivity in mesoporous silica.[138]

In 2013, Gregori *et al.* examined the proton transport in porous CeO_2. They discussed about the influence of space-charge region on the proton transport at oxide surfaces.[107] Here, the

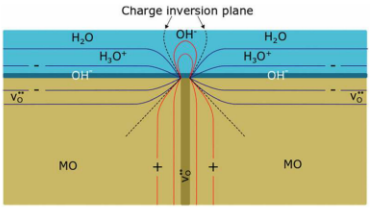

Fig. 12 Schematic illustration of the resistive behavior of a grain boundary with adsorbed water molecules on the surface of an oxide ceramic (MO). Because of the positive core, hydroxide ions accumulate at the grain boundary, impeding the transport of hydronium ions in the physisorbed water layer. Reprinted from ref. 136 with permission.

incorporation of water molecules into the space-charge region according to eqn (12) would result in an increase of hydroxide ions in the water layer at the surface, which may be responsible for the enhanced protonic conductivity at low temperature, too.

The importance of space-charge effects has also been addressed by Stub *et al.* in 2018.[136] EIS measurements conducted on nanocrystalline YSZ revealed two transport processes, one representing the proton transport along the grains (intra-grain transport), the other was attributed to a resistive transport across the grain boundaries. The positive core of the grain boundary (space-charge region of positive electric potential) results in accumulation of hydroxide ions, as schematically shown in Fig. 12, hindering the movement of hydronium ions in the physisorbed water layer.

In porous materials, the adsorption of water not only depends on the surface chemistry but also is strongly determined by the structure. Capillary condensation into the nanoscale pores facilitates water uptake.[107,124,127,130] As discussed by Vichi *et al.* for mesoporous TiO_2, the adsorption of water at the interface occurs in two steps.[137] First, water molecules are adsorbed depending on the surface chemistry of the material, while in the second step the pores are filled due to capillary condensation, independent of the surface properties. After filling of the pores with water, the protonic conductivity in mesoporous thin films can be maintained, even when changing the relative humidity.[139]

However, complete pore filling can also negatively affect the protonic conductivity. Vichi *et al.* observed an increase in activation energy of the proton transport in completely filled pores, which they attributed to bridges formed between water molecules of opposite walls.[137] Comparable results were also obtained for mesoporous SiO_2[140–142] and Al_2O_3;[111] the highest protonic conductivities were achieved with 4 and 12 nm pores, respectively. For smaller pore size, the movement of protonic carriers is hindered by geometrical restrictions.

For cubic mesoporous YSZ thin films with a pore size of about 24 nm, even a gradual decrease in total conductivity with increasing relative humidity was observed above 200 °C, as shown in Fig. 13.[135] However, porous YSZ thin films may show a significant increase in the same temperature range (Fig. 13).[129]

The decrease in total conductivity in case of the mesoporous films was attributed to the annihilation of oxygen vacancies at

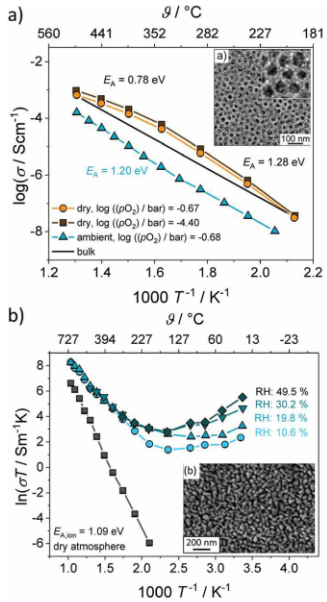

Fig. 13 Arrhenius plot of the conductivity for (a) mesoporous and (b) porous YSZ thin films under wet atmospheric conditions. Adapted from ref. 129 and 135 with permission.

the surface according to eqn (12), which are the majority charge carriers in YSZ. A decrease in total conductivity under wet atmospheric conditions has also been reported for microcrystalline CeO_2 by Chueh *et al.* They attributed this result to changes in the space-charge potential of grain boundaries upon hydration.[143] Although the influence of pore size on the protonic conductivity in oxide materials is not yet fully understood, the results clearly demonstrate the considerable effect that the pore structure has in general. In contrast to nanocrystalline oxides with an ill-defined porosity, the regular pore network of ordered mesostructured materials seems beneficial to device applications, as the pore size and structure, as well as the wall thickness, can be tailored to some degree to optimize water uptake (adsorption), and therefore the protonic conductivity.

4. Electrochemical applications

As discussed above, mesoporous oxides are characterized by a high specific surface area combined with a unique pore structure and nanocrystalline walls. These properties make them interesting for a broad range of electrochemical applications,[14,144–146] for example, as active electrode material in batteries, for (photo-)electrocatalysis and oxygen storage or as gas sensor. It should be noted that the favorable properties are not only a result of the increased surface area. Instead, the major advantage is the

presence of a uniform and continuous pore network, allowing effective transport of electronic and ionic charge carriers and providing good accessibility of the material and its internal structure to the surrounding medium, as gasses or liquids can readily penetrate into the porosity. In the following, we discuss in some more detail the pros and cons of mesoporous metal oxides and which properties are beneficial to the functionality and performance of electrochemical devices.

4.1. Mesoporous metal oxides for batteries

The working principle of an insertion- or intercalation-type material for secondary battery applications relies on both the reversible storage of ions (Li^+, Na^+ *etc.*) during electrochemical cycling and the efficient transport of charge-compensating electrons (Fig. 14). In recent years, mesoporous electrode materials have been shown to possess promising properties, allowing for superior energy storage and high power density, among others.[147] The mesoporous morphology ensures equal distribution of electrolyte in the (bulk) structure, minimizing the fraction of inactive material and allowing fast ion diffusion along the pore system.[147–149] Furthermore, the interconnection of nanoscale particles in the pore walls provides short diffusion lengths and efficient transport pathways for both the ions and electrons.

The positive effect of mesoporosity on the charge-storage properties has been proven for a variety of cathode and anode active materials, mainly for lithium-ion battery (LIB) applications, such as $LiCoO_2$,[150] $LiFePO_4$,[151] β-MnO_2,[152] $LiMn_2O_4$,[152,153] $Li_4Ti_5O_{12}$,[38] TiO_2,[19,154–156] α-Fe_2O_3[157] or NiO.[158] For example, Jiao *et al.* compared the electrochemical performance of nanowire and mesoporous $LiCoO_2$ to that of "normal" $LiCoO_2$. The mesoporous material delivered the largest specific discharge capacity and showed the best capacity retention, which was attributed to the unique pore–solid architecture with good connection among adjacent crystallites.[150] Brezesinski *et al.* came to the same conclusion from studying polymer-templated and nontemplated (nanocrystalline) TiO_2 thin films.[19] These results confirm the beneficial effect of nanoscale porosity on the electrochemical performance.

An important parameter when characterizing battery materials is the amount of stored charge. In general, the total amount consists of three contributions, as summarized in Fig. 15, namely, the faradaic contribution from the insertion of ions into the bulk of the material, the faradaic contribution from charge-transfer processes at the solid/liquid interface (pseudocapacitive charge storage) and the nonfaradaic contribution due to formation of a Helmholtz double layer.[19,156,159–161] Analysis of cyclic voltammetry (CV) data obtained at different sweep rates v allows distinguishing between diffusion- and nondiffusion-controlled charge storage. Because ion insertion into the bulk is a semi-infinite diffusion process, the current is proportional to $v^{1/2}$. In contrast, for capacitive processes, the current depends linearly on the sweep rate. Hence, current as a function of sweep rate is given by:[162]

$$j(v) = k_1 v + k_2 v^{1/2}, \tag{13}$$

where k_1 depends on the surface area A and the capacitance C of the electrode, while k_2 is given by the Randles–Ševčík equation:[163]

$$k_2 = 0.4958nFAc\left(\frac{nFD}{RT}\right)^{1/2}, \tag{14}$$

with F being the Faraday constant, D the diffusion coefficient and n the number of electrons transferred in the redox reaction. Rearranging eqn (13) then allows separating between both contributions:

$$\frac{j(v)}{v^{1/2}} = k_1 v^{1/2} + k_2. \tag{15}$$

Especially for nanocrystalline materials, capacitive charge storage becomes significant and plays an important role in the performance and for the kinetics.[19,156,159,164–166] Analysis of CV data for mesoporous TiO_2 thin films showed that the capacitive contribution to charge storage is virtually independent of the sweep rate, while the bulk insertion significantly decreases with increasing sweep rate.[19] For mesoporous MoS_2, Cook *et al.* found that 80% of the theoretical specific capacity is accessible within 20 s due to pseudocapacitive charge storage.[167] These results indicate that fast kinetics in mesoporous materials also originates from nondiffusion-controlled surface charge-storage processes.

Significant pseudocapacitive charge storage has also been observed for mesoporous group V transition-metal oxides, including Nb_2O_5 and Ta_2O_5, and for MoO_3.[166,168] Direct comparison of crystalline and amorphous thin films showed that the pseudocapacitance achieved with the crystalline samples exceeds that

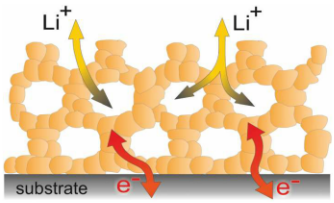

Fig. 14 Schematic illustration of the charge-transport processes accompanying lithium insertion/extraction into/from a mesoporous material, with the nanoscale porosity allowing for short diffusion path lengths.

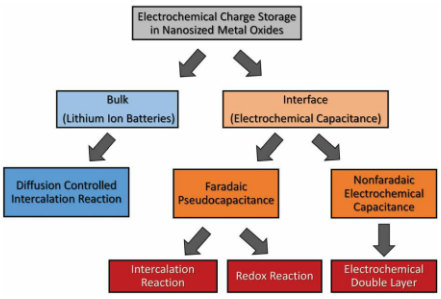

Fig. 15 Charge-storage mechanisms in nanocrystalline metal oxides. Adapted from ref. 156 with permission.

View Article Online
Perspective PCCP

of the amorphous films by large. The increased pseudocapacitive contribution to charge storage was attributed to the lithium insertion into the interlayer gaps of the layered crystalline materials (referred to as intercalation pseudocapacitance).

An aspect that is rarely being considered is that the amount of charge stored at the interface can be much larger than that stored in the bulk due to formation of the space-charge region.[169–172] This effect may even allow to store, *e.g.*, lithium at the interface between two materials, for which such behavior is not possible in the individual phases.[173] For example, Yue *et al.* investigated the pseudocapacitive charge storage in mesoporous Nb-doped TiO_2.[156] Because TiO_2 has a low electronic conductivity, doping with Nb, acting as a donor, can significantly improve the conductivity of the material.[174,175] Apart from the increase in electronic conductivity, the authors found that the pseudocapacitance is also increased up to doping levels of about 5 at%. Higher concentrations led to a decrease in pseudocapacitive charge storage. This behavior was explained by changes in the space-charge layer at the interface, as shown in Fig. 16. For TiO_2 in contact with a Li^+-containing electrolyte, the space-charge region results in depletion of electrons at the interface and accumulation of lithium ions due to differences in electrical potential between the surface (interface) and the bulk.[170] For low doping concentration, the space-charge region of opposite sites overlaps, resulting in negligible potential differences,[176,177] and therefore in low surface charge storage. With increasing doping level, the space-charge region decreases. Hence, the potential differences increase and more ions can be stored at the interface, leading to increased pseudocapacitance. However, the width of the space-charge region continues to decrease with further increasing doping concentration. For that reason, the pseudocapacitive contribution to charge storage starts to decrease again at some point.

Although the extension of the space-charge region in oxides is typically less than a few nanometers, this example shows that, in mesoporous materials with crystallites of similar dimensions, the charge storage in the space-charge region can become significant and even dominate the overall behavior.

Another major advantage of mesoporous materials is their mechanical flexibility. The insertion/extraction of ions into/from the electrode during electrochemical cycling is usually accompanied by volume changes,[178–181] often resulting in mechanical degradation (fracturing or even pulverization of the active material).[182–188] In mesoporous materials, such adverse effects can be mitigated, as mechanical strain is accommodated to some degree by pore flexing.[144,189,190] Liu *et al.* investigated the electrochemical properties and cycling stability of ordered mesoporous NiO produced by hard templating.[158] While NiO as anode in LIBs typically suffers from pulverization and accelerated capacity fading due to volume changes during the conversion reaction, among others,[191,192] the mesoporous material maintained a specific capacity of 680 mA h g^{-1} at 0.1C rate after 50 cycles. Lee *et al.* studied ordered mesoporous niobium nitride/N-doped carbon composite as an advanced anode material for application in K-ion batteries.[193] Structural characterization using *in situ* X-ray diffraction (XRD) showed that the high cycling stability (stable performance for >2000 cycles) is due, in part, to the negligible mechanical strain that the material experiences during cycling.

The mechanical flexibility also improved the lithium storage in mesoporous CeO_2. Specifically, Brezesinski *et al.* probed the charge-storage behavior of polymer-templated and nontemplated thin films (Fig. 17). As expected, the authors observed a significant increase in pseudocapacitive charge storage in the

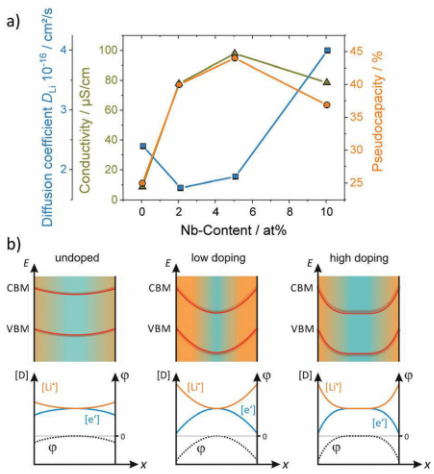

Fig. 16 (a) Electrical conductivity and pseudocapacitive charge storage of mesoporous TiO_2 *versus* the Nb doping level. (b) Schematic illustration of the surface band bending and the corresponding defect concentration for different doping situations. Adapted from ref. 156 with permission.

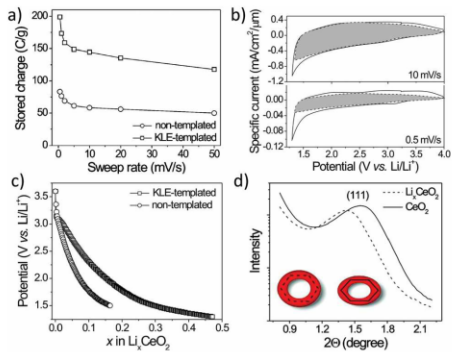

Fig. 17 (a) Charge-storage dependence on sweep rate for nanocrystalline (nontemplated) and mesoporous (KLE-templated) CeO_2 thin films. (b) CV curves for mesoporous CeO_2. The capacitive current is highlighted in gray. (c) Galvanostatic discharge curves at C/2 rate. (d) SAXS patterns for mesoporous CeO_2 and Li_xCeO_2. Adapted from ref. 165 with permission.

mesoporous CeO_2.[165] However, for slow sweep rates or long charging times, that is, if the lithium ions have enough time to diffuse into the lattice, the total amount of stored charge was also increased by a factor of about two compared to the nontemplated material. Using small-angle X-ray scattering (SAXS), they were able to show that the mesoporous CeO_2 thin films have tensile stress imposed by the substrate (note that templated sol–gel films usually undergo unidirectional volume contraction during heating). Upon ion insertion into the lattice, the porous structure expands normal to the substrate, relieving in-plane stress, which in turn facilitates charge storage.

The structural stability of ordered mesoporous $NiCo_2O_4$ during electrochemical cycling has been examined by Bhaway *et al.*[194] Using grazing-incidence SAXS (GISAXS) and XRD (GIXD), they were able to correlate structural changes of the anode material with the electrochemical performance. Electrodes with approx. 9 nm pores showed severe capacity fading caused by collapse of the nanostructure during the initial cycles. In contrast, for electrodes with larger pores, the nanostructure was retained, which agrees well with the improved cyclability.

Increased structural stability has also been observed by Krins *et al.* for mesoporous amorphous $NbVO_5$ thin films with a wormlike pore structure.[195] The authors found that their ability to accommodate the strain from lithium insertion increases with decreasing pore size from 100 to 15 nm, suggesting that the optimal size is closer to 10 nm.

Mesoporous nanocrystalline architectures offer an additional advantage in terms of ion uptake, as the particle size may have a strong impact on the thermodynamics.[196] For example, lithium insertion into bulk TiO_2 is accompanied by a phase transition from anatase TiO_2 to $Li_{0.55}TiO_2$.[197–200] With further insertion of lithium, a second phase transition occurs, resulting in the formation of a blocking $LiTiO_2$ layer at the particle surface. $LiTiO_2$ exhibits a low lithium-diffusion coefficient, and therefore prevents complete phase transformation (kinetic limitation).[198] However, as discussed by Wagemaker *et al.*, increasing contribution of surface free energy to the total free enthalpy of the system alters the solubility limit of lithium in TiO_2 and can even suppress phase separation.[198,199] For particles ≤ 7 nm in diameter, both phase transitions are suppressed, allowing full lithiation to form $LiTiO_2$,[198] which also helps explain the larger specific capacity of nanostructured TiO_2 compared with bulk material.[200–202]

Similar behavior has been observed for α-Fe_2O_3 (hematite). While larger particles undergo a phase transition from trigonal α-Fe_2O_3 to cubic $Li_xFe_2O_3$ at $x \approx 0.05$, in nanoparticles, this transition is suppressed and lithium can be inserted into the lattice up to $x \approx 1$. As the lithium uptake is reversible for α-$Li_xFe_2O_3$, nanoparticles exhibit much improved cyclability.[203,204] Note that increased lithium storage and good cycling stability have also been found for mesoporous hematite and other Fe-based oxide thin films.[205,206]

4.2. Mesoporous metal oxides in catalysis

Because of their unique structural properties, mesoporous oxides represent a promising class of materials for a variety of catalytic applications, for example, as catalyst or support for CO and NO conversion reactions or for (photo-)catalytic hydrogen production and water splitting. While their high surface area provides a large number of catalytically active sites, the 3-dimensional pore structure ensures good accessibility of the bulk and enables efficient transport of reaction species to/from the material. However, the catalytic properties not only depend on the specific surface area but also the wall structure (grain size, crystallinity *etc.*).

Ceria–zirconia solid solutions are among the most prominent catalytic materials for CO and NO conversion due to the high redox activity of the Ce^{3+}/Ce^{4+} couple.[207] Furthermore, because of its smaller ionic radius, the incorporation of Zr^{4+} ions into the lattice distorts the cubic fluorite structure, resulting in the formation of defects and higher reducibility.[97,208] Overall, ceria–zirconia solid solutions exhibit favorable catalytic properties as a result of their unique oxygen-storage capacity, despite the fact that Zr^{4+} is redox inactive.[207,209]

There are several reports on the investigation into catalytic properties of mesoporous $Ce_xZr_{1-x}O_{2-\delta}$.[210–214] For example, Petkovich *et al.* probed the catalytic activity of ordered macroporous versions of such materials, prepared using two different synthetic routes, for H_2O splitting and H_2 production.[215] They found increased H_2 production rates compared to commercial CeO_2 powder, which was attributed to the increased specific surface area. However, the reaction rate was not directly related to the surface area, but instead to the composition and homogeneity of the crystallites. The highest rate was observed for materials with a Zr content between 10 and 20%. Furthermore, samples with compositional heterogeneity, that is, the presence of Ce- and Zr-rich phases, offered better performance than the respective homogeneous (single-phase) materials. Mamontov *et al.* also observed a correlation between heterogeneity and oxygen-storage capacity in nanocrystalline ceria–zirconia powders.[216]

Ho *et al.* reported on mesoporous Pd/ceria–zirconia solid solutions with macrochannels,[217] showing superior activity for CO oxidation over reference samples without macrochannels. The improvement in performance was attributed to two main factors: first, alignment of macrochannels, enabling effective mass transport through the pore system, and second, increased Ce^{3+} and oxygen-vacancy concentrations at the surface (preferred reaction sites).[218] In contrast to the report by Petkovich *et al.*, crystal structure homogeneity was found to be advantageous, in agreement with other reports,[209,219] as oxygen vacancies are more readily formed in the cubic phase than in mixed-phase structures.[220] Cui *et al.* examined the influence of La and Pr doping on the catalytic properties of ceria–zirconia solid solutions. They came to the same conclusion that larger pores allow for more effective gas diffusion. They also observed that an increased fraction of Ce^{3+} ions due to doping is beneficial to the catalytic activity and the oxygen-storage capacity.[221] Similar results were obtained for mesoporous CeO_2-based catalysts used in methanol decomposition.[210,222]

The strong correlation between oxygen-storage capacity and catalytic activity has been theoretically studied by Sayle *et al.* for nanoscale CeO_2.[223] Molecular dynamics (MD) simulations

confirmed that the catalytic activity is strongly affected by its oxygen content, and therefore directly related to the oxygen-storage capacity. Furthermore, they found that the catalytic activity depends on the morphology of the material, such as wall diameter and particle size. In general, oxygen extraction from nanoparticles is more facile. This is in agreement with density-functional theory (DFT) calculations by Migani *et al.*, predicting the least oxygen-vacancy formation energy for nano-scale CeO_2.[224,225]

In 2018, Hao *et al.* confirmed the considerable effect that the particle size has on the oxygen-storage capacity of CeO_2.[226] The oxygen-storage capacity of 5 nm particles (approx. 260 μmol g^{-1} at 250 °C) was shown to be two times larger than that of 12 nm particles (Fig. 18). Using scanning tunneling microscopy (STEM) combined with electron energy loss spectroscopy (EELS), they observed an increase in Ce^{3+} concentration at the surface of the nanoparticles or, in other words, the presence of a space-charge layer. The space-charge layer extends over the whole nanoparticles when their size is below 6 nm, resulting in a total Ce^{3+} content of more than 50%. The increase of Ce^{3+} at the surface is accompanied by an increase of the lattice parameter, leading to a lower formation energy for oxygen vacancies. This helps explain the increase in oxygen-storage capacity with decreasing particle size.

Apart from ceria–zirconia solid solutions, other oxides have also been considered for catalytic applications. Ren *et al.* studied the CO conversion on ordered mesoporous metal oxides, such as Co_3O_4, Cr_2O_3 and Fe_2O_3, to name a few.[227] These materials

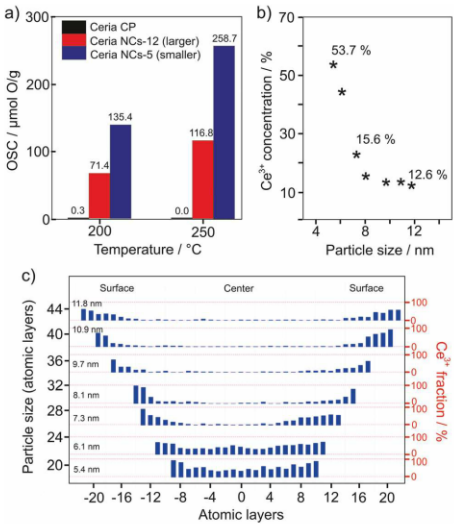

Fig. 18 (a) Comparison of the oxygen-storage capacity of CeO_2 nanoparticles of different size and commercially available nanopowder. (b) Ce^{3+} content as function of the particle size and (c) valence-state distribution. Adapted from ref. 226 with permission.

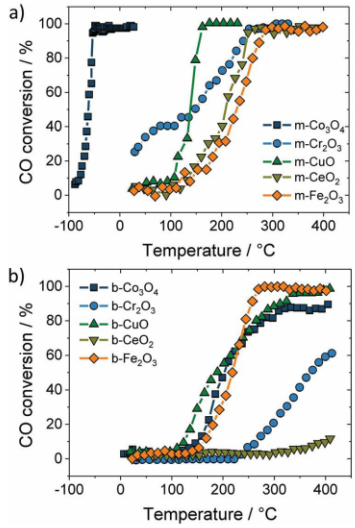

Fig. 19 CO conversion on (a) mesoporous and (b) bulk oxide catalysts. Adapted from ref. 227 with permission.

exhibited increased CO conversion rates compared to their bulk counterparts, as shown in Fig. 19. The improvements were attributed not only to the increased specific surface area but also to the presence of a regular 3-dimensional pore structure, providing well-defined pathways for gas transport and equally accessible internal surfaces. Similar results were obtained by both Sun *et al.* and Tüysüz *et al.* for CO oxidation over ordered mesoporous Co_3O_4.[228,229]

Furthermore, noble-metal nanoparticles as co-catalysts have been shown capable of strongly affecting the activity of oxides by facilitating the conversion reaction (for oxide-supported transition-metal catalysts). The reason is that metallic nanoclusters on the surface increase the oxygen-vacancy concentration and improve the charge transfer.[232,233] Both results in an enhancement of catalytic activity at the metal/oxide interface.[234,235] The beneficial effect of using metallic nanoclusters has been shown for a variety of mesoporous oxides.[210,217,236] However, the reaction rate also depends on the size (smaller particles are usually more active), shape and distribution of nanoparticles inside the mesoporous framework, as demonstrated, for example, by Kapoor *et al.*[210] Because the mesoporous support can be post-loaded,[236] this allows for pre-synthesis of tailored nanoparticles. Furthermore, the interaction with the oxide surface prevents the agglomeration of particles.

In addition to their application in conversion reactions, mesoporous metal oxides also gained great interest in the field of photo(electro-)catalysis for water splitting (hydrogen/oxygen production) or carbon dioxide reduction. The basic principle is based on the generation of an electron–hole pair in a semi-conducting material under light irradiation, as shown in Fig. 20

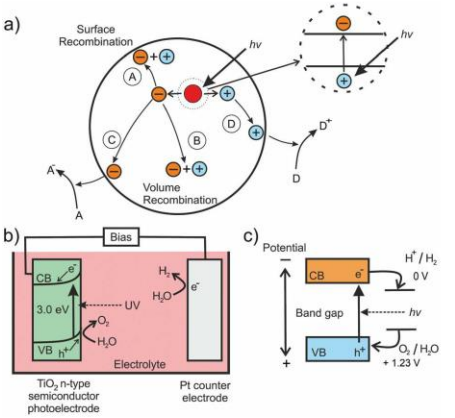

Fig. 20 (a) Schematic of the electron–hole pair generation in semiconducting nanoparticles and possible recombination mechanisms: (A) surface and (B) volume recombination and (C) reduction and (D) oxidation reactions. Adapted from ref. 230 with permission. (b) Schematic illustration of the setup for photoelectrocatalytic water splitting using TiO_2 as photoanode. (c) Energetic position of redox states relative to the bands of the semiconductor. Adapted from ref. 231 with permission.

for the water-splitting reaction using a particulate photocatalyst.[230,231,237] Both the electron and electron hole then undergo secondary reactions at the surface, which may also be supported by a metal co-catalyst. At the surface of the catalyst, electrons reduce H_2O molecules to form H_2, while H_2O molecules are oxidized by holes to produce O_2. Hence, for photocatalysis, semiconductors with a sufficiently large band gap are needed. Specifically, the valence band should be more positive than the potential for the O_2/H_2O redox reaction, while the conduction band has to be more negative than the potential of H^+/H_2.

In photoelectrocatalysis, both reactions are separated by applying an electrical bias (Fig. 20). The catalyst is used as photoelectrode, where only one of the redox reactions occurs. An important aspect for efficient photo(electro-)catalysis is the separation of electron and hole to ensure that both carriers can diffuse to the active surface sites for the redox reactions to occur. High (crystal) quality of the absorber material is advantageous, as defects act as carrier traps, increasing the probability of recombination. Overall, there are many reports on mesoporous semiconducting oxides for photocatalytic applications, including TiO_2,[20,238–240] Ta_2O_5,[241] $LiFe_5O_8$,[242] $ZnFe_2O_4$,[243–245] and Rh_2O_3.[246]

Given that the water-splitting reaction takes place at the surface of the photocatalytic material, it is reasonable to assume that a high specific surface area leads to superior activity. Cherevan *et al.* analyzed around 200 publications regarding the photocatalytic activity of mesoporous semiconductors, aiming at correlating improved performance with surface area.[247] They found that increased specific surface area is not the only reason and may even impede any performance improvements, as a high surface area may also increase the probability of carrier recombination. For example, for Ta_2O_5, an increase of the specific surface area by a factor of approx. 100 (mesoporous *vs.* nonporous material) only resulted in a relatively small activity rise by a factor of 1.5.[248] Instead, the crystallinity, the pore size, the pore connectivity and the wall thickness can significantly affect the performance of the material.

Kirchberg *et al.* compared the photocurrent density of mesoporous $ZnFe_2O_4$ photoanodes prepared using two different polymer templates and calcined at various temperatures. In fact, they observed that differences in pore morphology only have a minor influence on the photocurrent. Samples of high crystallinity showed better performance due to the relatively lower concentration of defects acting as recombination centers for the electron–hole pairs.[243] Increased photocatalytic activity because of improved crystallinity has also been reported for mesoporous Nb_2O_5, Mn_2O_3 and $NaTaO_3$.[249–251]

Tüysüz *et al.* compared mesoporous nanocrystalline $NaTaO_3$ and amorphous $NaTaO_x$ photoanodes and observed a decrease in photocatalytic activity for the crystalline material.[252] Although the crystallinity should reduce the probability of carrier recombination, crystallization of the amorphous matrix resulted in an increase in particle size and a decrease in specific surface area. As discussed by the authors, smaller particles are considered beneficial to the photocatalytic activity. The reason is that the space-charge regions of opposite surfaces overlap, resulting in complete depletion of the particle and negligible band bending at the surface (flat-band condition),[176,177] as mentioned previously. Both photogenerated charge carriers can then easily diffuse to the active surface sites, leading to improved photocatalytic activity, as schematically shown in Fig. 21. For larger particles/crystallites, increasing

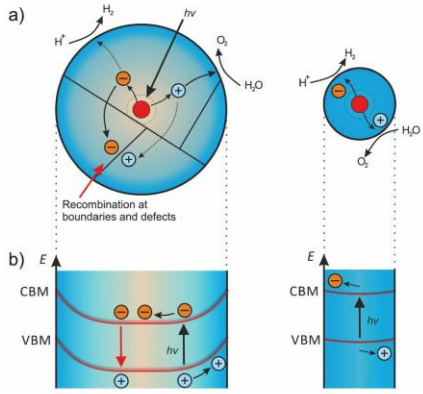

Fig. 21 Effect of particle size on the band bending and photocatalytic activity. (a) Generated carriers show high probability to recombine at boundaries or defects in larger particles. In smaller particles, the carriers can readily diffuse to the catalytically active surface sites. Adapted from ref. 231 with permission. (b) The corresponding band structure. In larger particles, the space-charge region separates the generated carriers, while smaller particles exhibit negligible band bending. Adapted from ref. 176 with permission.

band bending impedes the diffusion of one kind of charge carrier to the surface, resulting in higher recombination rates in the bulk, and therefore in lower efficiency.

The opposite holds true when the mesoporous material is used for photoelectrocatalytic applications, where the two redox reactions occur at different electrodes. In this case, the band bending in larger crystallites promotes charge separation, thus preventing undesirable recombination. For example, Hartmann *et al.* investigated the photoelectrocatalytic activity of mesoporous TiO_2 prepared from preformed nanoparticles and a classical sol–gel route.[20] They observed higher photocurrents and improved quantum efficiency for the sol–gel-derived thin films with thicker pore walls and larger crystallites. The results were explained, in part, by a reduced probability of electrons to react at the surface (Fig. 22). This can be directly related to the existing band bending, preventing the diffusion of electrons to the surface. Furthermore, the thicker wall structure gave rise to better connectivity between individual crystallites, allowing for more efficient transport of electrons in the pore–solid architecture and contributing to the higher efficiency. The positive effect that a 3-dimensional pore structure has on the photocatalytic performance (due to improved transport of electronic charge carriers) has also been discussed by Hossain *et al.*[253] and Zhou *et al.*[254]

As in case of battery applications, the pore connectivity and pore size are critical parameters affecting the photocatalytic activity, as they determine the transport of reactants and products. For example, Weller *et al.* investigated the influence of pore size of mesoporous $CsTaWO_6$ (with Rh as co-catalyst) on

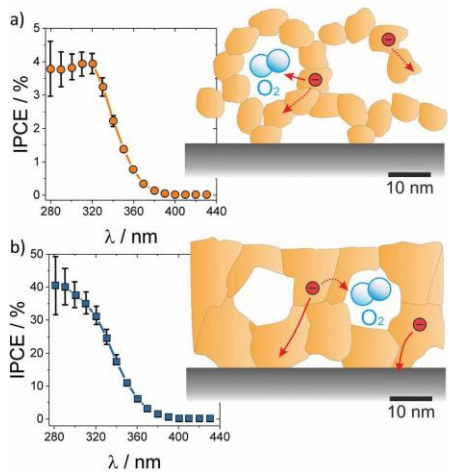

Fig. 22 Incident photon-to-current efficiency for water photoelectrocatalysis over (a) nanoparticle-derived and (b) sol–gel mesoporous TiO_2 thin films. The nanoparticles in the wall structure result in low electronic conductivity and high recombination rate, while the sol–gel films with thicker and continuous pore walls reveal high photocurrents with a relatively lower recombination rate. Adapted from ref. 20 with permission.

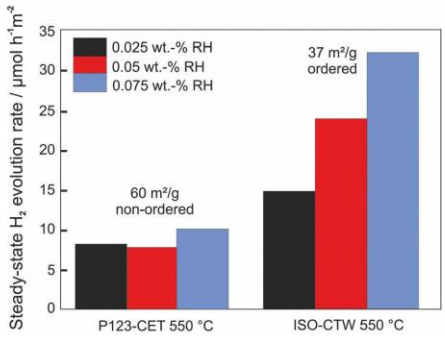

Fig. 23 Comparison of steady-state H_2 evolution rates for disordered and ordered mesoporous $CsTaWO_6$ with different amounts of Rh co-catalyst. Adapted from ref. 256 with permission.

the photocatalytic performance for H_2 evolution.[255] An optimized synthesis route allowed varying the pore size and mesoporous morphology without affecting the crystallinity of the material. Analysis of the photocatalytic activity revealed that the H_2 evolution rate strongly depends on the pore size and the pore size distribution. This result was explained by transport limitations, as the water/methanol mixture used as electrolyte was partly confined in the small pores due to capillary forces, blocking the release of gas bubbles.[256] Furthermore, comparison between samples with (large-pore) ordered and disordered mesoporous structures revealed higher H_2 evolution rates for the former material, despite having a lower specific surface area (Fig. 23). The increase in activity was rationalized by better accessibility of the bulk material and improved transport pathways in case of the regular pore structure. Similar results have been reported by Fang *et al.*, for example, who were capable of achieving efficient mass transport by introducing additional macropores.[240]

Another interesting aspect is that the regular arrangement of crystallites apparently affects the optical properties. For example, Hossain *et al.*[253] found that ordered mesoporous anatase TiO_2 with 5 nm thick walls exhibits a smaller band gap than individual 25 nm particles. The decrease in band-gap energy by about 0.2 eV was ascribed to the interconnectivity of nanoparticles, increasing their effective size.[253] Hufnagel *et al.* also observed a significant improvement in light-absorption properties (light-harvesting efficiency) for nanoscale $ZnFe_2O_4$ grown on macroporous antimony-doped tin oxide films compared to non-structured thin films.[244] This result was attributed to the presence of extended light paths caused by multiple light reflection and scattering in the porous electrode, as also reported by Fang *et al.* for hierarchically structured TiO_2 microspheres.[240]

Taken together, the results indicate that a favorable structure for catalytic applications depends on the interplay between surface area, crystallinity, particle size (often determined by the wall thickness), pore size and pore size distribution. However, the individual parameters can significantly differ among different materials, making it necessary to vary them independently.

For mesoporous oxides, unfortunately, this is only feasible to some degree, as *e.g.*, high crystallinity usually requires high-temperature treatment, which in turn results in grain growth and coarsening, and therefore in lowering of the active surface area.

4.3. Mesoporous metal oxides for gas sensors

Most gas sensors rely on the interaction of a specific gas with the surface of the sensing material. There are different kinds of sensing principles, all of which take advantage of changes in the materials properties under varying atmosphere. In capacitive gas sensors, the change of permittivity is measured, while optical gas sensors usually detect changes in photoluminescence, reflection or optical absorption.[119]

Because oxides are often used as resistive sensors, we only focus on this type in the following. The basic working principle of most resistive gas sensors is schematically shown in Fig. 24. Gas/oxide interactions induce changes of the surface potential, *e.g.*, due to chemisorption of gas molecules (receptor function). The change of the electronic surface structure then results in changes in conductivity, which are detected as the sensing signal (transducer function). In case of an n-type semiconductor, for example, the adsorption of oxygen species (O^-) typically gives rise to formation of an electron-depleted space-charge layer. In the presence of a gas, such as H_2, O^- species are consumed, resulting in a decrease of the space-charge width, and therefore in a decrease of resistance.[258–260] Hence, the working principle of a resistive gas sensor is directly related to the space-charge region at the interfaces (grain boundary or surface) of the oxide material. The largest sensitivity is achieved when the conductivity of the grains is completely determined by the space-charge region, that is, when the grain size is smaller than approx. twice the depletion layer.[261–263]

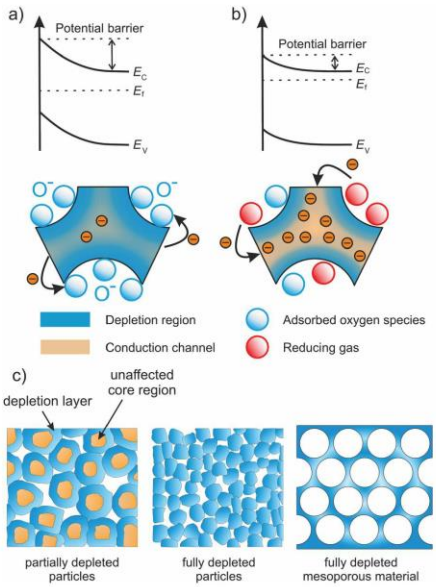

Fig. 24 Schematic illustration of the sensing mechanism in n-type semiconducting metal oxides. (a) The oxide is completely depleted under air exposure due to extension of the space-charge layer. (b) Upon adsorption of reducing gas molecules, the extension of the space-charge layer is reduced, thereby opening conductive channels in the sensor material. Adapted from ref. 257 with permission. (c) Electron-depletion layer in resistive sensors. Granular material with grain size larger than about twice the depletion layer (left), fully depleted granular material (middle) and fully depleted mesoporous material (right). Adapted from ref. 119 with permission.

The large influence of grain size on the resistance and sensitivity of granular SnO_2 sensors is depicted in Fig. 25. Both the sensitivity and response time depend strongly on the morphology and microstructure of the sensing material. To achieve high sensitivity, high surface area is desirable, while efficient and fast diffusion of gas molecules enables good response characteristics of the sensor to changes in the surrounding atmosphere. Consequently, mesoporous materials with tailorable pore and crystallite sizes are of great interest for sensor applications.[119]

Similar to granular materials, the crystallite size strongly affects the sensitivity of mesoporous materials. For example, Aqeel *et al.* probed the NO_2 detection capabilities of mesoporous SnO_2 calcined at 400 and 500 °C.[264] They found that the material heated at 400 °C shows significantly better sensing properties, as the crystallite size (4–5 nm) was smaller than twice the depletion layer. The material heated at 500 °C had larger crystallites of approx. 8 nm in diameter, and therefore showed worse sensing performance. Conductivity measurements confirmed the complete depletion of electrons in the smaller crystallites, which exhibited a much larger resistance. In addition, the selectivity for NO_2 was much improved in case of the smaller crystallites. Xu *et al.* obtained similar findings for SnO_2.[262,263] They noticed an increase in sensitivity and resistance with decreasing grain size (Fig. 25).

Waitz *et al.* examined the methane sensing properties of mesoporous In_2O_3 as function of the pore size and wall thickness.[265] The sensitivity scaled linearly with the specific surface area. The authors also found that especially the wall

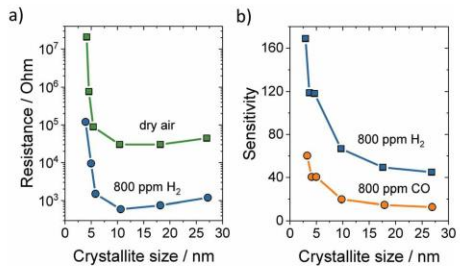

Fig. 25 (a) Electrical resistance at 300 °C in dry air or 800 ppm H_2 *versus* the crystallite size of SnO_2. (b) Sensitivity to 800 ppm H_2 or CO *versus* the crystallite size of SnO_2. Adapted from ref. 263 with permission.

thickness has a strong effect on sensitivity, confirming that a fully depleted pore wall gives rise to superior performance. However, they pointed out that the structural parameters are coupled to one another, and thus cannot be varied independently, making it difficult to distinguish between the impact of each parameter on sensitivity.

Ghom *et al.* tested mesoporous ceria–zirconia solid solutions as oxygen sensors at 600 °C.[266] In $Ce_xZr_{1-x}O_{2-\delta}$, the change in resistance is not caused by changes of the surface space-charge layer due to adsorbed oxygen species, but instead by the significant increase in conductivity because of the release of oxygen under reducing conditions, as described above. As discussed by the authors, the fast response time of such mesoporous sensors is directly related to the oxygen-storage capacity of the material.[209,219] Both the regular arrangement of pores and the pore size not only affect the sensitivity but are also responsible for fast diffusion of gas through the bulk of the material, the latter of which determines the sensor response time.[267]

Li *et al.* investigated ordered mesoporous WO_3 for H_2S sensing and observed a fast response of 2 s, with a recovery time of approx. 38 s, which they attributed to the unique (continuous) pore–solid architecture and the resulting fast gas diffusion.[269] The similar response time (1–3 s) of mesoporous α-Fe_2O_3 for ethanol sensing was also ascribed to the high diffusivity through the pore network.[157] Li *et al.* synthesized mesoporous–macroporous SnO_2.[268] Compared with conventional granular SnO_2 sensors, the hierarchical pore structure led to significant improvements in response and recovery times, as shown in Fig. 26, which was attributed to facilitated gas diffusion in the macropores.[268]

While the sensitivity and response times are determined by structural properties, the selectivity of a sensor depends strongly on the material type and its surface properties. To control or even tailor the selectivity for various gases, the sensing material can be loaded with catalytically active noble-metal nanoparticles, such as Au, Pd or Pt.[260,270,271] As shown in Fig. 27, electrons move from the active oxide to the metal nanoparticles due to different work functions, leading to the formation of a Schottky barrier at the interface, and therefore to an increased

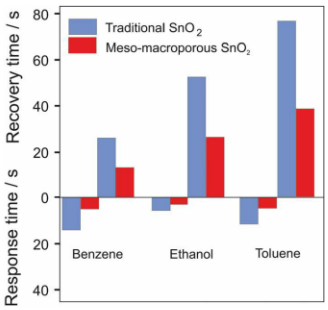

Fig. 26 Comparison of recovery and response times to 100 ppm benzene, ethanol or toluene for "traditional" SnO_2 and mesoporous–macroporous SnO_2. Adapted from ref. 268 with permission.

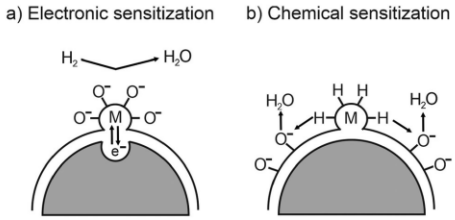

Fig. 27 Schematic illustration of (a) electronic and (b) chemical sensitization by metal or metal-oxide nanoparticles. Adapted from ref. 259 with permission.

electron depletion (electronic sensitization). However, the metal nanoparticles on the surface not only affect the adsorption and dissociation reactions by activating the gas molecules (chemical sensitization)[257,259] but also facilitate oxygen-vacancy formation.[232,233]

Shimizu *et al.* studied the gas sensing properties of porous thick films of SnO_2 loaded with 1 wt% Pt or Pd.[260,270] While the sensitivity to H_2 and CH_4 at the surface was improved in the presence of noble metals, it deteriorated in the interior. This result was explained by reduced permeation into the bulk due to increased surface reactivity, emphasizing the necessity of optimizing the gas diffusion pathways.

Ma *et al.* reported on a positive effect of partially oxidized Pt nanoparticles on the sensitivity and selectivity of mesoporous WO_3 for CO sensing.[272] The improvements were attributed to the sensitizing effect of nanoparticles on the WO_3 framework. Using X-ray photoelectron spectroscopy (XPS), they found W^{5+} states because of the formation of oxygen vacancies (note that they increase the adsorption of oxygen species at the surface). Furthermore, the good sensitivity was justified by changes in the depletion region at the Pt/WO_3 interface with varying atmosphere. After exposure to air, PtO nanoparticles were detected, leading to the formation of a depletion layer at the interface due to their p-type character. The PtO nanoparticles were reduced back to Pt(0) upon CO exposure, resulting in a vanishing depletion layer and pronounced changes in resistance with varying atmosphere. A positive impact of oxygen vacancies on the NO_2 sensing properties has also been reported for mesoporous WO_3 nanofibers[273] and CeO_2/graphene heterostructures.[274]

5. Surface modification

Although porous architectures are, without doubt, beneficial to various applications, there are certain constraints in using mesostructured powder and thin film materials. First, they tend to suffer from thermal stability issues. Especially for catalytic applications, elevated temperatures (or high relative humidity) are often required. However, such experimental conditions may result in changes of the pore structure due to phase transitions and/or growth of crystallites (sintering effects) or even complete collapse of the pore network. Second, while some variation in pore size (and wall thickness, pore symmetry *etc.*) can be achieved,

it is mainly determined by the template used. Nevertheless, small changes in pore size can significantly affect the performance of mesoporous materials, as discussed above. Hence, tailoring of structural features on the nanometer level and precise interfacial engineering are desirable.

It has been shown that the properties of mesoporous materials can be altered by coating the surface using atomic layer deposition (ALD). ALD is a variant of the chemical vapor deposition (CVD) technique and is receiving increasing attention in recent years.[275–278] The reason is that ALD is the only method that is suited to produce uniform and conformal coatings on complex surfaces. This is achieved by sequential pulsing of gaseous reactants with intermediate purging steps. The pulses represent self-limiting gas–solid surface reactions, leading to controlled film growth [2-dimensional layer-by-layer (Frank–van der Merwe) growth] and excellent step coverage, unlike other deposition techniques.

The deposition of thin coatings using ALD finds lots of applications, among others, in protection and functionalization of surfaces or stabilization of porous materials.[279] For instance, in the battery field, ALD is typically used to modify electrode surfaces.[280–284] The coating acts as an artificial interphase between the electrode and the electrolyte to suppress adverse side reactions, which may result in gas evolution and/or formation of an ion-transport-blocking layer (anode/cathode solid–electrolyte interface). However, ALD also lends itself to the preparation of active electrode materials.[285,286]

Apart from electrochemical energy-storage applications, ALD is actively used to improve the catalytic performance of materials by either depositing metal nanoparticles onto their top surface[287,288] or (partial) overcoating them with an oxide layer.[278,289–293] The growth of single nanoparticles on carbon or oxide surfaces is usually achieved at comparably high deposition temperatures, where the precursor tends to agglomerate depending on the presence of surface defects and the atmospheric conditions instead of forming a conformal coating during the initial ALD cycles.[294–296] In case of partial overcoating, one takes advantage of differences in surface chemistry of the solid (area-selective deposition, also referred to as AS-ALD).[292,297–300]

In the following, we focus on some selected examples, where ALD has been used to produce a uniform oxide coating in order to modify the structural and/or electrical properties of mesoporous oxides.

Mesoporous oxides are metastable, that is, accelerated grain growth occurs at elevated temperatures, leading to collapse of the pore structure. The deposition of a thin coating using ALD may help to enhance the thermal stability of mesoporous materials. For example, Kraffert *et al.* synthesized mesoporous ferrihydrite,[301] showing a phase transition to hematite at 400 °C. By depositing silica onto the pore walls of the mesostructured thin films using a single ALD cycle, the stability of the ferrihydrite phase could be increased to 600 °C. Similar results were achieved for alumina-coated samples. In addition, the onset temperature for sintering, and therefore the thermal stability of the mesoporous thin films, was found to be significantly increased by ALD coating (up to 800 °C for silica). Differences in the stabilizing effect were attributed to different interaction strengths of the coating materials with the mesoporous substrate. Significant improvement in thermal stability of mesoporous Rh_2O_3 thin films by ALD coating (by >300 °C compared to uncoated material) has also been observed by Dubraja *et al.*[246] Pagán-Torres *et al.* reversed the strategy to stabilize mesoporous materials for applications under harsh conditions. They deposited catalytically active niobia onto the pore walls of mesoporous silica.[302] The hybrid material revealed improved hydrothermal stability, with catalytic activity superior to that of commercial niobia.[303]

Optimizing the pore size to achieve a high active surface area while providing efficient mass transport through the material and/or efficient charge-transport pathways in the walls is crucial for many applications. Unfortunately, arbitrary variation of pore size on the nanometer level is experimentally not possible. However, ALD can be used to reduce the pore size of pre-synthesized materials in a systematic fashion.[304]

Dendooven *et al.* investigated the decrease in pore size in mesoporous TiO_2 thin films with ink-bottle shaped pores upon deposition of HfO_2 using ALD. Achieving a conformal coating in such films is challenging, as there are only small channels within the walls that connect the mesopores and may lead to pore clogging during deposition. Using X-ray fluorescence (XRF) measurements, the authors confirmed that the inner surfaces are uniformly coated until the pore necks are closed, preventing further diffusion of molecular precursor into the architecture, as schematically shown in Fig. 28. Additional ALD cycles then only result in growth of a top (sealing) layer.[304,305] Comparable results were obtained by Cop *et al.*, who investigated TiO_2 ALD coating of mesoporous $Ce_xZr_{1-x}O_{2-\delta}$ thin films.[306]

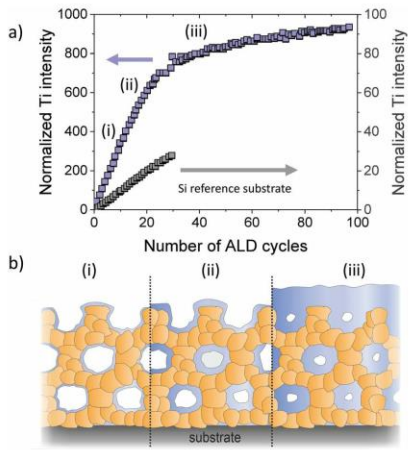

Fig. 28 (a) *In situ* XRF monitoring of filling of mesoporous thin films with an initial pore size of 4 nm during ALD of TiO_2. After pore filling, the growth rate decreases and TiO_2 only grows as a top layer on the films. (b) Schematic illustration of the pore filling process. Adapted from ref. 304 with permission.

Dendooven *et al.* also reported on the implementation of ellipsometric porosimetry onto an ALD reactor, allowing to determine the pore size, the film thickness and the mechanical properties *in situ* during ALD.[307] In another work, the authors monitored the pore shrinkage by means of *in situ* GISAXS, also confirming uniform and conformal coating of the inner surfaces.[308] Note that for sub-nm control of the coating thickness, the process parameters must be tailored.[309] Too long exposure and/or insufficient purging result in precursor condensation (at the bottom of the pores) and pore plugging, whereas insufficient doses prevent full coverage of the inner surfaces. Especially for materials with a complex porosity, precursor diffusion limitations can lead to anisotropic ALD profiles, as reported for example by Pulinthanathu Sree *et al.*[310]

Spatial control of deposition has been achieved using plasma-assisted ALD. Here, ALD precursors are employed that need to be activated through plasma irradiation. As shown by Jiang *et al.*, this method allows sealing the pores of mesoporous materials at the immediate surface, as the plasma cannot penetrate into the inner structure.[311]

These and other examples demonstrate that conformal surface coating of mesoporous materials can be achieved using ALD.[313–316] However, in order to tailor the surface properties to a certain application, it is necessary to control the crystallinity of the deposited material (note that the lattice structure determines the electrical or catalytic properties, among others). Mitchell *et al.* characterized ALD-derived TiO_2 thin films on silicon substrates.[317] They found that native-oxide-free silicon promotes the growth of crystalline TiO_2 islands. In contrast, an initially amorphous TiO_2 film is formed on silicon with an amorphous interfacial SiO_x layer. Nevertheless, after exceeding a critical thickness, the amorphous TiO_2 crystallizes. Zscherp *et al.* also examined the nanostructure of an ALD oxide coating, namely, 9–20 nm ceria deposited onto porous YSZ thin films.[312] TEM investigations revealed epitaxial growth of ceria with a columnar structure and excellent conformality (Fig. 29). An amorphous-to-crystalline phase transition with increasing layer thickness has also been reported by Celik *et al.*[129] They coated porous YSZ thin films by ALD of TiO_2. While the deposition of 6 nm TiO_2 resulted in the formation of amorphous material, a crystalline coating (anatase TiO_2) was found for a thickness of approx. 18 nm using the same deposition conditions (150 °C substrate temperature). Furthermore, the authors studied the influence of crystallinity on the surface protonic conductivity. The amorphous TiO_2 coating led to a lower protonic conductivity compared with bare YSZ thin films. However, it increased again for the sample with the crystalline surface shell (accompanied by a decrease in proton mobility at high relative humidity, as the reduced pore size resulted in complete filling with water).

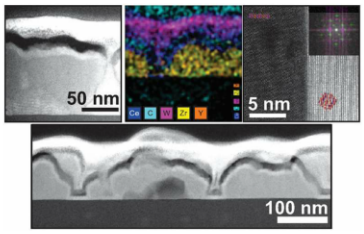

Fig. 29 TEM images and mapping results showing the epitaxial growth of ALD-derived ceria on porous YSZ thin films. Reprinted from ref. 312 with permission.

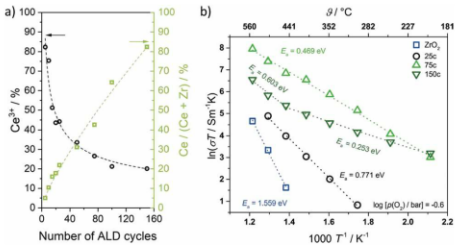

Fig. 30 (a) Ce^{3+} content of ceria deposited onto mesoporous ZrO_2 thin films as function of the ALD cycle number. The Ce^{3+} content decreases with increasing coating thickness. (b) Temperature-dependence of total conductivity for mesoporous ZrO_2 and CeO_2–ZrO_2 composite thin films (25, 75 and 150 ALD cycles). Adapted from ref. 318 with permission.

Cop *et al.* further probed the electrical properties of mesoporous ZrO_2 thin films coated with ceria using different numbers of ALD cycles.[318] Characterization *via* ellipsometry confirmed the homogeneity of coating in the pores up to 100 ALD cycles, after which pore plugging occurred. XPS measurements revealed a large Ce^{3+} fraction in the coating because of the space-charge layer at the surface, which decreased with increasing thickness, as shown in Fig. 30. In addition, the total conductivity of the composite thin films was found to be strongly affected by the coating and its thickness due to the non-stoichiometry of the ceria layer. High Ce^{3+} concentration resulted in dominant electronic conductivity because of small polaron hopping of electrons between the Ce^{3+} and Ce^{4+} ions.

Collectively, these studies demonstrate the profound effect that the coating thickness has on the structural and electrical properties. Because the thickness can be controlled precisely, post ALD treatment allows for rational materials design.

6. Conclusions

Herein, developments in the field of ordered mesoporous metal oxides for electrochemical applications are reviewed. Advantages and disadvantages arising from the unique architecture, consisting of open $\lesssim$50 nm pores surrounded by interconnected crystallites, are discussed. In the last decades, much research has been carried out into assessing the potential of mesoporous metal oxides for energy applications, ranging from batteries and catalysis to sensors. The presence of an ordered 3-dimensional pore network is advantageous, as it offers a large number of active surface sites and facilitates the accessibility of the material and its internal structure to the surrounding medium. For instance, high-surface-area metal

oxide electrodes may increase the charge-storage capacity of batteries due to pseudocapacitive redox reactions, while the porosity is capable of somewhat mediating the transport of reaction species in catalysis. It also endows the materials with a certain degree of mechanical flexibility, which helps accommodate volume changes during electrochemical cycling, among others. However, the favorable properties cannot only be attributed to the increased surface area and uniform pore size distribution, but also to the interconnectivity of crystallites in the wall structure, giving rise to short diffusion pathways for electron and ion transport.

An important aspect affecting the properties of mesoporous metal oxides is the existence of a space-charge region at the surface, which has been shown to exert a profound effect on the charge transport. Resistive oxide sensors are based on this working principle. Considering the surface space-charge region is also critical when evaluating the performance of mesoporous battery electrodes, as it directly affects the interfacial charge storage. In case of catalytic applications, the space-charge potential facilitates the separation of photogenerated charge carriers. This is beneficial for photoelectrocatalytic devices, but counterproductive in photocatalysis, where both redox reactions occur at the surface of the catalyst. However, the structural features of mesoporous metal oxides come at a price. For instance, the high surface area may lead to severe corrosion and adverse side reactions with liquid electrolytes or reactive gases. Furthermore, the nanoscale porosity negatively affects the thermal stability of the material, which in turn limits the temperature range for operation, especially in catalysis. In general, there is a complex interplay between the structural parameters, which makes it difficult to vary them independently (note that this is one of the major drawbacks of mesoporous materials).

Finally, this review article also summarizes recent work on post-surface modification of mesoporous metal oxides using atomic layer deposition (ALD). Because ALD allows conformal coating of complex substrates, it represents a promising technique to tackle the above-mentioned problems. Recent results confirm that surface coating helps to improve the thermal and structural stability. The thickness of the deposited material can also be controlled on the atomic level, since the ALD process relies on self-limiting surface reactions. Hence, the pore size can be adjusted without altering other structural parameters. In addition, the surface potential/chemistry can be manipulated *via* interfacial engineering, thus directly affecting the space-charge region and offering the possibility to tailor the electrical and electrochemical properties of mesoporous metal oxides for future device applications.

Conflicts of interest

There are no conflicts to declare.

Acknowledgements

Financial support by the German Research Foundation (to T. B., grant no. BR 3499/5-1 and to M. T. E., grant no. EL 863/3-1) is gratefully acknowledged. M. T. E. is grateful to the German Federal Ministry of Education and Research (BMBF) for funding the NanoMatFutur project NiKo (03XP0093).

References

1 T. Yanagisawa, T. Shimizu, K. Kuroda and C. Kato, The preparation of alkyltriinethylaininonium–kaneinite complexes and their conversion to microporous materials, *Bull. Chem. Soc. Jpn.*, 1990, **63**, 988–992.
2 C. T. Kresge, M. E. Leonowicz, W. J. Roth, J. C. Vartuli and J. S. Beck, Ordered mesoporous molecular sieves synthesized by a liquid-crystal template mechanism, *Nature*, 1992, **359**, 710–712.
3 J. S. Beck, J. C. Vartuli, W. J. Roth, M. E. Leonowicz, C. T. Kresge, K. D. Schmitt, C. T. W. Chu, D. H. Olson, E. W. Sheppard, S. B. McCullen, J. B. Higgins and J. L. Schlenker, A new family of mesoporous molecular sieves prepared with liquid crystal templates, *J. Am. Chem. Soc.*, 1992, **114**, 10834–10843.
4 M. Ogawa, Formation of novel oriented transparent films of layered silica-surfactant nanocomposites, *J. Am. Chem. Soc.*, 1994, **116**, 7941–7942.
5 C. J. Brinker, Y. Lu, A. Sellinger and H. Fan, Evaporation-induced self-assembly: Nanostructures made easy, *Adv. Mater.*, 1999, **11**, 579–585.
6 Y. Lu, R. Ganguli, C. A. Drewien, M. T. Anderson, C. J. Brinker, W. Gong, Y. Guo, H. Soyez, B. Dunn, M. H. Huang and J. I. Zink, Continuous formation of supported cubic and hexagonal mesoporous films by sol–gel dip-coating, *Nature*, 1997, **389**, 364–368.
7 P. Yang, D. Zhao, D. I. Margolese, B. F. Chmelka and G. D. Stucky, Block copolymer templating syntheses of mesoporous metal oxides with large ordering lengths and semicrystalline framework, *Chem. Mater.*, 1999, **11**, 2813–2826.
8 P. Yang, D. Zhao, D. I. Margolese, B. F. Chmelka and G. D. Stucky, Generalized syntheses of large-pore mesoporous metal oxides with semicrystalline frameworks, *Nature*, 1998, **396**, 152–155.
9 D. Li, H. Zhou and I. Honma, Design and synthesis of self-ordered mesoporous nanocomposite through controlled in-situ crystallization, *Nat. Mater.*, 2004, **3**, 65–72.
10 S. Y. Choi, M. Mamak, N. Coombs, N. Chopra and G. A. Ozin, Thermally stable two-dimensional hexagonal mesoporous nanocrystalline anatase, meso-nc-TiO_2: Bulk and crack-free thin film morphologies, *Adv. Funct. Mater.*, 2004, **14**, 335–344.
11 B. Smarsly, D. Grosso, T. Brezesinski, N. Pinna, C. Boissière, M. Antonietti and C. Sanchez, Highly crystalline cubic mesoporous TiO_2 with 10-nm pore diameter made with a new block copolymer template, *Chem. Mater.*, 2004, **16**, 2948–2952.
12 D. Grosso, C. Boissiere, B. Smarsly, T. Brezesinski, N. Pinna, P. A. Albouy, H. Amenitsch, M. Antonietti and C. Sanchez, Periodically ordered nanoscale islands and mesoporous films composed of nanocrystalline multimetallic oxides, *Nat. Mater.*, 2004, **3**, 787–792.

13 C. Sanchez, C. Boissière, D. Grosso, C. Laberty and L. Nicole, Design, synthesis, and properties of inorganic and hybrid thin films having periodically organized nanoporosity, *Chem. Mater.*, 2008, **20**, 682–737.
14 Y. Ren, Z. Ma and P. G. Bruce, Ordered mesoporous metal oxides: Synthesis and applications, *Chem. Soc. Rev.*, 2012, **41**, 4909–4927.
15 P. Innocenzi and L. Malfatti, Mesoporous thin films: Properties and applications, *Chem. Soc. Rev.*, 2013, **42**, 4198–4216.
16 Y. Deng, J. Wei, Z. Sun and D. Zhao, Large-pore ordered mesoporous materials templated from non-Pluronic amphiphilic block copolymers, *Chem. Soc. Rev.*, 2013, **42**, 4054–4070.
17 D. Gu and F. Schüth, Synthesis of non-siliceous mesoporous oxides, *Chem. Soc. Rev.*, 2014, **43**, 313–344.
18 J. Ba, J. Polleux, M. Antonietti and M. Niederberger, Non-aqueous synthesis of tin oxide nanocrystals and their assembly into ordered porous mesostructures, *Adv. Mater.*, 2005, **17**, 2509–2512.
19 T. Brezesinski, J. Wang, J. Polleux, B. Dunn and S. H. Tolbert, Templated nanocrystal-based porous TiO_2 films for next-generation electrochemical capacitors, *J. Am. Chem. Soc.*, 2009, **131**, 1802–1809.
20 P. Hartmann, D.-K. Lee, B. M. Smarsly and J. Janek, Mesoporous TiO_2: Comparison of classical sol–gel and nanoparticle based photoelectrodes for the water splitting reaction, *ACS Nano*, 2010, **4**, 3147–3154.
21 I. E. Rauda, R. Buonsanti, L. C. Saldarriaga-Lopez, K. Benjauthrit, L. T. Schelhas, M. Stefik, V. Augustyn, J. Ko, B. Dunn, U. Wiesner, D. J. Milliron and S. H. Tolbert, General method for the synthesis of hierarchical nanocrystal-based mesoporous materials, *ACS Nano*, 2012, **6**, 6386–6399.
22 D. J. Milliron, R. Buonsanti, A. Llordes and B. A. Helms, Constructing functional mesostructured materials from colloidal nanocrystal building blocks, *Acc. Chem. Res.*, 2014, **47**, 236–246.
23 A. M. Seayad and D. M. Antonelli, Recent advances in hydrogen storage in metal-containing inorganic nanostructures and related materials, *Adv. Mater.*, 2004, **16**, 765–777.
24 D. R. Rolison, Catalytic nanoarchitectures – the importance of nothing and the unimportance of periodicity, *Science*, 2003, **299**, 1698–1701.
25 M. Tiemann, Porous metal oxides as gas sensors, *Chem. – Eur. J.*, 2007, **13**, 8376–8388.
26 M. Grätzel, Mesoscopic solar cells for electricity and hydrogen production from sunlight, *Chem. Lett.*, 2005, **34**, 8–13.
27 J. W. Long, B. Dunn, D. R. Rolison and H. S. White, Three-dimensional battery architectures, *Chem. Rev.*, 2004, **104**, 4463–4492.
28 B. Smarsly and M. Antonietti, Block copolymer assemblies as templates for the generation of mesoporous inorganic materials and crystalline films, *Eur. J. Inorg. Chem.*, 2006, 1111–1119.
29 S. Fujita and S. Inagaki, Self-organization of organosilica solids with molecular-scale and mesoscale periodicities, *Chem. Mater.*, 2008, **20**, 891–908.
30 S. Mann, Self-assembly and transformation of hybrid nano-objects and nanostructures under equilibrium and non-equilibrium conditions, *Nat. Mater.*, 2009, **8**, 781–792.
31 M. Rawolle, M. A. Niedermeier, G. Kaune, J. Perlich, P. Lellig, M. Memesa, Y.-J. Cheng, J. S. Gutmann and P. Müller-Buschbaum, Fabrication and characterization of nanostructured titania films with integrated function from inorganic–organic hybrid materials, *Chem. Soc. Rev.*, 2012, **41**, 5131–5142.
32 N. D. Petkovich and A. Stein, Controlling macro- and mesostructures with hierarchical porosity through combined hard and soft templating, *Chem. Soc. Rev.*, 2013, **42**, 3721–3739.
33 A. Thomas, H. Schlaad, B. Smarsly and M. Antonietti, Replication of lyotropic block copolymer mesophases into porous silica by nanocasting: Learning about finer details of polymer self-assembly, *Langmuir*, 2003, **19**, 4455–4459.
34 M. Groenewolt, T. Brezesinski, H. Schlaad, M. Antonietti, P. W. Groh and B. Iván, Polyisobutylene-*block*-poly(ethylene oxide) for robust templating of highly ordered mesoporous materials, *Adv. Mater.*, 2005, **17**, 1158–1162.
35 E. Ortel, A. Fischer, L. Chuenchom, J. Polte, F. Emmerling, B. Smarsly and R. Kraehnert, New triblock copolymer templates, PEO-PB-PEO, for the synthesis of titania films with controlled mesopore size, wall thickness, and bimodal porosity, *Small*, 2012, **8**, 298–309.
36 J. Wei, Z. Sun, W. Luo, Y. Li, A. A. Elzatahry, A. M. Al-Enizi, Y. Deng and D. Zhao, New insight into the synthesis of large-pore ordered mesoporous materials, *J. Am. Chem. Soc.*, 2017, **139**, 1706–1713.
37 C. Reitz, J. Haetge, C. Suchomski and T. Brezesinski, Facile and general synthesis of thermally stable ordered mesoporous rare-earth oxide ceramic thin films with uniform mid-size to large-size pores and strong crystalline texture, *Chem. Mater.*, 2013, **25**, 4633–4642.
38 J. Haetge, P. Hartmann, K. Brezesinski, J. Janek and T. Brezesinski, Ordered large-pore mesoporous $Li_4Ti_5O_{12}$ spinel thin film electrodes with nanocrystalline framework for high rate rechargeable lithium batteries: Relationships among charge storage, electrical conductivity, and nanoscale structure, *Chem. Mater.*, 2011, **23**, 4384–4393.
39 C. Reitz, C. Suchomski, C. Weidmann and T. Brezesinski, Block copolymer-templated $BiFeO_3$ nanoarchitectures composed of phase-pure crystallites intermingled with a continuous mesoporosity: Effective visible-light photocatalysts?, *Nano Res.*, 2011, **4**, 414–424.
40 C. Weidmann, K. Brezesinski, C. Suchomski, K. Tropp, N. Grosser, J. Haetge, B. M. Smarsly and T. Brezesinski, Morphology-controlled synthesis of nanocrystalline η-Al_2O_3 thin films, powders, microbeads, and nanofibers with tunable pore sizes from preformed oligomeric oxo-hydroxo building blocks, *Chem. Mater.*, 2012, **24**, 486–494.
41 C. Reitz, P. M. Leufke, H. Hahn and T. Brezesinski, Ordered mesoporous thin film ferroelectrics of biaxially textured lead zirconate titanate (PZT) by chemical solution deposition, *Chem. Mater.*, 2014, **26**, 2195–2202.

42 C. Reitz, B. Smarsly and T. Brezesinski, General synthesis of ordered mesoporous rare-earth orthovanadate thin films and their use as photocatalysts and phosphors for lighting applications, *ACS Appl. Nano Mater.*, 2019, **2**, 1063–1071.
43 M. Kuemmel, D. Grosso, C. Boissière, B. Smarsly, T. Brezesinski, P. A. Albouy, H. Amenitsch and C. Sanchez, Thermally stable nanocrystalline γ-alumina layers with highly ordered 3D mesoporosity, *Angew. Chem., Int. Ed.*, 2005, **44**, 4589–4592.
44 T. Brezesinski, B. Smarsly, K.-i. Iimura, D. Grosso, C. Boissière, H. Amenitsch, M. Antonietti and C. Sanchez, Self-assembly and crystallization behavior of mesoporous, crystalline HfO_2 thin films: A model system for the generation of mesostructured transition-metal oxides, *Small*, 2005, **1**, 889–898.
45 T. Brezesinski, M. Antonietti, M. Groenewolt, N. Pinna and B. Smarsly, The generation of mesostructured crystalline CeO_2, ZrO_2 and CeO_2–ZrO_2 films using evaporation-induced self-assembly, *New J. Chem.*, 2005, **29**, 237–242.
46 T. Brezesinski, M. Groenewolt, N. Pinna, H. Amenitsch, M. Antonietti and B. Smarsly, Surfactant-mediated generation of iso-oriented dense and mesoporous crystalline metal-oxide layers, *Adv. Mater.*, 2006, **18**, 1827–1831.
47 T. Brezesinski, A. Fischer, K.-i. Iimura, C. Sanchez, D. Grosso, M. Antonietti and B. M. Smarsly, Generation of self-assembled 3D mesostructured SnO_2 thin films with highly crystalline frameworks, *Adv. Funct. Mater.*, 2006, **16**, 1433–1440.
48 T. Brezesinski, M. Antonietti and B. M. Smarsly, Self-assembled metal oxide bilayer films with "single-crystalline" overlayer mesopore structure, *Adv. Mater.*, 2007, **19**, 1074–1078.
49 T. Coquil, C. Reitz, T. Brezesinski, E. J. Nemanick, S. H. Tolbert and L. Pilon, Thermal conductivity of ordered mesoporous titania films made from nanocrystalline building blocks and sol–gel reagents, *J. Phys. Chem. C*, 2010, **114**, 12451–12458.
50 B. Niu, X. Wang, K. Wu, X. He and R. Zhang, Mesoporous titanium dioxide: Synthesis and applications in photocatalysis, energy and biology, *Materials*, 2018, **11**, 1910.
51 W. Zhang, Y. Tian, H. He, L. Xu, W. Li and D. Zhao, Recent advances in the synthesis of hierarchically mesoporous TiO_2 materials for energy and environmental applications, *Natl. Sci. Rev.*, 2020, **7**, 1702–1725.
52 A. E. H. Machado, K. A. Borges, T. A. Silva, L. M. Santos, M. F. Borges, W. A. Machado, B. P. Caixeta, S. M. Oliveira, A. G. Trovó and A. O. T. Patrocínio, in *Solar Radiation Applications*, 2015.
53 W. Li, Z. Wu, J. Wang, A. A. Elzatahry and D. Zhao, A perspective on mesoporous TiO_2 materials, *Chem. Mater.*, 2014, **26**, 287–298.
54 D. Fattakhova-Rohlfing, M. Wark, T. Brezesinski, B. M. Smarsly and J. Rathouský, Highly organized mesoporous TiO_2 films with controlled crystallinity: A Li-insertion study, *Adv. Funct. Mater.*, 2007, **17**, 123–132.
55 J. Maier, Ionic conduction in space charge regions, *Prog. Solid State Chem.*, 1995, **23**, 171–263.
56 K. L. Kliewer and J. S. Koehler, Space charge in ionic crystals. I. General approach with application to NaCl, *Phys. Rev.*, 1965, **140**, 897–902.
57 J. Maier, Defect chemistry and conductivity effects in heterogeneous solid electrolytes, *J. Electrochem. Soc.*, 1987, **134**, 1524–1535.
58 J. Maier, Space charge regions in solid two-phase systems and their conduction contribution-I. Conductance enhancement in the system ionic conductor-'inert' phase and application on AgC1:Al_2O_3 and AgC1:SiO_2, *J. Phys. Chem. Solids*, 1985, **46**, 309–320.
59 S. Kim, J. Fleig and J. Maier, Space charge conduction: Simple analytical solutions for ionic and mixed conductors and application to nanocrystalline ceria, *Phys. Chem. Chem. Phys.*, 2003, **5**, 2268–2273.
60 G. Gregori, R. Merkle and J. Maier, Ion conduction and redistribution at grain boundaries in oxide systems, *Prog. Mater. Sci.*, 2017, **89**, 252–305.
61 M. C. Göbel, G. Gregori and J. Maier, Numerical calculations of space charge layer effects in nanocrystalline ceria. Part I: Comparison with the analytical models and derivation of improved analytical solutions, *Phys. Chem. Chem. Phys.*, 2014, **16**, 10214–10231.
62 M. C. Göbel, G. Gregori and J. Maier, Numerical calculations of space charge layer effects in nanocrystalline ceria. Part II: Detailed analysis of the space charge layer properties, *Phys. Chem. Chem. Phys.*, 2014, **16**, 10175–10186.
63 D. S. Mebane and R. A. De Souza, A generalised space-charge theory for extended defects in oxygen-ion conducting electrolytes: From dilute to concentrated solid solutions, *Energy Environ. Sci.*, 2015, **8**, 2935–2940.
64 A. F. Zurhelle, X. Tong, A. Klein, D. S. Mebane and R. A. De Souza, A space-charge treatment of the increased concentration of reactive species at the surface of a ceria solid solution, *Angew. Chem., Int. Ed.*, 2017, **56**, 14516–14520.
65 A. R. C. Bredar, A. L. Chown, A. R. Burton and B. H. Farnum, Electrochemical impedance spectroscopy of metal oxide electrodes for energy applications, *ACS Appl. Energy Mater.*, 2020, **3**, 66–98.
66 J. T. S. Irvine, D. C. Sinclair and A. R. West, Electroceramics: Characterization by impedance spectroscopy, *Adv. Mater.*, 1990, **2**, 132–138.
67 J. E. Bauerle, Study of solid electrolyte polarization by a complex admittance method, *J. Phys. Chem. Solids*, 1969, **30**, 2657–2670.
68 I. M. Hodge, M. D. Ingram and A. R. West, Impedance and modulus spectroscopy of polycrystalline solid electrolytes, *J. Electroanal. Chem. Interfacial Electrochem.*, 1976, **74**, 125–143.
69 D. D. Macdonald, Reflections on the history of electrochemical impedance spectroscopy, *Electrochim. Acta*, 2006, **51**, 1376–1388.
70 J. R. Macdonald and W. B. Johnson, in *Impedance Spectroscopy*, John Wiley & Sons, Inc., Hoboken, NJ, USA, 2018, pp. 1–20.
71 J. Fleig and J. Maier, A finite element study on the grain boundary impedance of different microstructures, *J. Electrochem. Soc.*, 1998, **145**, 2081–2089.
72 H. L. Tuller, Ionic conduction in nanocrystalline materials, *Solid State Ionics*, 2000, **131**, 143–157.

73 J. Maier, On the conductivity of polycrystalline materials, *Ber. Bunseng. Phys. Chem.*, 1986, **90**, 26–33.
74 X. Guo, W. Sigle and J. Maier, Blocking grain boundaries in yttria-doped and undoped ceria ceramics of high purity, *J. Am. Ceram. Soc.*, 2003, **86**, 77–87.
75 X. Guo and R. Waser, Space charge concept for acceptor-doped zirconia and ceria and experimental evidences, *Solid State Ionics*, 2004, **173**, 63–67.
76 X. Guo and J. Maier, Grain boundary blocking effect in zirconia: A Schottky barrier analysis, *J. Electrochem. Soc.*, 2001, **148**, E121–E126.
77 I. Kosacki and H. U. Anderson, Microstructure—property relationships in nanocrystalline oxide thin films, *Ionics*, 2000, **6**, 294–311.
78 J. Maier, Defect chemistry and ionic conductivity in thin films, *Solid State Ionics*, 1987, **23**, 59–67.
79 O. J. Durá, M. A. López De La Torre, L. Vázquez, J. Chaboy, R. Boada, A. Rivera-Calzada, J. Santamaria and C. Leon, Ionic conductivity of nanocrystalline yttria-stabilized zirconia: Grain boundary and size effects, *Phys. Rev. B: Condens. Matter Mater. Phys.*, 2010, **81**, 7126–7133.
80 J.-S. Lee and D.-Y. Kim, Space-charge concepts on grain boundary impedance of a high-purity yttria-stabilized tetragonal zirconia polycrystal, *J. Mater. Res.*, 2001, **16**, 2739–2751.
81 M. Gödickemeier, B. Michel, A. Orliukas, P. Bohac, K. Sasaki, L. Gauckler, H. Heinrich, P. Schwander, G. Kostorz, H. Hofmann and O. Frei, Effect of intergranular glass films on the electrical conductivity of 3Y-TZP, *J. Mater. Res.*, 1994, **9**, 1228–1240.
82 S. P. S. Badwal and J. Drennan, Evaluation of conducting properties of yttria-zirconia wafers, *Solid State Ionics*, 1990, **40–41**, 869–873.
83 J. Maier, Nanoionics: Ion transport and electrochemical storage in confined systems, *Nat. Mater.*, 2005, **4**, 805–815.
84 J. Maier, Nanoionics: Ionic charge carriers in small systems, *Phys. Chem. Chem. Phys.*, 2009, **11**, 3011–3022.
85 Y. M. Chiang, E. B. Lavik, I. Kosacki, H. L. Tuller and J. Y. Ying, Defect and transport properties of nanocrystalline CeO_{2-x}, *Appl. Phys. Lett.*, 1996, **69**, 185–187.
86 X. Guo, I. Matei, J. Jamnik, J.-S. Lee and J. Maier, Defect chemical modeling of mesoscopic ion conduction in nanosized CaF_2/BaF_2 multilayer heterostructures, *Phys. Rev. B: Condens. Matter Mater. Phys.*, 2007, **76**, 125429.
87 Y. M. Chiang, E. B. Lavik, I. Kosacki, H. L. Tuller and J. Y. Ying, Nonstoichiometry and electrical conductivity of nanocrystalline CeO_{2-x}, *J. Electroceram.*, 1997, **1**, 7–14.
88 A. Tschöpe, Grain size-dependent electrical conductivity of polycrystalline cerium oxide. II: Space charge model, *Solid State Ionics*, 2001, **139**, 267–280.
89 A. Tschöpe, E. Sommer and R. Birringer, Grain size-dependent electrical conductivity of polycrystalline cerium oxide: I. Experiments, *Solid State Ionics*, 2001, **139**, 255–265.
90 A. Tschöpe and R. Birringer, Grain size dependence of electrical conductivity in polycrystalline cerium oxide, *J. Electroceram.*, 2001, **7**, 169–177.
91 A. Tschöpe, Interface defect chemistry and effective conductivity in polycrystalline cerium oxide, *J. Electroceram.*, 2005, **14**, 5–23.
92 A. Tschöpe, J. Y. Ying and H. L. Tuller, Catalytic redox activity and electrical conductivity of nanocrystalline nonstoichiometric cerium oxide, *Sens. Actuators, B*, 1996, **31**, 111–114.
93 J.-H. Hwang and T. O. Mason, Defect chemistry and transport properties of nanocrystalline cerium oxide, *Z. Phys. Chem.*, 1998, **207**, 21–38.
94 P. Hartmann, T. Brezesinski, J. Sann, A. Lotnyk, J.-P. Eufinger, L. Kienle and J. Janek, Defect chemistry of oxide nanomaterials with high surface area: Ordered mesoporous thin films of the oxygen storage catalyst CeO_2–ZrO_2, *ACS Nano*, 2013, **7**, 2999–3013.
95 M. Boaro, A. Trovarelli, J. H. Hwang and T. O. Mason, Electrical and oxygen storage/release properties of nanocrystalline ceria-zirconia solid solutions, *Solid State Ionics*, 2002, **147**, 85–95.
96 J. H. Lee, S. M. Yoon, B. K. Kim, H. W. Lee and H. S. Song, Electrical conductivity and defect structure of CeO_2–ZrO_2 mixed oxide, *J. Mater. Sci.*, 2002, **37**, 1165–1171.
97 J.-P. Eufinger, M. Daniels, K. Schmale, S. Berendts, G. Ulbrich, M. Lerch, H.-D. Wiemhöfer and J. Janek, The model case of an oxygen storage catalyst – non-stoichiometry, point defects and electrical conductivity of single crystalline CeO_2–ZrO_2–Y_2O_3 solid solutions, *Phys. Chem. Chem. Phys.*, 2014, **16**, 25583–25600.
98 H. L. Tuller and A. S. Nowick, Small polaron electron transport in reduced CeO_2 single crystals, *J. Phys. Chem. Solids*, 1977, **38**, 859–867.
99 K. Michel, J.-P. Eufinger, G. Ulbrich, M. Lerch, J. Janek and M. T. Elm, Combining two redox active rare earth elements for oxygen storage – electrical properties and defect chemistry of ceria–praseodymia single crystals, *Phys. Chem. Chem. Phys.*, 2017, **19**, 17661–17669.
100 S. Miyoshi, Y. Akao, N. Kuwata, J. Kawamura, Y. Oyama, T. Yagi and S. Yamaguchi, Low-temperature protonic conduction based on surface protonics: An example of nanostructured yttria-doped zirconia, *Chem. Mater.*, 2014, **26**, 5194–5200.
101 K. L. Duncan, Y. Wang, S. R. Bishop, F. Ebrahimi and E. D. Wachsman, The role of point defects in the physical properties of nonstoichiometric ceria, *J. Appl. Phys.*, 2007, **101**, 44906.
102 L. J. Gauckler, M. Gödickemeier and D. Schneider, Nonstoichiometry and defect chemistry of ceria solid solutions, *J. Electroceram.*, 1997, **1**, 165–172.
103 C. Tandé, D. Pérez-Coll and G. C. Mather, Surface proton conductivity of dense nanocrystalline YSZ, *J. Mater. Chem.*, 2012, **22**, 11208–11213.
104 B. Scherrer, M. V. F. Schlupp, D. Stender, J. Martynczuk, J. G. Grolig, H. Ma, P. Kocher, T. Lippert, M. Prestat and L. J. Gauckler, On proton conductivity in porous and dense yttria stabilized zirconia at low temperature, *Adv. Funct. Mater.*, 2013, **23**, 1957–1964.

105 H. J. Avila-Paredes, J. Zhao, S. Wang, M. Pietrowski, R. A. De Souza, A. Reinholdt, Z. A. Munir, M. Martin and S. Kim, Protonic conductivity of nano-structured yttria-stabilized zirconia: Dependence on grain size, *J. Mater. Chem.*, 2010, **20**, 990–994.
106 S. Kim, U. Anselmi-Tamburini, H. J. Park, M. Martin and Z. A. Munir, Unprecedented room-temperature electrical power generation using nanoscale fluorite-structured oxide electrolytes, *Adv. Mater.*, 2008, **20**, 556–559.
107 G. Gregori, M. Shirpour and J. Maier, Proton conduction in dense and porous nanocrystalline ceria thin films, *Adv. Funct. Mater.*, 2013, **23**, 5861–5867.
108 M. Shirpour, G. Gregori, R. Merkle and J. Maier, On the proton conductivity in pure and gadolinium doped nanocrystalline cerium oxide, *Phys. Chem. Chem. Phys.*, 2011, **13**, 937–940.
109 E. Ruiz-Trejo and J. A. Kilner, Possible proton conduction in $Ce_{0.9}Gd_{0.1}O_{2-\delta}$ nanoceramics, *J. Appl. Electrochem.*, 2009, **39**, 523–528.
110 H. J. Avila-Paredes, C.-T. Chen, S. Wang, R. A. De Souza, M. Martin, Z. Munir and S. Kim, Grain boundaries in dense nanocrystalline ceria ceramics: Exclusive pathways for proton conduction at room temperature, *J. Mater. Chem.*, 2010, **20**, 10110–10112.
111 H. Shen, H. Maekawa, J. Kawamura, Y. Matsumoto, T. Yamamura, Y. Kawakita, K. Shibata and M. Kawai, Effect of pore size and salt doping on the protonic conductivity of mesoporous alumina, *Solid State Ionics*, 2008, **179**, 1133–1137.
112 R. Fan, S. Huh, R. Yan, J. Arnold and P. Yang, Gated proton transport in aligned mesoporous silica films, *Nat. Mater.*, 2008, **7**, 303–307.
113 F. Maglia, I. G. Tredici, G. Spinolo and U. Anselmi-Tamburini, Low temperature proton conduction in bulk nanometric TiO_2 prepared by high-pressure field assisted sintering, *J. Mater. Res.*, 2012, **27**, 1975–1981.
114 G. Chiodelli, F. Maglia, U. Anselmi-Tamburini and Z. A. Munir, Characterization of low temperature protonic conductivity in bulk nanocrystalline fully stabilized zirconia, *Solid State Ionics*, 2009, **180**, 297–301.
115 M. T. Colomer, Nanoporous anatase thin films as fast proton-conducting materials, *Adv. Mater.*, 2006, **18**, 371–374.
116 K. D. Kreuer, Proton-conducting oxides, *Annu. Rev. Mater. Res.*, 2003, **33**, 333–359.
117 K.-D. Kreuer, Proton conductivity: Materials and applications, *Chem. Mater.*, 1996, **8**, 610–641.
118 L. Almar, A. Tarancón, T. Andreu, M. Torrell, Y. Hu, G. Dezanneau and A. Morata, Mesoporous ceramic oxides as humidity sensors: A case study for gadolinium-doped ceria, *Sens. Actuators, B*, 2015, **216**, 41–48.
119 T. Wagner, S. Haffer, C. Weinberger, D. Klaus and M. Tiemann, Mesoporous materials as gas sensors, *Chem. Soc. Rev.*, 2013, **42**, 4036–4053.
120 J. Zhao, Y. Liu, X. Li, G. Lu, L. You, X. Liang, F. Liu, T. Zhang and Y. Du, Highly sensitive humidity sensor based on high surface area mesoporous $LaFeO_3$ prepared by a nanocasting route, *Sens. Actuators, B*, 2013, **181**, 802–809.
121 P. M. Faia, C. S. Furtado and A. J. Ferreira, Humidity sensing properties of a thick-film titania prepared by a slow spinning process, *Sens. Actuators, B*, 2004, **101**, 183–190.
122 P. Zhang, S.-Y. Huang and B. N. Popov, Mesoporous tin oxide as an oxidation-resistant catalyst support for proton exchange membrane fuel cells, *J. Electrochem. Soc.*, 2010, **157**, B1163.
123 J. D. Halla, M. Mamak, D. E. Williams and G. A. Ozin, Meso-SiO_2–$C_{12}EO_{10}OH$–CF_3SO_3H—a novel proton-conducting solid electrolyte, *Adv. Funct. Mater.*, 2003, **13**, 133–138.
124 F. M. Vichi, M. T. Colomer and M. A. Anderson, Nanopore ceramic membranes as novel electrolytes for proton exchange membranes, *Electrochem. Solid-State Lett.*, 1999, **2**, 313–316.
125 W. H. J. Hogarth, J. C. Diniz da Costa, J. Drennan and G. Q. (Max) Lu, Proton conductivity of mesoporous sol–gel zirconium phosphates for fuel cell applications, *J. Mater. Chem.*, 2005, **15**, 754–758.
126 S. Kim, H. J. Avila-Paredes, S. Wang, C.-T. Chen, R. A. De Souza, M. Martin and Z. A. Munir, On the conduction pathway for protons in nanocrystalline yttria-stabilized zirconia, *Phys. Chem. Chem. Phys.*, 2009, **11**, 3035–3038.
127 S. Miyoshi, Y. Akao, N. Kuwata, J. Kawamura, Y. Oyama, T. Yagi and S. Yamaguchi, Water uptake and conduction property of nano-grained yttria-doped zirconia fabricated by ultra-high pressure compaction at room temperature, *Solid State Ionics*, 2012, **207**, 21–28.
128 I. G. Tredici, F. Maglia, C. Ferrara, P. Mustarelli and U. Anselmi-Tamburini, Mechanism of low-temperature protonic conductivity in bulk, high-density, nanometric titanium oxide, *Adv. Funct. Mater.*, 2014, **24**, 5137–5146.
129 E. Celik, R. S. Negi, M. Bastianello, D. Boll, A. Mazilkin, T. Brezesinski and M. T. Elm, Tailoring the protonic conductivity of porous yttria-stabilized zirconia thin films by surface modification, *Phys. Chem. Chem. Phys.*, 2020, **22**, 11519–11528.
130 M. J. Pietrowski, R. A. De Souza, S. Kim, Z. A. Munir and M. Martin, Dehydration kinetics of nano-YSZ ceramics monitored by *in situ* infrared spectroscopy, *Solid State Ionics*, 2012, **225**, 241–244.
131 S. Ø. Stub, E. Vøllestad and T. Norby, Mechanisms of protonic surface transport in porous oxides: Example of YSZ, *J. Phys. Chem. C*, 2017, **121**, 12817–12825.
132 S. Ø. Stub, K. Thorshaug, P. M. Rørvik, T. Norby and E. Vøllestad, The influence of acceptor and donor doping on the protonic surface conduction of TiO_2, *Phys. Chem. Chem. Phys.*, 2018, **20**, 15653–15660.
133 S. Raz, K. Sasaki, J. Maier and I. Riess, Characterization of adsorbed water layers on Y_2O_3-doped ZrO_2, *Solid State Ionics*, 2001, **143**, 181–204.
134 E.-M. Köck, M. Kogler, B. Klötzer, M. F. Noisternig and S. Penner, Structural and electrochemical properties of physisorbed and chemisorbed water layers on the ceramic oxides Y_2O_3, YSZ, and ZrO_2, *ACS Appl. Mater. Interfaces*, 2016, **8**, 16428–16443.
135 M. T. Elm, J. D. Hofmann, C. Suchomski, J. Janek and T. Brezesinski, Ionic conductivity of mesostructured yttria-stabilized zirconia thin films with cubic pore symmetry—on

the influence of water on the surface oxygen ion transport, *ACS Appl. Mater. Interfaces*, 2015, **7**, 11792–11801.

136 S. Ø. Stub, E. Vøllestad and T. Norby, Protonic surface conduction controlled by space charge of intersecting grain boundaries in porous ceramics, *J. Mater. Chem. A*, 2018, **6**, 8265–8270.

137 F. M. Vichi, M. I. Tejedor-Tejedor and M. A. Anderson, Effect of pore-wall chemistry on proton conductivity in mesoporous titanium dioxide, *Chem. Mater.*, 2000, **12**, 1762–1770.

138 R. Marschall, I. Bannat, J. Caro and M. Wark, Proton conductivity of sulfonic acid functionalised mesoporous materials, *Microporous Mesoporous Mater.*, 2007, **99**, 190–196.

139 H. Li and M. Nogami, Pore-controlled proton conducting silica films, *Adv. Mater.*, 2002, **14**, 912–914.

140 M. T. Colomer and M. A. Anderson, High porosity silica xerogels prepared by a particulate sol–gel route: Pore structure and proton conductivity, *J. Non-Cryst. Solids*, 2001, **290**, 93–104.

141 Y. Daiko, T. Kasuga and M. Nogami, Pore size effect on proton transfer in sol–gel porous silica glasses, *Microporous Mesoporous Mater.*, 2004, **69**, 149–155.

142 N. Koone, Y. Shao and T. W. Zerda, Diffusion of simple liquids in porous sol–gel glass, *J. Phys. Chem.*, 1995, **99**, 16976–16981.

143 W. C. Chueh, C.-K. Yang, C. M. Garland, W. Lai and S. M. Haile, Unusual decrease in conductivity upon hydration in acceptor doped, microcrystalline ceria, *Phys. Chem. Chem. Phys.*, 2011, **13**, 6442–6451.

144 Y. Yan, G. Chen, P. She, G. Zhong, W. Yan, B. Y. Guan and Y. Yamauchi, Mesoporous nanoarchitectures for electrochemical energy conversion and storage, *Adv. Mater.*, 2020, **32**, 2004654.

145 A. Vu, Y. Qian and A. Stein, Porous electrode materials for lithium-ion batteries – how to prepare them and what makes them special, *Adv. Energy Mater.*, 2012, **2**, 1056–1085.

146 A. Walcarius, Mesoporous materials and electrochemistry, *Chem. Soc. Rev.*, 2013, **42**, 4098–4140.

147 P. G. Bruce, B. Scrosati and J.-M. Tarascon, Nanomaterials for rechargeable lithium batteries, *Angew. Chem., Int. Ed.*, 2008, **47**, 2930–2946.

148 W. Li, J. Liu and D. Zhao, Mesoporous materials for energy conversion and storage devices, *Nat. Rev. Mater.*, 2016, **1**, 16023.

149 L. Zu, W. Zhang, L. Qu, L. Liu, W. Li, A. Yu and D. Zhao, Mesoporous materials for electrochemical energy storage and conversion, *Adv. Energy Mater.*, 2020, **10**, 2002152.

150 F. Jiao, K. M. Shaju and P. G. Bruce, Synthesis of nanowire and mesoporous low-temperature $LiCoO_2$ by a post-templating reaction, *Angew. Chem., Int. Ed.*, 2005, **44**, 6550–6553.

151 G. Wang, H. Liu, J. Liu, S. Qiao, G. M. Lu, P. Munroe and H. Ahn, Mesoporous $LiFePO_4$/C nanocomposite cathode materials for high power lithium ion batteries with superior performance, *Adv. Mater.*, 2010, **22**, 4944–4948.

152 Y. Ren, A. R. Armstrong, F. Jiao and P. G. Bruce, Influence of size on the rate of mesoporous electrodes for lithium batteries, *J. Am. Chem. Soc.*, 2010, **132**, 996–1004.

153 J. Luo, Y. Wang, H. Xiong and Y. Xia, Ordered mesoporous spinel $LiMn_2O_4$ by a soft-chemical process as a cathode material for lithium-ion batteries, *Chem. Mater.*, 2007, **19**, 4791–4795.

154 M. G. Fischer, X. Hua, B. D. Wilts, I. Gunkel, T. M. Bennett and U. Steiner, Mesoporous titania microspheres with highly tunable pores as an anode material for lithium ion batteries, *ACS Appl. Mater. Interfaces*, 2017, **9**, 22388–22397.

155 H. Liu, W. Li, D. Shen, D. Zhao and G. Wang, Graphitic carbon conformal coating of mesoporous TiO_2 hollow spheres for high-performance lithium ion battery anodes, *J. Am. Chem. Soc.*, 2015, **137**, 13161–13166.

156 J. Yue, C. Suchomski, P. Voepel, R. Ellinghaus, M. Rohnke, T. Leichtweiss, M. T. Elm and B. M. Smarsly, Mesoporous niobium-doped titanium dioxide films from the assembly of crystalline nanoparticles: Study on the relationship between the band structure, conductivity and charge storage mechanism, *J. Mater. Chem. A*, 2017, **5**, 1978–1988.

157 B. Sun, J. Horvat, H. S. Kim, W.-S. Kim, J. Ahn and G. Wang, Synthesis of mesoporous α-Fe_2O_3 nanostructures for highly sensitive gas sensors and high capacity anode materials in lithium ion batteries, *J. Phys. Chem. C*, 2010, **114**, 18753–18761.

158 H. Liu, G. Wang, J. Liu, S. Qiao and H. Ahn, Highly ordered mesoporous NiO anode material for lithium ion batteries with an excellent electrochemical performance, *J. Mater. Chem.*, 2011, **21**, 3046–3052.

159 I. E. Rauda, V. Augustyn, B. Dunn and S. H. Tolbert, Enhancing pseudocapacitive charge storage in polymer templated mesoporous materials, *Acc. Chem. Res.*, 2013, **46**, 1113–1124.

160 S. Fleischmann, J. B. Mitchell, R. Wang, C. Zhan, D. Jiang, V. Presser and V. Augustyn, Pseudocapacitance: From fundamental understanding to high power energy storage materials, *Chem. Rev.*, 2020, **120**, 6738–6782.

161 T. Brezesinski, J. Wang, S. H. Tolbert and B. Dunn, Next generation pseudocapacitor materials from sol–gel derived transition metal oxides, *J. Sol–Gel Sci. Technol.*, 2011, **57**, 330–335.

162 H. Lindström, S. Södergren, A. Solbrand, H. Rensmo, J. Hjelm, A. Hagfeldt and S.-E. Lindquist, Li^+ ion insertion in TiO_2 (anatase). 2. Voltammetry on nanoporous films, *J. Phys. Chem. B*, 1997, **101**, 7717–7722.

163 A. J. Bard and L. R. Faulkner, *Electrochemical Methods: Fundamentals and Applications*, 2nd edn, John Wiley & Sons, Inc., 2000.

164 Y. Ma, Y. Ma, G. Giuli, H. Euchner, A. Groß, G. O. Lepore, F. D'Acapito, D. Geiger, J. Biskupek, U. Kaiser, H. M. Schütz, A. Carlsson, T. Diemant, R. J. Behm, M. Kuenzel, S. Passerini and D. Bresser, Introducing highly redox-active atomic centers into insertion-type electrodes for lithium-ion batteries, *Adv. Energy Mater.*, 2020, **10**, 2000783.

165 T. Brezesinski, J. Wang, R. Senter, K. Brezesinski, B. Dunn and S. H. Tolbert, On the correlation between mechanical flexibility, nanoscale structure, and charge storage in periodic mesoporous CeO_2 thin films, *ACS Nano*, 2010, **4**, 967–977.

166 K. Brezesinski, J. Wang, J. Haetge, C. Reitz, S. O. Steinmueller, S. H. Tolbert, B. M. Smarsly, B. Dunn and T. Brezesinski,

Pseudocapacitive contributions to charge storage in highly ordered mesoporous group v transition metal oxides with iso-oriented layered nanocrystalline domains, *J. Am. Chem. Soc.*, 2010, **132**, 6982–6990.

167 J. B. Cook, H. S. Kim, Y. Yan, J. S. Ko, S. Robbennolt, B. Dunn and S. H. Tolbert, Mesoporous MoS_2 as a transition metal dichalcogenide exhibiting pseudocapacitive Li and Na-ion charge storage, *Adv. Energy Mater.*, 2016, **6**, 1501937.

168 T. Brezesinski, J. Wang, S. H. Tolbert and B. Dunn, Ordered mesoporous α-MoO_3 with iso-oriented nanocrystalline walls for thin-film pseudocapacitors, *Nat. Mater.*, 2010, **9**, 146–151.

169 J. Maier, Thermodynamics of electrochemical lithium storage, *Angew. Chem., Int. Ed.*, 2013, **52**, 4998–5026.

170 C. Li, L. Gu, X. Guo, D. Samuelis, K. Tang and J. Maier, Charge carrier accumulation in lithium fluoride thin films due to Li-ion absorption by titania(100) subsurface, *Nano Lett.*, 2012, **12**, 1241–1246.

171 J. Maier, Pushing nanoionics to the limits: Charge carrier chemistry in extremely small systems, *Chem. Mater.*, 2014, **26**, 348–360.

172 C.-C. Chen and J. Maier, Space charge storage in composites: Thermodynamics, *Phys. Chem. Chem. Phys.*, 2017, **19**, 6379–6396.

173 C.-C. Chen, L. Fu and J. Maier, Synergistic, ultrafast mass storage and removal in artificial mixed conductors, *Nature*, 2016, **536**, 159–164.

174 Y. Wang, B. M. Smarsly and I. Djerdj, Niobium doped TiO_2 with mesoporosity and its application for lithium insertion, *Chem. Mater.*, 2010, **22**, 6624–6631.

175 Y. Liu, J. M. Szeifert, J. M. Feckl, B. Mandlmeier, J. Rathousky, O. Hayden, D. Fattakhova-Rohlfing and T. Bein, Niobium-doped titania nanoparticles: Synthesis and assembly into mesoporous films and electrical conductivity, *ACS Nano*, 2010, **4**, 5373–5381.

176 Z. Zhang and J. T. Yates, Band bending in semiconductors: Chemical and physical consequences at surfaces and interfaces, *Chem. Rev.*, 2012, **112**, 5520–5551.

177 K. Ozawa, M. Emori, S. Yamamoto, R. Yukawa, S. Yamamoto, R. Hobara, K. Fujikawa, H. Sakama and I. Matsuda, Electron–hole recombination time at TiO_2 single-crystal surfaces: Influence of surface band bending, *J. Phys. Chem. Lett.*, 2014, **5**, 1953–1957.

178 M. N. Obrovac and V. L. Chevrier, Alloy negative electrodes for Li-ion batteries, *Chem. Rev.*, 2014, **114**, 11444–11502.

179 K. Ishidzu, Y. Oka and T. Nakamura, Lattice volume change during charge/discharge reaction and cycle performance of $Li[Ni_xCo_yMn_z]O_2$, *Solid State Ionics*, 2016, **288**, 176–179.

180 P. Li, Y. Zhao, Y. Shen and S.-H. Bo, Fracture behavior in battery materials, *J. Phys. Energy*, 2020, **2**, 022002.

181 F. Strauss, L. de Biasi, A.-Y. Kim, J. Hertle, S. Schweidler, J. Janek, P. Hartmann and T. Brezesinski, Rational design of quasi-zero-strain NCM cathode materials for minimizing volume change effects in all-solid-state batteries, *ACS Mater. Lett.*, 2020, **2**, 84–88.

182 R. Ruess, S. Schweidler, H. Hemmelmann, G. Conforto, A. Bielefeld, D. A. Weber, J. Sann, M. T. Elm and J. Janek, Influence of NCM particle cracking on kinetics of lithium-ion batteries with liquid or solid electrolyte, *J. Electrochem. Soc.*, 2020, **167**, 100532.

183 J. Gonzalez, K. Sun, M. Huang, J. Lambros, S. Dillon and I. Chasiotis, Three dimensional studies of particle failure in silicon based composite electrodes for lithium ion batteries, *J. Power Sources*, 2014, **269**, 334–343.

184 R. S. Negi, S. P. Culver, A. Mazilkin, T. Brezesinski and M. T. Elm, Enhancing the electrochemical performance of $LiNi_{0.70}Co_{0.15}Mn_{0.15}O_2$ cathodes using a practical solution-based Al_2O_3 coating, *ACS Appl. Mater. Interfaces*, 2020, **12**, 31392–31400.

185 A. Mukhopadhyay and B. W. Sheldon, Deformation and stress in electrode materials for Li-ion batteries, *Prog. Mater. Sci.*, 2014, **63**, 58–116.

186 H. Wang, Y. Jang, B. Huang, D. R. Sadoway and Y. Chiang, TEM study of electrochemical cycling-induced damage and disorder in $LiCoO_2$ cathodes for rechargeable lithium batteries, *J. Electrochem. Soc.*, 1999, **146**, 473–480.

187 X. H. Liu, L. Zhong, S. Huang, S. X. Mao, T. Zhu and J. Y. Huang, Size-dependent fracture of silicon nanoparticles during lithiation, *ACS Nano*, 2012, **6**, 1522–1531.

188 S. Schweidler, L. de Biasi, G. Garcia, A. Mazilkin, P. Hartmann, T. Brezesinski and J. Janek, Investigation into mechanical degradation and fatigue of high-Ni NCM cathode material: A long-term cycling study of full cells, *ACS Appl. Energy Mater.*, 2019, **2**, 7375–7384.

189 F. Jiao, J. Bao, A. H. Hill and P. G. Bruce, Synthesis of ordered mesoporous Li–Mn–O spinel as a positive electrode for rechargeable lithium batteries, *Angew. Chem., Int. Ed.*, 2008, **47**, 9711–9716.

190 Y. Ma, Y. Ma, G. Kim, T. Diemant, R. J. Behm, D. Geiger, U. Kaiser, A. Varzi and S. Passerini, Superior lithium storage capacity of α-MnS nanoparticles embedded in S-doped carbonaceous mesoporous frameworks, *Adv. Energy Mater.*, 2019, **9**, 1902077.

191 W. Wen, J. M. Wu and M. H. Cao, NiO/Ni powders with effective architectures as anode materials in Li-ion batteries, *J. Mater. Chem. A*, 2013, **1**, 3881–3885.

192 G. Li, Y. Li, J. Chen, P. Zhao, D. Li, Y. Dong and L. Zhang, Synthesis and research of egg shell-yolk NiO/C porous composites as lithium-ion battery anode material, *Electrochim. Acta*, 2017, **245**, 941–948.

193 J. Lee, S. Kim, J.-H. Park, C. Jo, J. Chun, Y.-E. Sung, E. Lim and J. Lee, A small-strain niobium nitride anode with ordered mesopores for ultra-stable potassium-ion batteries, *J. Mater. Chem. A*, 2020, **8**, 3119–3127.

194 S. M. Bhaway, Z. Qiang, Y. Xia, X. Xia, B. Lee, K. G. Yager, L. Zhang, K. Kisslinger, Y.-M. Chen, K. Liu, Y. Zhu and B. D. Vogt, *Operando* grazing incidence small-angle X-ray scattering/X-ray diffraction of model ordered mesoporous lithium-ion battery anodes, *ACS Nano*, 2017, **11**, 1443–1454.

195 N. Krins, J. D. Bass, D. Grosso, C. Henrist, R. Delaigle, E. M. Gaigneaux, R. Cloots, B. Vertruyen and C. Sanchez, $NbVO_5$ mesoporous thin films by evaporation induced micelles packing: Pore size dependence of the mechanical

stability upon thermal treatment and Li insertion/extraction, *Chem. Mater.*, 2011, **23**, 4124–4131.

196 S.-K. Jung, I. Hwang, D. Chang, K.-Y. Park, S. J. Kim, W. M. Seong, D. Eum, J. Park, B. Kim, J. Kim, J. H. Heo and K. Kang, Nanoscale phenomena in lithium-ion batteries, *Chem. Rev.*, 2020, **120**, 6684–6737.

197 D.-H. Lee, B.-H. Lee, A. K. Sinha, J.-H. Park, M.-S. Kim, J. Park, H. Shin, K.-S. Lee, Y.-E. Sung and T. Hyeon, Engineering titanium dioxide nanostructures for enhanced lithium-ion storage, *J. Am. Chem. Soc.*, 2018, **140**, 16676–16684.

198 N. J. J. de Klerk, A. Vasileiadis, R. B. Smith, M. Z. Bazant and M. Wagemaker, Explaining key properties of lithiation in TiO_2-anatase Li-ion battery electrodes using phase-field modelling, *Phys. Rev. Mater.*, 2017, **1**, 025404.

199 M. Wagemaker, W. J. H. Borghols and F. M. Mulder, Large impact of particle size on insertion reactions. A case for anatase Li_xTiO_2, *J. Am. Chem. Soc.*, 2007, **129**, 4323–4327.

200 T. Fröschl, U. Hörmann, P. Kubiak, G. Kučerová, M. Pfanzelt, C. K. Weiss, R. J. Behm, N. Hüsing, U. Kaiser, K. Landfester and M. Wohlfahrt-Mehrens, High surface area crystalline titanium dioxide: Potential and limits in electrochemical energy storage and catalysis, *Chem. Soc. Rev.*, 2012, **41**, 5313–5360.

201 V. Gentili, S. Brutti, L. J. Hardwick, A. R. Armstrong, S. Panero and P. G. Bruce, Lithium insertion into anatase nanotubes, *Chem. Mater.*, 2012, **24**, 4468–4476.

202 U. Lafont, D. Carta, G. Mountjoy, A. V. Chadwick and E. M. Kelder, *In situ* structural changes upon electrochemical lithium insertion in nanosized anatase TiO_2, *J. Phys. Chem. C*, 2010, **114**, 1372–1378.

203 D. Larcher, C. Masquelier, D. Bonnin, Y. Chabre, V. Masson, J.-B. Leriche and J.-M. Tarascon, Effect of particle size on lithium intercalation into α-Fe_2O_3, *J. Electrochem. Soc.*, 2003, **150**, A133–A139.

204 X. L. Wu, Y. G. Guo, L. J. Wan and C. W. Hu, α-Fe_2O_3 nanostructures: Inorganic salt-controlled synthesis and their electrochemical performance toward lithium storage, *J. Phys. Chem. C*, 2008, **112**, 16824–16829.

205 K. Brezesinski, J. Haetge, J. Wang, S. Mascotto, C. Reitz, A. Rein, S. H. Tolbert, J. Perlich, B. Dunn and T. Brezesinski, Ordered mesoporous α-Fe_2O_3 (Hematite) thin-film electrodes for application in high rate rechargeable lithium batteries, *Small*, 2011, **7**, 407–414.

206 L. A. Dubraja, C. Reitz, L. Velasco, R. Witte, R. Kruk, H. Hahn and T. Brezesinski, Electrochemical tuning of magnetism in ordered mesoporous transition-metal ferrite films for micromagnetic actuation, *ACS Appl. Nano Mater.*, 2018, **1**, 65–72.

207 P. Li, X. Chen, Y. Li and J. W. Schwank, A review on oxygen storage capacity of CeO_2-based materials: Influence factors, measurement techniques, and applications in reactions related to catalytic automotive emissions control, *Catal. Today*, 2019, **327**, 90–115.

208 R. Si, Y.-W. Zhang, S.-J. Li, B.-X. Lin and C.-H. Yan, Urea-based hydrothermally derived homogeneous nanostructured $Ce_{1-x}Zr_xO_2$ (x = 0–0.8) solid solutions: A strong correlation between oxygen storage capacity and lattice strain, *J. Phys. Chem. B*, 2004, **108**, 12481–12488.

209 S. Abdollahzadeh-Ghom, C. Zamani, T. Andreu, M. Epifani and J. R. Morante, Improvement of oxygen storage capacity using mesoporous ceria-zirconia solid solutions, *Appl. Catal., B*, 2011, **108–109**, 32–38.

210 M. P. Kapoor, A. Raj and Y. Matsumura, Methanol decomposition over palladium supported mesoporous CeO_2–ZrO_2 mixed oxides, *Microporous Mesoporous Mater.*, 2001, **44–45**, 565–572.

211 Q. Yuan, Q. Liu, W.-G. Song, W. Feng, W.-L. Pu, L.-D. Sun, Y.-W. Zhang and C.-H. Yan, Ordered mesoporous $Ce_{1-x}Zr_xO_2$ solid solutions with crystalline walls, *J. Am. Chem. Soc.*, 2007, **129**, 6698–6699.

212 Q. Yuan, L.-L. Li, S.-L. Lu, H.-H. Duan, Z.-X. Li, Y.-X. Zhu and C.-H. Yan, Facile synthesis of Zr-based functional materials with highly ordered mesoporous structures, *J. Phys. Chem. C*, 2009, **113**, 4117–4124.

213 J. Xiong, Y. Wei, Y. Zhang, X. Mei, Q. Wu, Z. Zhao, J. Liu, D. Wu and J. Li, Facile synthesis of 3D ordered macro-mesoporous $Ce_{1-x}Zr_xO_2$ catalysts with enhanced catalytic activity for soot oxidation, *Catal. Today*, 2020, **355**, 587–595.

214 J. Ouyang and H. Yang, Enhanced reduction properties of mesostructured $Ce_{0.5}Zr_{0.5}O_2$ solid solutions, *Mater. Chem. Phys.*, 2013, **140**, 294–299.

215 N. D. Petkovich, S. G. Rudisill, L. J. Venstrom, D. B. Boman, J. H. Davidson and A. Stein, Control of heterogeneity in nanostructured $Ce_{1-x}Zr_xO_2$ binary oxides for enhanced thermal stability and water splitting activity, *J. Phys. Chem. C*, 2011, **115**, 21022–21033.

216 E. Mamontov, R. Brezny, M. Koranne and T. Egami, Nanoscale heterogeneities and oxygen storage capacity of $Ce_{0.5}Zr_{0.5}O_2$, *J. Phys. Chem. B*, 2003, **107**, 13007–13014.

217 C. Ho, J. C. Yu, X. Wang, S. Lai and Y. Qiu, Meso- and macro-porous Pd/$Ce_xZr_{1-x}O_2$ as novel oxidation catalysts, *J. Mater. Chem.*, 2005, **15**, 2193–2201.

218 J. G. Nunan, H. J. Robota, M. J. Cohn and S. A. Bradley, Physicochemical properties of Ce-containing three-way catalysts and the effect of Ce on catalyst activity, *J. Catal.*, 1992, **133**, 309–324.

219 M. Epifani, T. Andreu, S. Abdollahzadeh-Ghom, J. Arbiol and J. R. Morante, Synthesis of ceria–zirconia nanocrystals with improved microstructural homogeneity and oxygen storage capacity by hydrolytic sol–gel process in coordinating environment, *Adv. Funct. Mater.*, 2012, **22**, 2867–2875.

220 P. Fornasiero, R. Dimonte, G. R. Rao, J. Kaspar, S. Meriani, A. Trovarelli and M. Graziani, Rh-Loaded CeO_2–ZrO_2 solid-solutions as highly efficient oxygen exchangers: Dependence of the reduction behavior and the oxygen storage capacity on the structural-properties, *J. Catal.*, 1995, **151**, 168–177.

221 Y. Cui, L. Lan, Z. Shi, S. Yuan, M. Gong, Y. Chen and Y. Dan, Effect of surface tension on the properties of a doped CeO_2–ZrO_2 composite and its application in a Pd-only three-way catalyst, *RSC Adv.*, 2016, **6**, 66524–66536.

222 J. Roggenbuck, H. Schäfer, T. Tsoncheva, C. Minchev, J. Hanss and M. Tiemann, Mesoporous CeO_2: Synthesis by nanocasting, characterisation and catalytic properties, *Microporous Mesoporous Mater.*, 2007, **101**, 335–341.

223 T. X. T. Sayle, F. Caddeo, X. Zhang, T. Sakthivel, S. Das, S. Seal, S. Ptasinska and D. C. Sayle, Structure-activity map of ceria nanoparticles, nanocubes, and mesoporous architectures, *Chem. Mater.*, 2016, **28**, 7287–7295.

224 A. Migani, G. N. Vayssilov, S. T. Bromley, F. Illas and K. M. Neyman, Dramatic reduction of the oxygen vacancy formation energy in ceria particles: A possible key to their remarkable reactivity at the nanoscale, *J. Mater. Chem.*, 2010, **20**, 10535–10546.

225 A. Migani, G. N. Vayssilov, S. T. Bromley, F. Illas and K. M. Neyman, Greatly facilitated oxygen vacancy formation in ceria nanocrystallites, *Chem. Commun.*, 2010, **46**, 5936–5938.

226 X. Hao, A. Yoko, C. Chen, K. Inoue, M. Saito, G. Seong, S. Takami, T. Adschiri and Y. Ikuhara, Atomic-scale valence state distribution inside ultrafine CeO_2 nanocubes and its size dependence, *Small*, 2018, **14**, 1802915.

227 Y. Ren, Z. Ma, L. Qian, S. Dai, H. He and P. G. Bruce, Ordered crystalline mesoporous oxides as catalysts for CO oxidation, *Catal. Lett.*, 2009, **131**, 146–154.

228 S. Sun, Q. Gao, H. Wang, J. Zhu and H. Guo, Influence of textural parameters on the catalytic behavior for CO oxidation over ordered mesoporous Co_3O_4, *Appl. Catal., B*, 2010, **97**, 284–291.

229 H. Tüysüz, M. Comotti and F. Schüth, Ordered mesoporous Co_3O_4 as highly active catalyst for low temperature CO-oxidation, *Chem. Commun.*, 2008, 4022–4024.

230 A. L. Linsebigler, G. Lu and J. T. Yates, Photocatalysis on TiO_2 surfaces: Principles, mechanisms, and selected results, *Chem. Rev.*, 1995, **95**, 735–758.

231 A. Kudo and Y. Miseki, Heterogeneous photocatalyst materials for water splitting, *Chem. Soc. Rev.*, 2009, **38**, 253–278.

232 M. V. Grabchenko, G. V. Mamontov, V. I. Zaikovskii, V. La Parola, L. F. Liotta and O. V. Vodyankina, The role of metal–support interaction in Ag/CeO_2 catalysts for CO and soot oxidation, *Appl. Catal., B*, 2020, **260**, 118148.

233 B. P. Bastakoti, D. Kuila, C. Salomon, M. Konarova, M. Eguchi, J. Na and Y. Yamauchi, Metal-incorporated mesoporous oxides: Synthesis and applications, *J. Hazard. Mater.*, 2021, **401**, 123348.

234 J. A. Rodriguez, J. Graciani, J. Evans, J. B. Park, F. Yang, D. Stacchiola, S. D. Senanayake, S. Ma, M. Pérez, P. Liu, J. F. Sanz and J. Hrbek, Water-gas shift reaction on a highly active inverse $CeO_x/Cu(111)$ catalyst: Unique role of ceria nanoparticles, *Angew. Chem., Int. Ed.*, 2009, **48**, 8047–8050.

235 G. N. Vayssilov, Y. Lykhach, A. Migani, T. Staudt, G. P. Petrova, N. Tsud, T. Skála, A. Bruix, F. Illas, K. C. Prince, V. Matolín, K. M. Neyman and J. Libuda, Support nanostructure boosts oxygen transfer to catalytically active platinum nanoparticles, *Nat. Mater.*, 2011, **10**, 310–315.

236 K. An, S. Alayoglu, N. Musselwhite, S. Plamthottam, G. Melaet, A. E. Lindeman and G. A. Somorjai, Enhanced CO oxidation rates at the interface of mesoporous oxides and Pt nanoparticles, *J. Am. Chem. Soc.*, 2013, **135**, 16689–16696.

237 R. Abe, Recent progress on photocatalytic and photoelectrochemical water splitting under visible light irradiation, *J. Photochem. Photobiol., C*, 2010, **11**, 179–209.

238 W. Zhou, W. Li, J.-Q. Wang, Y. Qu, Y. Yang, Y. Xie, K. Zhang, L. Wang, H. Fu and D. Zhao, Ordered mesoporous black TiO_2 as highly efficient hydrogen evolution photocatalyst, *J. Am. Chem. Soc.*, 2014, **136**, 9280–9283.

239 J. Cai, J. Shen, X. Zhang, Y. H. Ng, J. Huang, W. Guo, C. Lin and Y. Lai, Light-driven sustainable hydrogen production utilizing TiO_2 nanostructures: A review, *Small Methods*, 2019, **3**, 1800184.

240 B. Fang, A. Bonakdarpour, K. Reilly, Y. Xing, F. Taghipour and D. P. Wilkinson, Large-scale synthesis of TiO_2 microspheres with hierarchical nanostructure for highly efficient photodriven reduction of CO_2 to CH_4, *ACS Appl. Mater. Interfaces*, 2014, **6**, 15488–15498.

241 J. N. Kondo and K. Domen, Crystallization of mesoporous metal oxides, *Chem. Mater.*, 2008, **20**, 835–847.

242 S. Waitz, C. Suchomski, T. Brezesinski and R. Marschall, Ordered mesoporous $LiFe_5O_8$ thin-film photoanodes for water splitting, *ChemPhotoChem*, 2018, **2**, 1022–1026.

243 K. Kirchberg, S. Wang, L. Wang and R. Marschall, Mesoporous $ZnFe_2O_4$ photoanodes with template-tailored mesopores and temperature-dependent photocurrents, *ChemPhysChem*, 2018, **19**, 2313–2320.

244 A. G. Hufnagel, K. Peters, A. Müller, C. Scheu, D. Fattakhova-Rohlfing and T. Bein, Zinc ferrite photoanode nanomorphologies with favorable kinetics for water-splitting, *Adv. Funct. Mater.*, 2016, **26**, 4435–4443.

245 A. A. Tahir and K. G. U. Wijayantha, Photoelectrochemical water splitting at nanostructured $ZnFe_2O_4$ electrodes, *J. Photochem. Photobiol., A*, 2010, **216**, 119–125.

246 L. A. Dubraja, D. Boll, C. Reitz, D. Wang, D. Belić, A. Mazilkin, B. Breitung, H. Hahn, M. T. Elm and T. Brezesinski, Thin films of thermally stable ordered mesoporous Rh2O3(I) for visible-light photocatalysis and humidity sensing, *ACS Appl. Nano Mater.*, 2019, **2**, 7126–7133.

247 A. S. Cherevan, L. Deilmann, T. Weller, D. Eder and R. Marschall, Mesoporous semiconductors: A new model to assess accessible surface area and increased photocatalytic activity?, *ACS Appl. Energy Mater.*, 2018, **1**, 5787–5799.

248 T. Grewe and H. Tüysüz, Alkali metals incorporated ordered mesoporous tantalum oxide with enhanced photocatalytic activity for water splitting, *J. Mater. Chem. A*, 2016, **4**, 3007–3017.

249 H.-Y. Lin, H.-C. Yang and W.-L. Wang, Synthesis of mesoporous Nb_2O_5 photocatalysts with Pt, Au, Cu and NiO cocatalyst for water splitting, *Catal. Today*, 2011, **174**, 106–113.

250 C.-H. Kuo, I. M. Mosa, A. S. Poyraz, S. Biswas, A. M. El-Sawy, W. Song, Z. Luo, S.-Y. Chen, J. F. Rusling, J. He and S. L. Suib, Robust mesoporous manganese oxide catalysts for water oxidation, *ACS Catal.*, 2015, **5**, 1693–1699.

251 C. Reitz, K. Brezesinski, J. Haetge, J. Perlich and T. Brezesinski, Nanocrystalline $NaTaO_3$ thin film materials with ordered 3D mesoporous and nanopillar-like structures through PIB-*b*-PEO polymer templating: Towards high-performance UV-light photocatalysts, *RSC Adv.*, 2012, **2**, 5130–5133.

252 H. Tüysüz and C. K. Chan, Preparation of amorphous and nanocrystalline sodium tantalum oxide photocatalysts with

porous matrix structure for overall water splitting, *Nano Energy*, 2013, **2**, 116–123.

253 M. K. Hossain, U. S. Akhtar, A. R. Koirala, I. C. Hwang and K. B. Yoon, Steam-assisted synthesis of uniformly mesoporous anatase and its remarkably superior photocatalytic activities, *Catal. Today*, 2015, **243**, 228–234.

254 M. Zhou, H. Bin Wu, J. Bao, L. Liang, X. W. (David) Lou and Y. Xie, Ordered macroporous $BiVO_4$ architectures with controllable dual porosity for efficient solar water splitting, *Angew. Chem., Int. Ed.*, 2013, **52**, 8579–8583.

255 T. Weller, J. Sann and R. Marschall, Pore structure controlling the activity of mesoporous crystalline $CsTaWO_6$ for photocatalytic hydrogen generation, *Adv. Energy Mater.*, 2016, **6**, 1600208.

256 T. Weller, L. Deilmann, J. Timm, T. S. Dörr, P. A. Beaucage, A. S. Cherevan, U. B. Wiesner, D. Eder and R. Marschall, A crystalline and 3D periodically ordered mesoporous quaternary semiconductor for photocatalytic hydrogen generation, *Nanoscale*, 2018, **10**, 3225–3234.

257 X. Zhou, X. Cheng, Y. Zhu, A. A. Elzatahry, A. Alghamdi, Y. Deng and D. Zhao, Ordered porous metal oxide semiconductors for gas sensing, *Chin. Chem. Lett.*, 2018, **29**, 405–416.

258 G. Heiland, Homogeneous semiconducting gas sensors, *Sens. Actuators*, 1981, **2**, 343–361.

259 N. Yamazoe, G. Sakai and K. Shimanoe, Oxide semiconductor gas sensors, *Catal. Surv. Asia*, 2003, **7**, 63–75.

260 Y. Shimizu, T. Maekawa, Y. Nakamura and M. Egashira, Effects of gas diffusivity and reactivity on sensing properties of thick film SnO_2-based sensors, *Sens. Actuators, B*, 1998, **46**, 163–168.

261 A. Rothschild and Y. Komem, The effect of grain size on the sensitivity of nanocrystalline metal-oxide gas sensors, *J. Appl. Phys.*, 2004, **95**, 6374–6380.

262 C. Xu, J. Tamaki, N. Miura and N. Yamazoe, Correlation between gas sensitivity and crystallite size in porous SnO_2-based sensors, *Chem. Lett.*, 1990, 441–444.

263 C. Xu, J. Tamaki, N. Miura and N. Yamazoe, Grain size effects on gas sensitivity of porous SnO_2-based elements, *Sens. Actuators, B*, 1991, **3**, 147–155.

264 T. Aqeel, V. Galstyan and E. Comini, Mesoporous polycrystalline SnO_2 framework synthesized by direct soft templating method for highly selective detection of NO_2, *Nanotechnology*, 2019, **31**, 105502.

265 T. Waitz, T. Wagner, T. Sauerwald, C.-D. Kohl and M. Tiemann, Ordered mesoporous In_2O_3: Synthesis by structure replication and application as a methane gas sensor, *Adv. Funct. Mater.*, 2009, **19**, 653–661.

266 S. A. Ghom, C. Zamani, S. Nazarpour, T. Andreu and J. R. Morante, Oxygen sensing with mesoporous ceria–zirconia solid solutions, *Sens. Actuators, B*, 2009, **140**, 216–221.

267 J.-H. Lee, Gas sensors using hierarchical and hollow oxide nanostructures: Overview, *Sens. Actuators, B*, 2009, **140**, 319–336.

268 H. Li, F. Meng, J. Liu, Y. Sun, Z. Jin, L. Kong, Y. Hu and J. Liu, Synthesis and gas sensing properties of hierarchical meso-macroporous SnO_2 for detection of indoor air pollutants, *Sens. Actuators, B*, 2012, **166–167**, 519–525.

269 Y. Li, W. Luo, N. Qin, J. Dong, J. Wei, W. Li, S. Feng, J. Chen, J. Xu, A. A. Elzatahry, M. H. Es-Saheb, Y. Deng and D. Zhao, Highly ordered mesoporous tungsten oxides with a large pore size and crystalline framework for H_2S sensing, *Angew. Chem., Int. Ed.*, 2014, **53**, 9035–9040.

270 Y. Shimizu, Y. Nakamura and M. Egashira, Effects of diffusivity of hydrogen and oxygen through pores of thick film SnO_2-based sensors on their sensing properties, *Sens. Actuators, B*, 1993, **13**, 128–131.

271 A. Kolmakov, D. O. Klenov, Y. Lilach, S. Stemmer and M. Moskovits, Enhanced gas sensing by individual SnO_2 nanowires and nanobelts functionalized with Pd catalyst particles, *Nano Lett.*, 2005, **5**, 667–673.

272 J. Ma, Y. Ren, X. Zhou, L. Liu, Y. Zhu, X. Cheng, P. Xu, X. Li, Y. Deng and D. Zhao, Pt nanoparticles sensitized ordered mesoporous WO_3 semiconductor: Gas sensing performance and mechanism study, *Adv. Funct. Mater.*, 2018, **28**, 1705268.

273 J. Zhang, D. Leng, L. Zhang, G. Li, F. Ma, J. Gao, H. Lu and B. Zhu, Porosity and oxygen vacancy engineering of mesoporous WO_3 nanofibers for fast and sensitive low-temperature NO_2 sensing, *J. Alloys Compd.*, 2021, **853**, 157339.

274 L. Zhang, Q. Fang, Y. Huang, K. Xu, P. K. Chu and F. Ma, Oxygen vacancy enhanced gas-sensing performance of CeO_2/graphene heterostructure at room temperature, *Anal. Chem.*, 2018, **90**, 9821–9829.

275 S. M. George, Atomic layer deposition: An overview, *Chem. Rev.*, 2010, **110**, 111–131.

276 S. R. Bishop, K. L. Duncan and E. D. Wachsman, Defect equilibria and chemical expansion in non-stoichiometric undoped and gadolinium-doped cerium oxide, *Electrochim. Acta*, 2009, **54**, 1436–1443.

277 A. S. Asundi, J. A. Raiford and S. F. Bent, Opportunities for atomic layer deposition in emerging energy technologies, *ACS Energy Lett.*, 2019, **4**, 908–925.

278 J. Lu, J. W. Elam and P. C. Stair, Atomic layer deposition—sequential self-limiting surface reactions for advanced catalyst "bottom-up" synthesis, *Surf. Sci. Rep.*, 2016, **71**, 410–472.

279 J. W. Elam, N. P. Dasgupta and F. B. Prinz, ALD for clean energy conversion, utilization, and storage, *MRS Bull.*, 2011, **36**, 899–906.

280 S. Neudeck, A. Mazilkin, C. Reitz, P. Hartmann, J. Janek and T. Brezesinski, Effect of low-temperature Al_2O_3 ALD coating on Ni-rich layered oxide composite cathode on the long-term cycling performance of lithium-ion batteries, *Sci. Rep.*, 2019, **9**, 5328.

281 A. C. Kozen, C.-F. Lin, A. J. Pearse, M. A. Schroeder, X. Han, L. Hu, S.-B. Lee, G. W. Rubloff and M. Noked, Next-generation lithium metal anode engineering *via* atomic layer deposition, *ACS Nano*, 2015, **9**, 5884–5892.

282 X. Meng, X.-Q. Yang and X. Sun, Emerging applications of atomic layer deposition for lithium-ion battery studies, *Adv. Mater.*, 2012, **24**, 3589–3615.

283 X. Wang and G. Yushin, Chemical vapor deposition and atomic layer deposition for advanced lithium ion batteries

and supercapacitors, *Energy Environ. Sci.*, 2015, **8**, 1889–1904.

284 B. Yan, X. Li, Z. Bai, X. Song, D. Xiong, M. Zhao, D. Li and S. Lu, A review of atomic layer deposition providing high performance lithium sulfur batteries, *J. Power Sources*, 2017, **338**, 34–48.

285 I. E. Rauda, V. Augustyn, L. C. Saldarriaga-Lopez, X. Chen, L. T. Schelhas, G. W. Rubloff, B. Dunn and S. H. Tolbert, Nanostructured pseudocapacitors based on atomic layer deposition of V_2O_5 onto conductive nanocrystal-based mesoporous ITO scaffolds, *Adv. Funct. Mater.*, 2014, **24**, 6717–6728.

286 C. Reitz, B. Breitung, A. Schneider, D. Wang, M. von der Lehr, T. Leichtweiss, J. Janek, H. Hahn and T. Brezesinski, Hierarchical carbon with high nitrogen doping level: A versatile anode and cathode host material for long-life lithium-ion and lithium–sulfur batteries, *ACS Appl. Mater. Interfaces*, 2016, **8**, 10274–10282.

287 A. Pandiyan, V. Di Palma, V. Kyriakou, W. M. M. Kessels, M. Creatore, M. C. M. van de Sanden and M. N. Tsampas, Enhancing the electrocatalytic activity of redox stable perovskite fuel electrodes in solid oxide cells by atomic layer-deposited Pt nanoparticles, *ACS Sustainable Chem. Eng.*, 2020, **8**, 12646–12654.

288 J. Dendooven, R. K. Ramachandran, E. Solano, M. Kurttepeli, L. Geerts, G. Heremans, J. Rongé, M. M. Minjauw, T. Dobbelaere, K. Devloo-Casier, J. A. Martens, A. Vantomme, S. Bals, G. Portale, A. Coati and C. Detavernier, Independent tuning of size and coverage of supported Pt nanoparticles using atomic layer deposition, *Nat. Commun.*, 2017, **8**, 1074.

289 J. Cai, J. Zhang, K. Cao, M. Gong, Y. Lang, X. Liu, S. Chu, B. Shan and R. Chen, Selective passivation of Pt nanoparticles with enhanced sintering resistance and activity toward CO oxidation *via* atomic layer deposition, *ACS Appl. Nano Mater.*, 2018, **1**, 522–530.

290 J. Lu, A perspective on new opportunities in atom-by-atom synthesis of heterogeneous catalysts using atomic layer deposition, *Catal. Lett.*, 2020, DOI: 10.1007/s10562-020-03412-8.

291 B. J. O'Neill, D. H. K. Jackson, J. Lee, C. Canlas, P. C. Stair, C. L. Marshall, J. W. Elam, T. F. Kuech, J. A. Dumesic and G. W. Huber, Catalyst design with atomic layer deposition, *ACS Catal.*, 2015, **5**, 1804–1825.

292 B. Zhang and Y. Qin, Interface tailoring of heterogeneous catalysts by atomic layer deposition, *ACS Catal.*, 2018, **8**, 10064–10081.

293 Z. Weng and F. Zaera, Atomic layer deposition (ALD) as a way to prepare new mixed-oxide catalyst supports: The case of alumina addition to silica-supported platinum for the selective hydrogenation of cinnamaldehyde, *Top. Catal.*, 2019, **62**, 838–848.

294 A. J. M. Mackus, M. A. Verheijen, N. Leick, A. A. Bol and W. M. M. Kessels, Influence of oxygen exposure on the nucleation of platinum atomic layer deposition: Consequences for film growth, nanopatterning, and nanoparticle synthesis, *Chem. Mater.*, 2013, **25**, 1905–1911.

295 N. Cheng, S. Stambula, D. Wang, M. N. Banis, J. Liu, A. Riese, B. Xiao, R. Li, T.-K. Sham, L.-M. Liu, G. A. Botton and X. Sun, Platinum single-atom and cluster catalysis of the hydrogen evolution reaction, *Nat. Commun.*, 2016, **7**, 13638.

296 F. Grillo, H. Van Bui, D. La Zara, A. A. I. Aarnink, A. Y. Kovalgin, P. Kooyman, M. T. Kreutzer and J. R. van Ommen, From single atoms to nanoparticles: Autocatalysis and metal aggregation in atomic layer deposition of Pt on TiO_2 nanopowder, *Small*, 2018, **14**, 1800765.

297 R. L. Puurunen, Surface chemistry of atomic layer deposition: A case study for the trimethylaluminum/water process, *J. Appl. Phys.*, 2005, **97**, 121301.

298 G. N. Parsons and R. D. Clark, Area-selective deposition: Fundamentals, applications, and future outlook, *Chem. Mater.*, 2020, **32**, 4920–4953.

299 A. J. M. Mackus, M. J. M. Merkx and W. M. M. Kessels, From the bottom-up: Toward area-selective atomic layer deposition with high selectivity, *Chem. Mater.*, 2019, **31**, 2–12.

300 P. Klement, D. Anders, L. Gümbel, M. Bastianello, F. Michel, J. Schörmann, M. T. Elm, C. Heiliger and S. Chatterjee, Surface diffusion control enables tailored aspect ratio nanostructures in area-selective atomic layer deposition, 2020, arXiv:2012.04465.

301 K. Kraffert, M. Karg, R. Schmack, G. Clavel, C. Boissiere, T. Wirth, N. Pinna and R. Kraehnert, Stabilization of mesoporous iron oxide films against sintering and phase transformations via atomic layer deposition of alumina and silica, *Adv. Mater. Interfaces*, 2018, **5**, 1800360.

302 Y. J. Pagán-Torres, J. M. R. Gallo, D. Wang, H. N. Pham, J. A. Libera, C. L. Marshall, J. W. Elam, A. K. Datye and J. A. Dumesic, Synthesis of highly ordered hydrothermally stable mesoporous niobia catalysts by atomic layer deposition, *ACS Catal.*, 2011, **1**, 1234–1245.

303 H. N. Pham, Y. J. Pagan-Torres, J. C. Serrano-Ruiz, D. Wang, J. A. Dumesic and A. K. Datye, Improved hydrothermal stability of niobia-supported Pd catalysts, *Appl. Catal., A*, 2011, **397**, 153–162.

304 C. Detavernier, J. Dendooven, S. P. Sree, K. F. Ludwig and J. A. Martens, Tailoring nanoporous materials by atomic layer deposition, *Chem. Soc. Rev.*, 2011, **40**, 5242–5253.

305 J. Dendooven, B. Goris, K. Devloo-Casier, E. Levrau, E. Biermans, M. R. Baklanov, K. F. Ludwig, P. Van Der Voort, S. Bals and C. Detavernier, Tuning the pore size of ink-bottle mesopores by atomic layer deposition, *Chem. Mater.*, 2012, **24**, 1992–1994.

306 P. Cop, M. Göttlicher, J. Schörmann, C. Boissiere, A. Beyer, C. Becker, K. Volz, H. Over and B. M. Smarsly, Atomic layer deposition of titania in ordered mesoporous cerium zirconium oxide thin films: A case study, *J. Phys. Chem. C*, 2019, **123**, 12851–12861.

307 J. Dendooven, K. Devloo-Casier, E. Levrau, R. Van Hove, S. Pulinthanathu Sree, M. R. Baklanov, J. A. Martens and C. Detavernier, *In situ* monitoring of atomic layer deposition in nanoporous thin films using ellipsometric porosimetry, *Langmuir*, 2012, **28**, 3852–3859.

308 J. Dendooven, K. Devloo-Casier, M. Ide, K. Grandfield, M. Kurttepeli, K. F. Ludwig, S. Bals, P. Van Der Voort and

C. Detavernier, Atomic layer deposition-based tuning of the pore size in mesoporous thin films studied by in situ grazing incidence small angle X-ray scattering, *Nanoscale*, 2014, **6**, 14991–14998.

309 Z. Weng, Z. Chen, X. Qin and F. Zaera, Sub-monolayer control of the growth of oxide films on mesoporous materials, *J. Mater. Chem. A*, 2018, **6**, 17548–17558.

310 S. Pulinthanathu Sree, J. Dendooven, J. Jammaer, K. Masschaele, D. Deduytsche, J. D'Haen, C. E. A. Kirschhock, J. A. Martens and C. Detavernier, Anisotropic atomic layer deposition profiles of TiO_2 in hierarchical silica material with multiple porosity, *Chem. Mater.*, 2012, **24**, 2775–2780.

311 Y.-B. Jiang, N. Liu, H. Gerung, J. L. Cecchi and C. J. Brinker, Nanometer-thick conformal pore sealing of self-assembled mesoporous silica by plasma-assisted atomic layer deposition, *J. Am. Chem. Soc.*, 2006, **128**, 11018–11019.

312 M. F. Zscherp, J. Glaser, C. Becker, A. Beyer, P. Cop, J. Schörmann, K. Volz and M. T. Elm, Epitaxial growth and structural characterization of ceria deposited by atomic layer deposition on high-surface porous yttria-stabilized zirconia thin films, *Cryst. Growth Des.*, 2020, **20**, 2194–2201.

313 S. Mahurin, L. Bao, W. Yan, C. Liang and S. Dai, Atomic layer deposition of TiO_2 on mesoporous silica, *J. Non-Cryst. Solids*, 2006, **352**, 3280–3284.

314 J. A. Libera, J. W. Elam and M. J. Pellin, Conformal ZnO coatings on high surface area silica gel using atomic layer deposition, *Thin Solid Films*, 2008, **516**, 6158–6166.

315 J. W. Elam, G. Xiong, C. Y. Han, H. H. Wang, J. P. Birrell, J. N. Hryn, M. J. Pellin, J. F. Poco and J. H. Satcher, Atomic layer deposition for the conformal coating of nanoporous materials, *MRS Proc.*, 2005, **876**, R12.

316 V. Cremers, R. L. Puurunen and J. Dendooven, Conformality in atomic layer deposition: Current status overview of analysis and modelling, *Appl. Phys. Rev.*, 2019, **6**, 21302.

317 D. R. G. Mitchell, D. J. Attard and G. Triani, Transmission electron microscopy studies of atomic layer deposition TiO_2 films grown on silicon, *Thin Solid Films*, 2003, **441**, 85–95.

318 P. Cop, E. Celik, K. Hess, Y. Moryson, P. Klement, M. T. Elm and B. M. Smarsly, Atomic layer deposition of nanometer-sized CeO_2 layers in ordered mesoporous ZrO_2 films and their impact on the ionic/electronic conductivity, *ACS Appl. Nano Mater.*, 2020, **3**, 10757–10766.

3.2. Publication II: Tailoring the Protonic Conductivity of Porous Yttria-stabilized Zirconia Thin Films by Surface Modification

In order to elucidate the influence of the surface properties on the electrical and protonic transport in metal oxides, porous YSZ thin films were prepared by PLD. The surface was coated with thin TiO_2 layers of different thickness using ALD. Electrochemical impedance spectroscopy (EIS) measurements of the pristine and TiO_2-coated YSZ were performed as a function of temperature, humidity or oxygen partial pressure. Several structural analysis methods, like SEM, TEM, GI-XRD and Raman spectroscopy were performed to support the detailed examination of the prepared TiO_2-YSZ composites.

Structural characterization reveals that the crystallinity of the titania layer can be adjusted by varying the thickness, which significantly affects the transport properties of the thin films as well as the oxygen partial pressure dependence of the ionic and electronic contributions in the composite material. EIS measurements under dry conditions as a function of temperature and oxygen partial pressure show that the total conductivity of porous YSZ increases by coating the surface with amorphous and crystalline titania layers of only a few nanometer thickness. The results reveal two transport regimes caused by additional transport pathways in the coating. Additionally, impedance measurements were performed under varying relative humidity. For the composite with a 6 nm thin amorphous TiO_2 layer, the protonic contribution is suppressed compared to the pristine YSZ thin film, whereas for the composite with a 18 nm thin crystalline TiO_2 layer, the protonic conductivity contribution increases again, caused by the different hydrophilic properties of the surfaces and the pore size. The underlying transport mechanisms are analyzed and discussed in the publication. This work highlights that transport properties can be tailored precisely by modifying the surface properties using ALD.

The experiments were designed and conducted by me with assistance from Rajendra S. Negi and Michele Bastianello. TEM measurements of the thin films were performed by Andrey Mazilkin. The porosity values were determined by Dominic Boll. The publication was written by me and edited by Torsten Brezesinski and Matthias T. Elm. Reprinted with permission from *Physical Chemistry Chemical Physics*. Copyright (2020) Royal Society of Chemistry.

Erdogan Celik, Rajendra S. Negi, Michele Bastianello, Dominic Boll, Andrey Mazilkin, Torsten Brezesinski and Matthias T. Elm, Tailoring the protonic conductivity of porous

yttria-stabilized zirconia thin films by surface modification, *Phys. Chem. Chem. Phys*., **2020**, 22, 11519-11528.

PCCP

ROYAL SOCIETY OF CHEMISTRY

PAPER

View Article Online
View Journal | View Issue

Check for updates

Cite this: *Phys. Chem. Chem. Phys.*, 2020, **22**, 11519

Tailoring the protonic conductivity of porous yttria-stabilized zirconia thin films by surface modification

Erdogan Celik,*[a] Rajendra S. Negi,[a] Michele Bastianello,[a] Dominic Boll,[b] Andrey Mazilkin,[b] Torsten Brezesinski[b] and Matthias T. Elm*[acd]

Received 25th March 2020,
Accepted 1st May 2020

DOI: 10.1039/d0cp01619e

rsc.li/pccp

Porous yttria-stabilized zirconia (YSZ) thin films were prepared by pulsed laser deposition to investigate the influence of specific surface area on the electronic, oxygen ion, and protonic transport properties. Electrochemical impedance spectroscopy was carried out as a function of temperature, oxygen activity and humidity of the surrounding atmosphere. At high humidity, protons on the surface of the porous YSZ thin films lead to increased conductivity, even for temperatures up to 700 °C. With increasing relative humidity, the activation energy of proton transport decreases because of changes in the transport mechanism from Grotthuss-type to vehicle-type transport. By coating the porous YSZ films with an amorphous titania (TiO_2) layer of only a few nanometer thickness using atomic layer deposition, the protonic contribution to conductivity is significantly reduced. Depositing an 18 nm-thick anatase TiO_2 surface layer, the protonic conductivity contribution increases again, which can be attributed to enhanced capillary condensation because of the lower pore size. Interestingly, the filling of pores is accompanied by a decrease in proton mobility. Theses results demonstrate the significant effect that the porosity and the surface properties have on the protonic transport and further provide new design principles for developing nanostructured proton-conducting oxides.

Introduction

Besides tailoring the composition, the properties of oxide ceramics can also be altered by nanostructuring,[1–4] *i.e.*, by increasing the density of interfaces, such as grain boundaries or free surface. The reason is that, because of the formation of a space charge region, the defect chemistry at interfaces differs significantly from that of the bulk,[5–10] resulting in changes in electronic and oxygen ion conductivity of the nanostructured material (especially when the interfaces dominate the overall behavior). Additionally, nanostructured oxides attracted much interest in recent years, since a significant increase in protonic conductivity at low temperatures has been reported for several materials, such as Y_2O_3-stabilized ZrO_2 (YSZ),[11–13] CeO_2[14–17] and TiO_2.[18–21] Because of their protonic conductivity at ambient conditions, these materials are interesting for applications as sensors,[22–24] in energy storage and conversion[12,25] or heterogeneous catalysis.[26]

Although there are many literature reports on proton conductivity in oxide materials, the transport mechanisms in fluorite-type oxides are still under debate. The measurements conducted on dense hydrated ceria and zirconia showed no evidence of proton conductivity,[14] indicating that proton transport in the bulk is negligible and the protonic conductivity in nanomaterials can be directly related to the nanostructure. In principle, it is not obvious whether a large specific surface area or a high grain boundary density is decisive for this effect. Studies by Avila-Paredes *et al.* and Chiodelli *et al.* suggested that the grain size has a significant effect on the protonic conductivity[15,27–29] and protonic transport occurs along the grain boundaries. On the other hand, a blocking behavior of the grain boundary for protons was reported, caused by the positively charged space charge region hindering proton transport.[30,31] However, most studies attribute the enhanced protonic conductivity at low and intermediate temperatures to the presence of transport paths along the pores and/or the inner sample surface.[12–14,32,33] Water molecules adsorbed at the surface can then contribute by two different transport mechanisms depending on the relative humidity in the

[a] *Center for Materials Research, Justus-Liebig-University Giessen, Heinrich-Buff Ring 16, 35392 Giessen, Germany. E-mail: Erdogan.Celik@materialwiss.uni-giessen.de, matthias.elm@phys.chemie.uni-giessen.de*
[b] *Institute of Nanotechnology, Karlsruhe Institute of Technology (KIT), Hermann-von-Helmholtz Platz 1, 76344 Eggenstein-Leopoldshafen, Germany*
[c] *Institute of Physical Chemistry, Justus-Liebig-University Giessen, Heinrich-Buff Ring 17, 35392 Giessen, Germany*
[d] *Institute of Experimental Physics I, Justus-Liebig-University Giessen, Heinrich-Buff Ring 16, 35392 Giessen, Germany*

surrounding atmosphere and the temperature. While for low water content and high temperatures a Grotthuss mechanism is responsible for protonic transport, at higher water partial pressure the proton conductivity arises from vehicle transport of H_3O^+ molecules.[11,13,33] Although a high surface area seems to be beneficial for protonic transport up to 500 °C,[11,12,34] the results on mesoporous YSZ thin films with a large specific surface area revealed no indication of proton conductivity, but instead a decrease in total conductivity under humidified atmosphere.[35] These results indicate that not only the surface area, but also the pore size and surface chemistry affect the protonic (surface) conductivity in nanostructured oxides.

Here, we report on the influence of surface modification on the protonic conductivity in porous YSZ thin films prepared by pulsed laser deposition (PLD). Because of their high surface-to-volume ratio, porous materials present an ideal model system to study the effect of surface on the transport properties. Furthermore, the surface properties can be tailored, which is useful to gain a basic understanding of the influence of free surface on the electrochemical properties. The electrochemical impedance measurements as a function of temperature and for different water contents in the atmosphere reveal that the porous YSZ thin films exhibit protonic conductivity contribution even at high temperatures of 700 °C. By surface coating with an amorphous titania ($aTiO_2$) film of about 6 nm thickness using atomic layer deposition (ALD), the protonic contribution is suppressed at temperatures above 120 °C. Increasing the thickness of the TiO_2 layer results in a crystalline TiO_2 ($cTiO_2$) coating and reduced pore size, which not only increases the surface protonic conductivity contribution again, but interestingly also results in a change in activation energy at high water content, thus indicating an altered proton transport mechanism. Overall, the results emphasize the significant effect that surface modification has on the protonic conductivity in porous oxide materials.

Experimental section

Porous thin films of 9.5 mol% YSZ were deposited on (0001)-oriented single-crystalline sapphire substrates using PLD at 10 Pa oxygen background pressure and 300 °C substrate temperature. The deposition was performed with a KrF-excimer laser, a repetition rate of 10 Hz, and with a distance of 6 cm between the substrate and the target. The laser fluence was set to about 2.3 J cm^{-2}. After deposition, the films were annealed for 3 days at 800 °C, resulting in a porous structure. After annealing, the films exhibit a thickness of approximately 70 nm. Interdigitated platinum microelectrodes[36] were prepared on the top surface of the porous thin films using photolithography. For this, a positive photoresist (ma-P 1215, micro resist technology GmbH) was used. The platinum electrodes with a thickness of 200 nm were deposited by electron-beam evaporation. The interdigitated electrodes used consist of 21 fingers of 3 mm length and 47 μm width, with the distance between the fingers being 33 μm.

For structural investigations, scanning electron microscopy (SEM) images were taken with a MERLIN from Carl Zeiss at 5 kV. The grazing incidence X-ray diffraction (GIXRD) measurements were performed at an angle of incidence of 1° on an X'Pert PRO MRD from PANalytical instruments (λ = 0.15406 nm). The Raman measurements were carried out on an inVia Raman microscope from Renishaw in backscattering geometry (λ = 633 nm). Electrochemical impedance spectroscopy (EIS) was performed in the frequency range from 10 MHz to 10 mHz at an AC amplitude of 100 mV using a Novocontrol Alpha-A impedance analyzer. The oxygen partial pressure in the gas atmosphere was controlled by gas mixtures of O_2 and Ar. The impedance spectra were evaluated using the software RelaxIS 3.[37]

TiO_2 was deposited by ALD on two YSZ thin films using an ALD R200 Standard system from Picosun. Titanium tetrachloride ($TiCl_4$) and water were used as precursors at a substrate temperature of 150 °C. Under these conditions, the growth rate of TiO_2 was determined to be 0.06 nm per cycle. The TiO_2 coatings had thicknesses of 6 and 18 nm. Transmission electron microscopy (TEM) was performed on an FEI Titan 80-300 aberration-corrected (image) microscope operated at 300 kV. The samples for TEM investigations were prepared using the FEI STRATA 400 S dual-beam system, with the Ga-ion beam operating at 30 kV, followed by final polishing at 2 kV for the surface quality improvement. Energy-filtered (EF) TEM was carried out with an image filter (Gatan Tridium 863) using the μ-probe EFTEM setup. The Zr M_{45}, O K and Ti L_{32} edges were used to determine the spatial distribution of the corresponding elements.

Structural characterization

Representative top view SEM images of the porous YSZ thin film before and after annealing at 800 °C are shown in Fig. 1(a and b), respectively. While the as-deposited YSZ thin film shows a relatively smooth surface, the material exhibits grains in the size range of 15 to 20 nm and increased porosity after the annealing step. Image processing using Otsu's method[38] revealed a porosity of 47% and an average pore size of (43 ± 2) nm.

To modify the surface properties and to vary the pore size, the porous YSZ thin films were coated with a TiO_2 layer of

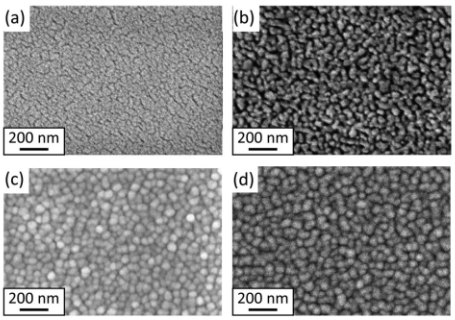

Fig. 1 SEM images of (a) as-deposited, (b) porous (annealed), (c) 6 nm and (d) 18 nm TiO_2 ALD-coated YSZ thin films.

thicknesses 6 and 18 nm using ALD. SEM images of the resulting thin films are shown in Fig. 1(c and d). It can clearly be seen that the pore size decreases compared to that of uncoated YSZ thin film shown in Fig. 1(b). The porosity estimated from the SEM images was 43% and 38%, respectively. Because of the TiO_2 coating, the average pore size was also significantly reduced to (29 ± 2) nm and (18 ± 2) nm, respectively.

Apart from SEM, the structural properties of the thin films were characterized by GIXRD. This method provides a way to avoid the strong reflections from the substrate and thus only the crystal structure of the material of interest is probed. The GIXRD pattern of an annealed YSZ thin film is shown in Fig. 2(a). Investigation of the coated YSZ films showed no differences because of the low thickness of the TiO_2 layer. The thin films exhibit the expected reflections of cubic YSZ according to the reference data.[39] The absence of additional reflections confirms the deposition of a single-phase material. Using the Scherrer equation,[40] the crystallite size was calculated to be about 17 nm, in good agreement with the values estimated from SEM imaging.

However, because of the small scattering factor of oxygen and the broad reflections caused by the small crystallites, it is difficult to distinguish between the cubic and the tetragonal phases of YSZ by XRD.[41,42] For reliable assessment of the crystal structure, the thin films were also probed using Raman spectroscopy. The Raman spectra of the uncoated and coated YSZ thin films are shown in Fig. 2(b). For the uncoated YSZ thin film and that with 6 nm TiO_2, only two modes are observed. The mode at

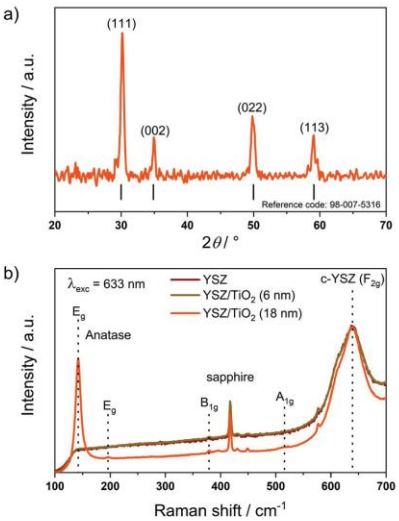

Fig. 2 (a) GIXRD pattern of porous (annealed) YSZ. For comparison, the reference pattern of cubic YSZ is also shown. (b) Raman spectra of porous (annealed) YSZ, YSZ/aTiO_2 (6 nm) and YSZ/cTiO_2 (18 nm).

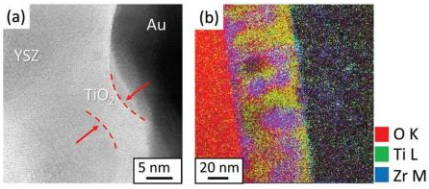

Fig. 3 (a) HRTEM image of YSZ/aTiO_2 (6 nm) and (b) EFTEM image demonstrating the uniformity of the amorphous titania coating.

420 cm^{-1} arises from the sapphire substrate,[43,44] while the second mode (F_{2g}) at about 640 cm^{-1} is characteristic of the cubic fluorite-type phase of YSZ.[35,45] No indication of the TiO_2 coating is observed, thus suggesting deposition of an amorphous (aTiO_2) layer. The YSZ thin film coated with 18 nm TiO_2 exhibits four additional modes at 143 [$E_g(1)$], 196 [$E_g(2)$], 379 [B_{1g}] and 516 cm^{-1} [A_{1g}], confirming the successful deposition of anatase TiO_2 (cTiO_2) with tetragonal symmetry.[46–48] From the literature, it is known that, below a critical thickness of approximately 6 nm, ALD-derived titania layers are amorphous in nature,[49] in agreement with the Raman results.

To confirm the successful coating of the surface, HRTEM measurements were performed. In Fig. 3(a), the HRTEM image is shown for the YSZ sample with a 6 nm-thick TiO_2 coating. The absence of any crystalline phase in the TiO_2 layer corroborates the amorphous structure. Furthermore, the EFTEM image shown in Fig. 3(b) indicates conformal and homogenous surface coating of the pores in the YSZ thin film.

Electrochemical characterization

Dry atmosphere. The electrical conductivity of the porous YSZ thin film was investigated by impedance spectroscopy in the temperature range between 200 and 700 °C and for varying oxygen partial pressure and humidity. Representative impedance spectra (Nyquist representation) recorded at ambient oxygen partial pressure, *i.e.*, $\lg(p(O_2)) = -0.67$, at 965 K under dry and ambient atmospheres are shown in Fig. 4. Under dry conditions and at low temperatures, a nearly ideal semicircle is observed at high frequencies. With increasing temperature, the Nyquist plot shows the onset of a second semicircle at low frequencies (not shown) and, finally, at high temperatures [Fig. 4(a)], a third semicircle is observed. Under ambient conditions, *i.e.*, 20.2% relative humidity [Fig. 4(b)], the resistance of the high-frequency semicircle is significantly reduced, indicating that the humidity has a significant effect on the transport properties, even at high temperatures.

To determine the total resistance of the thin films, the impedance spectra were fitted using an equivalent circuit consisting of three RQ elements in series (solid lines in Fig. 4). For the high frequency semicircle, a capacitance of about 5×10^{-12} F was determined, while for the second semicircle a capacitance of about 9×10^{-11} F is found. The first semicircle can be attributed to the response of the bulk material, which typically shows capacitances between 10^{-12}

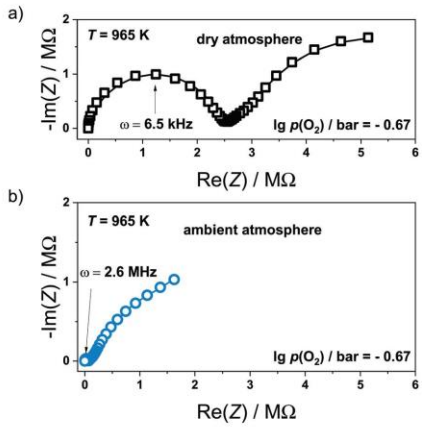

Fig. 4 Impedance spectra of porous (annealed) YSZ at high temperature and under dry (black) and ambient atmosphere conditions (blue).

and 10^{-10} F. The second semicircle corresponds to the response of the grain boundaries, exhibiting capacitances in the range between 10^{-10} and 10^{-8} F depending on the grain size.[50–53] For nanostructured materials, the capacity typically shifts to lower values, often resulting in an overlap of the bulk and the grain boundary semicircles.[1,35] The semicircle at low frequency with a capacitance of about 1×10^{-7} F corresponds to the electrochemical response of the electrode–electrolyte interface.[37,50] As the scope of this study is to take a closer look on the transport processes of the electrolyte, we did not investigate the electrode processes in detail. The total conductivity was calculated from the total resistance R, *i.e.*, the bulk and the grain boundary resistance, according to:

$$\sigma = \frac{1}{R}\frac{l}{bd} \tag{1}$$

where l denotes the electrode distance, b is the electrode length and d is the thickness of the porous thin film. Note that, by using eqn (1), the porosity is neglected, *i.e.*, a dense thin film is assumed. Thus, the obtained values underestimate the total conductivity and should be rather seen as a kind of lower limit.

The temperature dependence of the total conductivity of the porous YSZ thin film under the dry atmosphere and for varying humidity is presented in Fig. 5(a). At dry conditions, the conductivity shows a linear Arrhenius-type behavior over the whole temperature range, caused by a dominant oxygen ion conductivity. The high oxygen ion conductivity in YSZ arises from the isoelectric doping of zirconia with yttria, generating oxygen vacancies ($V_O^{\bullet\bullet}$) to maintain charge neutrality. Using Kroeger–Vink notation, the doping is described by:[54,55]

$$Y_2O_3 \xrightarrow{ZrO_2} 2Y'_{Zr} + V_O^{\bullet\bullet} + 3O_O^{\times} \tag{2}$$

where Y'_{Zr} denotes an Y^{3+} in the Zr^{4+} lattice site with a relative charge of -1 and $V_O^{\bullet\bullet}$ is the vacancy in the oxygen lattice site with a relative charge of +2. $O_O^{\times}$ denotes the lattice oxygen with a

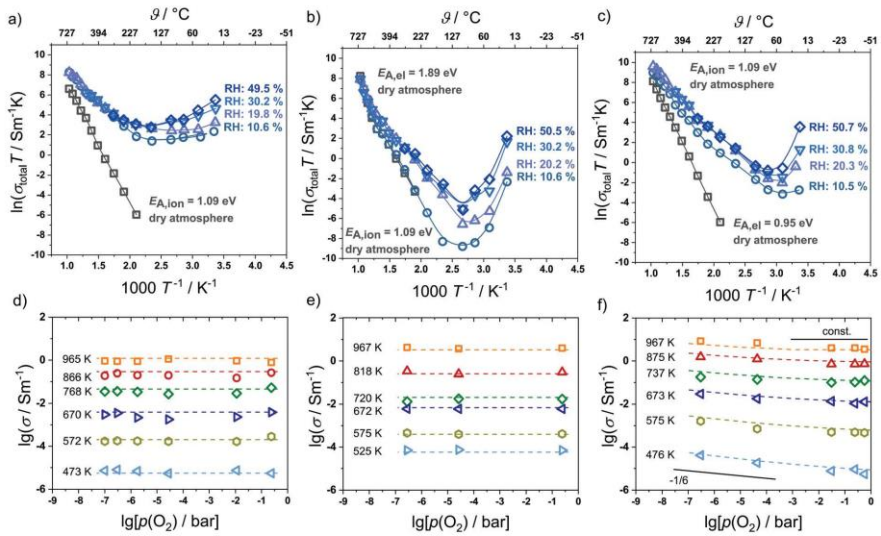

Fig. 5 Arrhenius plots of the total conductivity for (a) porous (annealed) YSZ, (b) YSZ/aTiO_2 (6 nm) and (c) YSZ/cTiO_2 (18 nm). Oxygen partial pressure dependence of the total conductivity for (d) porous (annealed) YSZ, (e) YSZ/aTiO_2 (6 nm) and (f) YSZ/cTiO_2 (18 nm).

charge of zero. By changing the oxygen partial pressure, the conductivity remains constant as shown in Fig. 5(d), also confirming that the oxygen ions are the dominant charge carriers.[35,54]

The total conductivity $\sigma(T)$ of the YSZ thin film is given by:

$$\sigma(T) = \frac{\sigma_{0,\mathrm{ion}}}{T}\exp\left(-\frac{E_{\mathrm{A,ion}}}{k_{\mathrm{B}}T}\right) \quad (3)$$

where k_{B} is the Boltzmann constant, $E_{\mathrm{A,ion}}$ is the activation energy representing the migration enthalpy of the oxygen ions ΔH_{mig}, and $\sigma_{0,\mathrm{ion}}$ is the conductivity pre-factor of the oxygen ions. By fitting the linear behavior in the Arrhenius representation using the expression:

$$\ln(\sigma T) = \ln\sigma_{0,\mathrm{ion}} - \frac{E_{\mathrm{A}}}{k_{\mathrm{B}}T} \quad (4)$$

an activation energy $E_{\mathrm{A,ion}} = (1.09 \pm 0.03)$ eV was determined, which is in good agreement with values in the range of 0.8–1.2 eV typically reported for oxygen ion conductivity in YSZ.[54,56–58] For the conductivity pre-factor, a value of $\sigma_{0,\mathrm{ion}} = 5.7 \times 10^8$ S K m^{-1} was obtained. The fits according to eqn (3) are shown in Fig. 5(d) as dashed lines.

After ALD coating with 6 nm amorphous TiO_2 (aTiO_2), the porous thin film reveals a distinct change in the temperature dependence of conductivity. Two transport regimes with different activation energies are observed in the Arrhenius representation, as shown in Fig. 5(b).

At low temperatures, the transport is again dominated by oxygen vacancies, as confirmed by a constant conductivity with varying oxygen partial pressure. Above 500 °C, the activation energy significantly increases, which is attributed to an additional conductivity contribution arising from electrical transport in the aTiO_2 layer. The total conductivity is then given by:

$$\sigma_{\mathrm{tot}}(T) = \frac{\sigma_{0,\mathrm{ion}}}{T}\exp\left(-\frac{E_{\mathrm{A,ion}}}{k_{\mathrm{B}}T}\right) + \sigma_{0,\mathrm{el}}\exp\left(-\frac{E_{\mathrm{A,el}}}{k_{\mathrm{B}}T}\right) \quad (5)$$

where $E_{\mathrm{A,el}}$ and $\sigma_{0,\mathrm{el}}$ are the activation energy and the conductivity pre-factor of the electronic charge carriers, respectively. In amorphous semiconductors, electrical transport at high temperatures arises from thermal activation of electrons from the valence band mobility edge to the conduction band mobility edge, *i.e.*, the formation of an electron–hole pair. The activation energy is then given by:[59]

$$E_{\mathrm{A,el}} \approx \frac{E_{\mathrm{g}}}{2} \quad (6)$$

with E_{g} being the band gap of the material. Using eqn (5), the fit to the experimental data shown as dashed lines in Fig. 5(e) revealed an activation energy $E_{\mathrm{A,ion}} = (1.09 \pm 0.05)$ eV for the ionic conductivity contribution, in agreement with the uncoated YSZ thin film, and a slightly higher pre-factor $\sigma_{0,\mathrm{ion}} = (8 \pm 0.2) \times 10^8$ S K m^{-1}. For the electronic contribution, an activation energy $E_{\mathrm{A,el}} = (1.89 \pm 0.02)$ eV and a pre-factor $\sigma_{0,\mathrm{el}} = 7.5 \times 10^9$ S K m^{-1} were determined. Amorphous TiO_2 exhibits an energetic band energy of approximately 3.3–3.5 eV[60,61] and, thus, an activation energy of 1.7–1.8 eV is expected, which is in good agreement with the observed value of 1.89 eV.

Finally, Fig. 5(c) shows the temperature dependence of conductivity for the porous YSZ thin film coated with 18 nm TiO_2. Again, two transport regimes of different activation energy are observed under dry conditions, although their difference is not as pronounced as for the sample with the 6 nm TiO_2 coating. In Fig. 5(f), the $p(O_2)$-dependence is shown for the conductivity in the investigated temperature range. At low temperatures, the conductivity decreases, with the characteristic −1/6 Brouwer slope for increasing $p(O_2)$. At high temperatures, a decrease in conductivity is only observed for low oxygen partial pressures, while at high $p(O_2)$, the conductivity remains constant. The observed behavior is again attributed to an additional electronic contribution of the cTiO_2 coating to the total conductivity of the porous YSZ thin film, as the observed slope of −1/6 is typical of anatase under reducing conditions.[62–64] In this regime, oxygen vacancies are formed in TiO_2 which is accompanied by an increase in electron concentration. In Kroeger–Vink notation, the reduction reaction can be written as:

$$\mathrm{O_O^\times} \rightleftharpoons \mathrm{V_O^{\bullet\bullet}} + 2e' + 1/2\mathrm{O_2} \quad (7)$$

with the equilibrium constant

$$K_{\mathrm{Red}} = K_0\exp\left(-\frac{\Delta G_{\mathrm{f}}}{k_{\mathrm{B}}T}\right) = [\mathrm{V_O^{\bullet\bullet}}][e']^2 p(\mathrm{O_2})^{\frac{1}{2}} \quad (8)$$

where ΔG_{f} denotes the Gibbs free enthalpy for the formation of oxygen vacancies. Using the Brouwer approximation for this regime, $[e'] = 2[\mathrm{V_O^{\bullet\bullet}}]$, the increase in electron concentration as a function of oxygen partial pressure is given by:[62]

$$[e'] \propto p(\mathrm{O_2})^{-\frac{1}{6}} \quad (9)$$

While at low oxygen partial pressure the electrons dominate the overall conductivity, as shown in Fig. 5(f), at high temperatures and oxygen partial pressure, the constant conductivity arises from the ionic plateau of the porous YSZ. Thus, the total conductivity of the 18 nm TiO_2-coated YSZ thin film is given by:

$$\sigma_{\mathrm{tot}}(T) = \sigma_{\mathrm{ion}}(T) + \sigma_{\mathrm{elec}}(T) \propto \frac{\sigma_{0,\mathrm{ion}}}{T}\exp\left(-\frac{E_{\mathrm{A,ion}}}{k_{\mathrm{B}}T}\right) + \frac{\sigma'_{0,\mathrm{el}}}{T}\exp\left(-\frac{E_{\mathrm{A,el}}}{k_{\mathrm{B}}T}\right)p(\mathrm{O_2})^{-\frac{1}{6}} \quad (10)$$

where $E_{\mathrm{A,ion}}$ is the migration enthalpy of the oxygen ions and $E_{\mathrm{A,el}} = \Delta H_{\mathrm{f}}/3$ is the activation energy related to the formation enthalpy ΔH_{f} of the titania layer. The fit to the total conductivity using eqn (10) is shown as solid lines in Fig. 5(c). For the oxygen ions, an activation energy $E_{\mathrm{A,ion}} = (1.09 \pm 0.2)$ eV is obtained, again in good agreement with the value determined for the uncoated sample. The electronic contribution shows an activation energy $E_{\mathrm{A,el}} = (0.95 \pm 0.03)$ eV, which is in the range of 0.89–0.98 eV reported for porous anatase,[65,66] thereby confirming the additional electronic contribution of the surface coating to the total conductivity of the coated YSZ thin film. The pre-factors are $\sigma_{0,\mathrm{ion}} = 1 \times 10^9$ S K m^{-1} and $\sigma'_{0,\mathrm{el}} = 2.1 \times 10^7$ S K bar$^{1/6}$ m^{-1}.

Humid atmosphere

To study the influence of porosity and surface coating on the protonic conductivity, the electrochemical impedance measurements were performed under varying relative humidity (RH) in the same temperature range. As shown in Fig. 5(a), the porous YSZ thin film exhibits a significant increase in conductivity even for a low RH of 10.6%. The presence of humidity leads to the formation of a water film at the free surface and thus to protonic surface conductivity, which increases with increasing RH by several orders of magnitude, in agreement with reports available in literature.[12–15,18,20] At temperatures above 150 °C and/or low humidity, only chemisorbed layers exist, consisting of hydroxyl groups bonded to the oxide and relatively strong hydrogen bonded water molecules.[11,13,67] The chemisorbed species are reported to be stable up to 600 °C and 200 °C, respectively.[11,13,33,67] The mechanism for the adsorption of water on an ideal surface is given by:[11]

$$\text{Zr–O–Zr} + H_2O \leftrightarrow \text{Zr–O} + \text{Zr–OH}_2 \leftrightarrow \text{Zr–OH} + \text{Zr–OH} \quad (11)$$

However, also surface defects, such as oxygen vacancies, play a significant role in the formation of surface protons, as water fills the oxygen vacancies and forms hydroxyl groups.[68–70] In Kroeger–Vink notation, their formation is given by the reaction:[15,35,71,72]

$$H_2O_{(g)} + V_O^{\bullet\bullet} + O_O^{\times} \leftrightarrow 2(OH)_O^{\bullet} \quad (12)$$

In the chemisorbed layer, the proton transport is expected to occur because of the formation of defects and proton hopping (Grotthuss-type mechanism):[11]

$$2[\text{Zr–OH}] \leftrightarrow \text{ZrOH}_2^{+} + \text{ZrO}^{-} \quad (13)$$

By combining eqn (9) and (10), the water partial pressure dependence of the protonic defects is given by:[17,34,72]

$$[\text{Zr–OH}_2^{+}] \propto [\text{Zr–OH}] \propto p_{H_2O}^{1/2} \quad (14)$$

The conductivity as a function of water partial pressure is shown in Fig. 6. As the conductivity is proportional to the charge carrier defects, the observed slope of approximately 1/2 confirms a dominant protonic conductivity under humidified conditions.

At lower temperatures, the physisorption of water molecules takes place and, at a RH ≈ 30%, an "ice-like" layer with an additional physisorbed layer is formed. With increasing RH, the number of physisorbed water layers further increases and, for RH > 60%, the transport is expected to take place by hydronium ions *via* vehicle mechanism.[11,13,33]

$$\text{Zr–OH}_2 + H_2O \leftrightarrow \text{Zr–OH}^{-} + H_3O^{+} \quad (15)$$

Interestingly, for the porous thin films studied in this work, the protonic contribution is significantly higher compared to other literature reports.[12,13,15] For example, even at 700 °C, a protonic contribution is clearly observed, while typically an increase in conductivity under humidified conditions is only found for temperatures up to 400 °C.

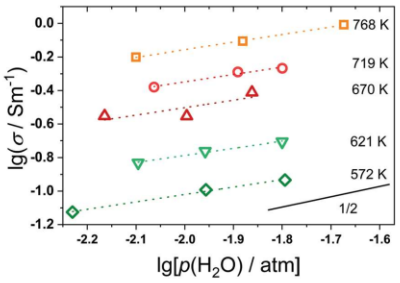

Fig. 6 Protonic conductivity of porous (annealed) YSZ depending on the water vapor partial pressure.

The large increase in protonic conductivity indicates that the nanostructure and the pore size are crucial for the incorporation of water and the transport of protons along inner surfaces of the oxide, in agreement with previous studies. Miyoshi *et al.* observed a comparable protonic contribution up to 650 °C for nano-grained YSZ.[33,34] They attributed the high conductivity under "wet" conditions to hopping transport of protons in interfacial hydrated layers within the YSZ material. Likewise, Gregori *et al.* ascribed the protonic conductivity of nanocrystalline samples to the presence of a water layer formed in residual pore openings due to capillary condensation.[14] However, sol–gel derived YSZ thin films with an average pore size of 24 nm revealed no signs of proton conduction at temperatures above 250 °C. Instead, a reduction of oxygen ion conductivity was found, which was attributed to the annihilation of oxygen ion vacancies at the surface due to water adsorption and the formation of hydroxyl ions.[35]

The situation changes completely when the surface of the porous YSZ thin film is coated with a TiO_2 layer, as shown in Fig. 5(b and c). Although the pore size is decreased in these samples, *i.e.*, capillary condensation should be more favorable, the coated YSZ thin films exhibit a significantly reduced protonic conductivity compared to the as-prepared porous YSZ thin film. At temperatures above 400 °C, YSZ/aTiO_2 (6 nm) shows no protonic conductivity contribution anymore and, in the temperature range between 150 and 400 °C, the proton conductivity is only observed for RH > 10%. At lower temperatures, an increase in conductivity with decreasing temperature and increasing RH is found, as typically observed for porous TiO_2.[18–21] In the case of YSZ/cTiO_2 (18 nm), the protonic conductivity increases again with a protonic contribution even at temperatures above 400 °C, as shown in Fig. 5(c), but it still remains lower compared to the uncoated thin film.

The decrease in conductivity compared to the uncoated material is attributed to the different hydrophilic properties of the TiO_2 surfaces. While water on YSZ surfaces is adsorbed mainly in its dissociative form,[67] the TiO_2 surfaces are predominantly covered by molecular water.[73] Thus, the TiO_2 surfaces exhibit a lower coverage with hydroxyl groups, which are responsible for the proton conduction in the chemisorbed layer.[11]

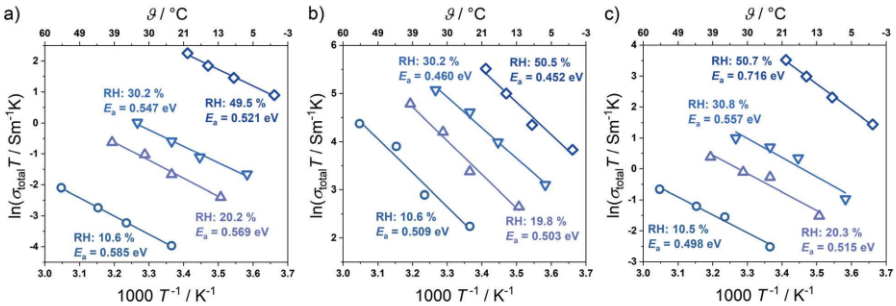

Fig. 7 Determination of the activation energy of protonic conduction for temperatures below 100 °C: (a) porous (annealed) YSZ, (b) YSZ/aTiO_2 (6 nm) and (c) YSZ/cTiO_2 (18 nm).

This behavior can be attributed mainly to the reduced amount of oxygen vacancies on TiO_2 surfaces compared to YSZ, which act as active sites for water adsorption.[69,70,74] Furthermore, DFT calculations suggest that on amorphous TiO_2 the adsorption of hydroxyl groups is even less favorable compared to anatase TiO_2,[75] which is also supported by the lower protonic conductivity in the case of the amorphous coating, especially at higher temperatures. However, water condensation in the pores may also play a role in the higher protonic conductivity in the case of the YSZ thin film with the crystalline TiO_2 (note that the pore size is also reduced due to the coating).

To gain further insights into the transport mechanism, the conductivity at fixed RH was plotted as a function of the inverse temperature (Fig. 7). For all three samples and RHs tested, a linear Arrhenius-type behavior is found, where the activation energy depends on the enthalpies of defect formation ΔH_D and mobility ΔH_{mob}.[11,13]

$$E_A = \frac{1}{2}\Delta H_D + \Delta H_{mob} \quad (16)$$

The activation energy of the transport process was determined by linear fitting of $\log(\sigma T)$ *versus* the reciprocal temperature $1/T$ and is shown as a function of RH in Fig. 8. At 10% RH, the YSZ thin film exhibits an activation energy of about 0.59 eV, which decreases with increasing RH. Comparable values for the activation energy of proton transport in porous YSZ (varying between 0.3 and 0.6 eV) and a decrease in E_A with increasing RH were reported by other groups.[11,13,34] Stub *et al.* interpreted the linear decrease in E_A with a change in the dominant transport mechanism from Grotthuss-type to vehicle-type transport, which was supported by measurements of the apparent proton transference number.[13]

However, a change in defect formation enthalpy with RH may also affect E_A. For the porous YSZ thin film coated with amorphous TiO_2, the same behavior is observed, in agreement with other reports available in literature,[20] indicating the same change in dominant transport mechanism, as observed for the uncoated YSZ. However, a slightly reduced activation energy of 0.5 eV is determined at low RH. The lower activation energy

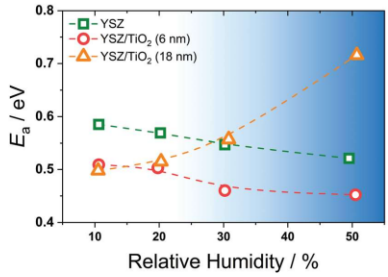

Fig. 8 Activation energy as a function of relative humidity for porous (annealed) YSZ, (b) YSZ/aTiO_2 (6 nm) and (c) YSZ/cTiO_2 (18 nm).

compared to pristine YSZ is attributed to a lower ΔH_D, as the same value is also observed for the thin film coated with anatase TiO_2. Interestingly, the activation energy is found to increase with increasing RH for YSZ/cTiO_2 (18 nm). A similar finding was made by Vichi *et al.*,[19] who also studied protonic conductivity in mesoporous TiO_2. They attributed the change in activation energy to a decrease in mobility, *i.e.*, an increase in ΔH_{mob} caused by complete filling of the pores. In the pores, the water molecules form bridges between the hydrated pore walls, leading to the observed decrease in mobility. The same should be true for the anatase-coated YSZ thin film, as the pore size is significantly reduced by the 18 nm-thick coating.

Conclusions

To investigate the influence of free surface on the electronic, oxygen ion and protonic transport properties in oxides, porous YSZ thin films were prepared by PLD and characterized using electrochemical impedance spectroscopy. Under high humidity conditions, the porous YSZ revealed a significant increase in total conductivity due to protonic transport taking place at the surface. Modifying the surface by depositing an amorphous TiO_2 layer of 6 nm thickness using ALD resulted in an

additional electronic transport pathway in the coating under dry atmosphere, while under humidified conditions, the protonic conductivity contribution was significantly suppressed. After deposition of an 18 nm-thick anatase coating, the protonic conductivity increased again because of filling of the reduced-size pores with water. Furthermore, with increasing humidity, the activation energy of the transport process also increased, which is attributed to a decrease in proton mobility when the pores are filled with water. The results demonstrate that not only the porosity but also the surface properties have a strong effect on the protonic transport, which may help in designing and optimizing proton-conducting (nanoscale) oxides for technological applications through tailored surface modification.

Conflicts of interest

There are no conflicts to declare.

Acknowledgements

We thank Karlsruhe Nano Micro Facility (KNMF), a Helmholtz Research Infrastructure at Karlsruhe Institute of Technology (KIT) for TEM. Financial support by the German Research Foundation (to T. B., grant no. BR 3499/5-1 and to M. T. E., grant no. EL 863/3-1) is gratefully acknowledged. M. T. E., R. S. N. and M. B. thank the German Federal Ministry of Education and Research (BMBF) for funding of the NanoMatFutur project NiKo (03XP0093).

References

1 H. L. Tuller, Ionic conduction in nanocrystalline materials, *Solid State Ionics*, 2000, **131**, 143–157.
2 J. Maier, On the Conductivity of Polycrystalline Materials, *Ber. Bunsenges. Phys. Chem.*, 1986, **90**, 26–33.
3 J. Maier, Pushing Nanoionics to the Limits: Charge Carrier Chemistry in Extremely Small Systems, *Chem. Mater.*, 2014, **26**, 348–360.
4 J. Maier, Nanoionics: ion transport and electrochemical storage in confined systems, *Nat. Mater.*, 2005, **4**, 805–815.
5 G. Gregori, R. Merkle and J. Maier, Ion conduction and redistribution at grain boundaries in oxide systems, *Prog. Mater. Sci.*, 2017, **89**, 252–305.
6 J. Maier, Ionic conduction in space charge regions, *Prog. Solid State Chem.*, 1995, **23**, 171–263.
7 J. Maier, Thermodynamics of Nanosystems with a Special View to Charge Carriers, *Adv. Mater.*, 2009, **21**, 2571–2585.
8 A. Tschöpe, E. Sommer and R. Birringer, Grain size-dependent electrical conductivity of polycrystalline cerium oxide: I. Experiments, *Solid State Ionics*, 2001, **139**, 255–265.
9 X. Guo and R. Waser, Space charge concept for acceptor-doped zirconia and ceria and experimental evidences, *Solid State Ionics*, 2004, **173**, 63–67.
10 J. Yue, C. Suchomski, P. Voepel, R. Ellinghaus, M. Rohnke, T. Leichtweiss, M. T. Elm and B. M. Smarsly, Mesoporous niobium-doped titanium dioxide films from the assembly of crystalline nanoparticles: study on the relationship between the band structure, conductivity and charge storage mechanism, *J. Mater. Chem. A*, 2017, **5**, 1978–1988.
11 S. Raz, K. Sasaki, J. Maier and I. Riess, Characterization of adsorbed water layers on Y_2O_3-doped ZrO_2, *Solid State Ionics*, 2001, **143**, 181–204.
12 B. Scherrer, M. V. F. Schlupp, D. Stender, J. Martynczuk, J. G. Grolig, H. Ma, P. Kocher, T. Lippert, M. Prestat and L. J. Gauckler, On Proton Conductivity in Porous and Dense Yttria Stabilized Zirconia at Low Temperature, *Adv. Funct. Mater.*, 2013, **23**, 1957–1964.
13 S. Ø. Stub, E. Vøllestad and T. Norby, Mechanisms of Protonic Surface Transport in Porous Oxides: Example of YSZ, *J. Phys. Chem. C*, 2017, **121**, 12817–12825.
14 G. Gregori, M. Shirpour and J. Maier, Proton Conduction in Dense and Porous Nanocrystalline Ceria Thin Films, *Adv. Funct. Mater.*, 2013, **23**, 5861–5867.
15 H. J. Avila-Paredes, C.-T. Chen, S. Wang, R. A. De Souza, M. Martin, Z. Munir and S. Kim, Grain boundaries in dense nanocrystalline ceria ceramics: exclusive pathways for proton conduction at room temperature, *J. Mater. Chem.*, 2010, **20**, 10110–10112.
16 M. Shirpour, G. Gregori, R. Merkle and J. Maier, On the proton conductivity in pure and gadolinium doped nanocrystalline cerium oxide, *Phys. Chem. Chem. Phys.*, 2011, **13**, 937–940.
17 E. Ruiz-Trejo and J. A. Kilner, Possible proton conduction in $Ce_{0.9}Gd_{0.1}O_{2-\delta}$ nanoceramics, *J. Appl. Electrochem.*, 2009, **39**, 523–528.
18 I. G. Tredici, F. Maglia, C. Ferrara, P. Mustarelli and U. Anselmi-Tamburini, Mechanism of Low-Temperature Protonic Conductivity in Bulk, High-Density, Nanometric Titanium Oxide, *Adv. Funct. Mater.*, 2014, **24**, 5137–5146.
19 F. M. Vichi, M. I. Tejedor-Tejedor and M. A. Anderson, Effect of Pore-Wall Chemistry on Proton Conductivity in Mesoporous Titanium Dioxide, *Chem. Mater.*, 2000, **12**, 1762–1770.
20 M. T. Colomer, Nanoporous Anatase Thin Films as Fast Proton-Conducting Materials, *Adv. Mater.*, 2006, **18**, 371–374.
21 F. Maglia, I. G. Tredici, G. Spinolo and U. Anselmi-Tamburini, Low temperature proton conduction in bulk nanometric TiO2 prepared by high-pressure field assisted sintering, *J. Mater. Res.*, 2012, **27**, 1975–1981.
22 L. Almar, A. Tarancón, T. Andreu, M. Torrell, Y. Hu, G. Dezanneau and A. Morata, Mesoporous ceramic oxides as humidity sensors: A case study for gadolinium-doped ceria, *Sens. Actuators, B*, 2015, **216**, 41–48.
23 H. Farahani, R. Wagiran and N. M. Hamidon, *Sensors*, 2014, 14.
24 X. Q. Fu, C. Wang, H. C. Yu, Y. G. Wang and T. H. Wang, Fast humidity sensors based on CeO_2 nanowires, *Nanotechnology*, 2007, **18**, 145503.
25 S. Kim, U. Anselmi-Tamburini, H. J. Park, M. Martin and Z. A. Munir, Unprecedented Room-Temperature Electrical Power Generation Using Nanoscale Fluorite-Structured Oxide Electrolytes, *Adv. Mater.*, 2008, **20**, 556–559.

26 R. Manabe, S. Okada, R. Inagaki, K. Oshima, S. Ogo and Y. Sekine, Surface Protonics Promotes Catalysis, *Sci. Rep.*, 2016, **6**, 38007.
27 S. Kim, H. J. Avila-Paredes, S. Wang, C.-T. Chen, R. A. De Souza, M. Martin and Z. A. Munir, On the conduction pathway for protons in nanocrystalline yttria-stabilized zirconia, *Phys. Chem. Chem. Phys.*, 2009, **11**, 3035–3038.
28 H. J. Avila-Paredes, J. Zhao, S. Wang, M. Pietrowski, R. A. De Souza, A. Reinholdt, Z. A. Munir, M. Martin and S. Kim, Protonic conductivity of nano-structured yttria-stabilized zirconia: dependence on grain size, *J. Mater. Chem.*, 2010, **20**, 990–994.
29 G. Chiodelli, F. Maglia, U. Anselmi-Tamburini and Z. A. Munir, Characterization of low temperature protonic conductivity in bulk nanocrystalline fully stabilized zirconia, *Solid State Ionics*, 2009, **180**, 297–301.
30 W. C. Chueh, C.-K. Yang, C. M. Garland, W. Lai and S. M. Haile, Unusual decrease in conductivity upon hydration in acceptor doped, microcrystalline ceria, *Phys. Chem. Chem. Phys.*, 2011, **13**, 6442–6451.
31 S. Ø. Stub, E. Vøllestad and T. Norby, Protonic surface conduction controlled by space charge of intersecting grain boundaries in porous ceramics, *J. Mater. Chem. A*, 2018, **6**, 8265–8270.
32 S. Ø. Stub, K. Thorshaug, P. M. Rørvik, T. Norby and E. Vøllestad, The influence of acceptor and donor doping on the protonic surface conduction of TiO_2, *Phys. Chem. Chem. Phys.*, 2018, **20**, 15653–15660.
33 S. Miyoshi, Y. Akao, N. Kuwata, J. Kawamura, Y. Oyama, T. Yagi and S. Yamaguchi, Low-Temperature Protonic Conduction Based on Surface Protonics: An Example of Nanostructured Yttria-Doped Zirconia, *Chem. Mater.*, 2014, **26**, 5194–5200.
34 S. Miyoshi, Y. Akao, N. Kuwata, J. Kawamura, Y. Oyama, T. Yagi and S. Yamaguchi, Water uptake and conduction property of nano-grained yttria-doped zirconia fabricated by ultra-high pressure compaction at room temperature, *Solid State Ionics*, 2012, **207**, 21–28.
35 M. T. Elm, J. D. Hofmann, C. Suchomski, J. Janek and T. Brezesinski, Ionic Conductivity of Mesostructured Yttria-Stabilized Zirconia Thin Films with Cubic Pore Symmetry—On the Influence of Water on the Surface Oxygen Ion Transport, *ACS Appl. Mater. Interfaces*, 2015, **7**, 11792–11801.
36 J. L. Hertz and H. L. Tuller, Electrochemical Characterization of Thin Films for a Micro-Solid Oxide Fuel Cell, *J. Electroceram.*, 2004, **13**, 663–668.
37 J. J. Neumeier, M. T. Elm, B. Luerßen and J. Janek, Platinum microelectrodes on gadolinia doped ceria single crystals – bulk properties and electrode kinetics, *Phys. Chem. Chem. Phys.*, 2018, **20**, 8294–8301.
38 N. Otsu and A. Threshold, Selection Method from Gray-Level Histograms, *IEEE Trans. Syst. Man Cybern.*, 1979, **9**, 62–66.
39 M. Yashima, S. Sasaki, M. Kakihana, Y. Yamaguchi, H. Arashi and M. Yoshimura, Oxygen-induced structural change of the tetragonal phase around the tetragonal–cubic phase boundary in ZrO_2–$YO_{1.5}$ solid solutions, *Acta Crystallogr., Sect. B: Struct. Sci., Cryst. Eng. Mater.*, 1994, **B50**, 663–672.
40 P. Debye and P. Scherrer, Atombau, *Nachr. Ges. Wiss. Goettingen, Math.-Phys. Kl.*, 1918, **1918**, 101–120.
41 P. Briois, F. Lapostolle, V. Demange, E. Djurado and A. Billard, Structural investigations of YSZ coatings prepared by DC magnetron sputtering, *Surf. Coat. Technol.*, 2007, **201**, 6012–6018.
42 R. Srinivasan, R. J. De Angelis, G. Ice and B. H. Davis, Identification of tetragonal and cubic structures of zirconia using synchrotron x-radiation source, *J. Mater. Res.*, 1991, **6**, 1287–1292.
43 A. Aminzadeh and H. Sarikhani-fard, Raman spectroscopic study of Ni/Al_2O_3 catalyst, *Spectrochim. Acta, Part A*, 1999, **55**, 1421–1425.
44 M. Kadleíková, J. Breza and M. Veselý, Raman spectra of synthetic sapphire, *Microelectron. J.*, 2001, **32**, 955–958.
45 J. Cai, C. Raptis, Y. S. Raptis and E. Anastassakis, Temperature dependence of Raman scattering in stabilized cubic zirconia, *Phys. Rev. B: Condens. Matter Mater. Phys.*, 1995, **51**, 201–209.
46 S. K. Mukherjee and D. Mergel, Thickness dependence of the growth of magnetron-sputtered TiO_2 films studied by Raman and optical transmittance spectroscopy, *J. Appl. Phys.*, 2013, **114**, 13501.
47 T. Ohsaka, F. Izumi and Y. Fujiki, Raman spectrum of anatase, TiO_2, *J. Raman Spectrosc.*, 1978, **7**, 321–324.
48 O. Frank, M. Zukalova, B. Laskova, J. Kürti, J. Koltai and L. Kavan, Raman spectra of titanium dioxide (anatase, rutile) with identified oxygen isotopes (16, 17, 18), *Phys. Chem. Chem. Phys.*, 2012, **14**, 14567–14572.
49 D. R. G. Mitchell, D. J. Attard and G. Triani, Transmission electron microscopy studies of atomic layer deposition TiO_2 films grown on silicon, *Thin Solid Films*, 2003, **441**, 85–95.
50 J. T. S. Irvine, D. C. Sinclair and A. R. West, Electroceramics: Characterization by Impedance Spectroscopy, *Adv. Mater.*, 1990, **2**, 132–138.
51 M. Gerstl, E. Navickas, G. Friedbacher, F. Kubel, M. Ahrens and J. Fleig, The separation of grain and grain boundary impedance in thin yttria stabilized zirconia (YSZ) layers, *Solid State Ionics*, 2011, **185**, 32–41.
52 C. Ahamer, A. K. Opitz, G. M. Rupp and J. Fleig, Revisiting the Temperature Dependent Ionic Conductivity of Yttria Stabilized Zirconia (YSZ), *J. Electrochem. Soc.*, 2017, **164**, F790–F803.
53 M. Bastianello, S. Gross and M. T. Elm, Thermal stability, electrochemical and structural characterization of hydrothermally synthesised cobalt ferrite ($CoFe_2O_4$), *RSC Adv.*, 2019, **9**, 33282–33289.
54 J. Park and R. N. Blumenthal, Electronic Transport in 8 Mole Percent Y_2O_3-ZrO_2, *J. Electrochem. Soc.*, 1989, **136**, 2867–2876.
55 M. A. Parkes, D. A. Tompsett, M. d'Avezac, G. J. Offer, N. P. Brandon and N. M. Harrison, The atomistic structure of yttria stabilised zirconia at 6.7 mol%: an ab initio study, *Phys. Chem. Chem. Phys.*, 2016, **18**, 31277–31285.

56 X. Guo, E. Vasco, S. Mi, K. Szot, E. Wachsman and R. Waser, Ionic conduction in zirconia films of nanometer thickness, *Acta Mater.*, 2005, **53**, 5161–5166.
57 S. Ikeda, O. Sakurai, K. Uematsu, N. Mizutani and M. Kato, Electrical conductivity of yttria-stabilized zirconia single crystals, *J. Mater. Sci.*, 1985, **20**, 4593–4600.
58 J. Jiang and J. L. Hertz, On the variability of reported ionic conductivity in nanoscale YSZ thin films, *J. Electroceram.*, 2014, **32**, 37–46.
59 D. Adler, Amorphous semiconductors, *CRC Crit. Rev. Solid State Sci.*, 1971, **2**, 317–465.
60 H. Takikawa, T. Matsui, T. Sakakibara, A. Bendavid and P. J. Martin, Properties of titanium oxide film prepared by reactive cathodic vacuum arc deposition, *Thin Solid Films*, 1999, **348**, 145–151.
61 S. B. Amor, L. Guedri, G. Baud, M. Jacquet and M. Ghedira, Influence of the temperature on the properties of sputtered titanium oxide films, *Mater. Chem. Phys.*, 2003, **77**, 903–911.
62 M. K. Nowotny, L. R. Sheppard, T. Bak and J. Nowotny, Defect Chemistry of Titanium Dioxide. Application of Defect Engineering in Processing of TiO_2-Based Photocatalysts, *J. Phys. Chem. C*, 2008, **112**, 5275–5300.
63 T. Bak, J. Nowotny, M. Rekas and C. C. Sorrell, Defect chemistry and semiconducting properties of titanium dioxide: II. Defect diagrams, *J. Phys. Chem. Solids*, 2003, **64**, 1057–1067.
64 A. Weibel, R. Bouchet and P. Knauth, Electrical properties and defect chemistry of anatase (TiO_2), *Solid State Ionics*, 2006, **177**, 229–236.
65 A. M. Azad, S. A. Akbar, L. B. Younkman and M. A. Alim, High-Temperature Immittance Response in Anatase-Based Sensor Materials, *J. Am. Ceram. Soc.*, 1994, **77**, 3145–3152.
66 S.-H. Song, X. Wang and P. Xiao, Effect of microstructural features on the electrical properties of TiO_2, *Mater. Sci. Eng., B*, 2002, **94**, 40–47.
67 E.-M. Köck, M. Kogler, B. Klötzer, M. F. Noisternig and S. Penner, Structural and Electrochemical Properties of Physisorbed and Chemisorbed Water Layers on the Ceramic Oxides Y_2O_3, YSZ, and ZrO_2, *ACS Appl. Mater. Interfaces*, 2016, **8**, 16428–16443.
68 R. Schaub, P. Thostrup, N. Lopez, E. Lægsgaard, I. Stensgaard, J. K. Nørskov and F. Besenbacher, Oxygen Vacancies as Active Sites for Water Dissociation on Rutile TiO_2(110), *Phys. Rev. Lett.*, 2001, **87**, 266104.
69 B. Hou, S. Kim, T. Kim, J. Kim, S. Hong, C. B. Bahn, C. Park and J. H. Kim, The Hydration Structure at Yttria-Stabilized Cubic Zirconia (110)-Water Interface with Sub-Ångström Resolution, *Sci. Rep.*, 2016, **6**, 27916.
70 O. Bikondoa, C. L. Pang, R. Ithnin, C. A. Muryn, H. Onishi and G. Thornton, Direct visualization of defect-mediated dissociation of water on TiO_2(110), *Nat. Mater.*, 2006, **5**, 189–192.
71 X. Guo, On the degradation of zirconia ceramics during low-temperature annealing in water or water vapor, *J. Phys. Chem. Solids*, 1999, **60**, 539–546.
72 K.-D. Kreuer, Proton Conductivity: Materials and Applications, *Chem. Mater.*, 1996, **8**, 610–641.
73 A. Ignatchenko, D. G. Nealon, R. Dushane and K. Humphries, Interaction of water with titania and zirconia surfaces, *J. Mol. Catal. A: Chem.*, 2006, **256**, 57–74.
74 Y. Li and Y. Gao, Interplay between Water and TiO_2 Anatase (101) Surface with Subsurface Oxygen Vacancy, *Phys. Rev. Lett.*, 2014, **112**, 206101.
75 K. K. Ghuman, Mechanistic insights into water adsorption and dissociation on amorphous TiO_2-based catalysts, *Sci. Technol. Adv. Mater.*, 2018, **19**, 44–52.

3.3. Publication III: Design of Ordered Mesoporous CeO_2–YSZ Nanocomposite Thin Films with Mixed Ionic/Electronic Conductivity via Surface Engineering

In the third publication of my thesis, the impact of cerium oxide (CeO_2) coatings on the transport properties of polymer-templated nanocrystalline YSZ thin films with a well-defined mesoporous morphology and different pore sizes (17, 24 and 40 nm) is presented. The temperature and $p(O_2)$-dependence of the electronic and ionic conductivity are investigated using EIS. Structural characterization using different analysis methods (SEM, TEM, EDX, XRD, Raman spectroscopy, ToF-SIMS and XPS) confirm the successful ALD coating of the complex surface of the mesoporous YSZ thin films.

The thickness of the ceria layer strongly affects the total conductivity of the CeO_2/YSZ composites. Impedance measurements show that the total conductivity significantly increases with increasing ceria layer thickness, which is accompanied by changes of the Ce^{3+}/ Ce^{4+} ratio as well as the activation energy of the transport process. Here, the Ce^{3+} concentration decreases with increasing layer thickness. The composites with a 7 nm thin ceria coating (190 ALD cycles) exhibit only dominant oxygen ion conductivity in the measured $p(O_2)$-range. In contrast, the composites with a 3 nm thin ceria coating show a dominant electronic contribution, especially at low temperatures, arising from small polaron hopping due to a higher Ce^{3+} concentration. In addition, the electrochemical transport measurements reveal no dependence of the total conductivity on the pore size of the composites.

The experiments were designed and conducted by me with assistance from Pascal Cop and Rajendra S. Negi. TEM measurements of the thin films were performed by Andrey Mazilkin. Mesoporous YSZ samples were manufactured by Yanjiao Ma. The publication was written by me and edited by Torsten Brezesinski and Matthias T. Elm. Reprinted with permission from *ACS Nano*. Copyright (2022) American Chemical Society.

Erdogan Celik, Pascal Cop, Rajendra S. Negi, Andrey Mazilkin, Yanjiao Ma, Philip Klement, Jörg Schörmann, Sangam Chatterjee, Torsten Brezesinski and Matthias T. Elm, Design of Ordered Mesoporous CeO_2–YSZ Nanocomposite Thin Films with Mixed Ionic/Electronic Conductivity via Surface Engineering, *ACS Nano*, **2022**, 16, 3182-3193.

ACSNANO

www.acsnano.org

ARTICLE

Design of Ordered Mesoporous CeO_2–YSZ Nanocomposite Thin Films with Mixed Ionic/Electronic Conductivity via Surface Engineering

Erdogan Celik,* Pascal Cop, Rajendra S. Negi, Andrey Mazilkin, Yanjiao Ma, Philip Klement, Jörg Schörmann, Sangam Chatterjee, Torsten Brezesinski, and Matthias T. Elm*

Cite This: *ACS Nano* 2022, 16, 3182–3193 Read Online

ABSTRACT: **Mixed ionic and electronic conductors represent a technologically relevant materials system for electrochemical device applications in the field of energy storage and conversion. Here, we report about the design of mixed-conducting nanocomposites by facile surface modification using atomic layer deposition (ALD). ALD is the method of choice, as it allows coating of even complex surfaces. Thermally stable mesoporous thin films of 8 mol-% yttria-stabilized zirconia (YSZ) with different pore sizes of 17, 24, and 40 nm were prepared through an evaporation-induced self-assembly process. The free surface of the YSZ films was uniformly coated via ALD with a ceria layer of either 3 or 7 nm thickness. Electrochemical impedance spectroscopy was utilized to probe the influence of the coating on the charge-transport properties. Interestingly, the porosity is found to have no effect at all. In contrast, the thickness of the ceria surface layer plays an important role. While the nanocomposites with a 7 nm coating only show ionic conductivity, those with a 3 nm coating exhibit mixed conductivity. The results highlight the possibility of tailoring the electrical transport properties by varying the coating thickness, thereby providing innovative design principles for the next-generation electrochemical devices.**

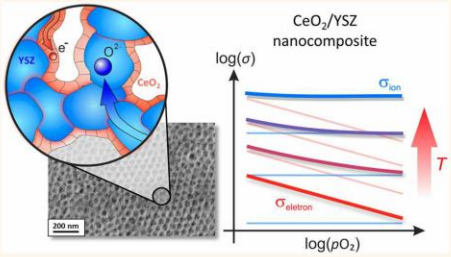

KEYWORDS: *Mesoporous oxides, Nanocomposites, Atomic layer deposition, Surface engineering, Mixed conductors*

Ordered mesoporous metal oxides are characterized by a regular structure made from pores of diameter 2–50 nm.[1,2] The pores are surrounded by crystallites that form an interconnected pathway for electrical charge carriers. The regular pore arrangement enables efficient penetration of gases or liquids into the bulk, thereby improving the accessibility of active surface sites. This characteristic structure qualifies mesoporous oxides for a variety of electrochemical applications,[3−9] e.g., in the field of (photo)-electrocatalysis, as electrode materials for batteries and supercapacitors or gas sensors. Several studies have shown that mesoporous architectures are favorable for electrochemical applications, which is mostly attributed to their large specific surface area. However, also other factors, such as the degree of crystallinity, the grain-size distribution, and the pore structure, play an important role in outperforming bulk (nanocrystalline) counterparts.[3,10−15]

Surface engineering may lead to further improvements in the properties of mesoporous oxides. The accessibility of the free surface through the porosity enables its effective modification,[16] e.g., by functionalization, deposition of thin coatings, or incorporation of guest species, such as metal nanoparticles.[17−19] A common approach is surface coating via atomic layer deposition (ALD).[20−22] ALD allows preparing conformal and uniform coatings on complex surfaces, with precise control over their thickness.[22−24] It is therefore often used in surface engineering of nanostructured materials for energy applica-

Received: December 12, 2021
Accepted: February 4, 2022
Published: February 9, 2022

https://doi.org/10.1021/acsnano.1c11032
ACS Nano 2022, 16, 3182–3193

ACS Nano www.acsnano.org Article

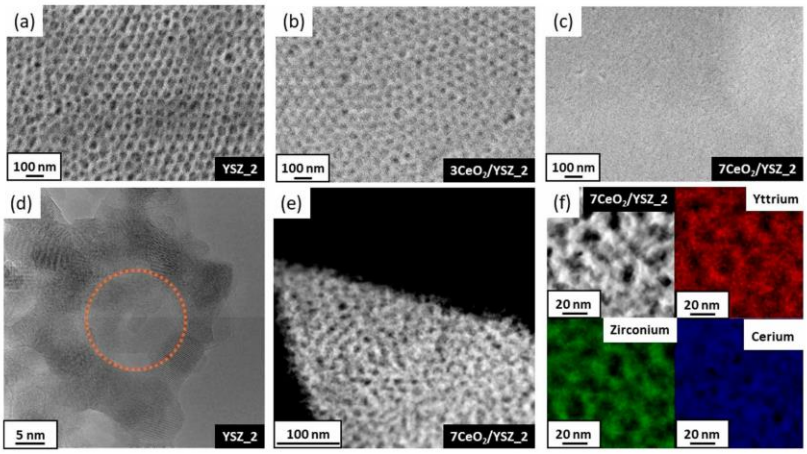

Figure 1. Top-view SEM images of (a) uncoated, (b) 3 nm, and (c) 7 nm CeO_2-coated YSZ_2 thin films. (d) HRTEM image of uncoated YSZ_2. (e, f) HAADF-STEM images of 7 nm CeO_2-coated YSZ_2 and corresponding EDS maps for Y (in red), Zr (in green), and Ce (in blue).

tions.[22,25−27] One of the benefits of ALD-derived thin surface coatings is that the deposition of a simple binary oxide, such as Al_2O_3 or SiO_2, can help increase the thermal stability of mesoporous materials,[28−30] whose structure often tends to collapse at elevated temperatures. Surface modification via ALD is also successfully applied to protect/stabilize cathode materials in lithium-ion and solid-state batteries[31−37] or to improve the performance of solid oxide fuel cells.[38−40] Apart from that, surface engineering of complex nanostructures using ALD allows developing innovative mixed-conducting composites. This can be achieved by coating an ion-conducting oxide with an electronically conductive material or vice versa. Artificial mixed conductors prepared from two different solid phases represent promising materials systems for various applications, e.g., in the field of energy storage and conversion. They are of importance as intercalation electrodes, permeation membranes, or sensors,[41] as they may exhibit high electronic and ionic partial conductivities. Furthermore, space-charge effects at the interface between two different phases can enable interfacial storage of neutral species, such as lithium or silver.[42−44]

Artificial composites are commonly formed by "mixing" an ion conductor with a metal.[45−48] In an alternative approach, mixed-conducting properties are achieved by coating the free surface of a porous oxygen-ion conductor with thin titania (TiO_2) layers.[49] Mixed-conducting properties have also been assumed for mesoporous zirconia (ZrO_2) thin films coated with ceria (CeO_2).[50] However, experimental proof of electronic conductivity of the ceria coating is lacking in the related study, mainly because the oxygen partial-pressure-dependence of the conductivity has not been examined. Nevertheless, using oxide-based coatings as an electronically conductive phase promises higher thermal stability of the resulting composite. In addition, electrochemical characterizations revealed that the thickness of the ALD coating has a profound effect on the electrical properties. This is attributed to changes in morphology and microstructure (crystallinity, grain size, etc.) of the coating with varying ALD cycles as well as to space-charge effects arising at the different interfaces. The strong correlation between thickness and electrical conductivity offers an additional degree of freedom in tailoring the conductivity of mesoporous oxide composites by altering the coating thickness. However, detailed understanding of the relation between coating thickness, morphology, and ionic/electronic conductivity is required to optimize the electrochemical properties for real-world (device) applications.

Here, we report about the characterization of mixed-conducting nanocomposites by surface-engineering of cubic mesoporous yttria-stabilized zirconia (YSZ) thin films. YSZ was chosen as a matrix, as it is one of the most prominent oxygen-ion conductors at elevated temperatures.[51−53] The high oxygen-ion conductivity arises from the incorporation of yttria (Y_2O_3) into the ZrO_2 lattice, stabilizing the cubic fluorite-type crystal structure and leading to the formation of oxygen vacancies.[54,55] The free surface of the mesoporous films was coated by ceria ALD. Ceria shows high redox activity of the Ce^{3+}/Ce^{4+} couple, thereby facilitating oxygen exchange with the surrounding atmosphere.[56] In addition, it is responsible for the $p(O_2)$-sensitive mixed ionic/electronic conductivity, as the release of oxygen under reducing conditions not only generates oxygen vacancies but also localized electrons, the latter of which reduce Ce^{4+} to Ce^{3+}:

$$2Ce_{Ce}^{x} + O_{O}^{x} \leftrightharpoons V_{O}^{\cdot\cdot} + 2Ce_{Ce}^{\prime} + \frac{1}{2}O_2 \quad (1)$$

These electrons can hop as small polarons between the Ce^{3+} and Ce^{4+} sites, giving rise to an electronic conductivity contribution.[57−59] Thus, the electrical properties of $CeO_{2-\delta}$ strongly vary with the nonstoichiometry δ.[60,61]

Specifically, polymer-templated, mesoporous CeO_2−YSZ nanocomposite thin films with different pore sizes and varying thicknesses of the ceria coating are examined. Structural characterization confirms the uniform coating of the free surface via ALD. Temperature and oxygen partial-pressure-

https://doi.org/10.1021/acsnano.1c11032
ACS Nano 2022, 16, 3182−3193

ACS Nano www.acsnano.org Article

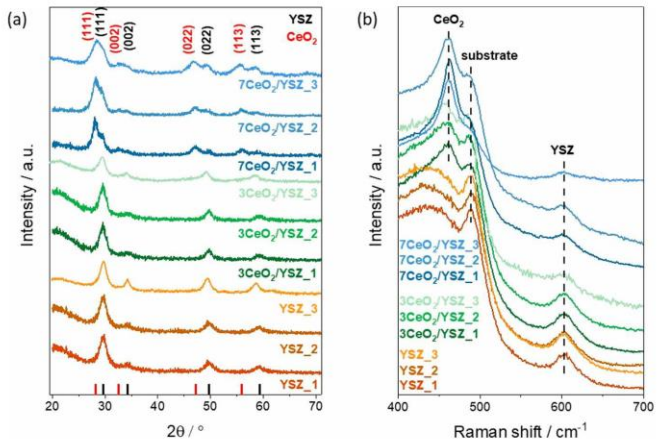

Figure 2. (a) GIXRD patterns and (b) Raman spectra of uncoated and CeO_2-coated YSZ thin films at room temperature. For comparison, the reference patterns for cubic YSZ (PDF 98-007-5316) and cubic CeO_2 (PDF 98-002-8709) are shown in part a.

dependent electrochemical impedance spectroscopy (EIS) measurements indicate that the electrical transport properties are independent of the pore size but strongly change with the thickness of the coating. Mixed ionic/electronic conductivity arises when the surface is coated with a 3 nm ceria layer, as clearly confirmed by $p(O_2)$-dependent conductivity measurements. The electronic partial conductivity of the ceria layer dominates the transport properties at low temperatures and under reducing conditions. In contrast, nanocomposites with a 7 nm ceria coating only show ionic conductivity. The results demonstrate that surface modification of mesoporous oxides is a viable approach to produce and explore mixed-conducting materials systems with tailorable properties.

RESULTS AND DISCUSSION

Structural and Compositional Characterization. Representative top-view SEM images of uncoated mesoporous YSZ thin films (thickness $d \simeq 180$ nm) are shown in Figure 1a and Figure S1. The pores have average in-plane diameters of 17, 24, and 40 nm. In the following, the corresponding films are referred to as YSZ_1, YSZ_2, and YSZ_3, respectively. Both YSZ_1 and YSZ_2 are crack-free and have a continuous pore structure with a distorted cubic symmetry. The high-resolution TEM (HRTEM) images in Figure 1d and Figure S2 confirm that the pores (denoted by an orange circle) are surrounded by crystalline walls having grains of average diameter 5 nm, independent of the pore size. As opposed to YSZ_1 and YSZ_2, YSZ_3 shows a disordered but macroscopically uniform porous network (see Figure S1), a result that we attribute to the lower solubility of the high-molecular-weight structure-directing agent (SDA) used in the synthesis.

For the preparation of nanocomposites, the different thin films were coated via ALD with a ceria layer of either 3 nm ($3CeO_2$/YSZ_x) or 7 nm ($7CeO_2$/YSZ_x) thickness. After surface coating, they were probed using SEM, mainly focusing on the change in pore size with the number of ALD cycles. As shown in Figure 1b,c and Figure S2 for YSZ_2, the pores shrink significantly with increasing ALD cycles. For $7CeO_2$/YSZ_1, the pores were virtually completely filled (Figure S1). Also for YSZ_2 (Figure 1c), the pores appeared to be largely filled after coating with 7 nm ceria. However, STEM images of the corresponding $7CeO_2$/YSZ_2 nanocomposite (Figure 1e,f and Figure S2) demonstrate that some of the porosity is maintained. This is further supported by energy-dispersive X-ray spectroscopy (EDS) maps of the elemental distribution for the $3CeO_2$/YSZ_2 and $7CeO_2$/YSZ_2 thin films in Figure 1f and Figure S2. The mapping of Ce reveals a uniform coating distribution, suggesting good surface coverage of the YSZ matrix.

The crystallinity and phase purity of the nanocomposites were investigated by GIXRD at room temperature. Figure 2a presents GIXRD patterns for all samples. The uncoated YSZ films show characteristic reflections of cubic YSZ, indicating successful preparation of a single-phase material.[62] Applying the Scherrer equation to the (111) reflection, a crystallite size of approximately 6 nm was calculated, in good agreement with the value estimated from TEM imaging.[63] After ALD coating, additional broad reflections are visible in the diffraction patterns. These reflections can be assigned to the cubic fluorite structure of CeO_2. They sharpen and increase in intensity for the films coated with a 7 nm ceria layer, which is in line with previous results.[50] However, for YSZ and ceria, the low scattering factor of oxygen and the broad reflections, due to the small crystallite size, make a clear differentiation between the cubic and tetragonal phases difficult.[64−66]

Raman spectroscopy measurements were conducted to confirm the cubic lattice symmetry of both the mesoporous YSZ and the ceria coating. As shown in Figure 2b, Raman spectra of the uncoated YSZ films display the characteristic triply degenerate F_{2g} mode at 604 cm^{-1}, which is typical of the cubic fluorite phase.[54,67,68] Note that the intense mode at 490 cm^{-1} and the broad Raman band at 430 cm^{-1} arise from the quartz glass substrate.[69] For the CeO_2−YSZ nanocomposites, the Raman measurements also confirm the fluorite crystal structure of ceria, due to the presence of the prominent Raman-active band at $\omega = 461$ cm^{-1}. The samples show a red-

https://doi.org/10.1021/acsnano.1c11032
ACS Nano 2022, 16, 3182−3193

ACS Nano www.acsnano.org Article

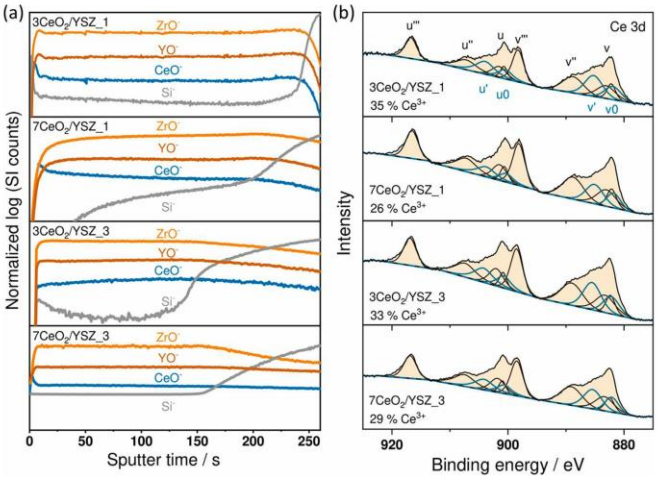

Figure 3. (a) ToF-SIMS depth profiles for 3 and 7 nm CeO_2-coated YSZ_1 and YSZ_3 thin films and (b) corresponding Ce 3d XP spectra.

shift and broadening of the F_{2g} mode, compared to single crystals (ω = 465 cm^{-1}),[70,71] both of which slightly increase with decreasing coating thickness. This behavior is characteristic of nanoscale ceria[72−77] and indicates its columnar growth on the YSZ surface.[23] Phonon confinement and changes in the lattice constant (tensile strain) result in broadening of the Raman mode and a shift to lower wavenumbers with decreasing particle size. Thus, the red shift of the F_{2g} mode observed for decreasing coating thickness suggests a smaller grain size for the 3 nm CeO_2. However, strain effects arising at the CeO_2/YSZ interface may be responsible for the broadening and shift of the F_{2g} mode too.[78]

The homogeneity of the CeO_2 coating throughout the films was examined by time-of-flight-secondary ion mass spectrometry (ToF-SIMS). Figure 3a shows depth profiles for YSZ_1 and YSZ_3 after the deposition of 3 and 7 nm CeO_2. For all samples, a constant ratio of YO^- and ZrO^- species (until reaching the film/substrate interface) is found, indicating uniform distribution of Y and Zr throughout the mesoporous films. In addition, the CeO^- signal clearly follows that of YO^- and ZrO^-, confirming the conformal coating of the inner (bulk) porosity. The slight decrease/increase of the CeO^- signal with increasing sputtering depth seen for 7CeO_2/YSZ_1 and 3CeO_2/YSZ_3 is related to the porous structure of the nanocomposites, as discussed previously.[23] Interestingly, no SiO^- signal is detected for the 7CeO_2/YSZ_1 at short sputtering times. This result suggests complete coverage of the top surface, as also indicated by SEM imaging in Figure S1. This was somewhat expected though, as in that case, the pore radius is similar to the thickness of the ALD ceria layer. Note that blocking of the interconnecting channels (necks) between the pores prevents proper filling and results in growth of a sealing layer.[21,50,79] However, a nearly constant CeO^- signal is found after a short sputtering time, accompanied by the presence of the Si^- substrate signal, thereby corroborating the uniform coverage of the solid/air interfaces in the YSZ_1 thin film.

It is well-known that the mixed-conducting properties of ceria are strongly correlated with its ability to switch between the +3 and +4 oxidation states.[57,58,61] For that reason, the CeO_2/YSZ nanocomposites were investigated by XPS to determine the Ce^{3+} content in the surface coating. To calculate the Ce^{3+} content, the integral areas of the six signals from Ce^{4+} (v, v'', v''' and u, u'', u''') and the four signals from Ce^{3+} (v_0, v' and u_0, u') were compared.[80] Figure 3b shows Ce 3d XP spectra and corresponding fits for the 3 and 7 nm CeO_2-coated YSZ_1 and YSZ_3 thin films. The analysis reveals that the Ce^{3+}/Ce^{4+} ratio is independent of the pore size but varies with the coating thickness. With increasing thickness of the CeO_2 layer, the Ce^{3+} concentration decreases, in good agreement with previous data[50] and the results from Artiglia et al.[81] Despite the different pore structures and surface areas (for the CeO_2 to be deposited onto), only small differences in the Ce^{3+} content between the 3CeO_2/YSZ_1 (35%) and 3CeO_2/YSZ_3 (33%), as well as between the 7CeO_2/YSZ_1 (26%) and 7CeO_2/YSZ_3 (29%), are observed. Thus, the difference clearly derives from the thickness of the coating in the nanocomposites. Typically, the nonstoichiometry of $CeO_{2-\delta}$, and therefore the Ce^{3+} content, is determined by the surrounding atmosphere (refer to eq 1). However, because the XPS measurements were performed under identical conditions, the decrease in Ce^{3+} signal with increasing coating thickness suggests the presence of a surface space-charge region (where the electrons accumulate).[3,54,82] Since XPS is a surface-sensitive technique with a typical penetration depth of approximately 5 nm,[32] the width of the space-charge layer can be considered to be confined to only a few nanometers. Note that a high surface concentration of Ce^{3+} has also been reported by Hao et al. They monitored the Ce^{3+} distribution in ceria nanoparticles using scanning tunneling microscopy (STM) combined with electron energy-loss spectroscopy (EELS).[83]

Electrochemical Characterization. The electrochemical properties of the uncoated YSZ films and corresponding

https://doi.org/10.1021/acsnano.1c11032
ACS Nano 2022, 16, 3182−3193

ACS Nano www.acsnano.org Article

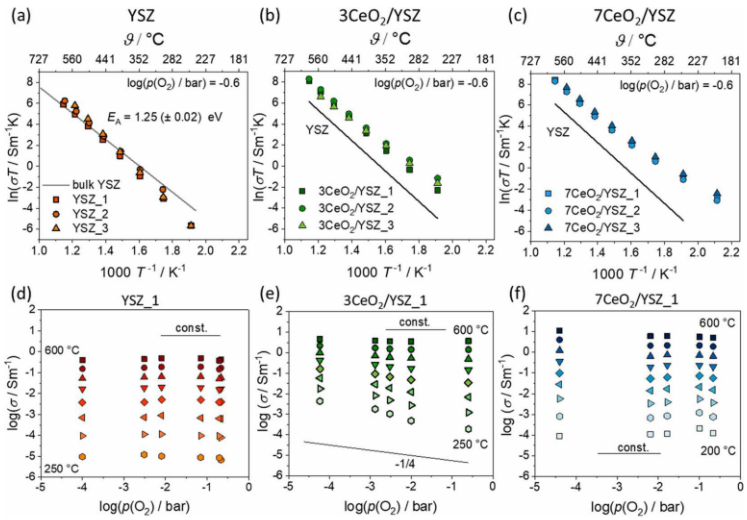

Figure 4. Arrhenius plots of the total conductivity for (a) uncoated, (b) 3 nm, and (c) 7 nm CeO_2-coated YSZ thin films. The gray line in part a is the average of reported values for bulk YSZ taken from ref 91. Oxygen partial-pressure-dependence of the total conductivity for (d) uncoated, (e) 3 nm, and (f) 7 nm CeO_2-coated YSZ_1.

nanocomposites were studied as a function of temperature between 200 and 600 °C in 50 °C steps and oxygen partial pressure (approximately 10^{-5} and 0.2 bar) using electrochemical impedance spectroscopy (EIS). Representative impedance spectra (Nyquist plots) recorded at 450 °C are shown in Figure S3. Figure S4 shows the impedance spectra for the $7CeO_2$/YSZ_1 measured at different temperatures (200–600 °C). All spectra exhibit an almost ideal semicircle at high frequencies, as commonly observed for mesoporous metal oxide thin films.[54,84] At low frequencies, the appearance of a second semicircle is apparent. Consequently, the EIS data were fitted using an equivalent circuit with two *RQ* elements connected in series. The elements represent one of the two semicircles and consist of a resistance element *R* and a constant phase element *Q* connected in parallel. The capacitance values were calculated from the parameters α and C_Q of the constant phase element according to[85,86]

$$C = R^{(1-\alpha)} C_Q^{(1/\alpha)} \tag{2}$$

For the semicircle at high frequencies, capacitances of 1.6–4.3 × 10^{-12} F were obtained. Typical values for the bulk of ceramic materials vary between 10^{-12} and 10^{-10} F.[87,88] Thus, the first semicircle is attributed to the response of the nanocomposite. At low frequencies, the tail of the second semicircle can be described by a capacitance of approximately 10^{-7} F, which corresponds to the contribution of the nanocomposite/electrode interface.[87,88] It is worth noting that in microcrystalline materials, a third semicircle in the intermediate frequency range arises, due to the transport across the grain boundaries. However, in nanocrystalline samples, the semicircles representing the grain and grain boundary contributions merge, making a separation impossible.[3,61,89] For that reason, only the total resistance (i.e., grain and grain boundary) is obtained from the analysis of the high-frequency semicircle. The total conductivity σ_{tot} was determined from the resistance *R* and the geometry of the interdigitated electrodes used for the electrical characterization:[90]

$$\sigma_{tot} = \frac{1}{R} \cdot \frac{b}{d l_{finger} n} \tag{3}$$

where b = 33 μm is the distance between the electrode fingers, n = 20 the number of fingers, l_{finger} = 3 mm the length of an electrode finger, and d = 180 nm represents the film thickness (see also Figure S5). Using eq 3, the porosity is neglected, meaning the samples are treated as being dense.

Figure 4a shows the temperature-dependence of the conductivity for the uncoated YSZ films in an Arrhenius-type representation. The same conductivity was found for YSZ_1, YSZ_2, and YSZ_3. This is somewhat surprising, as the microstructure can significantly affect the impedance of polycrystalline ceramics.[86,92,93] The pore-size-independent conductivity can probably be attributed to the characteristic architecture of the mesoporous YSZ thin films. Despite differences in the average pore size, they all exhibit a regular arrangement of crystallites of very similar size, giving rise to comparable transport pathways for the charge carriers. As is evident from the data, the samples showed a linear Arrhenius behavior over the whole temperature range investigated. This is expected, as YSZ exhibits ionic conductivity because of the presence of oxygen vacancies resulting from the introduction of yttria into the zirconia lattice. This kind of substitution can be described in Kroeger–Vink notation by:[55]

$$Y_2O_3 \xrightarrow{ZrO_2} 2Y'_{Zr} + V_O^{\cdot\cdot} + 3O_O^x \tag{4}$$

https://doi.org/10.1021/acsnano.1c11032
ACS Nano 2022, 16, 3182–3193

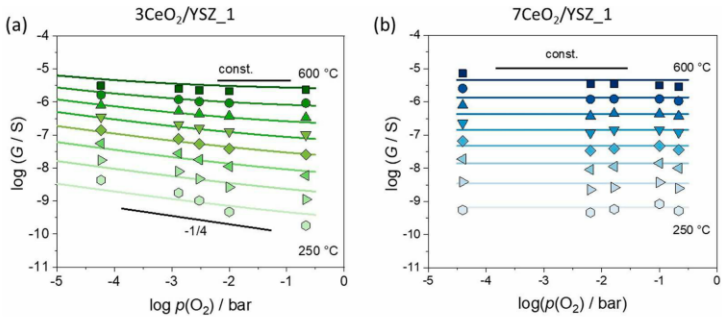

Figure 5. Calculated oxygen partial-pressure-dependence of the conductance for (a) 3 nm and (b) 7 nm CeO_2-coated YSZ_1 thin films. Solid lines are fits to the experimental data.

where Y'_{Zr} represents a Y^{3+} ion on a Zr^{4+} site with a relative charge of −1, and $V_O^{\cdot\cdot}$ is an oxygen vacancy with a relative charge of +2. O_O^x denotes the oxygen lattice sites with a relative charge of zero. From the temperature-dependence of the conductivity, the activation energy E_A and the pre-exponential conductivity factor σ_0 were derived:

$$\sigma_{ion}(T) = \frac{\sigma_{0,ion}}{T} \exp\left(-\frac{E_A}{k_B T}\right) \tag{5}$$

where k_B is the Boltzmann constant, $\sigma_{0,ion}$ the conductivity prefactor, and T represents the temperature. For the uncoated YSZ samples, an activation energy $E_{A,ion}$ = 1.25 (±0.02) eV was obtained. This is in good agreement with the values reported for oxygen-ion conductivity in nanocrystalline YSZ, ranging from 1.02 to 1.23 eV.[49,54,88,91] Also, the measured conductivities are similar to the average of reported values for bulk YSZ taken from ref 91 (shown as a solid gray line in Figure 4a). A dominant oxygen-ion conductivity is also confirmed by the $p(O_2)$-independent conductivity shown in Figure 4d.[55] As the concentration of oxygen ions is fixed for varying $p(O_2)$, due to the "doping" with yttria, the activation energy represents the migration enthalpy ΔH_{mig} of the oxygen ions. For the conductivity prefactor $\sigma_{0,ion}$, a value of 7.5 (±0.3) × 10^9 $Sm^{-1}K$ was obtained.

Coating the mesoporous YSZ films significantly changes their electrical properties. After the deposition of 3 nm ceria, the total conductivity of the nanocomposites increases by at least 2 orders of magnitude compared to that of the pristine YSZ material (Figure 4b). Two transport regimes with different activation energies can be observed at ambient conditions in the Arrhenius representation. The change in activation energy becomes even more evident when calculating the activation energy as a function of the inverse temperature:

$$E_A = -k_B \frac{d(\ln(\sigma T))}{d(1/T)} \tag{6}$$

As shown in Figure S6, the activation energy clearly decreases with decreasing temperature. In addition, the CeO_2 coating affects the $p(O_2)$-dependence of the conductivity in the temperature range between 250 and 600 °C, as shown in Figure 4e. At lower temperatures, the conductivity varies with a characteristic slope of −1/4, while at higher temperatures, it remains constant in the $p(O_2)$-range investigated.

The $7CeO_2$/YSZ nanocomposites show the highest total conductivity at all temperatures (Figure 4c). Again, two different transport regimes characterized by changes in activation energy are observed (see also Figure S6). However, in contrast to the $3CeO_2$/YSZ samples, the $7CeO_2$/YSZ nanocomposites reveal a constant $p(O_2)$-dependence of the conductivity at all temperatures (Figure 4f). Similar to the uncoated YSZ films, the effect of pore size on the transport properties is negligible. Instead, the thickness of the CeO_2 layer determines the differences in conductivity seen.

Direct comparison of the conductivity is somewhat questionable when analyzing the influence of the coating on the electrical properties of the nanocomposites, because the deposition of the surface layer decreases the pore size, which was neglected in the calculation, as discussed previously. It is more reasonable to compare the total conductance $G = R^{-1}$, comprising the ionic conductance G_{YSZ} of the mesoporous YSZ matrix and the conductance G_{CeO_2} of the ceria coating. The transport through the coating occurs in parallel to the transport of the oxygen ions in the YSZ, i.e., the total conductance is given by $G_{total} = G_{YSZ} + G_{CeO_2}$. The contribution of the CeO_2 layer was determined from the total conductance of the nanocomposites by subtracting the conductance of the mesoporous YSZ films ($G_{CeO_2} = G_{total} - G_{YSZ}$). This is possible because the YSZ samples exhibit the same conductivity (independent of pore size, see above). The resulting $p(O_2)$-dependence of the individual conductance contributions from the 3 and 7 nm ceria coatings are shown in Figure 5a,b.

The 7 nm CeO_2 coating shows a $p(O_2)$-independent conductivity over the whole temperature and oxygen partial-pressure range (Figure 5b). This behavior suggests that the surface layer exhibits a dominant oxygen-ion conductivity, as ceria tends to form intrinsic anti-Frenkel defect pairs.[57] We attribute the two transport regimes with different activation energies to the presence of a small amount of acceptor impurities (A) in the coating. The formation of oxygen vacancies, due to acceptor impurities, is given in Kroeger−Vink notation by:[94]

$$A_2O_3 \xrightarrow{CeO_2} 2A'_{Ce} + V_O^{\cdot\cdot} + 3O_O^x \tag{7}$$

https://doi.org/10.1021/acsnano.1c11032
ACS Nano 2022, 16, 3182−3193

At low temperatures, the presence of these impurities leads to a constant oxygen-vacancy concentration $[V_O^{\cdot\cdot}]_A$, which is significantly larger than the intrinsic one due to anti-Frenkel defects, i.e., $[V_O^{\cdot\cdot}]_A \gg [V_O^{\cdot\cdot}]_{AF}$. The temperature-dependence of the conductivity is then only determined by the migration enthalpy $\Delta_{mig}H_{ion}$ of the oxygen vacancies:

$$\sigma_{ion,Imp}(T) = Zne\mu(T) \approx 2[V_O^{\cdot\cdot}]_A F\frac{\mu_0}{T}\exp\left(-\frac{\Delta_{mig}H_{ion}}{k_BT}\right) \tag{8}$$

where $[V_O^{\cdot\cdot}]_A = n/N_A$ is the oxygen-vacancy concentration (due to acceptor impurities), n the corresponding density of oxygen vacancies, N_A the Avogadro constant, e the elementary charge, F the Faraday constant, Z the valence, and μ_0 represents the mobility prefactor. Hence, the low-temperature activation energy $E_{A,Imp}$ corresponds to the migration enthalpy of the oxygen ions:

$$E_{A,Imp} = \Delta_{mig}H_{ion} \tag{9}$$

At higher temperatures, intrinsic anti-Frenkel defects are prevalent, leading to the formation of oxygen vacancies $V_O^{\cdot\cdot}$ and oxygen interstitials O_i'':

$$CeO_2 \rightarrow Ce_{Ce}^{x} + 2V_O^{\cdot\cdot} + 2O_i'' \tag{10}$$

Consequently, the concentration of the intrinsic oxygen vacancies increases and outweighs the constant vacancy concentration, due to the presence of acceptor defects. The ionic conductivity in the high-temperature region is therefore given by

$$\sigma_{ion,AF}(T) = Zn(T)e\mu(T) \approx 2[V_O^{\cdot\cdot}]_{AF}F\frac{\mu_0}{T}\exp\left(-\frac{\Delta_{mig}H_{ion}}{k_BT}\right)\exp\left(-\frac{\Delta_fH_{ion}}{2k_BT}\right) \tag{11}$$

where $n(T)/N_A \approx [V_O^{\cdot\cdot}]_A F \exp(-\Delta_fH_{ion}/2k_BT)$ is the concentration of the intrinsic oxygen vacancies (due to anti-Frenkel defects). In this case, the activation energy of the ionic conductivity $E_{A,AF}$ comprises the $\Delta_{mig}H_{ion}$ and the enthalpy of formation Δ_fH_{ion} of the anti-Frenkel defects:

$$E_{A,AF} = \Delta_{mig}H_{ion} + \frac{\Delta_fH_{ion}}{2} \tag{12}$$

The temperature-dependence of the ionic conductance of the ceria coating is then given by

$$G_{ion,CeO_2}(T) = G_{ion,Imp}(T) + G_{ion,AF}(T) \tag{13}$$

with

$$G_{ion,Imp}(T) = \frac{G_{0,Imp}}{T}\exp\left(-\frac{E_{A,Imp}}{k_BT}\right) \tag{14}$$

and

$$G_{ion,AF}(T) = \frac{G_{0,AF}}{T}\exp\left(-\frac{E_{A,AF}}{k_BT}\right) \tag{15}$$

A good description of the experimental results (see solid line fits in Figure 5b) is achieved for $E_{A,Imp} = \Delta_{mig}H_{ion} = 0.91$ ($\pm$0.03) eV and $E_{A,AF} = 1.96$ ($\pm$0.02) eV and the conductance prefactors $G_{0,Imp} = 200$ ($\pm$12) SK and $G_{0,AF} = 5.9$ ($\pm$1.0) $\times 10^8$ SK. The activation energies are in excellent agreement with previous studies.[94,95] From eq 12, the Δ_fH_{ion} is calculated to be approximately 2.1 eV, which is also consistent with literature values.[96−98]

In case of the 3 nm CeO_2 coating (Figure 5a), the conductance decreases with increasing oxygen partial pressure, which is typical of CeO_2 with a dominant electronic conductance. In the near-stoichiometric $p(O_2)$-range (intrinsic regime), a decrease in oxygen partial pressure results in the release of molecular oxygen (reduction reaction) according to eq 1. As the concentration of oxygen vacancies is much larger than that of the electrons, the vacancy concentration can be assumed constant (Brouwer approximation). Then, the electron concentration, and therefore the conductance, varies with $p(O_2)^{-1/4}$, in agreement with the experimental results.[3,57,81,84,99] However, at higher temperatures, the conductance again becomes $p(O_2)$-independent, indicating a dominant ionic conductivity, as observed for the $7CeO_2$/YSZ thin films. Thus, the results provide clear evidence that the $3CeO_2$/YSZ nanocomposites exhibit a mixed ionic/electronic conductance:

$$G_{tot,CeO_2}(T, p(O_2)) = G_{ion,CeO_2}(T) + G_{elec}(T, p(O_2)) \tag{16}$$

Like for the 7 nm coating, the ionic conductance of the nanocrystalline CeO_2 surface layer is described by eq 13. The additional electronic contribution, due to hopping of electrons between the Ce^{3+} and Ce^{4+} sites, is given by[60,100,101]

$$G_{elec}(T, p(O_2)) = \frac{G'_{0,elec}}{T}\exp\left(-\frac{E_{A,elec}}{k_BT}\right)\cdot p(O_2)^{-1/4} \tag{17}$$

The corresponding fits of the temperature and $p(O_2)$-dependences of the total conductivity are shown in Figure 5a. Fits to the experimental data for the 3 and 7 nm CeO_2-coated YSZ_2 and YSZ_3 thin films are presented in Figure S7, while in Figure S8, the electronic and ionic contributions to the total conductance are displayed separately. A good data description is achieved for $E_{A,Imp} = 0.93$ ($\pm$0.03) eV and $E_{A,AF} = 1.94$ ($\pm$0.02) eV, in agreement with the results for the $7CeO_2$/YSZ nanocomposite. The prefactors $G_{0,Imp} = 66.7$ ($\pm$12.0) SK and $G_{0,AF} = 2.8$ ($\pm$0.3) $\times 10^8$ SK are reduced by a factor of 3 and 2.1, respectively (see also Table S1), corresponding to the difference in thickness of the coatings. Overall, the results indicate that both the 3 and 7 nm CeO_2 surface layers exhibit a comparable ionic conductivity. For the electronic conductance, an activation energy $E_{A,elec} = 0.86$ ($\pm$0.02) eV and a conductance prefactor $G'_{0,elec} = 18.2$ ($\pm$1.0) SK bar$^{1/4}$ are obtained. In the intrinsic regime, the activation energy again comprises the migration enthalpy $\Delta_{mig}H_{elec}$ and the enthalpy of formation Δ_fH_{elec} of the electronic defects:[61,99,102,103]

$$E_{A,elec} = \Delta_{mig}H_{elec} + \frac{\Delta_fH_{elec}}{2} \tag{18}$$

A typical value of 0.4 eV for $\Delta_{mig}H_{elec}$ has been reported for a small polaron hopping in ceria.[50,59,60,102] Using this, Δ_fH_{elec} is calculated to be approximately 0.92 eV, which is significantly lower than for single crystals (4.2−4.7 eV).[59,61] However, comparable values have been reported for nanocrystalline ceria.[61] The decrease in Δ_fH_{elec} originates from the space-charge potential at the grain boundaries. As shown by Tschöpe et al. using the space-charge model, the apparent activation energy of the electrons decreases from 2.7 eV to approximately 1.0 eV when decreasing the grain size to 30 nm. In addition,

https://doi.org/10.1021/acsnano.1c11032
ACS Nano 2022, 16, 3182−3193

calculations using density-functional theory (DFT) predict that the high surface area of ceria nanoparticles strongly affects $\Delta_f H_{elec}$ and facilitates oxygen release.[104,105] The low reduction enthalpy further confirms that space-charge effects are responsible for the high Ce^{3+} concentration in the 3 nm coating.

The increased electronic conductivity of the $3CeO_2$/YSZ nanocomposites can directly be related to the higher Ce^{3+} concentration, as observed by XPS (see Figure 3b). Because the electrons can only move as small polarons between the Ce^{3+} and Ce^{4+}, the conductivity prefactor depends on the number of available hopping sites in the lattice:[57,58]

$$\sigma_{elec}(T, p(O_2)) = \frac{n_{Ce} x_{Ce^{3+}}(1 - x_{Ce^{3+}}) e^2 a^2 \nu_0}{k_B T} \exp\left(-\frac{E_{A,elec}}{k_B T}\right) \quad (19)$$

Here, n_{Ce} is the number of Ce lattice sites per unit volume, $x_{Ce^{3+}}$ the fraction of Ce^{3+} ions, which is dependent on the oxygen partial pressure of the surrounding atmosphere, e the elementary charge, a the distance between the hopping sites, i.e., the lattice constant, and ν_0 represents the attempt frequency for the jump process. In addition, a high nonstoichiometry increases the lattice constant a (chemical strain effect), due to the larger ionic radius of Ce^{3+} compared to Ce^{4+},[106] which further increases the conductivity prefactor. This assumption is supported by the Raman data shown in Figure 2b, where the red-shift and broadening of the F_{2g} mode are related to tensile strain in the coating.

CONCLUSIONS

In this work, we have successfully synthesized polymer-templated, cubic mesoporous YSZ thin films with different pore sizes. The free surface of the YSZ matrix was coated with a CeO_2 layer of defined thickness using ALD to produce mixed-conducting nanocomposites. Structural characterization confirmed the single-phase nature and uniformity of the nanocrystalline YSZ (framework) and CeO_2 (coating) materials. Electrochemical impedance spectroscopy measurements were conducted on the samples at different temperatures and oxygen partial pressures to examine the effect that the coating thickness has on the transport properties. Our study indicates that the thickness of the CeO_2 coating affects the total conductivity because of changes in the Ce^{3+}/Ce^{4+} ratio and microstructure properties of the surface layer. For 3 nm coating, the total conductivity exhibits an additional electronic contribution. In contrast, nanocomposite thin films with a 7 nm coating only show oxygen-ion conductivity over the whole temperature and oxygen partial pressure ranges investigated. The results emphasize that surface engineering of mesoporous metal oxides via ALD holds great potential for the development of nanocomposites, whose electrical properties can be tailored by varying the coating thickness. Overall, this approach offers promising possibilities for the synthesis of mixed conductors with optimized transport properties for electrochemical applications.

METHODS AND EXPERIMENTAL DETAILS

Materials. $YCl_3 \cdot 6H_2O$, $ZrCl_4$, glacial acetic acid, absolute ethanol, 2-methoxyethanol, and tetrahydrofuran were purchased in the highest available purity from Sigma-Aldrich and used as received. $H[C(CH_3)_2CH_2]_xC_6H_4(OCH_2CH_2)_yOH$ (PIB_x-b-PEO_y) diblock copolymers with $x = 53/y = 45$, $x = 107/y = 150$, and $x = 357/y = 454$, referred to as PIB_{53}-b-PEO_{45}, PIB_{107}-b-PEO_{150}, and PIB_{357}-b-PEO_{454},[107−110] respectively, served as structure-directing agents (SDAs).

Synthesis. Ordered mesoporous YSZ thin films were prepared by the dip-coating method on quartz glass substrates using an evaporation-induced self-assembly (EISA) process.[54,111,112] The dip-coating solutions consisted of 40 mg of SDA, 35.9 mg of $YCl_3 \cdot 6H_2O$, and 145 mg of $ZrCl_4$ dissolved in a mixed solvent of glacial acetic acid, absolute ethanol (or tetrahydrofuran), and 2-methoxyethanol (see summary in Table S2, Supporting Information, for more details). The withdrawal rate was set to 5−15 mm/s. During the film formation process, the relative humidity was controlled in the range between 15 and 25%. The as-made samples were transferred to an oven for drying at 120 °C for 1 h. Subsequently, they were heated to 300 °C at 5 °C/min with 12 h dwell time to stabilize the mesostructure. Crystallization and SDA removal were achieved by heating to 600 °C at 5 °C/min with 1 h dwell time.

Atomic Layer Deposition. CeO_2 was deposited onto the surface of the mesoporous YSZ films at a temperature of 250 °C using a commercial ALD system (PicoSun R200 Standard). For the deposition, the cerium precursor, tetrakis(2,2,6,6-tetramethyl-3,5-heptanedionato)cerium(IV) (97%, abcr GmbH), referred to as $Ce(TMHD)_4$, was heated to 195 °C and the corresponding valve block connected to the reaction chamber kept at 230 °C. For a single ALD cycle, a 2 s pulse $Ce(TMHD)_4$ with 150 sccm nitrogen carrier gas was followed by a 60 s nitrogen purging step. Next, ozone, generated by an AC-2025 ozone generator-2000 from Teledyne API, was pulsed for 2 s. The ALD cycle was completed by an additional nitrogen purge pulse of 60 s. Under these conditions, the growth rate of CeO_2 is 0.3 Å per cycle, as discussed in more detail elsewhere.[50] The YSZ films were coated using 80 and 190 cycles, resulting in CeO_2 thicknesses of around 3 and 7 nm, respectively.

Structural Characterization. The crystallinity was investigated by grazing incidence X-ray diffraction (GIXRD) on a PANalytical X'Pert³ MRD diffractometer using an incidence angle of $\omega = 0.25°$ and a 2θ scanning range of 20−70°. The scan speed was set to 0.6° min^{-1}, and the step size was 0.01°. Raman measurements were carried out using an inVia Raman microscope from Renishaw in back-scattering geometry with an excitation wavelength of $\lambda = 633$ nm. Scanning electron microscopy (SEM) images were recorded on a MERLIN from Carl Zeiss at 3 kV. Transmission electron microscopy (TEM) was performed on a Themis Z (ThermoFisher Scientific) double-corrected transmission electron microscope operated at 300 kV. Pieces of the samples were placed on Quantifoil Cu grids with a carbon film of thickness 2 nm. Scanning TEM (STEM) images were recorded using a high-angle annular dark-field (HAADF) detector. Elemental maps were acquired using a Super-X EDS (EDAX) detector. X-ray photoelectron spectroscopy (XPS) measurements were performed with a PHI 5000 VersaProbe II from Ulvac-Phi using Al−Kα radiation ($\lambda = 1486.6$ eV). A spot of diameter 200 μm was measured utilizing 50 W, 0.5 kV, and 20 ms per step. A pass energy of 23.5 eV was applied for the survey spectra, while 117.4 eV was applied for the detailed spectra of Ce 3d, Y 3d, and Zr 3d. The spectra were calibrated by setting the C 1s peak at 284.8 eV. The software CasaXPS V2.3.17 was used for peak analysis. In addition to the six signals from CeO_2 (v, v'', v''' and u, u'', u'''), four signals from Ce_2O_3 (v_0, v' and u_0, u') were considered,[113] the latter of which typically arise because of the presence of Ce^{3+} at the interface.[23,50] In order to achieve better results, a combination of two signals for fitting the asymmetry (u and v) was used, in agreement with the findings of Skála et al.[114] Time-of-flight secondary ion mass spectrometry (ToF-SIMS) was performed using a ToF.SIMS 5-10 instrument from IONTOF GmbH (Muenster, Germany) equipped with at 25 keV Bi cluster primary-ion gun. Depth profiling was done using Cs^+ ions at 1 keV and 50 nA, generating a 100 × 100 μm^2 crater. A 50 × 50 μm^2 of the crater was analyzed with a resolution of 256 × 256 $pixel^2$ using a Bi(1) primary-ion source, collecting only the negatively charged ions. Data evaluation was done with the software SurfaceLab7.0 from IONTOF GmbH.

Preparation of Microelectrodes. Interdigitated Pt microelectrodes on the top surface of the films were produced by

https://doi.org/10.1021/acsnano.1c11032
ACS Nano 2022, 16, 3182−3193

photolithography. To this end, a positive photoresist was used (ma-P 1215, micro resist technology GmbH). For metallization, Pt was deposited by pulsed laser deposition (PLD) using a KrF excimer laser with a wavelength of λ = 248 nm. The interdigitated Pt electrodes had a thickness of around 200 nm and were made of 20 fingers of 3 mm length and 47 μm width. The distance between the fingers was 33 μm. The Pt electrode configuration is schematically shown in Figure S5 of the Supporting Information.

Electrochemical Characterization. The electrochemical properties of the YSZ thin films were investigated by electrochemical impedance spectroscopy (EIS) in the frequency range between 1 mHz and 10 MHz using a Novocontrol Alpha-A impedance bridge. The voltage amplitude was 100 mV. The temperature was varied between 200 and 600 °C. The oxygen partial pressure was controlled in the range of $-5 < \log(p(O_2)/\text{bar}) < 0$ using gas mixtures of argon and oxygen. EIS data were evaluated by means of the software RelaxIS 3.[49]

ASSOCIATED CONTENT

Supporting Information

The Supporting Information is available free of charge at https://pubs.acs.org/doi/10.1021/acsnano.1c11032.

Top-view SEM images of the investigated thin films; HRTEM images of uncoated YSZ; HAADF-STEM images and EDS maps of ceria-coated YSZ; impedance spectra of uncoated and ceria-coated YSZ; schematic illustration of the interdigitated Pt electrodes; activation energy as a function of temperature for uncoated and ceria-coated YSZ; oxygen partial-pressure-dependence of the total conductivity; Arrhenius plots of the total conductance and fitting parameters of the transport properties for ceria-coated YSZ; and recipes for the synthesis of mesoporous 8YSZ thin films (PDF)

AUTHOR INFORMATION

Corresponding Authors

Erdogan Celik − *Center for Materials Research, Justus-Liebig-University Giessen, 35392 Giessen, Germany;* Email: erdogan.celik@materialwiss.uni-giessen.de

Matthias T. Elm − *Center for Materials Research, Justus-Liebig-University Giessen, 35392 Giessen, Germany; Institute of Physical Chemistry, Justus-Liebig-University Giessen, 35392 Giessen, Germany; Institute of Experimental Physics I, Justus-Liebig-University Giessen, 35392 Giessen, Germany;* orcid.org/0000-0001-7014-5772; Email: matthias.elm@phys.chemie.uni-giessen.de

Authors

Pascal Cop − *Center for Materials Research, Justus-Liebig-University Giessen, 35392 Giessen, Germany; Institute of Physical Chemistry, Justus-Liebig-University Giessen, 35392 Giessen, Germany*

Rajendra S. Negi − *Center for Materials Research, Justus-Liebig-University Giessen, 35392 Giessen, Germany*

Andrey Mazilkin − *Institute of Nanotechnology, Karlsruhe Institute of Technology (KIT), 76344 Eggenstein-Leopoldshafen, Germany*

Yanjiao Ma − *Institute of Nanotechnology, Karlsruhe Institute of Technology (KIT), 76344 Eggenstein-Leopoldshafen, Germany;* orcid.org/0000-0002-4125-2867

Philip Klement − *Center for Materials Research, Justus-Liebig-University Giessen, 35392 Giessen, Germany; Institute of Experimental Physics I, Justus-Liebig-University Giessen, 35392 Giessen, Germany;* orcid.org/0000-0001-7044-713X

Jörg Schörmann − *Center for Materials Research, Justus-Liebig-University Giessen, 35392 Giessen, Germany; Institute of Experimental Physics I, Justus-Liebig-University Giessen, 35392 Giessen, Germany*

Sangam Chatterjee − *Center for Materials Research, Justus-Liebig-University Giessen, 35392 Giessen, Germany; Institute of Experimental Physics I, Justus-Liebig-University Giessen, 35392 Giessen, Germany;* orcid.org/0000-0002-0237-5880

Torsten Brezesinski − *Institute of Nanotechnology, Karlsruhe Institute of Technology (KIT), 76344 Eggenstein-Leopoldshafen, Germany;* orcid.org/0000-0002-4336-263X

Complete contact information is available at: https://pubs.acs.org/10.1021/acsnano.1c11032

Notes

The authors declare no competing financial interest.

ACKNOWLEDGMENTS

Financial support by the German Research Foundation (to T.B., Grant No. BR 3499/5-1 and to M.T.E., Grant No. EL 863/3-1) is gratefully acknowledged. P.K., R.S.N., and M.T.E. acknowledge the German Federal Ministry of Education and Research for funding the NanoMatFutur Project NiKo (Grant 03XP0093). S.C. acknowledges financial support by the Heisenberg Program (Grant CH660/8). The authors acknowledge the support from the Karlsruhe Nano Micro Facility (KNMF, www.knmf.kit.edu), a Helmholtz research infrastructure at Karlsruhe Institute of Technology (KIT, www.kit.edu).

REFERENCES

(1) Walcarius, A. Mesoporous Materials and Electrochemistry. *Chem. Soc. Rev.* **2013**, *42* (9), 4098.

(2) Rolison, D. R. Catalytic Nanoarchitectures - The Importance of Nothing and the Unimportance of Periodicity. *Science* **2003**, *299* (5613), 1698−1701.

(3) Celik, E.; Ma, Y.; Brezesinski, T.; Elm, M. T. Ordered Mesoporous Metal Oxides for Electrochemical Applications: Correlation between Structure, Electrical Properties and Device Performance. *Phys. Chem. Chem. Phys.* **2021**, *23* (18), 10706−10735.

(4) Li, W.; Liu, J.; Zhao, D. Mesoporous Materials for Energy Conversion and Storage Devices. *Nat. Rev. Mater.* **2016**, *1* (6), 16023.

(5) Zu, L.; Zhang, W.; Qu, L.; Liu, L.; Li, W.; Yu, A.; Zhao, D. Mesoporous Materials for Electrochemical Energy Storage and Conversion. *Adv. Energy Mater.* **2020**, *10* (38), 2002152.

(6) Ren, Y.; Ma, Z.; Bruce, P. G. Ordered Mesoporous Metal Oxides: Synthesis and Applications. *Chem. Soc. Rev.* **2012**, *41* (14), 4909−4927.

(7) Liu, H.; Wang, G.; Liu, J.; Qiao, S.; Ahn, H. Highly Ordered Mesoporous NiO Anode Material for Lithium Ion Batteries with an Excellent Electrochemical Performance. *J. Mater. Chem.* **2011**, *21* (9), 3046−3052.

(8) Wagner, T.; Haffer, S.; Weinberger, C.; Klaus, D.; Tiemann, M. Mesoporous Materials as Gas Sensors. *Chem. Soc. Rev.* **2013**, *42* (9), 4036−4053.

(9) Baiutti, F.; Blanco-Portals, J.; Anelli, S.; Torruella, P.; López-Haro, M.; Calvino, J.; Estradé, S.; Torrell, M.; Peiró, F.; Tarancón, A. Tailoring the Transport Properties of Mesoporous Doped Cerium Oxide for Energy Applications. *J. Phys. Chem. C* **2021**, *125* (30), 16451−16463.

(10) Cherevan, A. S.; Deilmann, L.; Weller, T.; Eder, D.; Marschall, R. Mesoporous Semiconductors: A New Model To Assess Accessible

Surface Area and Increased Photocatalytic Activity? *ACS Appl. Energy Mater.* **2018**, *1* (11), 5787−5799.
(11) Brezesinski, T.; Wang, J.; Tolbert, S. H.; Dunn, B. Ordered Mesoporous α-MoO_3 with Iso-Oriented Nanocrystalline Walls for Thin-Film Pseudocapacitors. *Nat. Mater.* **2010**, *9* (2), 146−151.
(12) Ren, Y.; Ma, Z.; Qian, L.; Dai, S.; He, H.; Bruce, P. G. Ordered Crystalline Mesoporous Oxides as Catalysts for CO Oxidation. *Catal. Lett.* **2009**, *131* (1−2), 146−154.
(13) Hartmann, P.; Lee, D.-K.; Smarsly, B. M.; Janek, J. Mesoporous TiO_2: Comparison of Classical Sol−Gel and Nanoparticle Based Photoelectrodes for the Water Splitting Reaction. *ACS Nano* **2010**, *4* (6), 3147−3154.
(14) Kirchberg, K.; Wang, S.; Wang, L.; Marschall, R. Mesoporous $ZnFe_2O_4$ Photoanodes with Template-Tailored Mesopores and Temperature-Dependent Photocurrents. *ChemPhysChem* **2018**, *19* (18), 2313−2320.
(15) Weller, T.; Sann, J.; Marschall, R. Pore Structure Controlling the Activity of Mesoporous Crystalline $CsTaWO_6$ for Photocatalytic Hydrogen Generation. *Adv. Energy Mater.* **2016**, *6* (16), 1600208.
(16) Tiemann, M.; Weinberger, C. Selective Modification of Hierarchical Pores and Surfaces in Nanoporous Materials. *Adv. Mater. Interfaces* **2021**, *8* (4), 2001153.
(17) Bastakoti, B. P.; Kuila, D.; Salomon, C.; Konarova, M.; Eguchi, M.; Na, J.; Yamauchi, Y. Metal-Incorporated Mesoporous Oxides: Synthesis and Applications. *J. Hazard. Mater.* **2021**, *401*, 123348.
(18) An, K.; Alayoglu, S.; Musselwhite, N.; Plamthottam, S.; Melaet, G.; Lindeman, A. E.; Somorjai, G. A. Enhanced CO Oxidation Rates at the Interface of Mesoporous Oxides and Pt Nanoparticles. *J. Am. Chem. Soc.* **2013**, *135* (44), 16689−16696.
(19) Tanaka, S.; Lin, J.; Kaneti, Y. V.; Yusa, S.; Jikihara, Y.; Nakayama, T.; Zakaria, M. B.; Alshehri, A. A.; You, J.; Hossain, M. S. A.; et al. Gold Nanoparticles Supported on Mesoporous Iron Oxide for Enhanced CO Oxidation Reaction. *Nanoscale* **2018**, *10* (10), 4779−4785.
(20) George, S. M. Atomic Layer Deposition: An Overview. *Chem. Rev.* **2010**, *110* (1), 111−131.
(21) Detavernier, C.; Dendooven, J.; Pulinthanathu Sree, S.; Ludwig, K. F.; Martens, J. A. Tailoring Nanoporous Materials by Atomic Layer Deposition. *Chem. Soc. Rev.* **2011**, *40* (11), 5242−5253.
(22) Asundi, A. S.; Raiford, J. A.; Bent, S. F. Opportunities for Atomic Layer Deposition in Emerging Energy Technologies. *ACS Energy Lett.* **2019**, *4* (4), 908−925.
(23) Zscherp, M. F.; Glaser, J.; Becker, C.; Beyer, A.; Cop, P.; Schörmann, J.; Volz, K.; Elm, M. T. Epitaxial Growth and Structural Characterization of Ceria Deposited by Atomic Layer Deposition on High-Surface Porous Yttria-Stabilized Zirconia Thin Films. *Cryst. Growth Des.* **2020**, *20* (4), 2194−2201.
(24) Elam, J. W.; Xiong, G.; Han, C. Y.; Wang, H. H.; Birrell, J. P.; Hryn, J. N.; Pellin, M. J.; Poco, J. F.; Satcher, J. H. Atomic Layer Deposition for the Conformal Coating of Nanoporous Materials. *MRS Proc.* **2005**, *876*, 126.
(25) Shin, J. W.; Go, D.; Kye, S. H.; Lee, S.; An, J. Review on Process-Microstructure-Performance Relationship in ALD-Engineered SOFCs. *J. Phys. Energy* **2019**, *1* (4), 042002.
(26) Wen, L.; Zhou, M.; Wang, C.; Mi, Y.; Lei, Y. Nanoengineering Energy Conversion and Storage Devices via Atomic Layer Deposition. *Adv. Energy Mater.* **2016**, *6* (23), 1600468.
(27) Marichy, C.; Bechelany, M.; Pinna, N. Atomic Layer Deposition of Nanostructured Materials for Energy and Environmental Applications. *Adv. Mater.* **2012**, *24* (8), 1017−1032.
(28) Kraffert, K.; Karg, M.; Schmack, R.; Clavel, G.; Boissiere, C.; Wirth, T.; Pinna, N.; Kraehnert, R. Stabilization of Mesoporous Iron Oxide Films against Sintering and Phase Transformations via Atomic Layer Deposition of Alumina and Silica. *Adv. Mater. Interfaces* **2018**, *5* (14), 1800360.
(29) Dubraja, L. A.; Boll, D.; Reitz, C.; Wang, D.; Belić, D.; Mazilkin, A.; Breitung, B.; Hahn, H.; Elm, M. T.; Brezesinski, T. Thin Films of Thermally Stable Ordered Mesoporous Rh_2O_3(I) for Visible-Light Photocatalysis and Humidity Sensing. *ACS Appl. Nano Mater.* **2019**, *2* (11), 7126−7133.
(30) Pagán-Torres, Y. J.; Gallo, J. M. R.; Wang, D.; Pham, H. N.; Libera, J. A.; Marshall, C. L.; Elam, J. W.; Datye, A. K.; Dumesic, J. A. Synthesis of Highly Ordered Hydrothermally Stable Mesoporous Niobia Catalysts by Atomic Layer Deposition. *ACS Catal.* **2011**, *1* (10), 1234−1245.
(31) Negi, R. S.; Culver, S. P.; Wiche, M.; Ahmed, S.; Volz, K.; Elm, M. T. Optimized Atomic Layer Deposition of Homogeneous, Conductive Al_2O_3 Coatings for High-Nickel NCM Containing Ready-to-Use Electrodes. *Phys. Chem. Chem. Phys.* **2021**, *23* (11), 6725−6737.
(32) Hemmelmann, H.; Dinter, J. K.; Elm, M. T. Thin Film NCM Cathodes as Model Systems to Assess the Influence of Coating Layers on the Electrochemical Performance of Lithium Ion Batteries. *Adv. Mater. Interfaces* **2021**, *8* (9), 2002074.
(33) Neudeck, S.; Mazilkin, A.; Reitz, C.; Hartmann, P.; Janek, J.; Brezesinski, T. Effect of Low-Temperature Al_2O_3 ALD Coating on Ni-Rich Layered Oxide Composite Cathode on the Long-Term Cycling Performance of Lithium-Ion Batteries. *Sci. Rep.* **2019**, *9* (1), 5328.
(34) Kitsche, D.; Tang, Y.; Ma, Y.; Goonetilleke, D.; Sann, J.; Walther, F.; Bianchini, M.; Janek, J.; Brezesinski, T. High Performance All-Solid-State Batteries with a Ni-Rich NCM Cathode Coated by Atomic Layer Deposition and Lithium Thiophosphate Solid Electrolyte. *ACS Appl. Energy Mater.* **2021**, *4* (7), 7338−7345.
(35) Meng, X.; Yang, X.-Q.; Sun, X. Emerging Applications of Atomic Layer Deposition for Lithium-Ion Battery Studies. *Adv. Mater.* **2012**, *24* (27), 3589−3615.
(36) Woo, J. H.; Trevey, J. E.; Cavanagh, A. S.; Choi, Y. S.; Kim, S. C.; George, S. M.; Oh, K. H.; Lee, S.-H. Nanoscale Interface Modification of $LiCoO_2$ by Al_2O_3 Atomic Layer Deposition for Solid-State Li Batteries. *J. Electrochem. Soc.* **2012**, *159* (7), A1120−A1124.
(37) Weber, D.; Tripković, Đ.; Kretschmer, K.; Bianchini, M.; Brezesinski, T. Surface Modification Strategies for Improving the Cycling Performance of Ni-Rich Cathode Materials. *Eur. J. Inorg. Chem.* **2020**, *2020* (33), 3117−3130.
(38) Fan, Z.; Prinz, F. B. Enhancing Oxide Ion Incorporation Kinetics by Nanoscale Yttria-Doped Ceria Interlayers. *Nano Lett.* **2011**, *11* (6), 2202−2205.
(39) Fan, Z.; Chao, C.-C.; Hossein-Babaei, F.; Prinz, F. B. Improving Solid Oxide Fuel Cells with Yttria-Doped Ceria Interlayers by Atomic Layer Deposition. *J. Mater. Chem.* **2011**, *21* (29), 10903−10906.
(40) Chen, Y.; Gerdes, K.; Song, X. Nanoionics and Nanocatalysts: Conformal Mesoporous Surface Scaffold for Cathode of Solid Oxide Fuel Cells. *Sci. Rep.* **2016**, *6* (1), 32997.
(41) Tuller, H. L. Oxygen Ion Conduction and Structural Disorder in Conductive Oxides. *J. Phys. Chem. Solids* **1994**, *55* (12), 1393−1404.
(42) Fu, L.; Chen, C.-C.; Maier, J. Interfacial Mass Storage in Nanocomposites. *Solid State Ionics* **2018**, *318*, 54−59.
(43) Chen, C.-C.; Maier, J. Decoupling Electron and Ion Storage and the Path from Interfacial Storage to Artificial Electrodes. *Nat. Energy* **2018**, *3* (2), 102−108.
(44) Chen, C.-C.; Fu, L.; Maier, J. Synergistic, Ultrafast Mass Storage and Removal in Artificial Mixed Conductors. *Nature* **2016**, *536* (7615), 159−164.
(45) Fu, L.; Tang, K.; Oh, H.; Manickam, K.; Bräuniger, T.; Chandran, C. V.; Menzel, A.; Hirscher, M.; Samuelis, D.; Maier, J. "Job-Sharing" Storage of Hydrogen in Ru/Li_2O Nanocomposites. *Nano Lett.* **2015**, *15* (6), 4170−4175.
(46) Liao, P.; MacDonald, B. L.; Dunlap, R. A.; Dahn, J. R. Combinatorially Prepared $LiF_{1-x}Fe_x$ Nanocomposites for Positive Electrode Materials in Li-Ion Batteries. *Chem. Mater.* **2008**, *20* (2), 454−461.
(47) Yu, X. Q.; Sun, J. P.; Tang, K.; Li, H.; Huang, X. J.; Dupont, L.; Maier, J. Reversible Lithium Storage in LiF/Ti Nanocomposites. *Phys. Chem. Chem. Phys.* **2009**, *11* (41), 9497−9503.

https://doi.org/10.1021/acsnano.1c11032
ACS Nano 2022, 16, 3182−3193

(48) Li, Q.; Li, H.; Xia, Q.; Hu, Z.; Zhu, Y.; Yan, S.; Ge, C.; Zhang, Q.; Wang, X.; Shang, X.; et al. Extra Storage Capacity in Transition Metal Oxide Lithium-Ion Batteries Revealed by in Situ Magnetometry. *Nat. Mater.* **2021**, *20* (1), 76−83.
(49) Celik, E.; Negi, R. S.; Bastianello, M.; Boll, D.; Mazilkin, A.; Brezesinski, T.; Elm, M. T. Tailoring the Protonic Conductivity of Porous Yttria-Stabilized Zirconia Thin Films by Surface Modification. *Phys. Chem. Chem. Phys.* **2020**, *22* (20), 11519−11528.
(50) Cop, P.; Celik, E.; Hess, K.; Moryson, Y.; Klement, P.; Elm, M. T.; Smarsly, B. M. Atomic Layer Deposition of Nanometer-Sized CeO_2 Layers in Ordered Mesoporous ZrO_2 Films and Their Impact on the Ionic/Electronic Conductivity. *ACS Appl. Nano Mater.* **2020**, *3* (11), 10757−10766.
(51) Jacobson, A. J. Materials for Solid Oxide Fuel Cells. *Chem. Mater.* **2010**, *22* (3), 660−674.
(52) Hui, S.; Roller, J.; Yick, S.; Zhang, X.; Decès-Petit, C.; Xie, Y.; Maric, R.; Ghosh, D. A Brief Review of the Ionic Conductivity Enhancement for Selected Oxide Electrolytes. *J. Power Sources* **2007**, *172* (2), 493−502.
(53) Kilner, J. A.; Burriel, M. Materials for Intermediate-Temperature Solid-Oxide Fuel Cells. *Annu. Rev. Mater. Res.* **2014**, *44* (1), 365−393.
(54) Elm, M. T.; Hofmann, J. D.; Suchomski, C.; Janek, J.; Brezesinski, T. Ionic Conductivity of Mesostructured Yttria-Stabilized Zirconia Thin Films with Cubic Pore Symmetry—On the Influence of Water on the Surface Oxygen Ion Transport. *ACS Appl. Mater. Interfaces* **2015**, *7* (22), 11792−11801.
(55) Park, J.; Blumenthal, R. N. Electronic Transport in 8 Mole Percent Y_2O_3 - ZrO_2. *J. Electrochem. Soc.* **1989**, *136* (10), 2867−2876.
(56) Trovarelli, A. Catalytic Properties of Ceria and CeO_2 -Containing Materials. *Catal. Rev.* **1996**, *38* (4), 439−520.
(57) Michel, K.; Eufinger, J.-P.; Ulbrich, G.; Lerch, M.; Janek, J.; Elm, M. T. Combining Two Redox Active Rare Earth Elements for Oxygen Storage − Electrical Properties and Defect Chemistry of Ceria−Praseodymia Single Crystals. *Phys. Chem. Chem. Phys.* **2017**, *19* (27), 17661−17669.
(58) Tuller, H. L.; Nowick, A. S. Small Polaron Electron Transport in Reduced CeO_2 Single Crystals. *J. Phys. Chem. Solids* **1977**, *38* (8), 859−867.
(59) Tuller, H. L.; Nowick, A. S. Defect Structure and Electrical Properties of Nonstoichiometric CeO_2 Single Crystals. *J. Electrochem. Soc.* **1979**, *126* (2), 209−217.
(60) Naik, I. K.; Tien, T. Y. Small-Polaron Mobility in Nonstoichiometric Cerium Dioxide. *J. Phys. Chem. Solids* **1978**, *39* (3), 311−315.
(61) Chiang, Y. M.; Lavik, E. B.; Kosacki, I.; Tuller, H. L.; Ying, J. Y. Nonstoichiometry and Electrical Conductivity of Nanocrystalline CeO_{2-x}. *J. Electroceramics* **1997**, *1* (1), 7−14.
(62) Yashima, M.; Sasaki, S.; Kakihana, M.; Yamaguchi, Y.; Arashi, H.; Yoshimura, M. Oxygen-Induced Structural Change of the Tetragonal Phase around the Tetragonal−Cubic Phase Boundary in ZrO_2−$YO_{1.5}$ Solid Solutions. *Acta Crystallogr. Sect. B Struct. Sci.* **1994**, *50* (6), 663−672.
(63) Debye, P.; Scherrer, P. Atombau. *Nachrichten von der Gesellschaft der Wissenschaften zu Göttingen, Math. Klasse* **1918**, *1918*, 101−120.
(64) Fujimori, H.; Yashima, M.; Sasaki, S.; Kakihana, M.; Mori, T.; Tanaka, M.; Yoshimura, M. Internal Distortion in Ceria-Doped Hafnia Solid Solutions: High-Resolution X-Ray Diffraction and Raman Scattering. *Phys. Rev. B* **2001**, *64* (13), 134104.
(65) Sun, Y.; Li, C.; Djerdj, I.; Khalid, O.; Cop, P.; Sann, J.; Weber, T.; Werner, S.; Turke, K.; Guo, Y.; et al. Oxygen Storage Capacity versus Catalytic Activity of Ceria−Zirconia Solid Solutions in CO and HCl Oxidation. *Catal. Sci. Technol.* **2019**, *9* (9), 2163−2172.
(66) Briois, P.; Lapostolle, F.; Demange, V.; Djurado, E.; Billard, A. Structural Investigations of YSZ Coatings Prepared by DC Magnetron Sputtering. *Surf. Coat. Technol.* **2007**, *201* (12), 6012−6018.
(67) Cai, J.; Raptis, C.; Raptis, Y. S.; Anastassakis, E. Temperature Dependence of Raman Scattering in Stabilized Cubic Zirconia. *Phys. Rev. B* **1995**, *51* (1), 201−209.
(68) Popović, Z. V.; Dohčević-Mitrović, Z.; Šćepanović, M.; Grujić-Brojčin, M.; Aškrabić, S. Raman Scattering on Nanomaterials and Nanostructures. *Ann. Phys.* **2011**, *523* (1−2), 62−74.
(69) Chan, C. K.; Peng, H.; Liu, G.; McIlwrath, K.; Zhang, X. F.; Huggins, R. A.; Cui, Y. High-Performance Lithium Battery Anodes Using Silicon Nanowires. *Nat. Nanotechnol.* **2008**, *3* (1), 31−35.
(70) Kosacki, I.; Suzuki, T.; Anderson, H. U.; Colomban, P. Raman Scattering and Lattice Defects in Nanocrystalline CeO_2 Thin Films. *Solid State Ionics* **2002**, *149* (1−2), 99−105.
(71) Kourouklis, G. A.; Jayaraman, A.; Espinosa, G. P. High-Pressure Raman Study of CeO_2 to 35 GPa and Pressure-Induced Phase Transformation from the Fluorite Structure. *Phys. Rev. B* **1988**, *37* (8), 4250−4253.
(72) Spanier, J. E.; Robinson, R. D.; Zhang, F.; Chan, S.-W.; Herman, I. P. Size-Dependent Properties of CeO_{2-y} Nanoparticles as Studied by Raman Scattering. *Phys. Rev. B* **2001**, *64* (24), 245407.
(73) Campbell, I. H.; Fauchet, P. M. The Effects of Microcrystal Size and Shape on the One Phonon Raman Spectra of Crystalline Semiconductors. *Solid State Commun.* **1986**, *58* (10), 739−741.
(74) Filtschew, A.; Hofmann, K.; Hess, C. Ceria and Its Defect Structure: New Insights from a Combined Spectroscopic Approach. *J. Phys. Chem. C* **2016**, *120* (12), 6694−6703.
(75) Dohčević-Mitrović, Z. D.; Šćepanović, M. J.; Grujić-Brojčin, M. U.; Popović, Z. V.; Bošković, S. B.; Matović, B. M.; Zinkevich, M. V.; Aldinger, F. The Size and Strain Effects on the Raman Spectra of $Ce_{1-x}Nd_xO_{2-\delta}$ ($0 \leq x \leq 0.25$) Nanopowders. *Solid State Commun.* **2006**, *137* (7), 387−390.
(76) Gupta, M.; Kumar, A.; Sagdeo, A.; Sagdeo, P. R. Doping-Induced Combined Fano and Phonon Confinement Effect in La-Doped CeO_2: Raman Spectroscopy Analysis. *J. Phys. Chem. C* **2021**, *125* (4), 2648−2658.
(77) Weber, W. H.; Hass, K. C.; McBride, J. R. Raman Study of CeO_2: Second-Order Scattering, Lattice Dynamics, and Particle-Size Effects. *Phys. Rev. B* **1993**, *48* (1), 178−185.
(78) Konetschny, A.; Weinhold, M.; Heiliger, C.; Elm, M. T.; Klar, P. J. Polarization-Dependence of the Raman Response of Free-Standing Strained $Ce_{0.8}Gd_{0.2}O_2$ Membranes. *Phys. Chem. Chem. Phys.* **2021**, *23* (11), 6903−6913.
(79) Dendooven, J.; Devloo-Casier, K.; Ide, M.; Grandfield, K.; Kurttepeli, M.; Ludwig, K. F.; Bals, S.; Van Der Voort, P.; Detavernier, C. Atomic Layer Deposition-Based Tuning of the Pore Size in Mesoporous Thin Films Studied by in Situ Grazing Incidence Small Angle X-Ray Scattering. *Nanoscale* **2014**, *6* (24), 14991−14998.
(80) Ma, Y.; Ma, Y.; Giuli, G.; Euchner, H.; Groß, A.; Lepore, G. O.; D'Acapito, F.; Geiger, D.; Biskupek, J.; Kaiser, U.; et al. Introducing Highly Redox-Active Atomic Centers into Insertion-Type Electrodes for Lithium-Ion Batteries. *Adv. Energy Mater.* **2020**, *10* (25), 2000783.
(81) Artiglia, L.; Agnoli, S.; Paganini, M. C.; Cattelan, M.; Granozzi, G. TiO_2@CeO_x Core-Shell Nanoparticles as Artificial Enzymes with Peroxidase-like Activity. *ACS Appl. Mater. Interfaces* **2014**, *6* (22), 20130−20136.
(82) Yue, J.; Suchomski, C.; Voepel, P.; Ellinghaus, R.; Rohnke, M.; Leichtweiss, T.; Elm, M. T.; Smarsly, B. M. Mesoporous Niobium-Doped Titanium Dioxide Films from the Assembly of Crystalline Nanoparticles: Study on the Relationship between the Band Structure, Conductivity and Charge Storage Mechanism. *J. Mater. Chem. A* **2017**, *5* (5), 1978−1988.
(83) Hao, X.; Yoko, A.; Chen, C.; Inoue, K.; Saito, M.; Seong, G.; Takami, S.; Adschiri, T.; Ikuhara, Y. Atomic-Scale Valence State Distribution inside Ultrafine CeO_2 Nanocubes and Its Size Dependence. *Small* **2018**, *14* (42), 1802915.
(84) Hartmann, P.; Brezesinski, T.; Sann, J.; Lotnyk, A.; Eufinger, J.-P.; Kienle, L.; Janek, J. Defect Chemistry of Oxide Nanomaterials with High Surface Area: Ordered Mesoporous Thin Films of the Oxygen Storage Catalyst CeO_2−ZrO_2. *ACS Nano* **2013**, *7* (4), 2999−3013.

https://doi.org/10.1021/acsnano.1c11032
ACS Nano 2022, 16, 3182−3193

(85) Sun, S.; Gao, Q.; Wang, H.; Zhu, J.; Guo, H. Influence of Textural Parameters on the Catalytic Behavior for CO Oxidation over Ordered Mesoporous Co_3O_4. *Appl. Catal. B Environ.* **2010**, *97* (1−2), 284−291.
(86) Fleig, J. The Grain Boundary Impedance of Random Microstructures: Numerical Simulations and Implications for the Analysis of Experimental Data. *Solid State Ionics* **2002**, *150* (1), 181−193.
(87) Irvine, J. T. S.; Sinclair, D. C.; West, A. R. Electroceramics: Characterization by Impedance Spectroscopy. *Adv. Mater.* **1990**, *2* (3), 132−138.
(88) Gerstl, M.; Navickas, E.; Friedbacher, G.; Kubel, F.; Ahrens, M.; Fleig, J. The Separation of Grain and Grain Boundary Impedance in Thin Yttria Stabilized Zirconia (YSZ) Layers. *Solid State Ionics* **2011**, *185* (1), 32−41.
(89) Kosacki, I.; Anderson, H. U. Microstructure — Property Relationships in Nanocrystalline Oxide Thin Films. *Ionics (Kiel).* **2000**, *6* (3), 294−311.
(90) Bieberle-Hütter, A.; Hertz, J. L.; Tuller, H. L. Fabrication and Electrochemical Characterization of Planar Pt−CGO Microstructures. *Acta Mater.* **2008**, *56* (2), 177−187.
(91) Jiang, J.; Hertz, J. L. On the Variability of Reported Ionic Conductivity in Nanoscale YSZ. Thin Films. *J. Electroceramics* **2014**, *32* (1), 37−46.
(92) Eckhardt, J. K.; Burkhardt, S.; Zahnow, J.; Elm, M. T.; Janek, J.; Klar, P. J.; Heiliger, C. Understanding the Impact of Microstructure on Charge Transport in Polycrystalline Materials Through Impedance Modelling. *J. Electrochem. Soc.* **2021**, *168* (9), 090516.
(93) Zahnow, J.; Bernges, T.; Wagner, A.; Bohn, N.; Binder, J. R.; Zeier, W. G.; Elm, M. T.; Janek, J. Impedance Analysis of NCM Cathode Materials: Electronic and Ionic Partial Conductivities and the Influence of Microstructure. *ACS Appl. Energy Mater.* **2021**, *4* (2), 1335−1345.
(94) Kogut, I.; Steiner, C.; Wulfmeier, H.; Wollbrink, A.; Hagen, G.; Moos, R.; Fritze, H. Comparison of the Electrical Conductivity of Bulk and Film $Ce_{1-x}Zr_xO_{2-\delta}$ in Oxygen-Depleted Atmospheres at High Temperatures. *J. Mater. Sci.* **2021**, *56* (30), 17191−17204.
(95) Chiodelli, G.; Flor, G.; Scagliotti, M. Electrical Properties of the ZrO_2-CeO_2 System. *Solid State Ionics* **1996**, *91* (1), 109−121.
(96) Huang, B.; Gillen, R.; Robertson, J. Study of CeO_2 and Its Native Defects by Density Functional Theory with Repulsive Potential. *J. Phys. Chem. C* **2014**, *118* (42), 24248−24256.
(97) Keating, P. R. L.; Scanlon, D. O.; Morgan, B. J.; Galea, N. M.; Watson, G. W. Analysis of Intrinsic Defects in CeO_2 Using a Koopmans-Like GGA+ U Approach. *J. Phys. Chem. C* **2012**, *116* (3), 2443−2452.
(98) Zacherle, T.; Schriever, A.; De Souza, R. A.; Martin, M. Ab Initio Analysis of the Defect Structure of Ceria. *Phys. Rev. B - Condens. Matter Mater. Phys.* **2013**, *87* (13), 134104.
(99) Neumeier, J. J.; Elm, M. T.; Luerßen, B.; Janek, J. Platinum Microelectrodes on Gadolinia Doped Ceria Single Crystals − Bulk Properties and Electrode Kinetics. *Phys. Chem. Chem. Phys.* **2018**, *20* (12), 8294−8301.
(100) Kosacki, I.; Suzuski, T.; Petrovsky, V.; Anderson, H. U. Electrical Conductivity of Nanocrystalline Ceria and Zirconia Thin Films. *Solid State Ionics* **2000**, *136−137* (1−2), 1225−1233.
(101) Tuller, H. L. Semiconduction and Mixed Ionic-Electronic Conduction in Nonstoichiometric Oxides: Impact and Control. *Solid State Ionics* **1997**, *94* (1), 63−74.
(102) Chiang, Y.-M.; Lavik, E. B.; Kosacki, I.; Tuller, H. L.; Ying, J. Y. Defect and Transport Properties of Nanocrystalline CeO_{2-x}. *Appl. Phys. Lett.* **1996**, *69* (2), 185−187.
(103) Tschöpe, A. Grain Size-Dependent Electrical Conductivity of Polycrystalline Cerium Oxide. II: Space Charge Model. *Solid State Ionics* **2001**, *139* (3−4), 267−280.
(104) Migani, A.; Vayssilov, G. N.; Bromley, S. T.; Illas, F.; Neyman, K. M. Dramatic Reduction of the Oxygen Vacancy Formation Energy in Ceria Particles: A Possible Key to Their Remarkable Reactivity at the Nanoscale. *J. Mater. Chem.* **2010**, *20* (46), 10535−10546.
(105) Migani, A.; Vayssilov, G. N.; Bromley, S. T.; Illas, F.; Neyman, K. M. Greatly Facilitated Oxygen Vacancy Formation in Ceria Nanocrystallites. *Chem. Commun.* **2010**, *46* (32), 5936−5938.
(106) Marrocchelli, D.; Bishop, S. R.; Tuller, H. L.; Yildiz, B. Understanding Chemical Expansion in Non-Stoichiometric Oxides: Ceria and Zirconia Case Studies. *Adv. Funct. Mater.* **2012**, *22* (9), 1958−1965.
(107) Weidmann, C.; Brezesinski, K.; Suchomski, C.; Tropp, K.; Grosser, N.; Haetge, J.; Smarsly, B. M.; Brezesinski, T. Morphology-Controlled Synthesis of Nanocrystalline η-Al_2O_3 Thin Films, Powders, Microbeads, and Nanofibers with Tunable Pore Sizes from Preformed Oligomeric Oxo-Hydroxo Building Blocks. *Chem. Mater.* **2012**, *24* (3), 486−494.
(108) Reitz, C.; Haetge, J.; Suchomski, C.; Brezesinski, T. Facile and General Synthesis of Thermally Stable Ordered Mesoporous Rare-Earth Oxide Ceramic Thin Films with Uniform Mid-Size to Large-Size Pores and Strong Crystalline Texture. *Chem. Mater.* **2013**, *25* (22), 4633−4642.
(109) Graberg, T. Von; Hartmann, P.; Rein, A.; Gross, S.; Seelandt, B.; Röger, C.; Zieba, R.; Traut, A.; Wark, M.; Janek, J.; et al. Mesoporous Tin-Doped Indium Oxide Thin Films: Effect of Mesostructure on Electrical Conductivity. *Sci. Technol. Adv. Mater.* **2011**, *12* (2), 025005.
(110) Wang, Y.; Brezesinski, T.; Antonietti, M.; Smarsly, B. Ordered Mesoporous Sb-, Nb-, and Ta-Doped SnO_2 Thin Films with Adjustable Doping Levels and High Electrical Conductivity. *ACS Nano* **2009**, *3* (6), 1373−1378.
(111) Brinker, C. J. Evaporation-Induced Self-Assembly: Functional Nanostructures Made Easy. *MRS Bull.* **2004**, *29* (9), 631−640.
(112) Crepaldi, E. L.; de A. A. Soler-Illia, G. J.; Bouchara, A.; Grosso, D.; Durand, D.; Sanchez, C. Controlled Formation of Highly Ordered Cubic and Hexagonal Mesoporous Nanocrystalline Yttria−Zirconia and Ceria−Zirconia Thin Films Exhibiting High Thermal Stability. *Angew. Chemie Int. Ed.* **2003**, *42* (3), 347−351.
(113) Romeo, M.; Bak, K.; El Fallah, J.; Le Normand, F.; Hilaire, L. XPS Study of the Reduction of Cerium Dioxide. *Surf. Interface Anal.* **1993**, *20* (6), 508−512.
(114) Skála, T.; Šutara, F.; Prince, K. C.; Matolín, V. Cerium Oxide Stoichiometry Alteration via Sn Deposition: Influence of Temperature. *J. Electron Spectrosc. Relat. Phenom.* **2009**, *169* (1), 20−25.

https://doi.org/10.1021/acsnano.1c11032
ACS Nano 2022, 16, 3182−3193

4. Conclusions and Outlook

The influence of the surface area on the electronic and ionic transport properties of nanocrystalline zirconia-based oxide materials with ordered and non-ordered (meso-) pores was elucidated in the framework of this doctoral thesis. Zirconia-based oxide materials, such as yttria-stabilized zirconia (YSZ) and CeO_2- and TiO_2-coated YSZ, are promising materials for electrochemical applications, for example, in catalysis, energy storage and gas sensing. The (meso-)porous oxides with a high specific surface area exhibit different defect chemical and transport properties compared to their bulk counterparts. These differences directly arise from their structure and morphology. Apart from the synthesis via EISA and PLD as well as the structural characterization by several techniques, this work comprises the electrochemical characterization via EIS of the different materials employed. Here, the total conductivity values are determined as a function of temperature, oxygen activity, and relative humidity.

Mesoporous 8YSZ thin films with nanocrystalline walls were synthesized by sol-gel dip-coating. While the samples with 17 and 24 nm pores have an ordered cubic pore network, the sample with the largest pores of 40 nm shows a non-ordered structure. The electrochemical investigations of sol–gel-derived YSZ thin films reveal no effect of pore size on the total electrical conductivity, i.e. the samples with different pore sizes but with a comparable wall thickness exhibits comparable conductivity values.

One major aspect of this thesis was the modification of the surface properties of (meso-)porous YSZ using ALD. ALD allows the design of novel thin-film composites with tailored physicochemical properties. It has a great influence on the electrical properties of the composite material due to changes in morphology and microstructure of the coating with varying thickness, affecting directly the space charge region at the interface between the two different phases. Structural characterization confirmed conformal and uniform TiO_2- and CeO_2-coatings on the inner surface of (meso-)porous YSZ thin films.

In this thesis, it is shown that the thickness of CeO_2 coating on mesoporous YSZ thin films affects the total conductivity of the composite material. The reason is that the Ce^{3+}/Ce^{4+} ratio depends on the coating thickness, which is directly related to changes in the total conductivity. The concentration of Ce^{3+} decreases with increasing ceria thickness at the surface. A high concentration of Ce^{3+} ions results in a dominant electronic conductivity, caused by small polaron hopping of electrons between Ce^{3+} and Ce^{4+} lattice sites. The CeO_2/YSZ nanocomposites with a 3 nm ceria coating show mixed ionic/electronic conductivity. Those with a 7 nm thin ceria coating only exhibit ionic conductivity due to a reduced concentration of Ce^{3+} in the coating layer.

The characterization of ALD-derived TiO_2 coatings on porous PLD-derived 9.5YSZ thin films reveals an amorphous-to-crystalline phase transition when increasing the coating thickness from 6 to 18 nm. Characterization using EIS confirms that the crystallinity significantly influences the total electrical and protonic conductivity of the composites. Under dry atmosphere, the results demonstrate that the modification of the surface by the deposition of a titania layer gives rise to an additional electronic transport pathway in the composite material. In addition, the surface protonic conductivity is determined by the thickness of the titania layer. While an amorphous titania coating layer results in a decrease of the protonic conductivity compared to pristine YSZ, the crystalline TiO_2 layer increases the protonic conductivity contribution again. Thus, the surface can be designed to optimize water adsorption on the surface for enhanced protonic conductivity, which can be beneficial to the performance of electrochemical devices, such as proton exchange membranes or water sensors.

The results emphasize that the transport properties and defect chemistry are directly related to the surface properties of the material. Here, the thickness and crystallinity of the surface coating play a decisive role. Therefore, surface engineering of (meso-)porous thin films via ALD allows the development of nanocomposites, with tailored electrochemical properties.

The findings of this doctoral thesis contribute to a better understanding of the influence of the surface on the defect chemical properties and conduction mechanisms in nanostructured metal oxides. They reveal that surface engineering is a promising approach for the design of composites with tailored properties for electrochemical device applications. However, there are still several aspects, which need to be considered in the future. In case of mesoporous YSZ, the influence of the pore wall thickness (fixed pore size) on the transport properties needs to be characterized. In addition, the ideal pore size (fixed pore wall thickness) for achieving the highest electrical conductivity may be of interest. Future investigations may also include the evaluation of the effect of surface area on the wettability properties and the protonic transport mechanisms. Finally, the influence of other coating materials, such as Al_2O_3, on the protonic transport properties of composite materials should be investigated.

5. References

1 M. N. Tsampas, F. M. Sapountzi and P. Vernoux, Applications of yttria stabilized zirconia (YSZ) in catalysis, *Catal. Sci. Technol.*, 2015, **5**, 4884–4900.

2 C. Julien, Technological applications of solid state ionics, *Mater. Sci. Eng. B*, 1990, **6**, 9–28.

3 P. Knauth and H. L. Tuller, Solid-State Ionics: Roots, Status, and Future Prospects, *J. Am. Ceram. Soc.*, 2004, **85**, 1654–1680.

4 C. S. Sunandana, *Introduction to Solid State Ionics*, CRC Press, 2015.

5 M. Han, X. Tang, H. Yin and S. Peng, Fabrication, microstructure and properties of a YSZ electrolyte for SOFCs, *J. Power Sources*, 2007, **165**, 757–763.

6 M. D. Gross, J. M. Vohs and R. J. Gorte, An Examination of SOFC Anode Functional Layers Based on Ceria in YSZ, *J. Electrochem. Soc.*, 2007, **154**, B694.

7 I. Chang, S. Ji, J. Park, M. H. Lee and S. W. Cha, Ultrathin YSZ Coating on Pt Cathode for High Thermal Stability and Enhanced Oxygen Reduction Reaction Activity, *Adv. Energy Mater.*, 2015, **5**, 1402251.

8 Y. Chen, N. Orlovskaya, M. Klimov, X. Huang, D. Cullen, T. Graule and J. Kuebler, Layered YSZ/SCSZ/YSZ Electrolytes for Intermediate Temperature SOFC Part I: Design and Manufacturing, *Fuel Cells*, 2012, **12**, 722–731.

9 O. Kwon and G. Choi, Electrical conductivity of thick film YSZ, *Solid State Ionics*, 2006, **177**, 3057–3062.

10 E. Ivers-Tiffée, in *Encyclopedia of Electrochemical Power Sources*, Elsevier, 2009, pp. 181–187.

11 A. Kirubakaran, S. Jain and R. K. Nema, A review on fuel cell technologies and power electronic interface, *Renew. Sustain. Energy Rev.*, 2009, **13**, 2430–2440.

12 H. Tuller, Ionic conduction in nanocrystalline materials, *Solid State Ionics*, 2000, **131**, 143–157.

13 J. Maier, Ionic transport in nano-sized systems, *Solid State Ionics*, 2004, **175**, 7–12.

14 J. Maier, Nanoionics: ion transport and electrochemical storage in confined systems, *Nat. Mater.*, 2005, **4**, 805–815.

15 I. Kosacki, C. Rouleau, P. Becher, J. Bentley and D. Lowndes, Nanoscale effects on the ionic conductivity in highly textured YSZ thin films, *Solid State Ionics*, 2005, **176**, 1319–1326.

16 I. Kosacki, C. M. Rouleau, P. F. Becher, J. Bentley and D. H. Lowndes, Surface/Interface-Related Conductivity in Nanometer Thick YSZ Films, *Electrochem. Solid-State Lett.*, 2004, **7**, A459.

17 A. Karthikeyan, C.-L. Chang and S. Ramanathan, High temperature conductivity studies on nanoscale yttria-doped zirconia thin films and size effects, *Appl. Phys. Lett.*, 2006, **89**, 183116.

18 Y. W. Zhang, S. Jin, Y. Yang, G. B. Li, S. J. Tian, J. T. Jia, C. S. Liao and C. H. Yan, Electrical conductivity enhancement in nanocrystalline $(RE_2O_3)_{0.08}(ZrO_2)_{0.92}$

(RE=Sc, Y) thin films, *Appl. Phys. Lett.*, 2000, **77**, 3409–3411.

19 R. A. De Souza, M. J. Pietrowski, U. Anselmi-Tamburini, S. Kim, Z. A. Munir and M. Martin, Oxygen diffusion in nanocrystalline yttria-stabilized zirconia: the effect of grain boundaries., *Phys. Chem. Chem. Phys.*, 2008, **10**, 2067–72.

20 C. Korte, A. Peters, J. Janek, D. Hesse and N. Zakharov, Ionic conductivity and activation energy for oxygen ion transport in superlattices—the semicoherent multilayer system YSZ (ZrO_2 + 9.5 mol% Y_2O_3)/Y_2O_3, *Phys. Chem. Chem. Phys.*, 2008, **10**, 4623.

21 C. Korte, J. Keppner, A. Peters, N. Schichtel, H. Aydin and J. Janek, Coherency strain and its effect on ionic conductivity and diffusion in solid electrolytes – an improved model for nanocrystalline thin films and a review of experimental data, *Phys. Chem. Chem. Phys.*, 2014, **16**, 24575–24591.

22 N. Schichtel, C. Korte, D. Hesse and J. Janek, Elastic strain at interfaces and its influence on ionic conductivity in nanoscaled solid electrolyte thin films—theoretical considerations and experimental studies, *Phys. Chem. Chem. Phys.*, 2009, **11**, 3043.

23 E. Navickas, M. Gerstl, G. Friedbacher, F. Kubel and J. Fleig, Measurement of the across-plane conductivity of YSZ thin films on silicon, *Solid State Ionics*, 2012, **211**, 58–64.

24 X. Guo, E. Vasco, S. Mi, K. Szot, E. Wachsman and R. Waser, Ionic conduction in zirconia films of nanometer thickness, *Acta Mater.*, 2005, **53**, 5161–5166.

25 J. L. M. Rupp, Ionic diffusion as a matter of lattice-strain for electroceramic thin films, *Solid State Ionics*, 2012, **207**, 1–13.

26 J. Jiang and J. L. Hertz, On the variability of reported ionic conductivity in nanoscale YSZ thin films, *J. Electroceramics*, 2014, **32**, 37–46.

27 A. Tschöpe, Grain size-dependent electrical conductivity of polycrystalline cerium oxide II: Space charge model, *Solid State Ionics*, 2001, **139**, 267–280.

28 Y. M. Chiang, E. B. Lavik, I. Kosacki, H. L. Tuller and J. Y. Ying, Nonstoichiometry and Electrical Conductivity of Nanocrystalline CeO_{2-x}, *J. Electroceramics*, 1997, **1**, 7–14.

29 S. P. Muhoza, T. E. Barrett, M. A. Cottam, S. E. Soll, M. D. Yuce, V. S. Prathab, S. K. Hambright, M. Rezazad, O. Racchi and M. D. Gross, High Surface Area SOFC Electrode Materials Prepared at Traditional Sintering Temperatures, *J. Electrochem. Soc.*, 2018, **165**, F46–F54.

30 M. T. Elm, J. D. Hofmann, C. Suchomski, J. Janek and T. Brezesinski, Ionic Conductivity of Mesostructured Yttria-Stabilized Zirconia Thin Films with Cubic Pore Symmetry—On the Influence of Water on the Surface Oxygen Ion Transport, *ACS Appl. Mater. Interfaces*, 2015, **7**, 11792–11801.

31 R. S. Kempegowda, N. Laosiripojana and S. Assabumrungrat, High temperature desulfurization over nano-scale high surface area ceria for application in SOFC, *Korean J. Chem. Eng.*, 2008, **25**, 223–230.

32 M. J. Synodis, C. L. Porter, N. M. Vo, A. J. L. Reszka, M. D. Gross and R. C. Snyder, A Model to Predict Percolation Threshold and Effective Conductivity of Infiltrated Electrodes for Solid Oxide Fuel Cells, *J. Electrochem. Soc.*, 2013, **160**, F1216–F1224.

33 A. J. L. Reszka, R. C. Snyder and M. D. Gross, Insights into the Design of SOFC

Infiltrated Electrodes with Optimized Active TPB Density via Mechanistic Modeling, *J. Electrochem. Soc.*, 2014, **161**, F1176–F1183.

34 P. Hartmann, T. Brezesinski, J. Sann, A. Lotnyk, J.-P. Eufinger, L. Kienle and J. Janek, Defect Chemistry of Oxide Nanomaterials with High Surface Area: Ordered Mesoporous Thin Films of the Oxygen Storage Catalyst CeO_2 –ZrO_2, *ACS Nano*, 2013, **7**, 2999–3013.

35 Q. Lu, G. Vardar, M. Jansen, S. R. Bishop, I. Waluyo, H. L. Tuller and B. Yildiz, Surface Defect Chemistry and Electronic Structure of $Pr_{0.1}Ce_{0.9}O_{2-\delta}$ Revealed in Operando, *Chem. Mater.*, 2018, **30**, 2600–2606.

36 S. Kim, R. Merkle and J. Maier, Oxygen nonstoichiometry of nanosized ceria powder, *Surf. Sci.*, 2004, **549**, 196–202.

37 Y.-L. Lee and D. Morgan, Ab initio defect energetics of perovskite (001) surfaces for solid oxide fuel cells: A comparative study of $LaMnO_3$ versus $SrTiO_3$ and $LaAlO_3$, *Phys. Rev. B*, 2015, **91**, 195430.

38 C.-C. Chao, J. S. Park, X. Tian, J. H. Shim, T. M. Gür and F. B. Prinz, Enhanced Oxygen Exchange on Surface-Engineered Yttria-Stabilized Zirconia, *ACS Nano*, 2013, **7**, 2186–2191.

39 J. Zhang, H. Kumagai, K. Yamamura, S. Ohara, S. Takami, A. Morikawa, H. Shinjoh, K. Kaneko, T. Adschiri and A. Suda, Extra-low-temperature oxygen storage capacity of CeO_2 nanocrystals with cubic facets., *Nano Lett.*, 2011, **11**, 361–4.

40 J. Druce and J. A. Kilner, Improvement of Oxygen Surface Exchange Kinetics for CGO with Surface Treatment, *J. Electrochem. Soc.*, 2014, **161**, F99–F104.

41 R. Di Monte and J. Kašpar, Nanostructured CeO_2–ZrO_2 mixed oxides, *J. Mater. Chem.*, 2005, **15**, 633–648.

42 B. Hu, Y. Wang, Z. Zhu, C. Xia and H. J. M. Bouwmeester, Measuring oxygen surface exchange kinetics on mixed-conducting composites by electrical conductivity relaxation, *J. Mater. Chem. A*, 2015, **3**, 10296–10302.

43 G. Preda, A. Migani, K. M. Neyman, S. T. Bromley, F. Illas and G. Pacchioni, Formation of Superoxide Anions on Ceria Nanoparticles by Interaction of Molecular Oxygen with Ce^{3+} Sites, *J. Phys. Chem. C*, 2011, **115**, 5817–5822.

44 X. Huang and M. J. Beck, Size-Dependent Appearance of Intrinsic O x q "Activated Oxygen" Molecules on Ceria Nanoparticles, *Chem. Mater.*, 2015, **27**, 5840–5844.

45 Y. Gong, R. L. Patel, X. Liang, D. Palacio, X. Song, J. B. Goodenough and K. Huang, Atomic Layer Deposition Functionalized Composite SOFC Cathode $La_{0.6}Sr_{0.4}Fe_{0.8}Co_{0.2}O_{3-\delta}$-$Gd_{0.2}Ce_{0.8}O_{1.9}$: Enhanced Long-Term Stability, *Chem. Mater.*, 2013, **25**, 4224–4231.

46 J. W. Shin, D. Go, S. H. Kye, S. Lee and J. An, Review on process-microstructure-performance relationship in ALD-engineered SOFCs, *J. Phys. Energy*, 2019, **1**, 042002.

47 J. M. Paige, Y. Cheng, P. A. Pepin, C. D. Curran, D. Sun, M. U. Chen, S. McIntosh, J. M. Vohs and R. J. Gorte, Surface modification of SOFC cathodes by Co, Ni, and Pd oxides, *Solid State Ionics*, 2019, **341**, 115051.

48 A. S. Yu, R. Küngas, J. M. Vohs and R. J. Gorte, Modification of SOFC Cathodes by Atomic Layer Deposition, *J. Electrochem. Soc.*, 2013, **160**, F1225–

F1231.

49 C. Brahim, A. Ringuedé, M. Cassir, M. Putkonen and L. Niinistö, Synthesis and Properties of ZrO2-In2O3 Overlayers by ALD on the Porous SOFC State-of-the Art Cathode, *ECS Trans.*, 2019, **3**, 261–269.

50 B. Medina-Lott, M. Tassé, C. Brahim, A. Ringuedé, L. Niinistö and M. Cassir, Challenges Of Thin Layers For SOFC Devices: From Low-Cost Chemical Bath Deposition (CBD) to Atomic Layer Deposition (ALD), *ECS Trans.*, 2019, **35**, 601–608.

51 L. A. Dubraja, D. Boll, C. Reitz, D. Wang, D. Belić, A. Mazilkin, B. Breitung, H. Hahn, M. T. Elm and T. Brezesinski, Thin Films of Thermally Stable Ordered Mesoporous Rh_2O_3(I) for Visible-Light Photocatalysis and Humidity Sensing, *ACS Appl. Nano Mater.*, 2019, **2**, 7126–7133.

52 P. Cop, E. Celik, K. Hess, Y. Moryson, P. Klement, M. T. Elm and B. M. Smarsly, Atomic Layer Deposition of Nanometer-Sized CeO_2 Layers in Ordered Mesoporous ZrO_2 Films and Their Impact on the Ionic/Electronic Conductivity, *ACS Appl. Nano Mater.*, 2020, **3**, 10757–10766.

53 R. J. D. Tilley, *Defects in Solids*, John Wiley & Sons, Inc., Hoboken, NJ, USA, 2008.

54 J. Jiang and J. L. Hertz, On the variability of reported ionic conductivity in nanoscale YSZ thin films, *J. Electroceramics*, 2014, **32**, 37–46.

55 S. Lany, Semiconducting transition metal oxides, *J. Phys. Condens. Matter*, 2015, **27**, 283203.

56 H. L. Tuller and A. S. Nowick, Small polaron electron transport in reduced CeO_2 single crystals, *J. Phys. Chem. Solids*, 1977, **38**, 859–867.

57 K. Michel, J.-P. Eufinger, G. Ulbrich, M. Lerch, J. Janek and M. T. Elm, Combining two redox active rare earth elements for oxygen storage – electrical properties and defect chemistry of ceria–praseodymia single crystals, *Phys. Chem. Chem. Phys.*, 2017, **19**, 17661–17669.

58 A. J. Bosman and H. J. van Daal, Small-polaron versus band conduction in some transition-metal oxides, *Adv. Phys.*, 1970, **19**, 1–117.

59 K. Moorjani and C. Feldman, Electrical Properties of Amorphous Semiconductors, *Rev. Mod. Phys.*, 1964, **36**, 1042–1049.

60 J. D. Bernal, in *Structural Chemistry of Glasses*, Elsevier, 2002, pp. 307–373.

61 S. Hunklinger, in *Festkörperphysik*, De Gruyter, 2014, pp. 411–476.

62 P. Riente and T. Noël, Application of metal oxide semiconductors in light-driven organic transformations, *Catal. Sci. Technol.*, 2019, **9**, 5186–5232.

63 L. Almar, A. Tarancón, T. Andreu, M. Torrell, Y. Hu, G. Dezanneau and A. Morata, Mesoporous ceramic oxides as humidity sensors: A case study for gadolinium-doped ceria, *Sensors Actuators B Chem.*, 2015, **216**, 41–48.

64 T. Wagner, S. Haffer, C. Weinberger, D. Klaus and M. Tiemann, Mesoporous materials as gas sensors, *Chem. Soc. Rev.*, 2013, **42**, 4036–4053.

65 J. Zhao, Y. Liu, X. Li, G. Lu, L. You, X. Liang, F. Liu, T. Zhang and Y. Du, Highly sensitive humidity sensor based on high surface area mesoporous $LaFeO_3$ prepared by a nanocasting route, *Sensors Actuators B Chem.*, 2013, **181**, 802–809.

66 P. Zhang, S.-Y. Huang and B. N. Popov, Mesoporous Tin Oxide as an Oxidation-Resistant Catalyst Support for Proton Exchange Membrane Fuel Cells, *J. Electrochem. Soc.*, 2010, **157**, B1163.

67 J. D. Halla, M. Mamak, D. E. Williams and G. A. Ozin, Meso-SiO_2–$C_{12}EO_{10}OH$–CF_3SO_3H—A Novel Proton-Conducting Solid Electrolyte, *Adv. Funct. Mater.*, 2003, **13**, 133–138.

68 F. M. Vichi, Nanopore Ceramic Membranes as Novel Electrolytes for Proton Exchange Membranes, *Electrochem. Solid-State Lett.*, 1999, **2**, 313.

69 S. Kim, H. J. Avila-Paredes, S. Wang, C.-T. Chen, R. A. De Souza, M. Martin and Z. A. Munir, On the conduction pathway for protons in nanocrystalline yttria-stabilized zirconia, *Phys. Chem. Chem. Phys.*, 2009, **11**, 3035.

70 B. Scherrer, M. V. F. Schlupp, D. Stender, J. Martynczuk, J. G. Grolig, H. Ma, P. Kocher, T. Lippert, M. Prestat and L. J. Gauckler, On Proton Conductivity in Porous and Dense Yttria Stabilized Zirconia at Low Temperature, *Adv. Funct. Mater.*, 2013, **23**, 1957–1964.

71 H. J. Avila-Paredes, J. Zhao, S. Wang, M. Pietrowski, R. A. De Souza, A. Reinholdt, Z. A. Munir, M. Martin and S. Kim, Protonic conductivity of nano-structured yttria-stabilized zirconia: dependence on grain size, *J. Mater. Chem.*, 2010, **20**, 990–994.

72 E. Celik, R. S. Negi, M. Bastianello, D. Boll, A. Mazilkin, T. Brezesinski and M. T. Elm, Tailoring the protonic conductivity of porous yttria-stabilized zirconia thin films by surface modification, *Phys. Chem. Chem. Phys.*, 2020, **22**, 11519–11528.

73 S. Miyoshi, Y. Akao, N. Kuwata, J. Kawamura, Y. Oyama, T. Yagi and S. Yamaguchi, Low-Temperature Protonic Conduction Based on Surface Protonics: An Example of Nanostructured Yttria-Doped Zirconia, *Chem. Mater.*, 2014, **26**, 5194–5200.

74 H. J. Avila-Paredes, C.-T. Chen, S. Wang, R. A. De Souza, M. Martin, Z. Munir and S. Kim, Grain boundaries in dense nanocrystalline ceria ceramics: exclusive pathways for proton conduction at room temperature, *J. Mater. Chem.*, 2010, **20**, 10110.

75 G. Gregori, M. Shirpour and J. Maier, Proton Conduction in Dense and Porous Nanocrystalline Ceria Thin Films, *Adv. Funct. Mater.*, 2013, **23**, 5861–5867.

76 H. Takamura and N. Takahashi, Electrical conductivity of dense nanocrystalline ceria under humidified atmosphere, *Solid State Ionics*, 2010, **181**, 100–103.

77 M. T. Colomer, Nanoporous Anatase Thin Films as Fast Proton-Conducting Materials, *Adv. Mater.*, 2006, **18**, 371–374.

78 I. G. Tredici, F. Maglia, C. Ferrara, P. Mustarelli and U. Anselmi-Tamburini, Mechanism of Low-Temperature Protonic Conductivity in Bulk, High-Density, Nanometric Titanium Oxide, *Adv. Funct. Mater.*, 2014, **24**, 5137–5146.

79 F. Maglia, I. G. Tredici, G. Spinolo and U. Anselmi-Tamburini, Low temperature proton conduction in bulk nanometric TiO_2 prepared by high-pressure field assisted sintering, *J. Mater. Res.*, 2012, **27**, 1975–1981.

80 D. H. Everett, Manual of Symbols and Terminology for Physicochemical Quantities and Units, Appendix II: Definitions, Terminology and Symbols in Colloid and Surface Chemistry, *Pure Appl. Chem.*, 1972, **31**, 577–638.

81 S. Ø. Stub, K. Thorshaug, P. M. Rørvik, T. Norby and E. Vøllestad, The influence of acceptor and donor doping on the protonic surface conduction of TiO_2, *Phys. Chem. Chem. Phys.*, 2018, **20**, 15653–15660.

82 B. Scherrer, M. V. F. Schlupp, D. Stender, J. Martynczuk, J. G. Grolig, H. Ma, P. Kocher, T. Lippert, M. Prestat and L. J. Gauckler, On Proton Conductivity in Porous and Dense Yttria Stabilized Zirconia at Low Temperature, *Adv. Funct. Mater.*, 2013, **23**, 1957–1964.

83 S. Raz, K. Sasaki, J. Maier and I. Riess, Characterization of adsorbed water layers on Y_2O_3-doped ZrO_2, *Solid State Ionics*, 2001, **143**, 181–204.

84 P. Atkins and P. J. de, Atkins' Physical Chemistry, 7th Edition, *Oxford Univ. Press*, 2002.

85 H. J. Avila-Paredes, C. T. Chen, S. Wang, R. A. De Souza, M. Martin, Z. Munir and S. Kim, Grain boundaries in dense nanocrystalline ceria ceramics: Exclusive pathways for proton conduction at room temperature, *J. Mater. Chem.*, 2010, **20**, 990–994.

86 K.-D. Kreuer, Proton Conductivity: Materials and Applications, *Chem. Mater.*, 1996, **8**, 610–641.

87 T. Ueki and M. Watanabe, Macromolecules in Ionic Liquids: Progress, Challenges, and Opportunities, *Macromolecules*, 2008, **41**, 3739–3749.

88 S. Ø. Stub, E. Vøllestad and T. Norby, Mechanisms of Protonic Surface Transport in Porous Oxides: Example of YSZ, *J. Phys. Chem. C*, 2017, **121**, 12817–12825.

89 S. Miyoshi, Y. Akao, N. Kuwata, J. Kawamura, Y. Oyama, T. Yagi and S. Yamaguchi, Water uptake and conduction property of nano-grained yttria-doped zirconia fabricated by ultra-high pressure compaction at room temperature, *Solid State Ionics*, 2012, **207**, 21–28.

90 K. L. Kliewer and J. S. Koehler, Space charge in ionic crystals. I. General approach with application to NaCl, *Phys. Rev.*, 1965, **140**, 897–902.

91 K. L. Kliewer, Space Charge in Ionic Crystals. II. The Electron Affinity and Impurity Accumulation, *Phys. Rev.*, 1965, **140**, A1241–A1246.

92 J. Maier, Ionic conduction in space charge regions, *Prog. Solid State Chem.*, 1995, **23**, 171–263.

93 J. Maier, *Physical Chemistry of Ionic Materials: Ions and Electrons in Solids*, 2004.

94 G. Gregori, R. Merkle and J. Maier, Ion conduction and redistribution at grain boundaries in oxide systems, *Prog. Mater. Sci.*, 2017, **89**, 252–305.

95 A. Tschöpe, Grain size-dependent electrical conductivity of polycrystalline cerium oxide I. Experiments, *Solid State Ionics*, 2001, **139**, 255–265.

96 P. Lejček, in *Springer Series in Materials Science*, 2010, pp. 5–24.

97 P. Lupetin, G. Gregori and J. Maier, Mesoscopic Charge Carriers Chemistry in Nanocrystalline $SrTiO_3$, *Angew. Chemie Int. Ed.*, 2010, **49**, 10123–10126.

98 X. Guo, W. Sigle and J. Maier, Blocking Grain Boundaries in Yttria-Doped and Undoped Ceria Ceramics of High Purity, *J. Am. Ceram. Soc.*, 2003, **86**, 77–87.

99 S. Kim and J. Maier, On the Conductivity Mechanism of Nanocrystalline Ceria, *J.*

Electrochem. Soc., 2002, **149**, J73.

100 J. M. Polfus, K. Toyoura, F. Oba, I. Tanaka and R. Haugsrud, Defect chemistry of a $BaZrO_3$ Σ3 (111) grain boundary by first principles calculations and space–charge theory, *Phys. Chem. Chem. Phys.*, 2012, **14**, 12339.

101 J. Joo and G. Choi, Electrical conductivity of YSZ film grown by pulsed laser deposition, *Solid State Ionics*, 2006, **177**, 1053–1057.

102 E. Ivers-Tiffée, A. Weber and D. Herbstritt, Materials and technologies for SOFC-components, *J. Eur. Ceram. Soc.*, 2001, **21**, 1805–1811.

103 P. Manning, The kinetics of oxygen transport in 9.5 mol % single crystal yttria stabilised zirconia, *Solid State Ionics*, 1997, **100**, 1–10.

104 M. A. Parkes, D. A. Tompsett, M. D'Avezac, G. J. Offer, N. P. Brandon and N. M. Harrison, The atomistic structure of yttria stabilised zirconia at 6.7 mol%: an ab initio study, *Phys. Chem. Chem. Phys.*, 2016, **18**, 31277–31285.

105 L. Treccani, T. Yvonne Klein, F. Meder, K. Pardun and K. Rezwan, Functionalized ceramics for biomedical, biotechnological and environmental applications., *Acta Biomater.*, 2013, **9**, 7115–50.

106 A. Nakamura and J. B. Wagner, Defect Structure, Ionic Conductivity, and Diffusion in Yttria Stabilized Zirconia and Related Oxide Electrolytes with Fluorite Structure, *J. Electrochem. Soc.*, 1986, **133**, 1542–1548.

107 A. Pimenov, Ionic conductivity and relaxations in ZrO_2–Y_2O_3 solid solutions, *Solid State Ionics*, 1998, **109**, 111–118.

108 J. Luo, D. P. Almond and R. Stevens, Ionic Mobilities and Association Energies from an Analysis of Electrical Impedance of ZrO_2–Y_2O_3 Alloys, *J. Am. Ceram. Soc.*, 2004, **83**, 1703–1708.

109 S. Ikeda, O. Sakurai, K. Uematsu, N. Mizutani and M. Kato, Electrical conductivity of yttria-stabilized zirconia single crystals, *J. Mater. Sci.*, 1985, **20**, 4593–4600.

110 D. W. Strickler and W. G. Carlson, Ionic Conductivity of Cubic Solid Solutions in the System CaO-Y_2O_3-ZrO_2, *J. Am. Ceram. Soc.*, 1964, **47**, 122–127.

111 I. Procházka, J. Čížek, O. Melikhova, J. Kuriplach, W. Anwand, G. Brauer, T. E. Konstantinova, I. A. Danilenko and I. A. Yashchishyn, Defect Behaviour in Yttria-Stabilised Zirconia Nanomaterials Studied by Positron Annihilation Techniques, *Defect Diffus. Forum*, 2012, **331**, 181–199.

112 C. Haering, A. Roosen and H. Schichl, Degradation of the electrical conductivity in stabilised zirconia systems Part I: yttria-stabilised zirconia, *Solid State Ionics*, 2005, **176**, 253–259.

113 X. Vendrell and A. R. West, Electrical Properties of Yttria-Stabilized Zirconia, YSZ Single Crystal: Local AC and Long Range DC Conduction, *J. Electrochem. Soc.*, 2018, **165**, F966–F975.

114 I. Valov, Nitrogen-doped zirconia (YSZ:N): Preparation, characterization and electrode processes, JLU Gießen, 2006.

115 S. Grieshammer, T. Zacherle and M. Martin, Entropies of defect formation in ceria from first principles, *Phys. Chem. Chem. Phys.*, 2013, **15**, 15935.

116 R. Gillen, S. J. Clark and J. Robertson, The nature of the electronic band gap in lanthanide oxides, *Phys. Rev. B*, 2012, **87**, 125116.

117 E. Kusmierek, A CeO_2 Semiconductor as a Photocatalytic and Photoelectrocatalytic Material for the Remediation of Pollutants in Industrial Wastewater: A Review, *Catalysts*, 2020, **10**, 1435.

118 M. Nolan, S. Grigoleit, D. C. Sayle, S. C. Parker and G. W. Watson, Density functional theory studies of the structure and electronic structure of pure and defective low index surfaces of ceria, *Surf. Sci.*, 2005, **576**, 217–229.

119 D. Reyes-Coronado, G. Rodríguez-Gattorno, M. E. Espinosa-Pesqueira, C. Cab, R. de Coss and G. Oskam, Phase-pure TiO_2 nanoparticles: anatase, brookite and rutile., *Nanotechnology*, 2008, **19**, 145605.

120 Y. Chimupala, G. Hyett, R. Simpson, R. Mitchell, R. Douthwaite, S. J. Milne and R. D. Brydson, Synthesis and characterization of mixed phase anatase TiO_2 and sodium-doped TiO_2 (B) thin films by low pressure chemical vapour deposition (LPCVD), *RSC Adv.*, 2014, **4**, 48507–48515.

121 T. Bak, J. Nowotny, M. Rekas and C. C. Sorrell, Defect chemistry and semiconducting properties of titanium dioxide: I. Intrinsic electronic equilibrium, *J. Phys. Chem. Solids*, 2003, **64**, 1043–1056.

122 T. Bak, J. Nowotny, M. Rekas and C. C. Sorrell, Defect chemistry and semiconducting properties of titanium dioxide: II. Defect diagrams, *J. Phys. Chem. Solids*, 2003, **64**, 1057–1067.

123 T. Bak, J. Nowotny, M. Rekas and C. C. Sorrell, Defect chemistry and semiconducting properties of titanium dioxide: III. Mobility of electronic charge carriers, *J. Phys. Chem. Solids*, 2003, **64**, 1069–1087.

124 M. K. Nowotny, T. Bak, J. Nowotny and C. C. Sorrell, Titanium vacancies in nonstoichiometric TiO_2 single crystal, *Phys. status solidi*, 2005, **242**, R88–R90.

125 T. Bak, J. Nowotny and M. K. Nowotny, Defect Disorder of Titanium Dioxide, *J. Phys. Chem. B*, 2006, **110**, 21560–21567.

126 V. C. Anitha, A. N. Banerjee and S. W. Joo, Recent developments in TiO_2 as n- and p-type transparent semiconductors: synthesis, modification, properties, and energy-related applications, *J. Mater. Sci.*, 2015, **50**, 7495–7536.

127 I. A. Hümmelgen, “Oxide semiconductors for solar energy conversion—titanium dioxide”. Author: Janusz Nowotny, *J. Solid State Electrochem.*, 2012, **16**, 2287–2287.

128 M. K. Nowotny, L. R. Sheppard, T. Bak and J. Nowotny, Defect Chemistry of Titanium Dioxide. Application of Defect Engineering in Processing of TiO_2 -Based Photocatalysts, *J. Phys. Chem. C*, 2008, **112**, 5275–5300.

129 M. K. Nowotny, T. Bak and J. Nowotny, Electrical Properties and Defect Chemistry of TiO_2 Single Crystal. I. Electrical Conductivity, *J. Phys. Chem. B*, 2006, **110**, 16270–16282.

130 J. Nowotny, M. Radecka and M. Rekas, Semiconducting Properties of undoped TiO_2, *J. Phys. Chem. Solids*, 1997, **58**, 927–937.

131 H. M. Smith and A. F. Turner, Vacuum Deposited Thin Films Using a Ruby Laser, *Appl. Opt.*, 1965, **4**, 147.

132 Y. Lin, *Advanced Nano Deposition Methods*, Wiley, 2016.

133 S. Rajendiran, D. Meehan and E. Wagenaars, Plasma-enhanced pulsed laser deposition of copper oxide and zinc oxide thin films, *AIP Adv.*, 2020, **10**, 065323.

134 J. Huotari, V. Kekkonen, J. Puustinen, J. Liimatainen and J. Lappalainen, Pulsed Laser Deposition for Improved Metal-oxide Gas Sensing Layers, *Procedia Eng.*, 2016, **168**, 1066–1069.

135 H. Guo, D. Sun, W. Wang, Z. Gai, I. Kravchenko, J. Shao, L. Jiang, T. Z. Ward, P. C. Snijders, L. Yin, J. Shen and X. Xu, Growth diagram of $La_{0.7}Sr_{0.3}MnO_3$ thin films using pulsed laser deposition, *J. Appl. Phys.*, 2013, **113**, 234301.

136 S. Zhang, J. M. Ting and W. Y. Wu, *Functional Thin Films Technology*, CRC Press, 2021.

137 H. Schwarz and H. A. Tourtellotte, Vacuum Deposition by High-Energy Laser with Emphasis on Barium Titanate Films, *J. Vac. Sci. Technol.*, 1969, **6**, 373–378.

138 A. Infortuna, A. S. Harvey and L. J. Gauckler, Microstructures of CGO and YSZ Thin Films by Pulsed Laser Deposition, *Adv. Funct. Mater.*, 2008, **18**, 127–135.

139 S. Heiroth, T. Lippert, A. Wokaun and M. Döbeli, Microstructure and electrical conductivity of YSZ thin films prepared by pulsed laser deposition, *Appl. Phys. A*, 2008, **93**, 639–643.

140 B. N. Nair, T. Suzuki, Y. Yoshino, S. Gopalakrishnan, T. Sugawara, S.-I. Nakao and H. Taguchi, An Oriented Nanoporous Membrane Prepared by Pulsed Laser Deposition, *Adv. Mater.*, 2005, **17**, 1136–1140.

141 S. Heiroth, R. Ghisleni, T. Lippert, J. Michler and A. Wokaun, Optical and mechanical properties of amorphous and crystalline yttria-stabilized zirconia thin films prepared by pulsed laser deposition, *Acta Mater.*, 2011, **59**, 2330–2340.

142 S. K. Pandey, O. P. Thakur, R. Raman, A. Goyal and A. Gupta, Structural and optical properties of YSZ thin films grown by PLD technique, *Appl. Surf. Sci.*, 2011, **257**, 6833–6836.

143 S. Heiroth, R. Frison, J. L. M. Rupp, T. Lippert, E. J. Barthazy Meier, E. Müller Gubler, M. Döbeli, K. Conder, A. Wokaun and L. J. Gauckler, Crystallization and grain growth characteristics of yttria-stabilized zirconia thin films grown by pulsed laser deposition, *Solid State Ionics*, 2011, **191**, 12–23.

144 C. Sanchez, C. Boissière, D. Grosso, C. Laberty and L. Nicole, Design, Synthesis, and Properties of Inorganic and Hybrid Thin Films Having Periodically Organized Nanoporosity, *Chem. Mater.*, 2008, **20**, 682–737.

145 Y. Ren, Z. Ma and P. G. Bruce, Ordered mesoporous metal oxides: synthesis and applications, *Chem. Soc. Rev.*, 2012, **41**, 4909.

146 P. Innocenzi and L. Malfatti, Mesoporous thin films: properties and applications, *Chem. Soc. Rev.*, 2013, **42**, 4198.

147 D. Gu and F. Schüth, Synthesis of non-siliceous mesoporous oxides, *Chem. Soc. Rev.*, 2014, **43**, 313–344.

148 Y. Deng, J. Wei, Z. Sun and D. Zhao, Large-pore ordered mesoporous materials templated from non-Pluronic amphiphilic block copolymers., *Chem. Soc. Rev.*, 2013, **42**, 4054–70.

149 N. D. Petkovich and A. Stein, Controlling macro- and mesostructures with hierarchical porosity through combined hard and soft templating, *Chem. Soc. Rev.*, 2013, **42**, 3721–3739.

150 C. J. Brinker, Y. Lu, A. Sellinger and H. Fan, Evaporation-Induced Self-

Assembly: Nanostructures Made Easy, *Adv. Mater.*, 1999, **11**, 579–585.

151 M. Ogawa, Formation of Novel Oriented Transparent Films of Layered Silica-Surfactant Nanocomposites, *J. Am. Chem. Soc.*, 1994, **116**, 7941–7942.

152 W. Zhang, Y. Tian, H. He, L. Xu, W. Li and D. Zhao, Recent advances in the synthesis of hierarchically mesoporous TiO_2 materials for energy and environmental applications, *Natl. Sci. Rev.*, 2020, **7**, 1702–1725.

153 W. Li, Z. Wu, J. Wang, A. A. Elzatahry and D. Zhao, A Perspective on Mesoporous TiO_2 Materials, *Chem. Mater.*, 2014, **26**, 287–298.

154 B. Sun, J. Horvat, H. S. Kim, W.-S. Kim, J. Ahn and G. Wang, Synthesis of Mesoporous α-Fe_2O_3 Nanostructures for Highly Sensitive Gas Sensors and High Capacity Anode Materials in Lithium Ion Batteries, *J. Phys. Chem. C*, 2010, **114**, 18753–18761.

155 K. Brezesinski, J. Haetge, J. Wang, S. Mascotto, C. Reitz, A. Rein, S. H. Tolbert, J. Perlich, B. Dunn and T. Brezesinski, Ordered Mesoporous α-Fe_2O_3 (Hematite) Thin-Film Electrodes for Application in High Rate Rechargeable Lithium Batteries, *Small*, 2011, **7**, 407–414.

156 J. Ma, Y. Ren, X. Zhou, L. Liu, Y. Zhu, X. Cheng, P. Xu, X. Li, Y. Deng and D. Zhao, Pt Nanoparticles Sensitized Ordered Mesoporous WO_3 Semiconductor: Gas Sensing Performance and Mechanism Study, *Adv. Funct. Mater.*, 2018, **28**, 1705268.

157 J. Zhang, D. Leng, L. Zhang, G. Li, F. Ma, J. Gao, H. Lu and B. Zhu, Porosity and oxygen vacancy engineering of mesoporous WO_3 nanofibers for fast and sensitive low-temperature NO_2 sensing, *J. Alloys Compd.*, 2021, **853**, 157339.

158 R. W. Johnson, A. Hultqvist and S. F. Bent, A brief review of atomic layer deposition: from fundamentals to applications, *Mater. Today*, 2014, **17**, 236–246.

159 A. Pakkala and M. Putkonen, in *Handbook of Deposition Technologies for Films and Coatings (Third Edition)*, ed. P. M. Martin, William Andrew Publishing, Boston, Third Edit., 2010, pp. 364–391.

160 S. M. George, Atomic Layer Deposition: An Overview, *Chem. Rev.*, 2010, **110**, 111–131.

161 T. Suntola and J. Antson, Method for producing compound thin films, *US Pat.*, 1977, **4**, 430.

6. Appendix

6.1. Supporting Information (Publication III)

Supporting Information

Design of ordered mesoporous CeO_2/YSZ nanocomposite thin films with mixed ionic/electronic conductivity via surface engineering

Erdogan Celik*[a], Pascal Cop[a,b], Rajendra S. Negi[a], Andrey Mazilkin[c], Yanjiao Ma[c], Philip Klement[a,d], Jörg Schörmann[a,d], Sangam Chatterjee[a,d], Torsten Brezesinski[c] and Matthias T. Elm*[a,b,d]

[a] Center for Materials Research, Justus-Liebig-University Giessen, Heinrich-Buff-Ring 16, 35392 Giessen, Germany.

[b] Institute of Physical Chemistry, Justus-Liebig-University Giessen, Heinrich-Buff-Ring 17, 35392 Giessen, Germany

[c] Institute of Nanotechnology, Karlsruhe Institute of Technology (KIT), Hermann-von-Helmholtz Platz 1, 76344 Eggenstein-Leopoldshafen, Germany

[d] Institute of Experimental Physics I, Justus-Liebig-University Giessen, Heinrich-Buff-Ring 16, 35392 Giessen, Germany

E-mail: erdogan.celik@materialwiss.uni-giessen.de, matthias.elm@phys.chemie.uni-giessen.de

S1

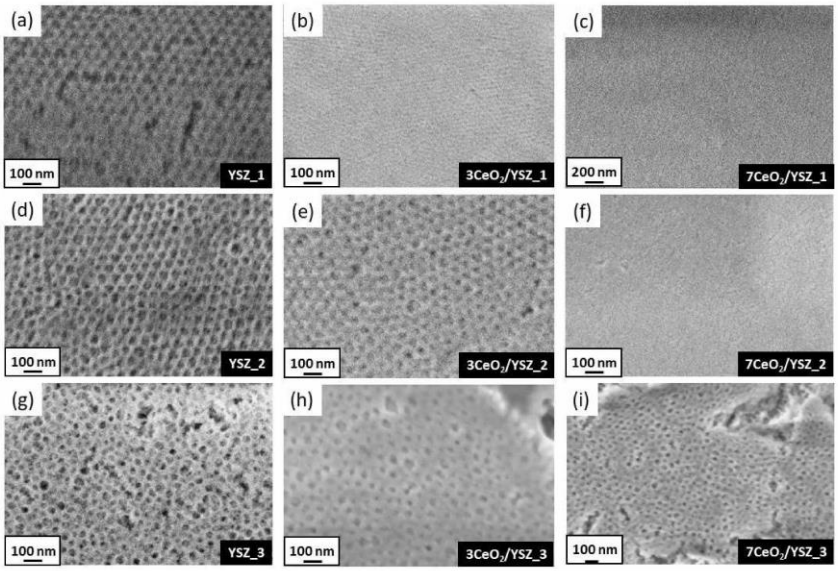

Figure S1. SEM images of uncoated as well as 3 and 7 nm CeO_2-coated (a-c) YSZ_1, (d-f) YSZ_2, and (g-i) YSZ_3 thin films.

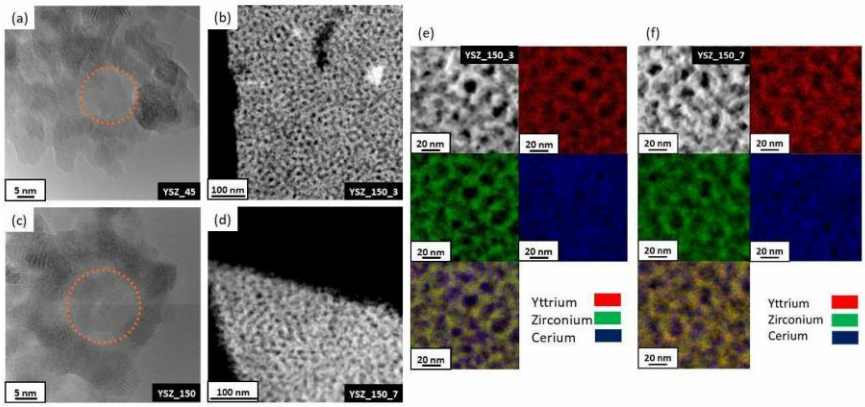

Figure S2. HRTEM images of uncoated (a) YSZ_1 and (c) YSZ_2 thin films. HAADF-STEM images of (b) 3 nm and (d) 7 nm CeO_2-coated YSZ_2 thin films and (e, f) corresponding EDS maps for Y (in red), Zr (in green), and Ce (in blue).

S2

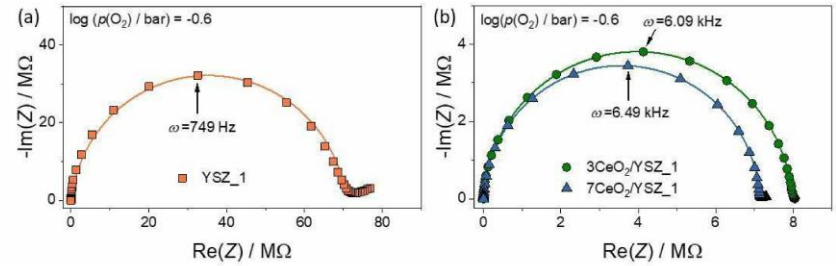

Figure S3. Impedance spectra of (a) uncoated YSZ_1 and (b) 3 and 7 nm CeO_2-coated YSZ_1 thin films at 450 °C.

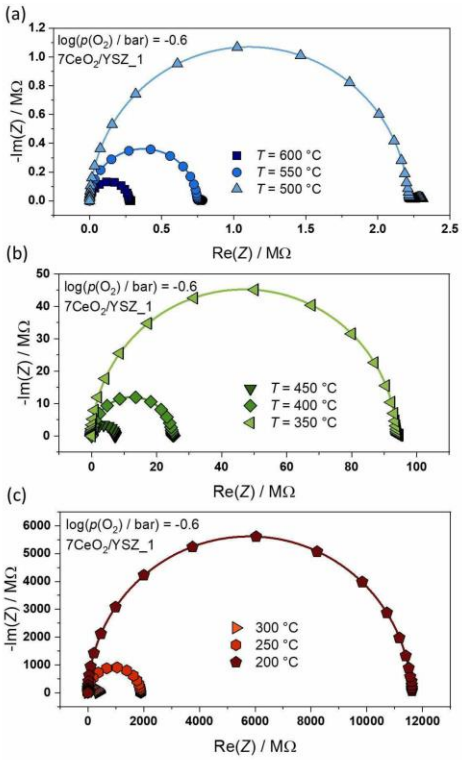

Figure S4. Impedance spectra of 7 nm CeO_2-coated YSZ_1 thin films (a) from 500 to 600 °C, (b) 350 to 450 °C, and (c) 200 to 300 °C.

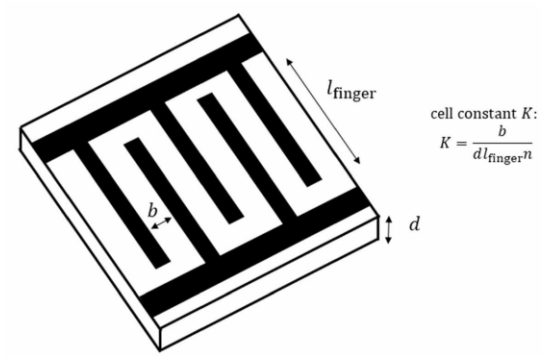

Figure S5. Schematic illustration of the interdigitated Pt electrodes used for electrochemical characterization. n denotes the number of electrode fingers, l_{finger} is their length, b is the distance between the fingers, and d represents the thickness of the thin film.

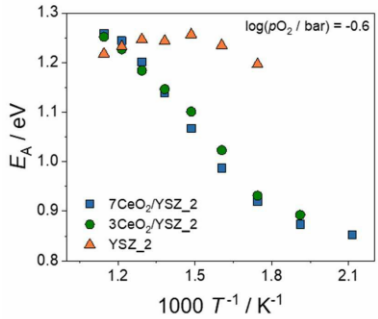

Figure S6. Activation energy as a function of temperature for uncoated as well as 3 and 7 nm CeO_2-coated YSZ_2 thin films.

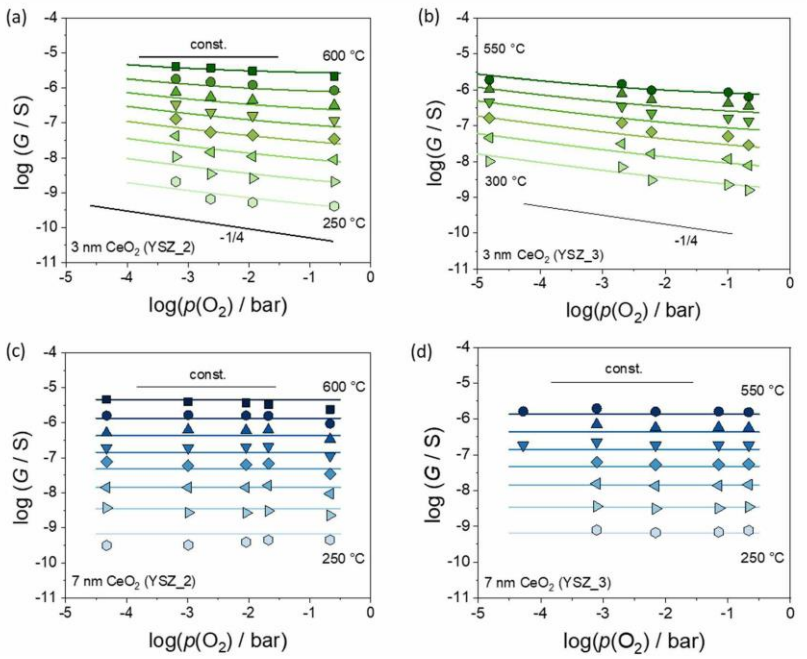

Figure S7. Oxygen partial-pressure-dependence of the total conductivity for (a, b) 3 nm and (c, d) 7 nm CeO_2-coated YSZ_2 and YSZ_3 thin films. Solid lines are fits to the experimental data.

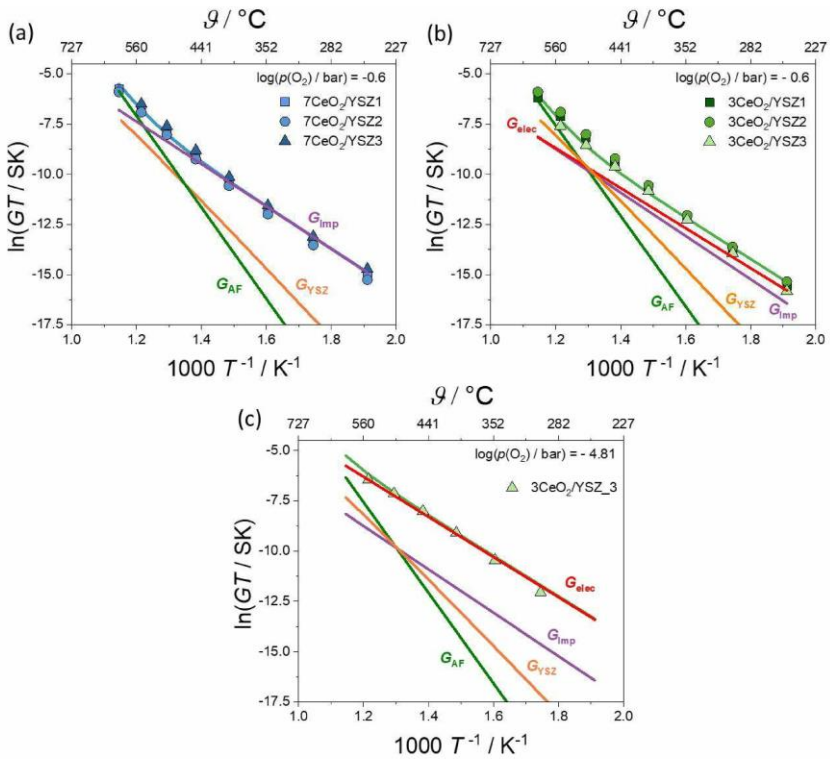

Figure S8. Arrhenius plots of the total conductance for (a) 7 nm and (b) 3 nm CeO_2-coated YSZ thin films at log(p(O_2)/bar) = -0.6 as well as for (c) 3 nm CeO_2-coated YSZ_3 at log(p(O_2)/bar) = -4.8.

Table S1. Fitting parameters of the transport properties for 3 and 7 nm CeO_2-coated YSZ thin films.

Sample	$G_{0,\mathrm{Imp}}$ / SK	$E_{\mathrm{A,mig}}$ / eV	$G_{0,\mathrm{AF}}$ / 10^8 SK	$E_{\mathrm{A,AF}}$ / eV	$G'_{0,\mathrm{elec}}$ / SKbar$^{1/4}$	$E_{\mathrm{A,elec}}$ / eV
3 nm CeO_2	66.7 (±12.0)	0.93 (±0.03)	2.8 (±0.3)	1.94 (±0.02)	18.2 (±1.0)	0.86 (±0.02)
7 nm CeO_2	200 (±12)	0.91 (±0.03)	5.9 (±1.0)	1.96 (±0.02)	-	-

Table S2. Recipes for the synthesis of mesoporous 8 mol-% yttria-stabilized zirconia (YSZ) thin films.

Sample	Diblock copolymer	Solvents			Pore size
YSZ_1	PIB_{53}-*b*-PEO_{45} (40 mg)	2-Methoxyethanol (0.5 mL)	Ethanol (1.5 mL)	Glacial acetic acid (0.25 mL)	17 nm
YSZ_2	PIB_{107}-*b*-PEO_{150} (40 mg)	2-Methoxyethanol (0.5 mL)	Ethanol (1.5 mL)	Glacial acetic acid (0.25 mL)	24 nm
YSZ_3	PIB_{357}-*b*-PEO_{454} (40 mg)	2-Methoxyethanol (0.8 mL)	Tetrahydrofuran (1.2 mL)	Glacial acetic acid (0.20 mL)	40 nm

6.2. Publications and Conference Contributions

Publications.

Erdogan Celik, Rajendra S. Negi, Michele Bastianello, Dominic Boll, Andrey Mazilkin, Torsten Brezesinski and Matthias T. Elm, Tailoring the protonic conductivity of porous yttria-stabilized zirconia thin films by surface modification, *Phys. Chem. Chem. Phys*., **2020**, 22, 11519-11528.

Erdogan Celik, Yanjiao Ma, Torsten Brezesinski and Matthias T. Elm, Ordered Mesoporous Metal Oxides for Electrochemical Applications: Correlation between Structure, Electrical Properties and Device Performance, *Phys. Chem. Chem. Phys*., **2021**, 23, 10706-10735.

Erdogan Celik, Pascal Cop, Rajendra S. Negi, Andrey Mazilkin, Yanjiao Ma, Philip Klement, Jörg Schörmann, Sangam Chatterjee, Torsten Brezesinski and Matthias T. Elm, Design of Ordered Mesoporous CeO_2–YSZ Nanocomposite Thin Films with Mixed Ionic/Electronic Conductivity via Surface Engineering, *ACS Nano*, **2022**, 16, 3182-3193.

Pascal Cop, Erdogan Celik, Kevin Hess, Yannik Moryson, Philip Klement, Matthias T. Elm and Bernd M. Smarsly, Atomic Layer Deposition of Nanometer-Sized CeO_2 Layers in Ordered Mesoporous ZrO_2 Films and Their Impact on the Ionic/Electronic Conductivity, *ACS Appl. Nano Mater.*, **2020**, 3, 11, 10757–10766.

Rajendra S. Negi, Erdogan Celik, Ruijun Pan, Robert Stäglich, Jürgen Senker and Matthias T. Elm, Insights into the Positive Effect of Post-Annealing on the Electrochemical Performance of Al_2O_3-Coated Ni-Rich NCM Cathodes for Lithium-Ion Batteries, *ACS Appl. Energy Mater*., **2021**, 4, 4, 3369–3380.

Conference Contributions.

Erdogan Celik and Matthias T. Elm, Influence of Surface Modification on The Electrical Conductivity of Porous Yttria-Stabilized Zirconia (YSZ) Thin Films, International Workshop on Impedance Spectroscopy, Chemnitz, **2018** (poster presentation).

Erdogan Celik and Matthias T. Elm, Influence of Surface Modification on The Electrical Conductivity of Porous Yttria-Stabilized Zirconia (YSZ) Thin Films, Materialforschungstag Mittelhessen, Marburg, **2018** (poster presentation).

Erdogan Celik and Matthias T. Elm, Influence of Surface Modification on The Electrical Conductivity of Porous Yttria-Stabilized Zirconia (YSZ) Thin Films, DPG-Frühjahrstagung, Regensburg, **2019** (oral presentation).

Erdogan Celik and Matthias T. Elm, Suppression of Proton Surface Conductivity in Porous Yttria-Stabilized Zirconia by Surface Modification, Materialforschungstag Mittelhessen, Gießen, **2019** (poster presentation).

Erdogan Celik and Matthias T. Elm, Suppression of Proton Surface Conductivity in Porous Yttria-Stabilized Zirconia by Surface Modification, SSI-22 International Conference on Solid State Ionics, PyeongChang, **2019** (poster presentation).